



b
**UNIVERSITÄT
BERN**

Graduate School for Cellular and Biomedical Sciences
University of Bern

Chemical effects on blood studied using label-free nanoscale analytics

PhD Thesis submitted by

Talia Bergaglio

for the degree of

PhD in Biomedical Sciences

Supervisor

Prof. Dr. Alex Dommann

ARTORG Center for Biomedical Engineering Research

Faculty of Medicine of the University of Bern

Co-advisor

Dr. Peter Niraj Nirmalraj

Transport at Nanoscale Interfaces Laboratory

Empa – Swiss Federal Laboratories for Material Science & Technology

Accepted by the Faculty of Medicine, the Faculty of Science and the
Vetsuisse Faculty of the University of Bern at the request of the Graduate
School for Cellular and Biomedical Sciences

Bern, Dean of the Faculty of Medicine

Bern, Dean of the Faculty of Science

Bern, Dean of the Vetsuisse Faculty Bern



This work is licensed under a Creative Commons Attribution 4.0 International License
except for Chapter 4

Acknowledgements

The research work presented in this thesis was performed at Empa. I would like to express my deepest gratitude to *Dr. Peter Nirmalraj* for giving me the possibility to do a PhD in his group. Peter, I cannot thank you enough for your mentorship, guidance, and continuous support. Your willingness to listen, offer advice, and share your own experiences has been a constant source of inspiration. You have not only guided my research but also provided invaluable life lessons. Your mentorship has taught me resilience in the face of challenges, the value of perseverance, and the art of critical thinking. I will always cherish our long conversations about research and life in general.

I am thankful to *Prof. Dr. Alex Dommann* for being my PhD supervisor and for always offering his support and invaluable insights that have been fundamental to the successful completion of my doctoral journey.

I also thank the members of my thesis committee, *Prof. Dominik Obrist* and *Prof. Dr. med. Susanne Wegener* for their valuable insights and critical feedback that have enriched the quality of this thesis.

I extend my appreciation to *Prof. Michel Calame* for providing the necessary resources, facilities, and research opportunities that have made this work possible.

My time at Empa could not have been the same without the support and friendship of numerous colleagues, to whom I extend my heartfelt appreciation. I am especially grateful for my past colleagues of the Biosensing group, *Dr. Yves Mermoud*, *Dr. Olena Synhaivska* and *Dr. Lars Lüder* for welcoming me in the group, for all the teamwork, and the fun moments we shared. Lars, thank you for all your support and help with Blender and for our endless office conversations.

I would also like to thank the whole team of the Transport at Nanoscale Interfaces Laboratory. *Roman Furrer*, thank you for all our conversations, for your entertaining insights about Switzerland and for the epic Durak tournaments during the coffee breaks. *Jacopo Oswald* and *Gökhan Kara*, my fellow soon-to-be Drs., thank you for always listening, for the great conversations and for all the moments we shared. *Dr. Eleni Mavrana*, thank you for being there for me and for all the wonderful

Acknowledgements

conversations. *Dr. Mirjana Dimitrievska*, thank you for all your valuable advices and enjoyable conversations.

I had the great pleasure of sharing the office with a fantastic group of colleagues. Special thanks to *Peter Lendway*, *Frederik Van Veen* and the newest member of the Biosensing group, *Dr. Lily Henry*, for creating a fun and enjoyable office atmosphere. Thanks to *Dr. Nico Kummer* for already supporting me with this work during his first month as a postdoc in the Biosensing group.

Also, I would like to give special thanks to *Rico Muff*, *Daniel Aeppli* and *Natalie Aeschbach-Jones* for all their assistance with IT and administrative matters.

During my time at Empa, I had the pleasure of partly working in Empa St. Gallen, where I received the greatest support from many colleagues. I would like to express my gratitude to *Dr. Cordula Hirsch* for welcoming me in St. Gallen, for introducing me to the laboratory facilities and for all her support with the experiments. I extend my appreciation to *Dr. Vanesa Ayala* for her support, collaboration and friendship. Special thanks also to *Dr. Giorgia Giovannini*, *Yvette Hannig* and *Alexandra Rippl*.

I could not have done this without the unconditional support of my family. Thank you for always being there for me even if geographically distant. To mom and dad, thank you for always believing in me and for giving me the opportunity and freedom to travel and explore the world. To my brother and sister, thank you for being my role models and for encouraging me to find my path in life. To my friends, both in Italy and Switzerland, thank you for your support and encouragement, for all the laughs, great dinners and board game nights.

A special thank goes to my rock, *Federico*. You have been my unwavering source of support and encouragement throughout this journey. Thank you for your patience, for the pep talks when I was feeling low, and for all your advices. Thank you for always listening to me talking about blood and all things related, and for simply being there, especially during the tough moments.

I also want to dedicate a special note of thanks to my dog *Cleo*. You are a constant source of joy and unconditional love. One of the perks of doing a PhD during a pandemic was that we got to spend a lot of extra time together at home.

This achievement is a reflection of the collective support and encouragement I have received from all of you. Thank you all for being part of my PhD journey!

Talia

Contents

Acknowledgements.....	iii
Contents.....	v
Notation	vii
Abstract	x
1. Introduction.....	1
1.1. Background	1
1.2. The current research gap	6
1.3. Label-free digital holotomography	7
1.4. Hypothesis and aim of the thesis	10
1.5. Outline of the thesis	11
2. Development of the imaging and analysis workflow for label-free digital holotomographic microscopy	12
2.1. Best practices for blood sample preparation	12
2.2. Image processing and analysis	18
3. Label-free digital holotomography reveals ibuprofen-induced morphological changes to red blood cells	21
3.1. Abstract	21
3.2. Introduction	22
3.3. Results	25
3.4. Discussion	40
3.5. Conclusions	44
3.6. Methods	45
4. 3D holo-tomographic mapping of COVID-19 microclots in blood to assess disease severity	49
4.1. Abstract	49
4.2. Introduction	50

4.3. Results	53
4.4. Discussion	62
4.5. Methods	66
5. Urea as a fibrin solubilizer: revisited using nanoscale imaging	70
5.1. Abstract	70
5.2. Introduction	71
5.3. Results	74
5.4. Discussion	79
5.5. Methods	84
6. Capturing the effect of Levodopa on α -Synuclein fibrils at the nanoscale	88
6.1. Abstract	88
6.2. Introduction	89
6.3. Results	90
6.4. Discussion	92
6.5. Methods	96
7. Overall discussion and outlook	98
7.1. A bird's eye view of the thesis.....	98
7.2. What's next?	101
Bibliography	104
List of figures	125
List of tables	129
Appendix	130
A. Appendix to Chapter 3.....	131
A.1. Molecular dynamics model details.....	131
B. Appendix to Chapter 4.....	160
C. Appendix to Chapter.....	169
List of scientific publications and presentations	170

Notation

Abbreviations

Symbol	Definition
3D	Three-dimensional
AD	Alzheimer's disease
AFM	Atomic force microscopy
AI	Artificial intelligence
AIS	acute ischemic stroke
ARDS	Acute respiratory disease syndrome
A β	Amyloid- β
CBC	Complete blood count
cDOT	Common-path diffraction tomography
CHL	Cholesterol
CIL	Confidence interval lower
CIU	Confidence interval upper
COVID-19	Coronavirus disease 2019
CSF	Cerebrospinal fluid
DHTM	Digital holo-tomographic microscopy
DIIHA	Drug-induced immune hemolytic anemia
DVT	Deep vein thrombosis
EDTA	Ethylenediaminetetraacetic acid
ExM	Expansion microscopy
Hb	Hemoglobin
HT	Holotomography
K2EDTA	Dipotassium ethylenediaminetetraacetic acid
L-dopa	Levodopa
MCH	Mean corpuscular Hb
MCHC	Mean corpuscular Hb concentration

Continued on next page

Notation

Symbol (cont.)	Definition (cont.)
MD	Molecular dynamics
MI	Myocardial infarction
ML	Machine learning
MRI	Magnetic resonance imaging
MSD	Mean square displacements
NA	Numerical aperture
NETS	Neutrophil extracellular traps
NPT	Isothermal-isobaric ensemble
NSAID	Nonsteroidal anti-inflammatory drugs
NVT	Canonical ensemble
OTC	Over-the-counter
PASC	Post-acute sequelae of COVID
PBS	Phosphate-buffered saline
PCVS	Post-COVID-19 vaccination syndrome
PD	Parkinson's disease
PE	Pulmonary embolism
PET	Positron emission tomography
PFA	Paraformaldehyde
PME	Particle-mesh Ewald
POC	Point-of-care
POPC	Palmitoyl Oleoyl PhosphoCholine
POPE	Palmitoyl Oleoyl PhosphoEthanolamine
POPS	Palmitoyl Oleoyl PhosphoSerine
PPP	Platelet-poor plasma
PRP	Platelet-rich plasma
PT	Prothrombin time
RBC	Red blood cell
RI	Refractive index
S/V	Surface area-to-volume
SA	Surface area
SARS-CoV-2	Severe acute respiratory syndrome coronavirus 2
SCA	Sickle cell anemia
SCD	Sickle cell disease
SCT	Sickle cell trait

Continued on next page

Notation

Symbol (cont.)	Definition (cont.)
SEM	Scanning electron microscopy
SIRS	Systemic inflammatory response syndrome
SSM	Stearoyl SphingoMyelin
TEG	Thromboelastography
VWF	von Willebrand factor

Abstract

The analysis of biofluids plays a pivotal role in the identification and tracking of disease-related biomarkers. Among these biofluids, blood is of particular interest due to its complex composition of cellular and molecular constituents, which offer insights into both organ-specific health (e.g., heart, liver, brain) and an individual's overall well-being. Furthermore, the minimally-invasive nature of blood collection makes it an ideal source for health information. Recent advancements in the digitization of diagnostic pathology and data analysis tools have paved the way for the automation of blood-based analytical tests, reducing the need for time-consuming and labor-intensive procedures. Leveraging high-throughput and automated techniques, driven by digital imaging and machine learning-based data analytics, holds great potential for improving the efficiency of blood sample processing and analysis, thereby expediting patient screening and monitoring.

In the first part of the thesis, we show the development of the image and analysis framework for blood screening, based on digital holo-tomographic microscopy (DHTM). First, we optimized the best practices for blood collection and blood dilution in order to achieve high-resolution images. We subsequently developed the image processing pipeline, including noise filtering, background removal, image segmentation, feature recognition, and data extraction. For the morphological assessment of blood cells, we trained a machine learning classifier to automatically classify red blood cells (RBCs) based on their shape. Finally, we validated the morphological and chemical parameters obtained from DHTM- and atomic force microscopy (AFM)-based measurements in the context of RBC rheological properties and blood coagulation dynamics.

In order to investigate the chemical effects on blood, we demonstrated the capability of DHTM to perform real-time, label-free monitoring of ibuprofen's concentration-dependent and time-dependent effects on red blood cells (RBCs) from a healthy donor. To do so, we first validated our imaging and analysis framework for the screening of RBCs to identify shape changes between healthy and sickle cell disease

donors. Additionally, we tested our methodology for the real-time monitoring of cell shape changes upon variations to the chemical environment, with the addition of urea and hydrogen peroxide-induced oxidative stress. We then applied our DHTM-based approach for the label-free detection and quantification of ibuprofen-induced RBC shape changes. Here, we propose the employment of our DHTM-based technique for drug monitoring and we highlight the importance of taking into account RBC rheological properties when assessing safety levels for dose-dependent drug intake.

The enduring health repercussions of the COVID-19 pandemic and its ongoing long-term effects have initiated extensive research efforts aimed at unraveling the pathogenic mechanisms and comprehending the heterogeneous nature of symptoms. We extended the application of our DHTM-based imaging and analysis framework for the detection and characterization of microclots by screening plasma samples of COVID-19 donors.

In order to delve into the nanoscale analysis of micrometer-sized blood clots and to elucidate the mechanisms by which chemicals and medications affect clot dissolution, we employed a combinatorial imaging platform, including DHTM and AFM analysis, to resolve and quantify the morphological parameters of synthetically-prepared blood clot fragments in aqueous solution. The proposed nanoscale investigation of fibrin-rich clots could provide comprehensive insights into the role of blood clot morphology and composition in the development of targeted treatment strategies for thrombotic diseases.

In the transition from cell to protein characterization using nanoscale analytics, we sought to investigate the dose dependent effect of Levodopa treatment on α -Synuclein aggregation dynamics using AFM. In view of the identification of protein aggregates implicated in neurodegenerative disorders, like Alzheimer's and Parkinson's disease, in blood, it is crucial to determine the role of such medications in dissolving these aggregates and the potential dose-dependent adverse effects on blood rheology.

Altogether, this thesis introduces an innovative imaging and analysis platform for clinical level screening of blood-related pathologies and drug-induced cytotoxic effect. As digital diagnostic hematology continues to progress, our point-of-care analytical tool could help develop tailored therapeutic approaches to optimize treatment outcomes and to mitigate the risk of drug-related side effects, thereby playing a pivotal role in advancing the field of personalized medicine.

1. Introduction

1.1. Background

In the era of rapidly advancing biomedical technologies, innovative approaches for biomarker discovery, disease diagnostics, and personalized medicine are revolutionizing global health outcomes, making healthcare delivery more accessible and expeditious. Amidst these transformative developments, the comprehensive analysis of bodily fluids has become instrumental, providing invaluable insights into the physiological and pathological processes occurring within the human body. Biofluids, including blood, urine, cerebrospinal fluid (CSF), saliva, and sweat, containing a mixture of cells, proteins, metabolites, nucleic acids, and other biomolecules, collectively reflect an individual's biological state (Figure 1.1). Moreover, biofluid analysis not only enables the identification of biomarkers indicative

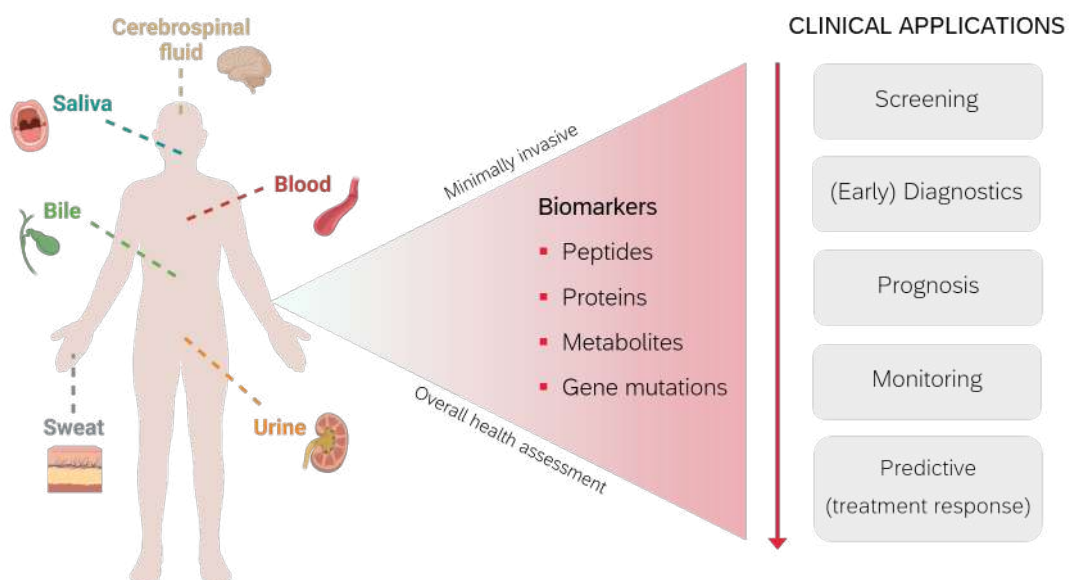


Figure 1.1. Overview of biofluids and the role of biomarkers for clinical applications, such as disease detection and monitoring. Partly created with BioRender.com.

1. Introduction

of various pathologies but also fosters a considerable understanding of the intricate interplay between different bodily systems [Xu & Veenstra, 2008]. Blood stands out as a dynamic and diverse source of information due to the abundance of cellular components and biomolecules it contains, including red blood cells (RBCs), white blood cells (WBCs), platelets, proteins, lipids, and metabolites [Bain, 2015]. The rich composition of blood and the minimal invasiveness of sampling make it routinely employed as an indispensable biofluid for disease diagnostics in the clinical setting. Over the years, scientific advancements have led to the identification of various blood-based biomarkers that serve as valuable indicators of disease, paving the way for early diagnosis and personalized treatment strategies.

Blood-based biomarkers encompass a wide range of molecular components within the blood, providing valuable information into the presence, progression, and prognosis of various diseases (Figure 1.2). For example, nucleic acid biomarkers, found in the bloodstream and including both DNA and RNA, have the capacity to carry genetic mutations that serve as indicators of inherited conditions or cancer-related changes [Schwarzenbach et al., 2011]. Additionally, cell-based biomarkers can offer insights

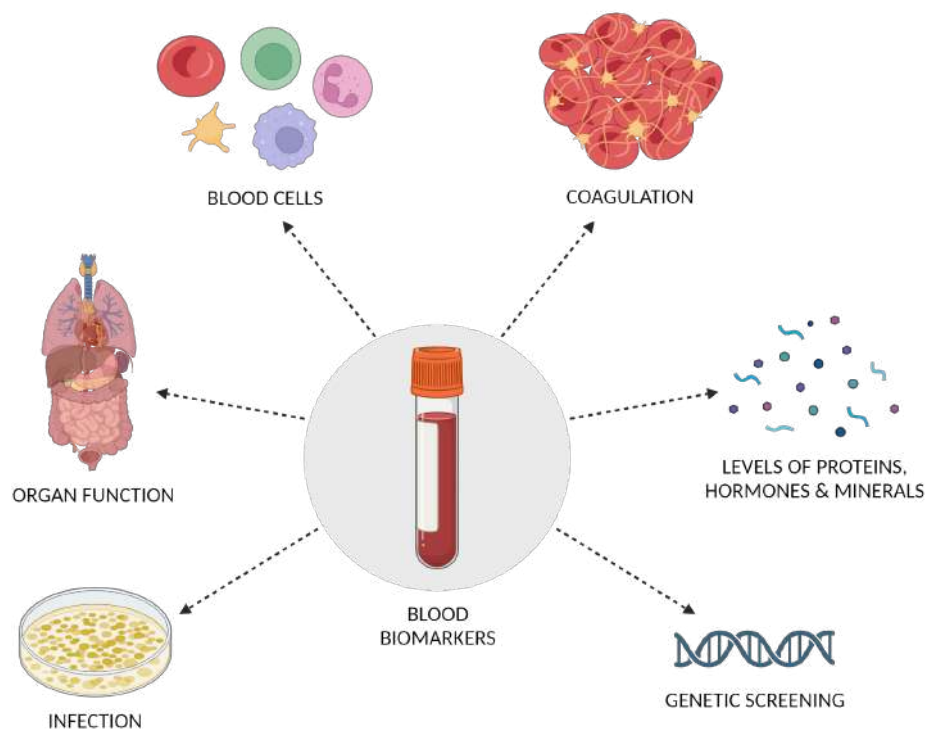


Figure 1.2. Overview of blood-based biomarkers used for diagnostics and prognostics in the clinical practice. Created with BioRender.com.

into infections, immune disorders, hematological malignancies, and drug-induced side effects, by assessing hemoglobin levels and the count and distribution of RBCs and WBCs, thus enabling the diagnosis of conditions such as anemia, leukemia, and autoimmune diseases [Bain, 2015]. Similarly, coagulation biomarkers, such as platelet count, prothrombin time (PT) and D-dimer levels, play an essential role in evaluating the presence of coagulation disorders, thrombotic events, and monitoring anticoagulant therapies [Gram et al., 2014]. With the advancements in proteomics and mass spectroscopy, protein biomarkers have become the most prominent type of blood-based biomarkers, serving as critical components in assessing organ function, advancing early disease diagnostics, and monitoring of disease progression [Veenstra et al., 2005]. Furthermore, protein biomarkers have facilitated the discovery of novel disease biomarkers, offering a deeper understanding of disease mechanisms and potential therapeutic targets in the realm of neurodegenerative diseases.

The ability to detect amyloid- β (A β) and tau proteins in blood makes blood a suitable biofluid that can mirror neuropathological changes and clinical decline in neurodegeneration [Carelli-Alinovi et al., 2019; Irmady et al., 2023; Iturria-Medina et al., 2020]. A recent example in the uncovering of blood-based biomarkers for early detection of neurodegenerative disorders was the observation of protein aggregates on RBCs that could serve as physical biomarkers for a screening platform for Alzheimer's disease (AD) [Nirmalraj et al., 2021]. Similarly, in Parkinson's disease, specific blood-based biomarkers associated with the aggregation of α -Synuclein (α -Syn) and alterations in metabolic pathways have been explored [Barbour et al., 2008; Chahine et al., 2014; Foulds et al., 2013; Magalhães & Lashuel, 2022]. These conditions, characterized by the gradual decline of cognitive and motor functions, have posed significant diagnostic and therapeutic challenges. Traditionally, the diagnosis of neurodegenerative diseases has relied heavily on clinical symptoms and neuroimaging techniques, which are often invasive and expensive [Koníčková et al., 2022]. However, recent advancements in the identification and validation of blood-based biomarkers have the potential to revolutionize the field by offering non-invasive and cost-effective diagnostic tools [Chahine et al., 2014; Magalhães & Lashuel, 2022; Mohanty et al., 2010; Nardini et al., 2022; Nirmalraj et al., 2021].

Optical imaging and quantitative analysis of cell and protein structures can provide invaluable insights on the pathophysiology of diseases, specifically in the field of hematology [Kim et al., 2021]. The digitization of standard diagnostic pathology information has made a remarkable transformation from traditional to digital practices [Lin et al., 2023]. Historically, pathologists relied on glass slides and

1. Introduction

microscopes to examine tissue specimens, a process limited by the physical distribution of samples, time-consuming workflows and the potential for human error [Bain, 2015]. However, advances in digital imaging technology and computational capabilities have enabled the digitization of tissue slides and the development of sophisticated image analysis algorithms [Baxi et al., 2022]. With the integration of digital pathology, pathologists can collaborate remotely, access vast digital data archives and improve automation, ultimately facilitating operation in resource-limited settings (Figure 1.3) [Dawson, 2022; El Alaoui et al., 2022]. This shift from traditional to digital pathology has not only enhanced the efficiency and accuracy of diagnosis but also opened doors to artificial intelligence (AI) and machine learning applications in pathology [Baxi et al., 2022; Lin et al., 2023].

Specifically, within the domain of diagnostic hematology, the automation of blood-based analytical processes can yield substantial benefits. Morphological examination of blood cells constitutes an essential element for the diagnosis of blood-related pathologies and infectious diseases [Bain, 2015; Beck, 2009]. Presently, the evaluation of cell morphology continues to rely on the manual examination of blood smears conducted by highly-trained personnel. This approach involves labor-intensive procedures and demands access to expensive laboratory facilities [Lin et al., 2023]. Image acquisition, cell recognition and shape classification processes can be automated to achieve more standardized, faster, and more efficient blood smear analysis. Digitalized methods for morphological assessment employ digital images and

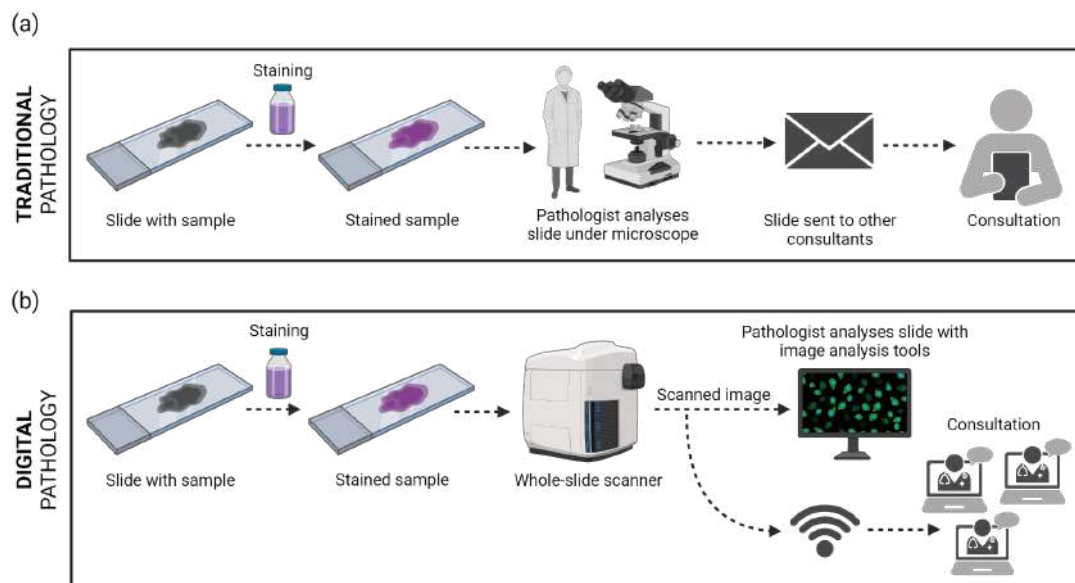


Figure 1.3. Overview of the transition from (a) traditional to (b) digital pathology. Created with BioRender.com.

1. Introduction

software algorithms to classify the shape and size of hematological cells, including RBCs and WBCs [Kim et al., 2022; Rawat et al., 2017; Yi et al., 2017; Yi et al., 2013]. For instance, an innovative method for the automated screening of sickle RBCs, indicative of sickle cell disease (SCD), was proposed by employing a 3D printed smartphone-based microscope combined with deep learning techniques [de Haan et al., 2020]. As a result, this would provide a point-of-care (POC) solution for the cost-effective and rapid screening of SCD even in resource-limited settings. Overall, the transition to digital pathology holds great promise in accelerating medical research, improving patient outcomes, and driving the development of personalized therapies.

Another important consideration is the integration of digital pathology into monitoring drug-induced effects on blood cells, leading to the development of patient-specific therapeutic strategies and efficient pharmacovigilance. Pharmaceutical agents, while designed to target specific biological pathways or diseases, can also impact hematopoiesis and the composition of blood [Garratty, 2010; Stoltz, 1981]. Hematological adverse reactions to medications can manifest as changes in blood cell morphology and function. By leveraging digital pathology, these alterations can be systematically and quantitatively assessed, providing a deeper understanding of how drugs impact hematological parameters and for the optimization of treatment regimens. Similarly, the effect of alterations to the chemical environment in the bloodstream on efficient oxygen transport can be assessed by monitoring RBC rheological properties [Sinha et al., 2015]. For instance, elevated levels of urea in the circulatory system, a condition known as uremia and primarily associated with chronic kidney disease, can be monitored by examining the occurrence of a morphological transition from normocytic RBCs to spherocytes and cell lysis [Khairy et al., 2010]. As personalized medicine continues to advance, the convergence of digital pathology and drug monitoring not only could enhance our capacity to customize drug therapies according to an individual's hematological profile but also holds great promise for incorporating diverse biomarkers into diagnostic and monitoring strategies, ultimately improving patient care.

1.2. The current research gap

Alongside the emergence of novel technological advancements, current hematology laboratories are encountering significant challenges in the contemporary medical landscape. One of the foremost issues is the need and concurrent shortage of highly-trained personnel for blood smear inspection, including experienced hematologists and skilled laboratory technologists, particularly in resource-limited areas [Obstfeld, 2023]. As the demand for diagnostic testing continues to surge, laboratories are confronted with the rising testing volume, which often strains existing resources and threatens timely test result turnaround. Simultaneously, there is an increase in patient complexity due to the presence of multiple comorbidities, thus demanding the interpretation of progressively intricate blood profiles [Roberts & De Montalembert, 2007]. Additionally, limitations in remote access to data and collaborative tools hinder pathologists' ability to share expertise and insights across geographical boundaries [de Haan et al., 2020]. Finally, inter-user variability in the interpretation of blood cell morphology poses a significant challenge in achieving consistent diagnostic outcomes. Addressing these challenges is imperative to ensure the continued effectiveness and efficiency of hematological diagnostics.

1.2.1. Clinical requirements

The digitization of diagnostic hematology processes unveils numerous prospects. Unlike traditional methods that rely on staining and the use of fluorescent markers to highlight specific cellular components, label-free imaging obviates the requirement for exogenous labeling agents while preserving the native state of blood cells, including their morphology. High-throughput and automated approaches, enabled by digital imaging and machine learning (ML)-based data analytics, can significantly enhance the efficiency of blood sample processing and analysis, facilitating the rapid screening and monitoring of patients. By leveraging such data-driven approaches, patterns, trends, and anomalies can be rapidly identified, ultimately facilitating the identification of novel biomarkers, the prediction of disease progression, and the tailoring of treatment strategies to individual patients [Walter et al., 2021]. This shift away from conventional "one-size-fits-all" approaches to medical treatment acknowledges the inherent variability among individuals in terms of genetics, metabolism, and overall health.

In view of the current challenges in the digitization of diagnostic hematology, there is a need for novel label-free, high-throughput and quantitative approaches, compatible

with clinical settings, aimed at enabling real-time analysis and characterization of blood components and thereby expediting disease detection and monitoring.

1.3. Label-free digital holotomography

Holotomography (HT) is a laser-based microscopy technique designed for the label-free acquisition of three-dimensional refractive index (RI) tomograms of microscopic specimens, including cells and tissues [Kim et al., 2021]. HT originates from the field of quantitative phase imaging (QPI), where both the amplitude and phase information of the light waves passing through a transparent specimen are converted into changes in brightness in the image and into a phase-shift image that is proportional to the optical thickness of the object, without the need for staining [Kim et al., 2021; Park et al., 2018]. Biological samples feature a valuable natural physical marker, namely the refractive index, which describes how the medium impacts the propagation of light [Liu et al., 2016]. RI is defined as follows (Equation 1.1):

$$n = \frac{c}{v} \quad (1.1)$$

Where c is the speed of light in vacuum and v is the speed of light. By exploiting the refractive index as an inherent imaging contrast for transparent or phase objects, RI tomogram measurements offer the advantage of label-free quantitative imaging of microscopic phase structures [Pollaro et al., 2016]. In contrast to the conventional interference microscopes, such as phase contrast and differential interference contrast microscopy, that can only provide qualitative information, holo-tomographic microscopy allows for the extraction of quantitative information about the three-dimensional morphology and the dry mass of individual cells and to perform continuous live cell imaging measurements of unstained cells [Barer, 1952; Kim et al., 2021; Sandoz et al., 2019].

One such tomographic QPI technique is digital holo-tomographic microscopy (DHTM). Although HT techniques have been studied in the field of cell biology since the early 2000s, the first commercially available DHT microscope was developed in 2013 [Cotte et al., 2013], namely the *3D Cell Explorer* (Nanolive SA, Switzerland) (Figure 1.4). DHTM operates based on the principles of holography and tomography. Holograms are 2D RI maps obtained via interferometry between the object and the reference laser beam ($\lambda = 520$ nm) (Figure 1.4). By acquiring multiple holographic images from different illumination angles through the rotation of a rotating arm 360° around the sample, a

1. Introduction

tomographic 3D reconstruction of the specimen is obtained (Figure 1.4). The combination of holography and tomography enables high-resolution imaging in all three spatial dimensions ($\Delta x,y = 200 \text{ nm}$, $\Delta z = 400 \text{ nm}$) and long-term monitoring of live cell dynamics in a label-free and non-invasive manner [Cotte et al., 2013; Pollaro et al., 2016].

DHTM has found diverse and impactful applications across various scientific disciplines, specifically in cell biology and in the biomedical field [Kim et al., 2021; Park et al., 2018]. This technique has enabled detailed investigations into cellular processes such as differentiation, motility, and response to stimuli, for instance in drug screening assays by monitoring the effects of pharmaceutical compounds on cellular behavior [Pollaro et al., 2016]. In particular, digital holography has been used for the rapid screening of blood cells, such as white blood cells (WBCs) [Yoon et al., 2015] and red blood cells (RBCs) [Kim et al., 2014; Memmolo et al., 2014; Moon et al., 2012], where the morphological and biochemical properties of thousands of single cells can be derived from small volumes of blood, thus allowing direct comparison to the current laboratory blood tests.

Contrary to fluorescence microscopy, the label-free nature of DHTM eliminates the reliance on exogenous fluorescent markers and chemical fixation processes, thus making it suitable for high-throughput screening and enabling the acquisition of artefact-free and biologically-relevant findings. Given the quantitative and reproducible imaging capabilities of DHTM, the integration of complementary techniques aimed at replicating physiological or pathological conditions, such as microfluidic systems [Rizzuto et al., 2021; Sung et al., 2014], and the utilization of deep learning algorithms for rapid and automated image processing [Javidi et al., 2018; Yi et al., 2017], has significantly advanced the implementation of DHTM for disease diagnostics.

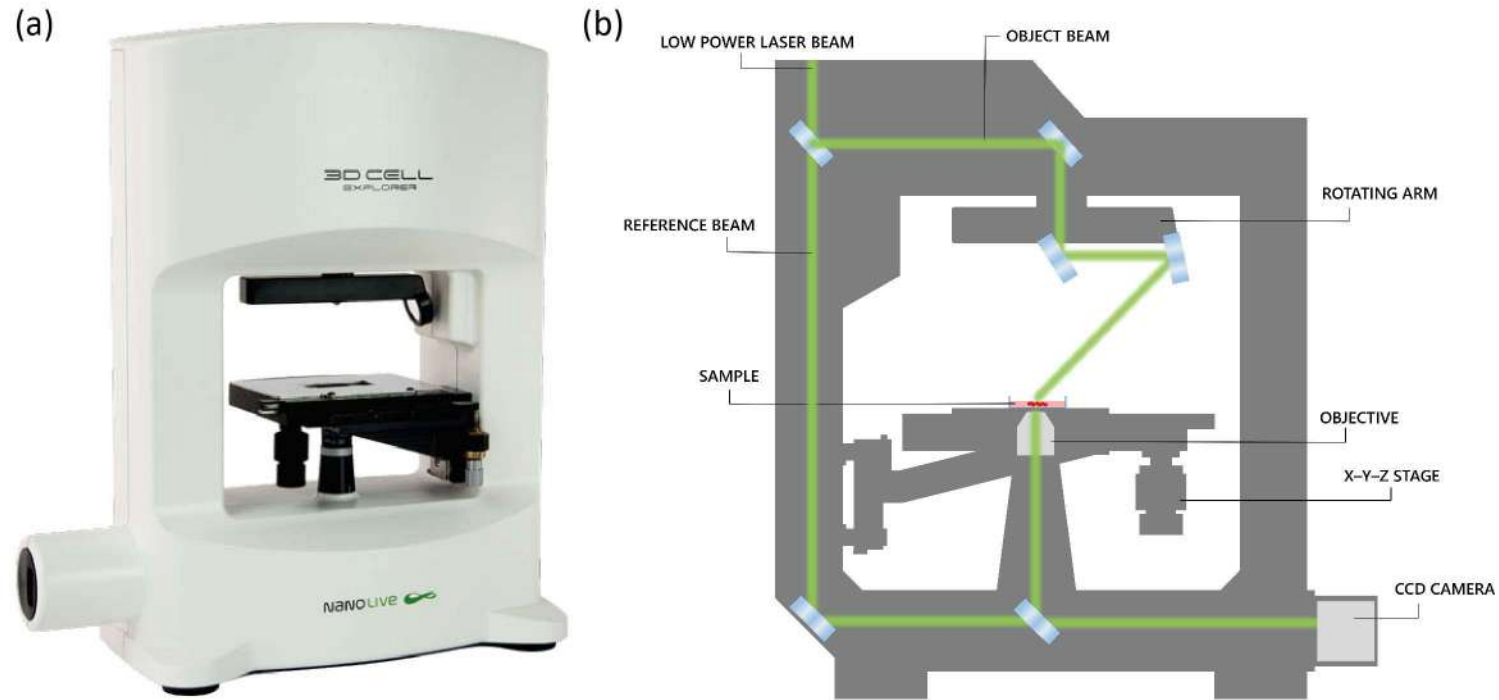


Figure 1.4. Overview of the DHT microscope used within the research projects presented in the context of this PhD thesis. (a) The *3D Cell Explorer* (Nanolive SA, Switzerland) DHT microscope, with a unibody design, composed of a single aluminum piece. (b) Schematic of the *3D Cell Explorer*, depicting the key elements and working principle of the microscope.

1.4. Hypothesis and aim of the thesis

This thesis hypothesizes that the tracking of the morphological, chemical and biophysical parameters of blood components would allow for the detection of blood-related diseases and for the monitoring of drug-induced cytotoxic effects in blood.

The central aim of this research is to develop an innovative imaging platform, guided by machine learning, for clinical level screening of pathological diseases by monitoring the shape, size and morphological changes occurring in RBCs. Following this approach, the goal is to extend our imaging and analysis framework for the detection and characterization of valuable disease biomarkers directly in blood, such as the presence of micrometer-size blood clots in COVID-19.

The novelty of the current project over the state-of-the art lies in the development of a combinatorial imaging approach, consisting of high-throughput digital holographic microscopy and high-resolution atomic force microscopy, for the nanoscale characterization of blood components in a label-free manner, focusing towards the realization of digital pathology. To this end, we focus on investigating the real-time dose-dependent chemical effects on RBCs and blood clots, with the ultimate goal of supporting clinicians in improving early disease detection, clinical prognosis and towards the development of more effective and personalized treatment strategies.

1.5. Outline of the thesis

Following this introduction (**Chapter 1**), the thesis includes six chapters, described as follows:

- **Chapter 2** provides an overview of the best practices for sample preparation and the development of the imaging and analysis workflow for studying blood using label-free digital holo-tomographic microscopy.
- **Chapter 3** investigates the chemically-induced effects on red blood cell morphology in real time and in a label-free manner using digital holotomography and focuses specifically on the dose-dependent effect of ibuprofen drug.
- **Chapter 4** explores the application of digital holotomography for the detection and characterization of microclots directly in blood in order to assess disease severity in individuals with COVID-19.
- **Chapter 5** focuses on the study of chemical effects on the morphology of micrometer-size blood clots, highlighting the role of urea as a fibrin solubilizer. This is demonstrated through the use of both digital holo-tomographic microscopy and atomic force microscopy.
- **Chapter 6** details the interaction between Levodopa and α -Synuclein at the nanoscale and hints to the application of digital holotomography for the study of drug-induced cytotoxicity on blood cells in neurodegenerative diseases.
- Finally, **Chapter 7** summarizes the main findings of the work and provides an outlook for future research.

Furthermore, the supplementary information for Chapters 3, 4 and 6 is available in Appendix A, B and C, respectively.

2. Development of the imaging and analysis workflow for label-free digital holo-tomographic microscopy

2.1. Best practices for blood sample preparation

Blood is a complex bodily fluid with a precise and dynamic composition that plays a vital role in maintaining homeostasis and sustaining life [Weiss & Jelkmann, 1989]. It is primarily composed of plasma, a yellowish fluid comprising water, electrolytes, proteins, hormones, and waste products [Bain, 2015] (Figure 2.1). Plasma constitutes about 55% of total blood volume and serves as a medium for the transport of cells and molecules throughout the body [Bain, 2015]. The cellular components of blood

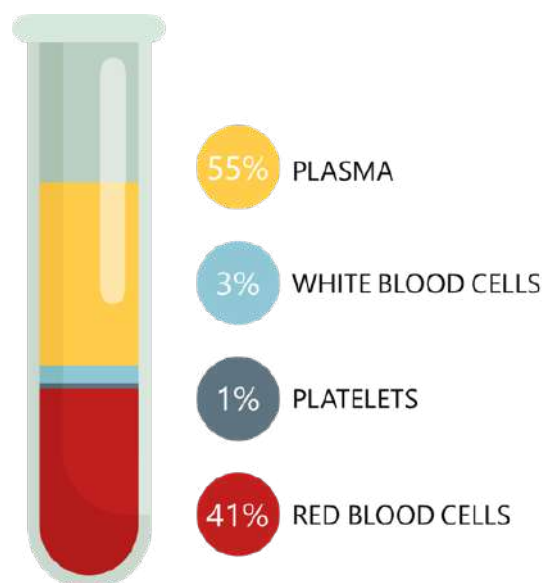


Figure 2.1. Blood composition

collectively account for about 45% of total blood volume and consist of erythrocytes (RBCs), leukocytes (WBCs), and platelets. RBCs are specialized for oxygen transport and make up the majority of blood cells, while WBCs serve as the body's immune response, defending against infections [Bain, 2015]. Platelets are essential for blood clotting and wound healing [Bain, 2015]. The precise balance and regulation of these components is paramount for overall health, as any disruption in blood composition can lead to a wide range of medical conditions and diseases.

Blood collection is a minimally invasive medical procedure used in various clinical and research applications. Several methods are employed to obtain blood samples, each tailored to specific needs [Bain, 2015] (Figure 2.2). Venipuncture collection is the most common method, involving puncturing a vein with a sterile needle and collecting blood into evacuated tubes [World Health Organization, 2010]. Alternatively, capillary blood sampling involves pricking the fingertip or heel to collect small volumes of blood, often used in pediatric and point-of-care testing [World Health Organization, 2010]. Arterial blood sampling, typically performed on the radial or femoral arteries, provides valuable information about blood gases and acid-base balance [World Health Organization, 2010]. For specialized applications, more invasive central venous catheters or arterial lines are utilized to obtain continuous blood samples or administer medications [World Health Organization, 2010]. Regardless of the method employed, strict adherence to aseptic techniques and proper patient identification is vital to ensure sample accuracy and minimize complications. Selecting the appropriate method depends on the clinical context and the specific analytes required, highlighting the importance of individualized approaches to blood collection in healthcare and research settings.

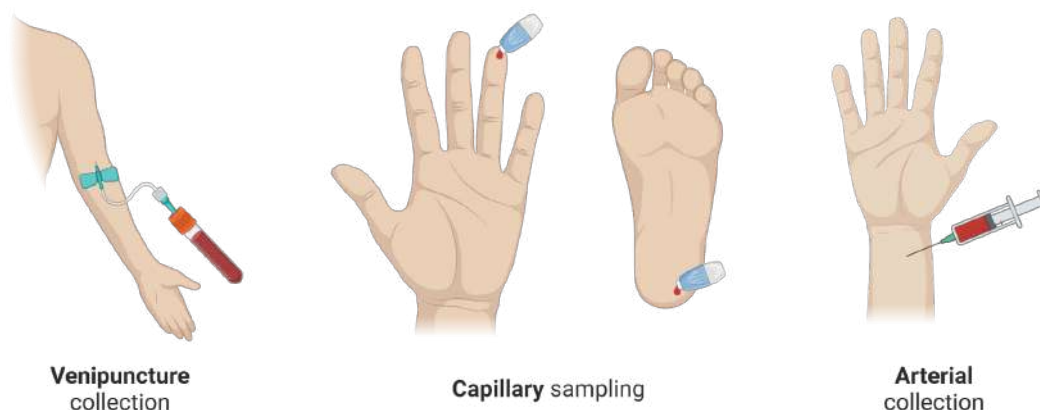


Figure 2.2. Blood collection methods, including venipuncture collection, capillary sampling via fingerstick or heel stick and arterial blood collection.

2. Development of the imaging and analysis workflow for label-free DHTM

For the imaging of blood using DHTM, a small volume of blood (~10 μL) is required for the assessment of cell morphology of WBCs, platelets and for thousands of RBCs. Hence, we mainly employed capillary blood collection by fingerstick sampling. Fingerstick blood sampling offers several distinct advantages in various clinical and research settings. First, it is minimally invasive, thus causing significantly less discomfort compared to traditional venipuncture, making it more tolerable for patients, particularly children and those with a fear of needles. Its simplicity and ease of use make it suitable for point-of-care testing, enabling rapid results and facilitating timely decision-making in clinical diagnoses. Moreover, fingerstick sampling allows for convenient and repeated sampling over time, essential for monitoring chronic conditions or assessing the dose-dependent effects of medications. Although capillary blood collection is not entirely immune to potential artifacts originating from the methodology itself, such as in coagulation assays, it is recognized as a reliable approach for the quantitative assessment of blood parameters, particularly when it comes to evaluating cell morphology [Cable et al., 2012; Fliervoet et al., 2022].

Using DHTM, blood can be assessed both in the wet or dry state. Sample preparation procedures for both methods rely on fingerstick sampling (Figure 2.3). Minimal sample preparation is required for imaging fresh and dry blood, including blood dilution and the creation of blood smears followed by coating with silicone oil, respectively. Blood dilution is particularly important to prevent the clustering of blood cells, particularly in the case of RBCs, which make up the majority of the visible cells (Figure 2.4). Furthermore, the use of petri dishes with a polymer coating, as opposed to an uncoated glass bottom, is essential for RBC imaging in order to prevent echinocytosis, an artifact that can occur when RBCs come into contact with glass surfaces. However, glass bottom petri dishes are preferred for the DHTM-based imaging of blood clots. For the measurement of dried blood samples, the creation of very thin blood smears is necessary to ensure that the cells are adequately dispersed (Figure 2.5). Additionally, the use of silicone oil as a coating medium, as opposed to PBS buffer, allows for optimal imaging and storage of the blood smears (Figure A.11).

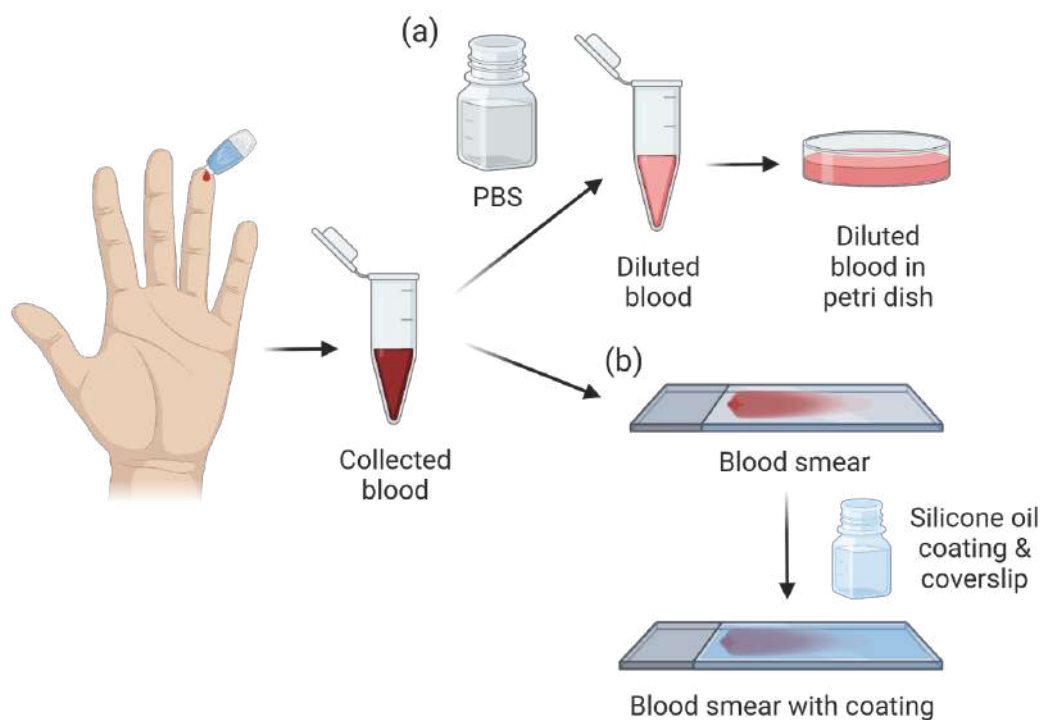


Figure 2.3. Sample preparation procedures for blood imaging with DHTM. Blood is collected via fingerstick. (a) For blood in the wet state, blood is diluted with PBS and added to a petri dish for imaging. (b) For blood in the dry state, a blood smear is created and air-dried. A few drops of silicone oil are deposited and a coverslip is added on top, followed by sealing the edges with nail polish.

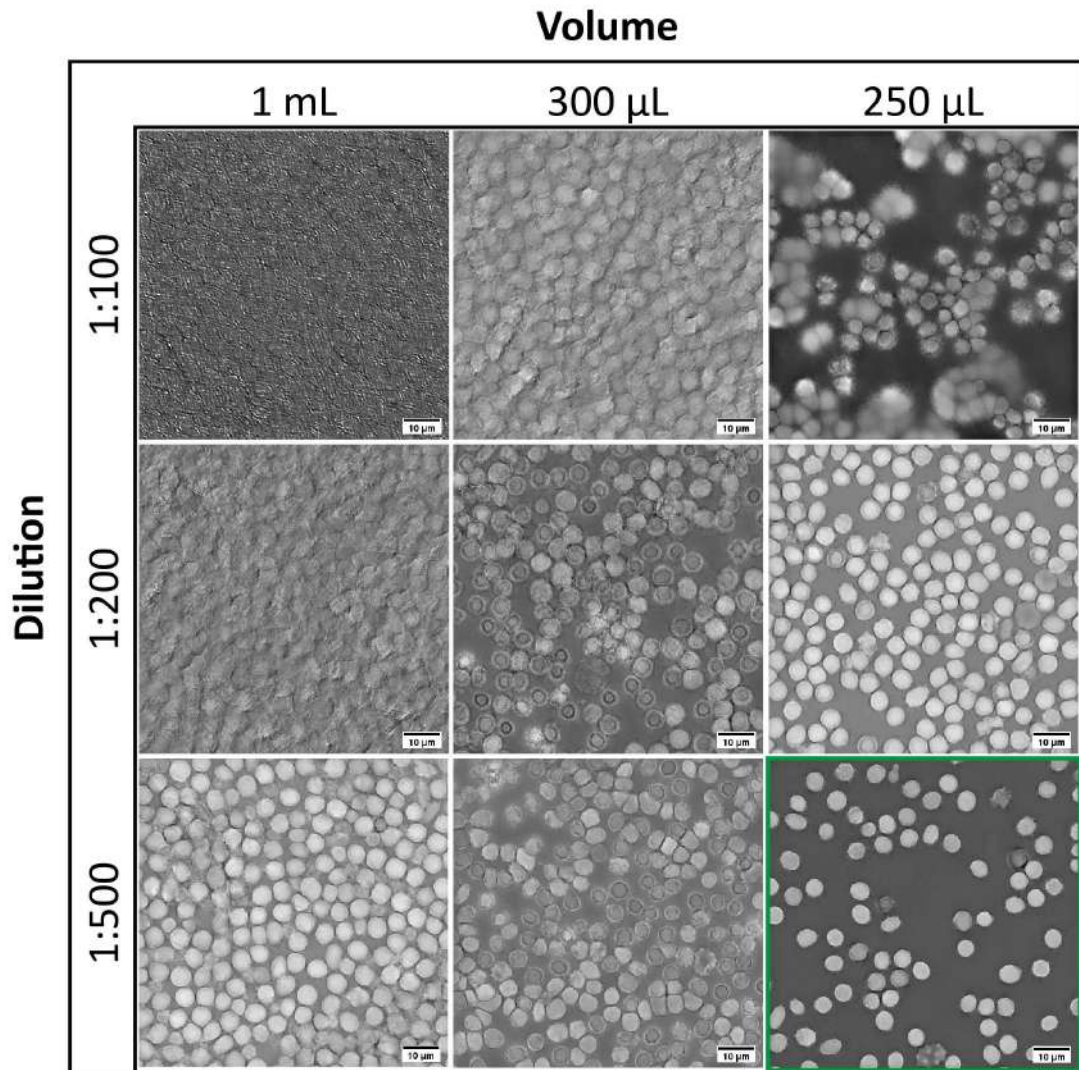


Figure 2.4. Optimization of the best combination of blood dilution (in PBS buffer) and volume to add to the petri dish. A dilution of 1 in 500 and a volume of 250 µL constitute the best solution for cell characterization in blood (green square).

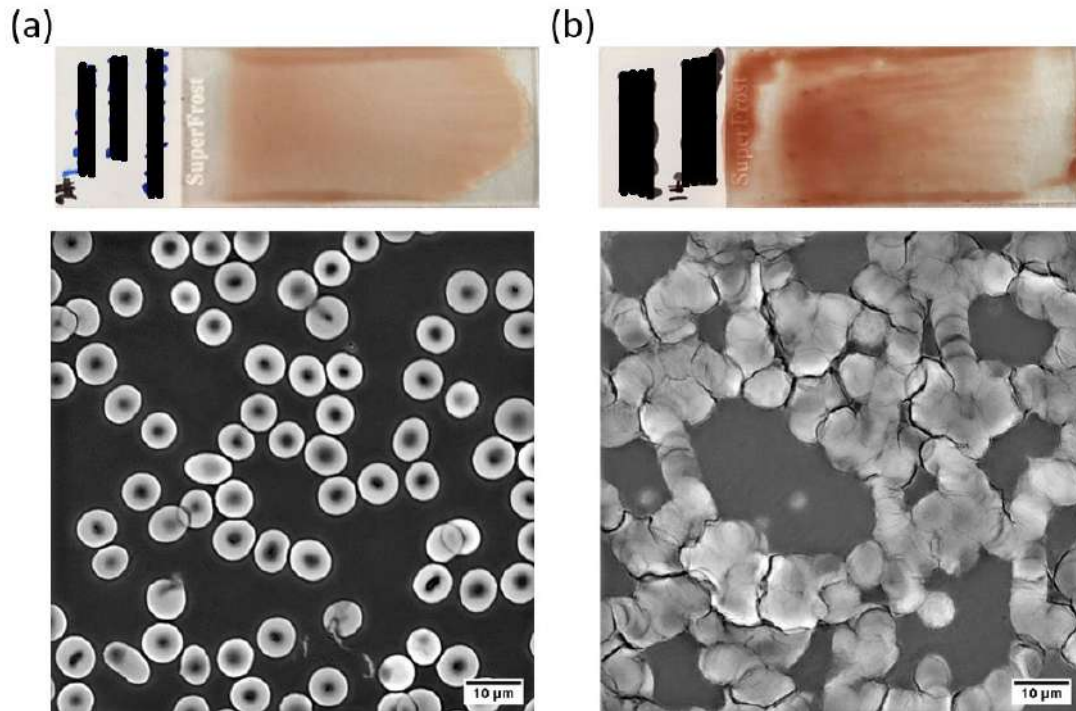


Figure 2.5. Preparation of blood smears for DHTM imaging. (a) A thin blood smear ensures that blood cells are evenly distributed across the glass slide. (b) A thicker blood smear results in cell clustering and a worse image resolution.

2.2. Image processing and analysis

Image processing and analysis provide the means to extract valuable information from complex visual data [Dufaux, 2021]. Employing DHTM for blood imaging requires the use of image analysis software capable of facilitating both 3D and 4D image processing and interpreting tomographic data. In our image processing and analysis workflow, we use the Imaris software for the processing of images obtained from DHTM, as well as for object detection, segmentation and classification. Figure 2.6 shows our image processing and analysis workflow for blood cell characterization. Acquired 3D images are exported as a single z-stack file, including 96 images corresponding to $\sim 30 \mu\text{m}$. Similarly, 4D data is exported as single 3D images (max. frame rate = 0.5 fps) and later merged as a video file using ImageJ. Next, 3D refractive index (RI) tomograms are imported into Imaris, where RI values are converted into intensity values. Imaris enables the 3D and 4D visualization of cells, allowing for more accurate image processing as opposed to software that processes each individual 2D image within the stack separately. A median filter is then applied in order to reduce noise without losing image features such as edges and sharp structures [Fan et al., 2019]. The use of a noise removal method as well as the type of filter should be adapted according to the nature of the sample. For example, when dealing with sharp structures such as those found in 3D RI tomograms of micrometer-sized blood clots, noise removal filters are typically avoided, as they could potentially eliminate crucial information from the image. Image segmentation is then implemented in order to eliminate the background signal and reconstruct the object signal in 3D through the creation of a surface. In the context of blood cells, segmentation also enables the detection of individual RBCs and the extraction of the quantitative parameters at a single cell level. Additionally, a machine learning (ML) classifier is used in order to achieve the automatic classification of RBC morphology. The decision tree classifier implemented in Imaris is a supervised ML method, where the data is iteratively divided based on specific parameters, ultimately resulting in distinct classes [Charbuty & Abdulazeez, 2021]. For RBCs, these parameters can include the cell diameter, thickness, sphericity, etc. Supervised ML algorithms require a training and a testing phase. To achieve RBC shape classification, a train-test data split of 33%-67% was applied. The training dataset consisted of individual RBCs of different morphologies imaged in blood from both healthy donors and donors with blood-related pathologies, such as sickle cell anemia (SCA).

2. Development of the imaging and analysis workflow for label-free DHTM

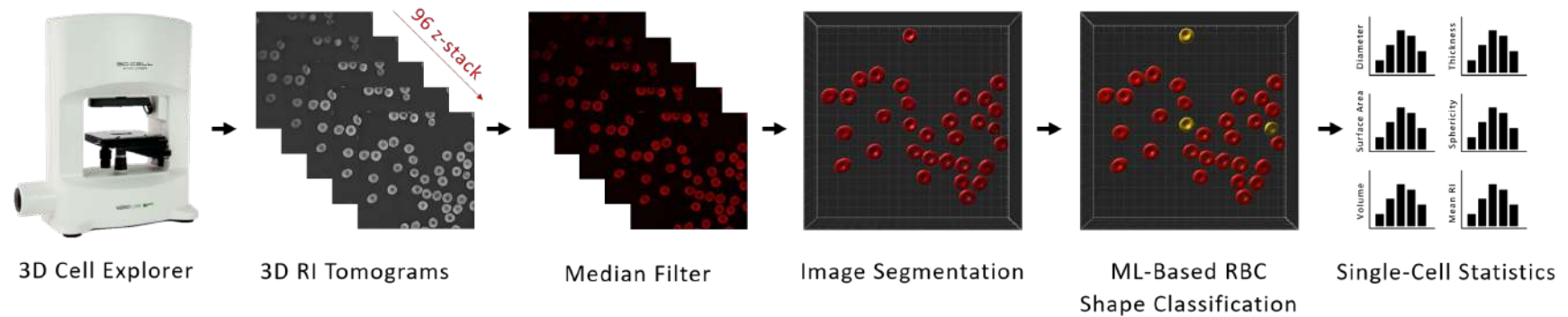


Figure 2.6. Image processing and analysis workflow for blood imaging using label-free DHTM. Acquired images are exported as 3D RI tomograms and imported into Imaris. A median filter is then applied for signal noise removal. Following, image segmentation enables the reconstruction of the object signal without the background. A machine learning algorithm is then used in order to automatically classify RBC morphology. Finally, morphological and chemical parameters are extracted at a single cell levels.

2. Development of the imaging and analysis workflow for label-free DHTM

At the end of the image processing and analysis workflow, the quantitative morphological and chemical parameters are automatically derived from each individual cell or segmented structure (Figure 2.7). In the context of RBCs characterization, the cell diameter, thickness, surface area, volume, sphericity, and hemoglobin (Hb) concentration and content, derived from the RI values, can be calculated. Similarly, the same parameters can be extracted from micrometer-sized blood clots, including clot size, fibril thickness and dry mass. In the case of 4D datasets, morphological and chemical parameters are extracted from every frame, providing both real-time qualitative and quantitative characterization. This is particularly valuable when investigating the impact of chemical compounds and medications on the morphology of RBCs and blood clots.

Further details on the calculation of each morphological and chemical parameter, as well as their relevance in the context of blood rheology and blood clot structure, are provided in each chapter.

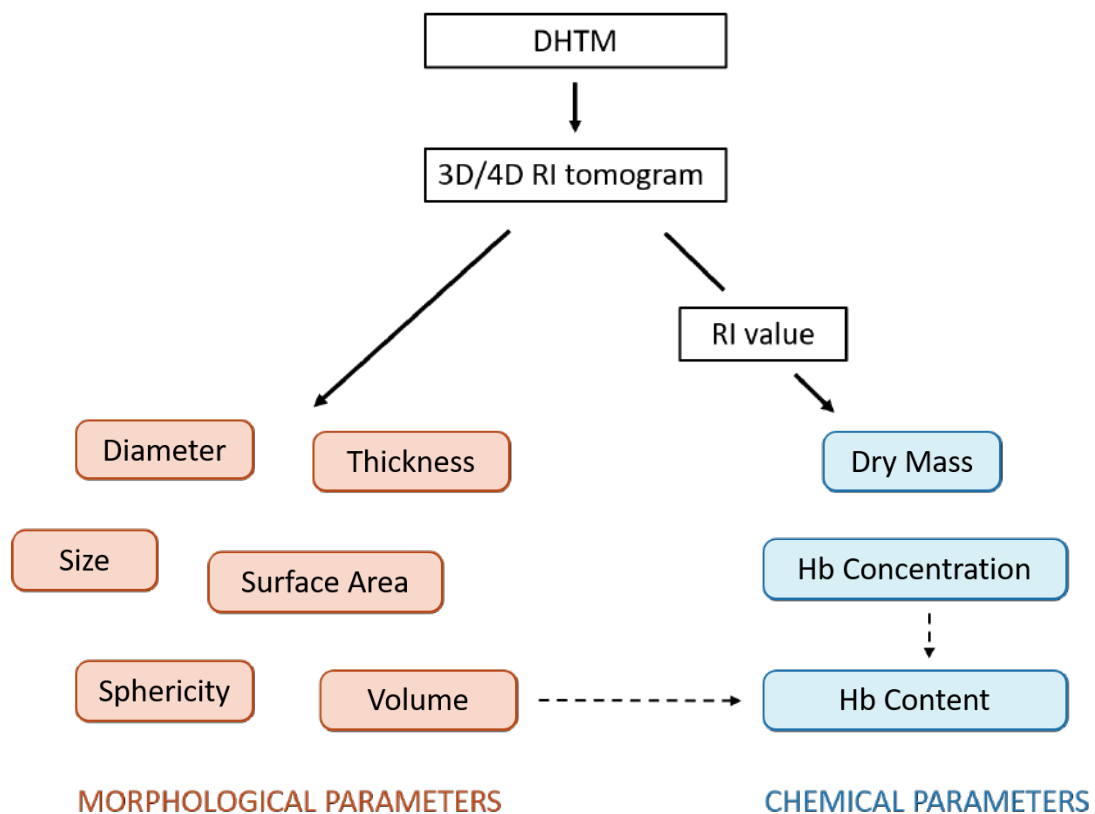


Figure 2.7. Quantitative morphological and chemical parameters that can be extracted from 3D and 4D refractive index tomograms acquired with DHTM.

3. Label-free digital holotomography reveals ibuprofen-induced morphological changes to red blood cells*

3.1. Abstract

Understanding the dose-dependent effect of over-the-counter drugs on red blood cells (RBCs) is crucial for hematology and digital pathology. Yet, it is challenging to continuously record the real-time, drug-induced shape changes of RBCs in a label-free manner. Here, we demonstrate digital holotomography (DHTM) enabled real-time, label-free concentration-dependent and time-dependent monitoring of ibuprofen on RBCs from a healthy donor. The RBCs are segmented based on 3D and 4D refractive index tomograms and their morphological and chemical parameters are retrieved with their shapes classified using machine learning. We directly observed the formation and motion of spicules on the RBC membranes when aqueous solutions of ibuprofen were drop cast on wet blood, creating rough-membraned echinocyte forms. At low concentrations of 0.25-0.50 mM, the ibuprofen-induced morphological change was transient but at high concentrations (1-3 mM) the spiculated RBC remained over a period of up to 1.5 hours. Molecular simulations confirmed that aggregates of

*[Bergaglio, T.](#), Bhattacharya, S., Thompson, D., Nirmalraj, P. N. *Label-Free Digital Holotomography Reveals Ibuprofen-Induced Morphological Changes to Red Blood Cells*. ACS Nanosci. Au, 3 (3), 241-255. 2023. DOI: doi.org/10.1021/acsnanoscienceau.3c00004

Contribution: T.B. was involved in the planning of the study, prepared the blood samples and conducted the holotomography and AFM measurements. T.B. performed the image processing, data analysis, interpretation and visualization of results. T.B wrote the original draft of the manuscript and revised it based on the suggestions from the co-authors.

ibuprofen molecules at high concentrations significantly disrupted the RBC membrane structural integrity and lipid order, but produced negligible effect at low ibuprofen concentrations. Control experiments on the effect of urea, hydrogen peroxide and aqueous solutions on RBCs showed zero spicule formation. Our work clarifies the dose-dependent chemical effects on RBCs using label-free microscopes that can be deployed for the rapid detection of overdose of over-the-counter (OTC) and prescribed drugs.

3.2. Introduction

The rheological properties of RBCs including deformability and aggregability help regulate blood flow through the circulatory system [Muravyov & Tikhomirova, 2015; Viallat & Abkarian, 2014]. Impaired RBC deformability can result in increased blood viscosity, impaired perfusion, occlusions in small blood vessels and could lead to ischemia [Jacob, 1975; Pretini et al., 2019]. Other factors can trigger changes to the membrane mechanical properties of RBCs, concentration changes of hemoglobin inside the cell and modifications of the RBC surface area or volume [Huisjes et al., 2018; Iglic et al., 1998; Jaferzadeh et al., 2018; Khairy et al., 2010]. These factors range from the primary genetic mutations in the different forms of hereditary hemolytic anemia to secondary processes arising from mechanical or chemical alterations in the surrounding environment. The overall RBC shape change is conventionally used to describe RBC deformability. Failure to maintain optimal red cell deformability results in a lower RBC life span and contributes to the development of hemolytic anemia [Huisjes et al., 2018]. One pathology resulting from hemolytic anemia is sickle cell disease (SCD), a group of inherited hematological disorders affecting hemoglobin [G. J. Kato et al., 2018]. In sickle cell anemia (SCA), a significant population of RBCs are shaped as sickles, thus becoming less deformable, with a lower life span and with an increased risk of blood clot formation, infections and pain [Arishi et al., 2021; G. J. Kato et al., 2018]. Interactions with drugs (for example, vinblastine, colchicine and chlorpromazine) and signaling molecules can also negatively influence red cell rheological properties, by decreasing RBC deformability and increasing RBC aggregation [Chen & Huestis, 1997; Jacob, 1975; Muravyov & Tikhomirova, 2015]. Hemolytic anemia can thus be induced by a wide range of medications including cephalosporin-based antibiotics and oxaliplatin anti-cancer drugs [Barbaryan et al., 2013; Chen & Zhan, 2014; Garratty, 2012]. Despite the low incidence rate of this side effect, drug-induced immune hemolytic anemia (DIIHA) is a serious condition most

3. Label-free DHTM reveals ibuprofen-induced morphological changes to RBCs

observed from the use of OTC medications due to the higher risk of their misuse [Barbaryan et al., 2013; Martini et al., 2015]. Among these medications are nonsteroidal anti-inflammatory drugs (NSAIDs) widely used for their anti-inflammatory, antipyretic and analgesic properties [Goldstein et al., 2011]. Ibuprofen is one such NSAID used for the treatment of rheumatoid arthritis and for the relief of pain, inflammation and fever [Martini et al., 2015]. In addition to increased risk of gastrointestinal injury, ibuprofen can influence hemostasis even at recommended doses, causing thrombocytopenia, reduced platelet aggregation resulting in increased clotting time and loss of hemoglobin, potentially leading to DIIHA [Goldstein et al., 2011; Manrique-Moreno et al., 2011; Martini et al., 2015]. NSAID toxic side effects may result from their interaction with cellular membranes, which primarily act as a protective barrier and regulate materials transfer into and out of the cell, including drug delivery, based on precise molecular-level organization, fluidity and permeability [Di Foggia et al., 2017; Manrique-Moreno et al., 2011]. The RBC membrane can be considered an ideal model for the investigation of drug–cell interaction due to the presence of a single phospholipid bilayer membrane and the absence of internal organelles inside RBCs [Chen & Huestis, 1997; Di Foggia et al., 2017; Du et al., 2006].

Hence, monitoring RBC deformability constitutes a crucial diagnostic tool, with shape change patterns allowing patient stratification by disease stage, and can be used in a pre-clinical setting to gauge the effect of pharmacological interventions on blood-related disorders such as SCD, thalassemia, diabetes and COVID-19 [Chaichompoo et al., 2019; de Haan et al., 2020; Huisjes et al., 2018; Lee et al., 2017; O'Connor et al., 2021]. Despite the well-reported interaction between ibuprofen and the lipid bilayer membrane [Du et al., 2006], to the best of our knowledge only one study has shown the potential effects of ibuprofen on RBC deformability [Manrique-Moreno et al., 2011]. In this study, Manrique *et al.* [Manrique-Moreno et al., 2011] used scanning electron microscopy (SEM) to obtain snapshots of RBC morphological changes after incubation at different concentrations of ibuprofen and provide evidence for spicule formation on the cell membrane and echinocytosis with increasing ibuprofen dosages. Importantly, although RBC shape changes were observed with ibuprofen concentrations as low as 10 μ M, the reversibility of these changes could not be determined due to the lack of dynamic cell behavior information. Hence, the effect of ibuprofen on RBC morphology and the dose-dependent interactions with the RBC lipid bilayer membrane remains to be clarified with high spatial clarity in real-time.

Label-free digital holotomographic microscopy (DHTM) enables 3D morphometric imaging of live cells with nanoscale resolution at room temperature [Cotte et al.,

3. Label-free DHTM reveals ibuprofen-induced morphological changes to RBCs

2013]. Unlike fluorescent microscopy, DHTM does not rely on fluorescent labelling and uses a low-power laser beam that avoids phototoxic effects [Cotte et al., 2013]. Several studies have demonstrated the potential of digital holography in the field of hematology [Kim et al., 2021; Kim et al., 2014; Memmolo et al., 2014; Moon et al., 2012; Park et al., 2018]. In particular, Kim *et al.* have previously demonstrated the use of common-path diffraction optical tomography (cDOT) for the visualization of RBCs and the quantification of RBC morphometric parameters [Kim et al., 2014]. Moreover, holotomography was employed to study the mechanobiology of RBCs upon exposure to Melittin [Hur et al., 2017]. Unlike previous studies, here we directly register the dosage dependent effect of ibuprofen on RBCs in real-time using DHTM.

We demonstrate here a DHTM based approach for label-free detection and quantification of ibuprofen-induced RBC shape changes with high spatial and temporal resolution. As a control, we recorded the DHTM RI maps of RBCs from healthy individuals and from those with sickle cell anemia (SCA) and sickle cell trait (SCT) condition. The 3D and 4D RI tomograms were analyzed using a machine learning (ML) based classifier to identify difference in shapes between RBCs in healthy and pathological individuals (SCA and SCT). Next, we extended the imaging and analytics protocols to investigate the concentration and time dependent effect of ibuprofen on RBCs from healthy individuals. Monitoring the real-time changes in RBC morphology upon ibuprofen introduction from 0 to 20 minutes, we observed the formation of spicules on the RBC membrane, defined as echinocytosis. The nanoscopic details of the spicule morphology was further analyzed using atomic force microscopy (AFM) and the real-time motion of the spicules on RBC membrane was captured using DHTM. Spicule formation was observed to be reversible at lower ibuprofen concentrations (0.25 mM and 0.5 mM), but the normal RBC discocyte morphology did not recover with higher ibuprofen concentrations (1 mM, 1.5 mM and 3 mM), over a period of up to 1.5 hours. To understand the interaction and effect of ibuprofen molecules on RBC membrane morphology at experimentally inaccessible timescales of molecule–molecule interaction (0-100 ns), we conducted atomic-scale molecular dynamics (MD) computer simulations. Models of membrane-bound single, very small (n=80), small (n=100), and large (n=1903) aggregates of ibuprofen molecules confirmed the extensive deformation of RBC lipid bilayer only at high concentrations with large aggregates of ibuprofen. Further control experimental measurements of drug-free RBCs in water and other chemicals such as urea and hydrogen peroxide (H₂O₂) confirmed that spicule formation only occurs with ibuprofen. These findings suggest that high-throughput microscopy and ML-driven automated image analysis methods

provide a valuable platform for the early diagnosis of blood disorders and for monitoring the efficiency of prescribed and OTC drugs in a simple, field-deployable and cost-effective manner [de Haan et al., 2020; Rawat et al., 2017].

3.3. Results

3.3.1. Quantification and classification of RBCs using label-free DHTM

In order to deduce the chemical effects on RBCs, we first compared samples from a healthy donor, a donor diagnosed with sickle cell trait (SCT) and a donor diagnosed with sickle cell anemia (SCA). This benchmarking of the DHTM tool enabled live cell and artefact-free imaging. The principle and experimental scheme of DHTM is explained in Figure 3.1(a). DHTM allows for the fast acquisition of refractive index (RI) tomograms rendered in 3D that provide quantitative information regarding RBC morphology. Details on the preparation of RBC samples for DHTM imaging are provided in Methods (Figure 3.1(b)) and the demographic information on donors is provided in Table A.1. Figure 3.2(a) shows a 3D RI tomogram of healthy RBCs diluted in phosphate-buffered saline (PBS) solution, with a field of view of 90x90x30 μm . Here, the distinctive biconcave disciform shape of an RBC can be observed, with the inner part of the cell having a lower RI value compared to the outer area due to the concavity of the disk shape [Kim et al., 2014; Moon et al., 2012]. Figure 3.2(b) shows the corresponding segmented RI tomogram with the background signal removed and the voxels extracted for the single RBCs. The RBCs could be classified based on their morphology using a ML-based algorithm. As shown in Figure 3.2(c), all cells shown in the image were classified as normocytes. The same approach was applied to RBCs extracted from donors with SCT (Figure 3.2(d-f)) and SCA (Figure 3.2(g-i)). A greater variability in RBC morphology was evident in both SCT and SCA samples, including the presence of echinocytes, acanthocytes, spherocytes and sickle RBCs (Figure 3.2(f) and (i)). Importantly, the observed variability in cell morphology could at least in part be attributed to the transport and long storage time (~15 days) between blood collection and analysis of the SCT and SCA samples. Long storage periods can negatively influence RBC rheological properties by altering RBC morphology from discocytes to echinocytes, creating a potential confounding effect in the assessment of RBC health, particularly in individuals with a blood-related pathology characterized by RBC

3. Label-free DHTM reveals ibuprofen-induced morphological changes to RBCs

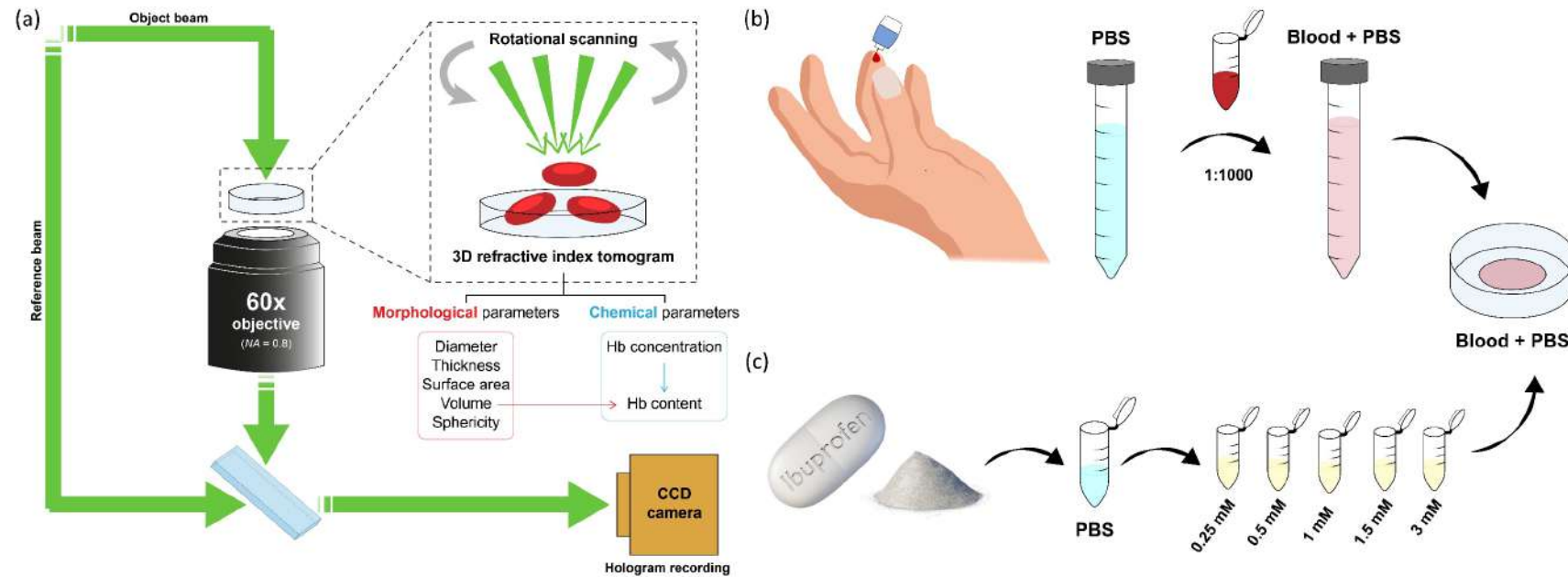


Figure 3.1. Principle of DHTM and sample preparation procedure for blood and ibuprofen solutions. (a) The holo-tomographic setup includes a low power laser beam ($\lambda = 520 \text{ nm}$) that splits into the reference and the object beam before rejoining below the objective, where the interference is recorded. A 3D RI map is obtained by recording holograms with a rotational arm at 360° around the sample, at a 45° angle. Morphological and chemical parameters can be quantified for individual RBCs from the 3D RI tomogram. (b) 10 μL of whole blood is obtained from a finger prick and diluted in PBS buffer at a final concentration of 1:1000. 250 μL of blood solution is added to a petri dish for imaging. (c) Ibuprofen powder is obtained by crushing an ibuprofen tablet and is dissolved in PBS buffer to obtain five final concentrations (0.25 mM, 0.5 mM, 1 mM, 1.5 mM, 3 mM). 50 μL of each ibuprofen solution is added to the blood solution in the petri dish during the live cell imaging experiments.

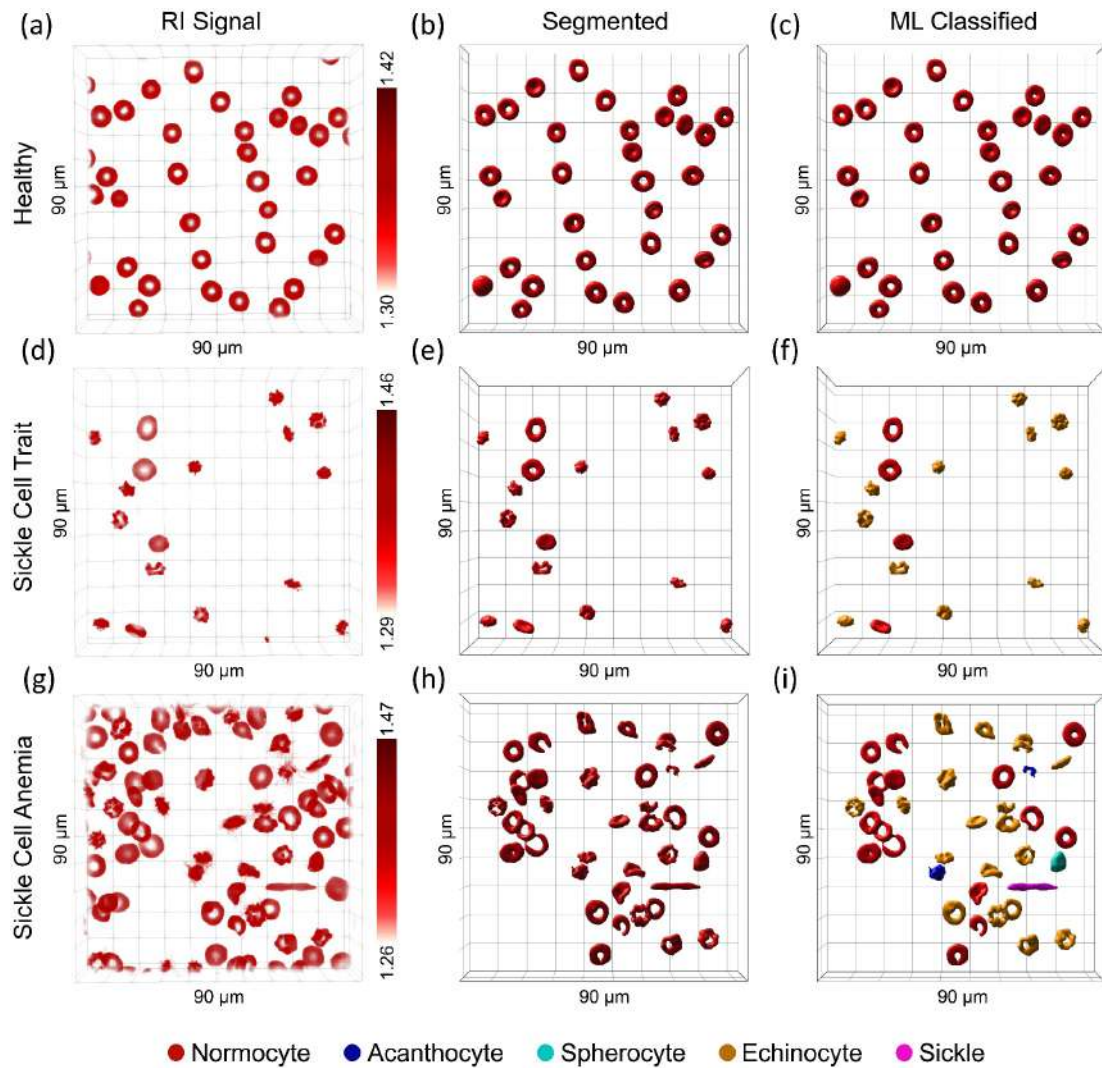


Figure 3.2. 3D holotomographic imaging of RBCs and classification using machine learning (ML). (a) 3D refractive index (RI) tomogram of RBCs obtained from a healthy donor. The corresponding segmented RI tomogram and ML-classified RBC types are shown in (b) and (c). (d) 3D RI tomogram of RBCs from a donor with sickle cell trait (SCT). The corresponding segmented RI tomogram and ML-classified RBC types are shown in (e) and (f). (g) 3D RI tomogram of RBCs from a donor diagnosed with sickle cell anemia (SCA). The corresponding segmented RI tomogram and ML-classified RBC types are shown in (h) and (i). Field of view 90x90x30 μm .

3. Label-free DHTM reveals ibuprofen-induced morphological changes to RBCs

morphological alterations, such as SCA [Doan et al., 2020; Moon et al., 2013]. For example, we observed from control experiments that blood from a healthy donor, diluted in PBS and stored at 4°C over a period of 11 days, resulted in the morphological transition of RBCs from mostly normocytes on day 0 to an increasing population of echinocytes over normocytes up to 70% on day 11 (Figure A.1).

From the segmented RI tomograms, the quantitative information of the RBC morphological and chemical parameters, including diameter, surface area, volume, thickness, sphericity, hemoglobin (Hb) concentration and Hb content, was extracted at a single cell level (Figure 3.3). In order to assess the accuracy of the quantification of the RBC morphological measurements based on DHTM RI tomograms, we used micro-particles of silicon dioxide with nominal sizes of 2 and 5 μm (Figure A.2). The Imaris-based segmentation and quantification method yielded similar results in terms of bead diameter, surface area and volume compared to the nominal values reported by the manufacturer. A total of 351 healthy, 459 SCT and 230 SCA RBCs were analyzed and classified into RBC types (Table A.2). The measured values for normocytes were comparable in both healthy, SCT and SCA samples and were consistent with the literature, with a reported mean diameter of 8 μm (Figure 3.3(a)), mean surface area of 130 μm^2 (Figure 3.3(b)) and mean volume of 90 fL (Figure 3.3(c)) [Canham & Burton, 1968]. Figure 3.3(a) reveals variations in mean diameter between different RBC types. Stomatocytes (healthy = 6.88 μm , SCT = 6.18 μm , SCA = 7.95 μm), echinocytes (healthy = 6.69 μm , SCT = 6.56 μm , SCA = 7.63 μm), acanthocytes (SCT = 5.60 μm , SCA = 8.31 μm) and spherocytes (SCT = 5.03 μm , SCA = 6.16 μm) had a lower diameter compared to normocytes (healthy = 7.77 μm , SCT = 7.81 μm , SCA = 8.45 μm). Conversely, sickle RBCs found in SCT (8.52 μm) and SCA (12 μm) samples had a higher diameter due to their elongated shape compared to normocytes. The values for the mean surface area (Figure 3.3(b)) and mean volume (Figure 3.3(c)) showed corresponding lower values for echinocytes (healthy: 100 μm^2 , 77.7 fL; SCT: 91.64 μm^2 , 59.28 fL; SCA: 115.79 μm^2 , 75.20 fL), acanthocytes (SCT: 72.35 μm^2 , 43.94 fL; SCA: 110.24 μm^2 , 74.10 fL) and spherocytes (SCT: 64.46 μm^2 , 45.27 fL; SCA: 79.78 μm^2 , 52.84 fL) compared to normocytes (healthy: 127.51 μm^2 , 96.29 fL; SCT: 119.75 μm^2 , 79.53 fL; SCA: 129.58 μm^2 , 86.88 fL). Spherocytes found in SCT and SCA samples also showed a slightly higher thickness (SCT = 2.26 μm , SCA = 1.77 μm) compared to normocytes (SCT = 2.03 μm , SCA = 1.56 μm) due to the transition from a biconcave disciform shape to a spheroid morphology (Figure 3.3(d)). Consequently, the same pattern was found for the sphericity morphological parameter (Figure 3.3(e)), with values closer to 1, indicating a perfect sphere, (SCT = 0.94, SCA = 0.85) compared to normocytes (SCT =

0.75, SCA = 0.73). A similar pattern was observed in terms of thickness (Figure 3.3(d)) and sphericity (Figure 3.3(e)) for both echinocytes (healthy: 2.21 μm , 0.88; SCT: 1.77 μm , 0.81; SCA: 1.67 μm , 0.75) and acanthocytes (SCT: 1.83 μm , 0.83; SCA: 1.47 μm , 0.78) due to the tendency of these RBC types to be more spherical in shape compared to normal RBCs. The results from DHTM and our analysis methodology indicate that the RI can be used as a metric assessing Hb concentration and Hb content, as the cytoplasm of RBCs contains mainly Hb solution (see Methods for details on the calculation of Hb concentration and Hb content from RI values) [Kim et al., 2021]. Based on DHTM measurements, we observed a slightly higher Hb concentration and a corresponding lower Hb content (Figure A.3) for all RBC types compared to normocytes, which we attribute to the changes in RBC shape, specifically a decrease in RBC volume, and thus the possible rearrangement of Hb within a single RBC (Figure 3.3(f)). The retrieved mean Hb concentration (healthy = 35.2 ± 0.5 g/dL, SCT = 35.5 ± 1.2 g/dL, SCA = 34.4 ± 0.7 g/dL) and mean Hb content (healthy = 33.9 ± 4.0 pg, SCT = 28.1 ± 5.3 pg, SCA = 29.9 ± 4.4 pg) for normocytes are in agreement with the reference values for the mean corpuscular Hb concentration (MCHC) and the mean corpuscular Hb (MCH) reported in a complete blood count (CBC) of healthy individuals (MCHC = 32-36 g/dL, MCH = 28-32 pg) [Bain, 2015].

With the imaging and analysis framework described in our study, we were able to optimize the DHTM based imaging technique to accurately resolve and quantify single RBCs in a label-free manner in both healthy and disease states. In addition, using a ML-based classification approach, we were able to distinguish between different RBC types and identify morphological and chemical parameters that could be used to describe changes in RBC shape, as benchmarked against previous studies on RBC morphology using other label-free imaging methods [de Haan et al., 2020; Jaferzadeh et al., 2018; Kim et al., 2014; Lee et al., 2017; Memmolo et al., 2014].

3.3.2. Dose-dependent effect of ibuprofen on RBCs

The dose-dependent effect of ibuprofen on healthy RBCs was evaluated in real-time using DHTM and analyzed using the protocols described above for the comparative analysis of RBCs from healthy, sickle cell trait and sickle cell anemia donors. Figure 3.4 shows the segmented and ML-classified RI tomograms of RBCs during incubation with different concentrations (0.25 mM-3 mM) of ibuprofen, over a period of 20 minutes. An overview of the total number of analyzed RBCs for each ibuprofen concentration is provided in Table A.6. For all ibuprofen concentrations, the formation of spicules on

3. Label-free DHTM reveals ibuprofen-induced morphological changes to RBCs

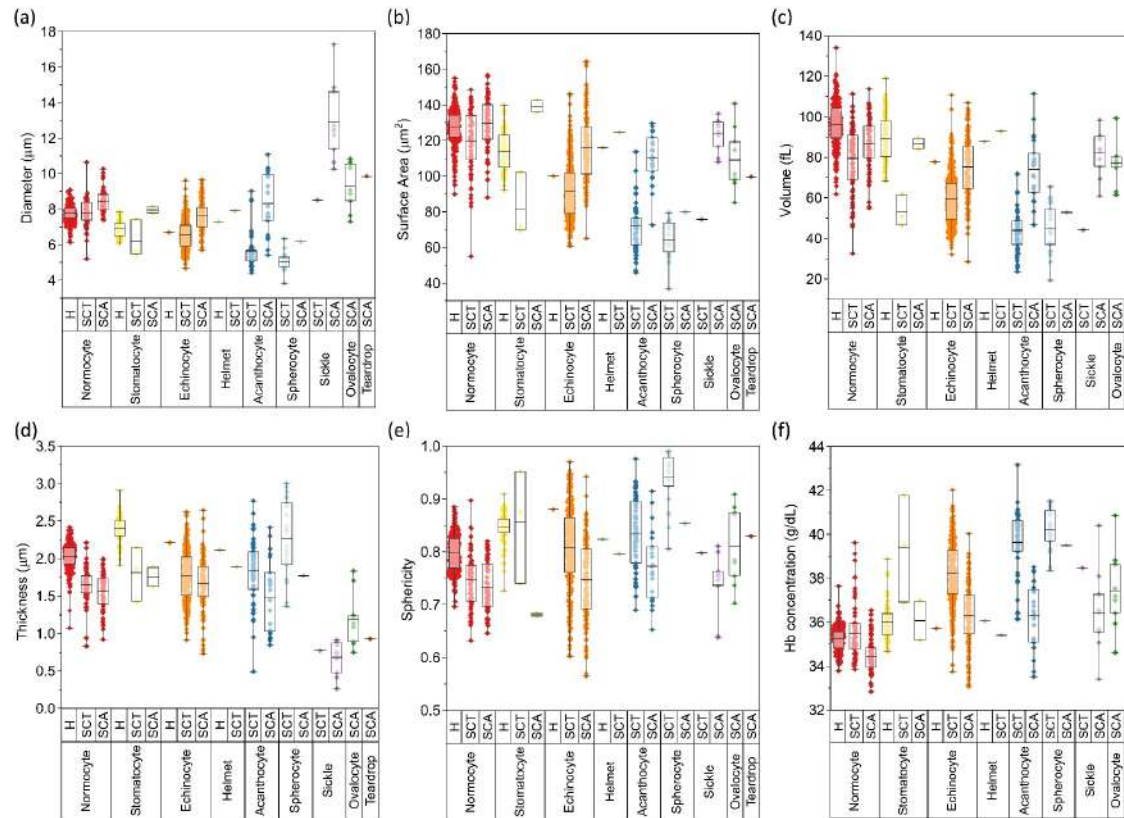


Figure 3.3. Quantification of size and shape variations in healthy, SCT and SCA RBC populations based on 3D tomograms. Single cell level comparison of (a) diameter, (b) surface area, (c) volume, (d) thickness, (e) sphericity and (f) Hb concentration between ML-based classified RBC types in healthy, SCT and SCA samples. Bars indicate mean values plus minimum and maximum values of all counted cells in each group.

3. Label-free DHTM reveals ibuprofen-induced morphological changes to RBCs

the RBC membrane and a clear transition from normocytes to echinocytes was observed upon introduction of ibuprofen in the RBC environment (>34s). At low ibuprofen concentrations (0.25 mM and 0.5 mM) (Figure 3.4(a-b)), the loss of the normal biconcave disciform morphology was determined to be transient, with most RBCs transitioning from normocytes to echinocytes and back to normocytes within 20 minutes (Movie A.1 and Movie A.2). However, at high ibuprofen concentrations (1 mM, 1.5 mM and 3 mM) (Figure 3.4(c-e)), the echinocytosis deformation did not result in the recovery of the normocyte RBC morphology (Movie A.3, Movie A.4 and Movie A.5). The quantified morphological and chemical parameters for each ibuprofen concentration are shown in Figure A.4. In order to further investigate the dynamics of spicule formation, movement and ultimately dissolution across the RBC membrane, we imaged and quantified single cell dynamics for low and high ibuprofen concentrations (0.25 mM and 1.5 mM) (Figure 3.5). As shown in Figure 3.5(a), the segmented 3D single RBC begins transitioning into an echinocyte upon exposure to 0.25 mM of ibuprofen ($t = 44$ s), with spicules forming on the RBC membrane, and continues to dynamically change before returning to a normal biconcave disciform shape at the 20 minutes time point. During this time, spicules can be observed forming ($t = 44$ s and 1:14 min), merging ($t = 7:04$ min), splitting ($t = 7:36$ min) and finally dissolving ($t = 20$ min) (Movie A.6). The corresponding variations in RI, as shown in the insets in Figure 3.5(a), reveal a rearrangement of hemoglobin inside the cell during the morphological transition, with areas containing protrusions having a higher RI value (1.39) compared to flatter regions (1.33). The time-dependent reversible morphological changes of the single RBC were quantified and are shown in Figure 3.5(b-e). Upon the introduction of ibuprofen, the cell diameter (Figure 3.5(b)) decreased from $7.39\ \mu\text{m}$ to as low as $6.57\ \mu\text{m}$ and was followed by a gradual increase back to $7.87\ \mu\text{m}$ at 20 minutes, associated with the transition from a normocyte to an echinocyte shape and later returning to a discocyte morphology. Likewise, the surface-area to volume (S/V) ratio suffered an initial drop from 1.36 to 1.20, driven by a decrease in surface area unmatched by a decrease in cell volume (Figure A.5(a-b)), that later recovered up to 1.28. Upon the transition to a more spherical echinocyte-shaped RBC, the cell sphericity (Figure 3.5(d)) also increased up to 0.90 and gradually returned within the range of a normocyte. Hb concentration (Figure 3.5(e)) was also subjected to a transient increase upon the introduction of ibuprofen, as reflected by the RI map inset in Figure 3.5(a). The higher values represent the time of spicule formation and movement across the RBC membrane, and the values gradually returning to a slightly lower Hb concentration compared to the starting point. Hb

3. Label-free DHTM reveals ibuprofen-induced morphological changes to RBCs

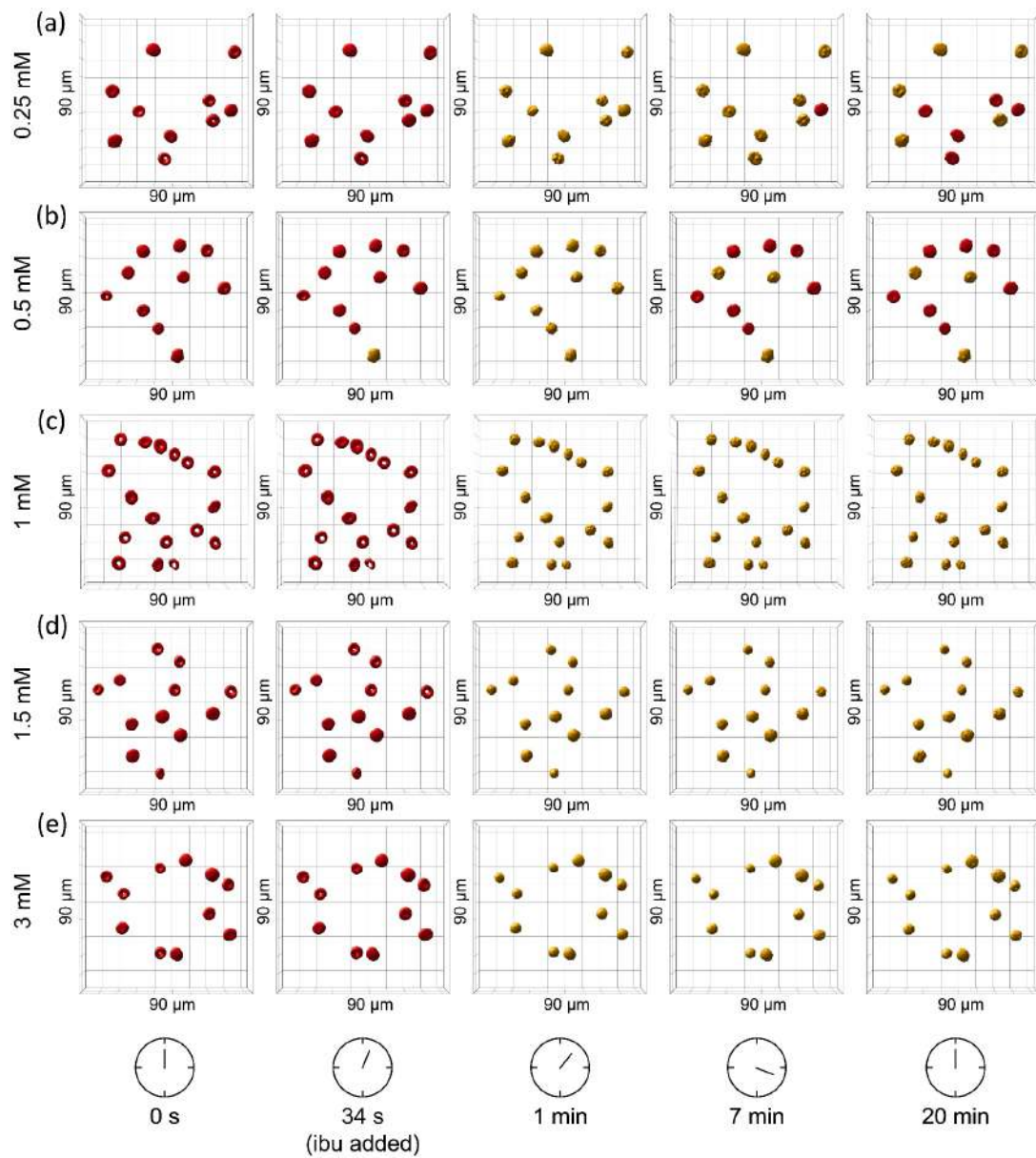


Figure 3.4. 3D rendering and classification of RBCs treated with ibuprofen at varying concentrations during a 20-minute time-lapse using 3D digital holo-tomographic microscopy. (A) 0.25 mM, (B) 0.5 mM, (C) 1 mM, (D) 1.5 mM and (E) 3 mM. Red and yellow color coding indicates normocytes and echinocytes, respectively. Field of view 90x90x30 μm. ibu = ibuprofen.

3. Label-free DHTM reveals ibuprofen-induced morphological changes to RBCs

content initially decreased upon the introduction of ibuprofen and later returned to slightly higher values by the 20 minutes time point (Figure 3.5(c)).

The segmented 3D individual RBCs treated with 1.5 mM ibuprofen is shown in Figure 3.5(f) and the quantified RBC parameters are shown in Figure 3.5(g-j). At high ibuprofen concentration, spicules were observed forming and slightly moving across the RBC membrane but never dissolved by the 20 minutes time point (Movie A.7). Upon exposure to ibuprofen, the RBC transitioned to a spherocytocyte with a lower diameter, from 7.74 μm to 6.69 μm (Figure 3.5(g)), a reduced S/V ratio ranging from 1.49 to 1.24 (Figure 3.5(h)) with decrease in surface area unmatched by decrease in cell volume (Figure A.5(d-e)), and a significant increase in cell sphericity (Figure 3.5(i)) up to 0.95 and later of 0.91 at the 20 minutes time point, reaching values very close to the sphericity of a perfect sphere. The increase in Hb concentration (Figure 3.5(j)) and Hb content (Figure A.5(f)) after exposure to high ibuprofen concentrations was associated with the morphological transition to a spherocytocyte, with the most significant protrusions showing the highest RI values (Figure 3.5(f) inset). Spicule movement on the RBC membrane was observed with high resolution and at a single cell level for all ibuprofen-treated RBCs. An example of a spicule that splits into two daughter spicules within a ~ 20 s time period is shown in Figure 3.5(k-m). Similarly, the dynamic dissolution of a spicule was observed in RBCs treated with low ibuprofen concentration and is portrayed in Figure 3.5(n-p).

For the nanoscopic characterization of spicules on the RBC membrane, we used AFM in tapping mode to analyze RBCs present in air-dried blood. The blood smears were prepared after incubation of healthy blood with different ibuprofen concentrations (0.25 mM, 0.5 mM, 1.5 mM, 3 mM) for up to 1.5 hours (see Methods for details on sample preparation). A progressive increase in the number of echinocytes over normocytes was observed with increasing ibuprofen concentrations, with the majority of the RBCs incubated with 3 mM ibuprofen maintaining the echinocyte morphology after 1.5 hours (Figure A.6). In view of the 1-2 hours half-life of ibuprofen [Holstege, 2005], we suggest that with a high ibuprofen concentrations (3 mM), echinocytosis is likely to persist even when ibuprofen has been excreted. Figure 3.6(a) shows a 3D rendered AFM height image of a single echinocyte RBC, with the white arrows indicating the individual spicules on the RBC membrane. The corresponding height and phase-contrast AFM images are shown in Figure 3.6(b-c). Variations in height between the flatter regions of RBC compared to the regions containing protrusions are visible in the AFM topograph shown in Figure 3.6(a) and were quantified using line sectional analysis as shown in Figure 3.6(d). Compared to the height profile extracted from a

3. Label-free DHTM reveals ibuprofen-induced morphological changes to RBCs

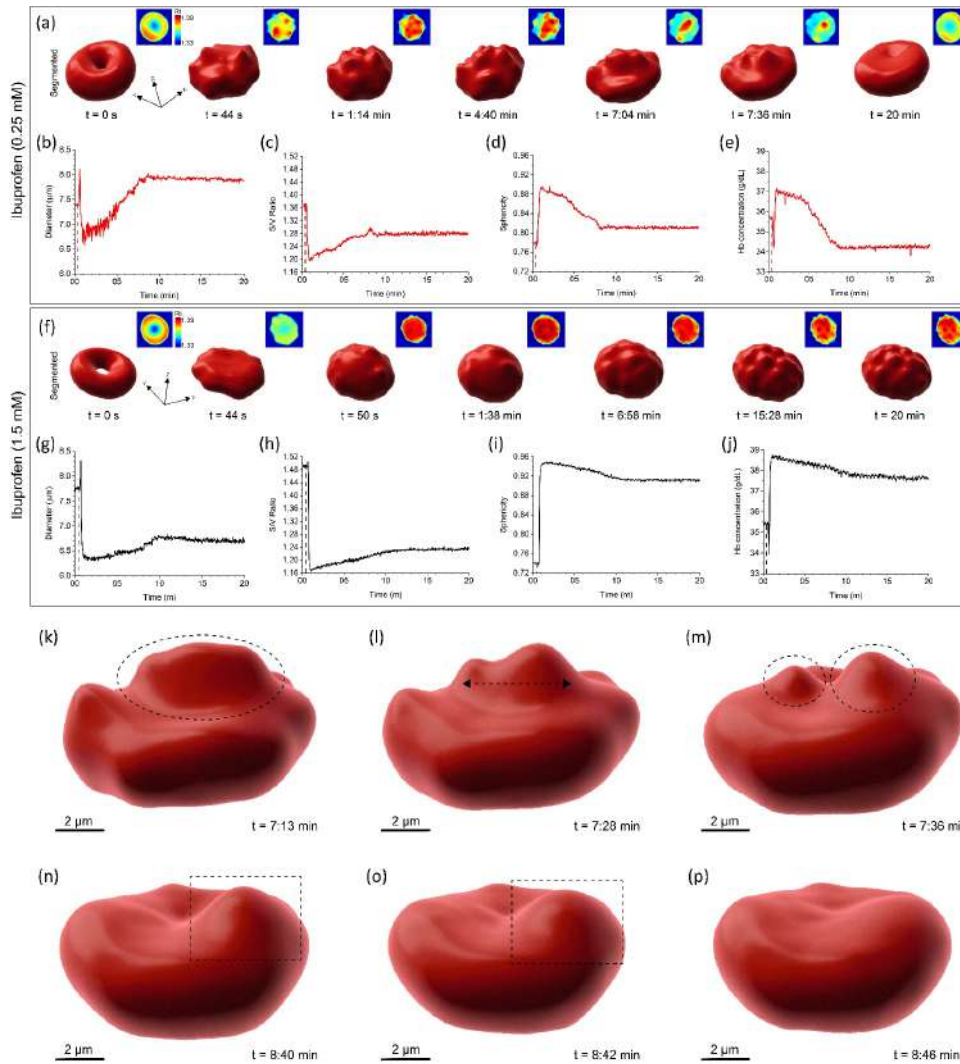


Figure 3.5. RBC morphological changes upon exposure to low and high concentrations of ibuprofen during a 20-minute time-lapse. (a) 3D renderings of a single RBC treated with 0.25 mM ibuprofen showing the transient morphological alteration from a normocyte to an echinocyte (scale bar: $x = 7.57 \mu\text{m}$, $y = 7.36 \mu\text{m}$, $z = 3.28 \mu\text{m}$). Insets in (a) show the corresponding 2D RI maps at each time point. (b-e) Quantification of time-dependent morphological parameters: diameter, S/V ratio, sphericity and Hb concentration. (f) 3D renderings of a single RBC treated with 1.5 mM ibuprofen showing sphero-echinocytosis (scale bar: $x = 7.74 \mu\text{m}$, $y = 6.92 \mu\text{m}$, $z = 2.82 \mu\text{m}$). Insets in (f) show the corresponding 2D RI maps at each time point. (g-j) Quantification of time-dependent morphological parameters: diameter, S/V ratio, sphericity and Hb concentration. (k-m) 3D rendering of a single RBC treated with 0.25 mM ibuprofen showing spicule splitting. (n-p) 3D rendering of a single RBC treated with 0.25 mM ibuprofen showing spicule dissolution.

healthy normocyte shown in green and in the inset in Figure 3.6(d), the height profile of the echinocyte (blue line) presents protrusions of variable sizes, ranging from ~100 to 300 nm, and does not show the typical biconcave disciform profile. Analysis of surface roughness, normalized over an RBC area of $1 \mu\text{m}^2$, between ibuprofen-treated RBCs and healthy RBCs revealed a stark difference, with a higher mean surface roughness of 40.5 ± 20.8 nm for ibuprofen-treated RBCs compared to 8.9 ± 6.6 nm for healthy RBCs (Figure 3.6(e)). Qualitative and quantitative variations in RBC morphology and membrane topography are clearly distinguishable between ibuprofen-treated RBCs and normocytes. In order to register the size of ibuprofen aggregates, ibuprofen solution (concentration: 9.7 mM) was deposited on a gold thin film and the particles were measured using AFM. Figure 3.6(f) shows a height AFM image of the ibuprofen particles. The ibuprofen aggregates were measured on an atomically clean gold surface (surface roughness: <0.5 nm) instead of directly on the RBC surface because the surface of RBCs could also contain other protein aggregates, even in healthy donors, which can result in the misleading estimation of ibuprofen particle size distribution [Nirmalraj et al., 2021]. Averaging over the result from several line sectional profiles similar to those shown in Figure 3.6(g), we calculate a mean ibuprofen particle size of 13.5 nm, with confidence interval lower (CIL) bound of 11.5 nm and confidence interval upper (CIU) of 14.9 nm. The confidence interval was calculated at 95% as shown in the non-gaussian statistical distribution plot (Figure 3.6(h)). The quantitative assessment of ibuprofen particle size distribution suggests that ibuprofen drug molecules could be mostly present in the form of aggregates on the surface of RBCs.

3.3.3. Control experiments to study the effect of other chemicals on RBC morphology

In order to verify that spicule formation is a result of ibuprofen treatment, we performed additional control experiments to investigate the effect of drug-free solutions of urea (Figure A.7), H_2O_2 (Figure A.8) and double-distilled water (ddH₂O) (Figure A.9) on RBC morphology. Urea is known to cross the red cell membrane and to weaken the membrane cytoskeleton by perturbing the structure of spectrin [Khairy et al., 2010]. RBCs treated with 2 M, 4 M and 6 M urea transitioned into spherocytes, with a lower diameter and an increased thickness, S/V ratio and sphericity (Figure A.7(a-c) and (e-j)). When 8 M urea was added to RBCs, spherocytosis was followed by vesiculation and lysis, associated with a drop in Hb concentration and Hb content,

3. Label-free DHTM reveals ibuprofen-induced morphological changes to RBCs

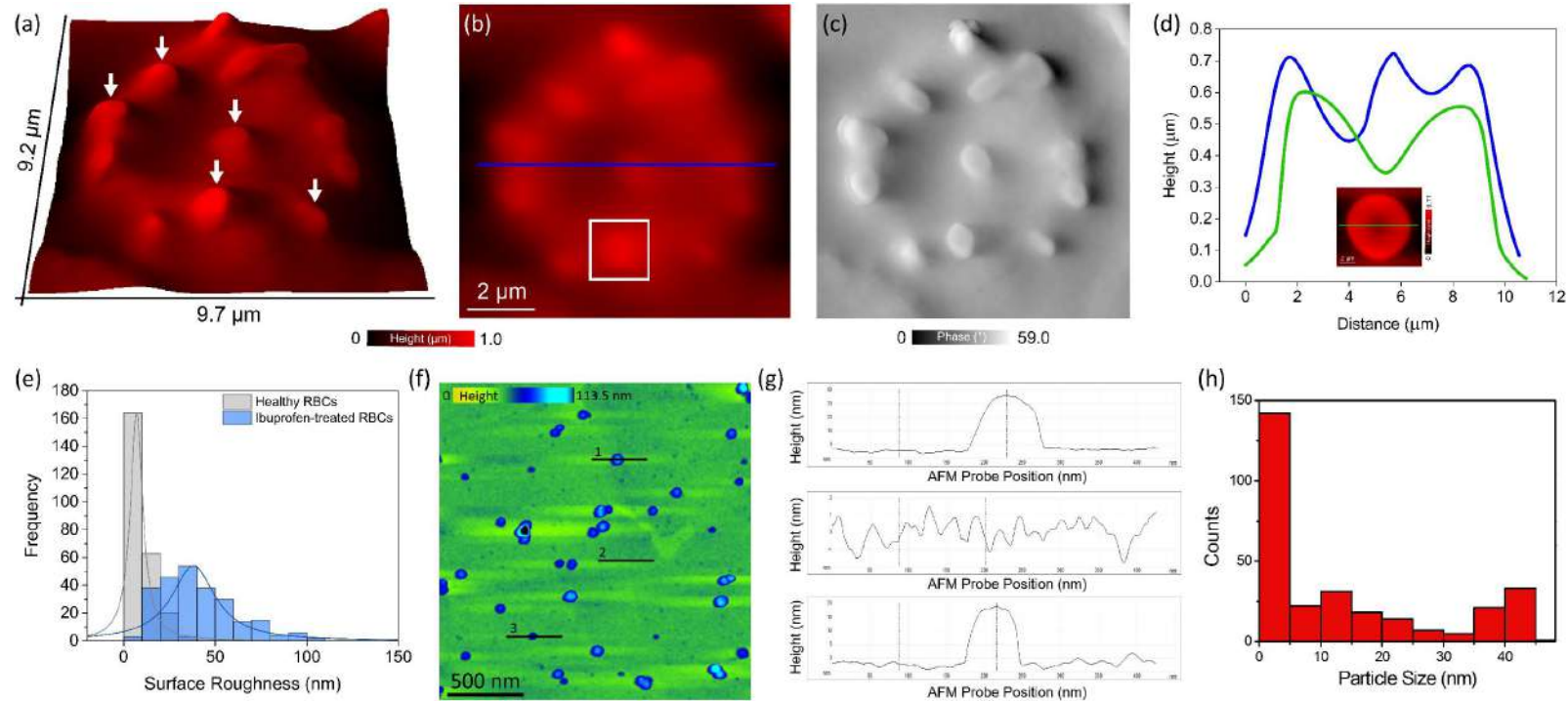


Figure 3.6. Characterization of spicules on ibuprofen-treated RBCs. (a) 3D AFM image of an echinocyte. White arrows indicate spicules on RBC membrane. (b) and (c) Height and phase-contrast AFM images of an echinocyte. (d) Height profile extracted along the blue line indicated in (b) across an echinocyte. The green line indicates the corresponding height profile of a normocyte taken from the inset in (d). (e) Statistical distribution of surface roughness values obtained from AFM based analysis of healthy and ibuprofen-treated RBCs. (f) AFM height image of ibuprofen particles on gold surface. (g) Height profiles of ibuprofen particles extracted along the corresponding lines indicated in (f). (h) Ibuprofen particle size distribution; mean particle size: 13.5 nm, CIL: 11.5 nm and CIU: 14.9 nm.

within ~2 minutes (Figure A.7(d-j)). Additionally, the effect of oxidative damage on RBC membrane function was assessed by introducing different concentrations of H₂O₂ (2M, 4M, 6M, 8M) into the RBC environment, which resulted in a transient morphological transformation into stomatocytes. The stomatocytes displayed slightly decreased diameter and Hb concentration, markedly lower sphericity values and a higher S/V ratio that later mostly recovered to their original normocyte shape at the 15 minutes time point (Figure A.8). H₂O₂ has been previously reported to impair RBC deformability by inducing oxidation of hemoglobin, alterations to membrane proteins and lipid peroxidation [Chen et al., 1991]. RBCs treated with ddH₂O did not undergo any significant morphological change within ~10 minutes, as reflected by a constant diameter, S/V ratio, sphericity and Hb concentration (Figure A.9). Based on these findings, echinocytosis was not observed as a result of urea, H₂O₂ and ddH₂O treatment. In contrast, a morphological transition from normocytes to echinocytes was observed when imaging the RBCs in a petri dish with a glass surface (Figure A.10) and when storing blood diluted in PBS and stored at 4°C over a period of 11 days, in agreement with previous findings, highlighting the importance of studying freshly-collected RBCs for the assessment of RBC morphology (Figure A.1) [Doan et al., 2020; Moon et al., 2013].

Taken together, the DHTM and AFM measurements provide evidence in support of a dose-dependent and time-dependent effect on the ibuprofen induced changes to RBC morphology. Our qualitative and quantitative data confirms that the RBC membrane undergoes distinctive changes when interfacing with ibuprofen drug molecules that can ultimately affect RBC morphology and RBC rheological properties.

3.3.4. Modelling the effect of low vs. high concentrations of ibuprofen on the RBC membrane structure

To understand the experimental dose-dependent effect and interactions of ibuprofen with the RBC membrane lipid bilayer (see Sub-section A.1.1, Figure A.12 and Table A.4 for details of the membrane model composition), we performed extensive molecular dynamics (MD) computer simulations at different ibuprofen concentrations: one molecule of ibuprofen, which we name “single ibu”; preformed aggregates of 80 ibuprofen molecules, “low ibu conc. I”; 100 ibuprofen molecules, “low ibu conc. II”; densely packed 1903 ibuprofen molecules under constant pressure, “high ibu conc. I”; and 1903 molecules at constant volume, “high ibu conc. II” (see Sub-section A.1.2 for more details on the computational models and methods). The structures formed

3. Label-free DHTM reveals ibuprofen-induced morphological changes to RBCs

during 0.1 μ s of equilibrated, unconstrained dynamics for each system reveal that a single molecule of ibuprofen quickly permeates the RBC lipid outer layer (Figure A.13(f)) and remains bound in the lipid core. This is reflected in the improvement in ibu–lipid interaction energies after 10 ns (Figure A.13(k)) facilitated by favorable hydrophobic van der Waals (vdW) interactions of the ibuprofen propyl tail with the lipid aliphatic chains. The small aggregates of ibuprofen at low ibu conc. I and II make only transient interactions with the membrane bilayer (Figure A.13(g-h) and (l-m)) and remain in strongly aggregated clusters driven by ibuprofen–ibuprofen hydrophobic forces (Figure A.14(a-b)). Despite the favorable ibuprofen–ibuprofen vdW interactions (Figure A.14(c-d)), at the high ibu conc. I and II, the densely packed ibuprofen shows significantly improved interactions with the lipid bilayer (Figure A.14(n-o)), leading to disruption of the RBC bilayer as described below.

Computed density profiles of all species (Figure A.14(e-i)) show that the thickness of the lipid bilayer is \sim 7 nm for all but the high ibu conc. II, where the bilayer is compressed to \sim 6 nm (Figure A.14(i)). The small dip in the water density profile marks the position of the aggregated ibuprofen at low concentrations (Figure A.14(f-g)). By contrast, the water density is significantly replaced by densely packed ibuprofen near the outer membrane leaflet at high concentrations (Figure A.14(h-i)), also facilitating diffusion of several ibuprofen molecules into the membrane. There is apparent lateral diffusion of lipid molecules across the membrane as evident from the flattening density of the membrane center at high ibu conc. II (Figure A.14(i)), which otherwise shows a dip in membrane density at high ibu conc. I (Figure A.14(h)). This indicates the presence of hydrophobic tails of each leaflet facing each other sampling a dissipated central membrane thickness. To confirm lateral diffusion of lipids in the membrane due to high concentrations of adsorbed ibuprofen, we computed the mean square displacements (MSD) and diffusion coefficients (D) of lipid headgroup atoms (P, N, and O) for each system. The MSD plots reveal an increased displacement of lipid headgroups mediated by ibuprofen aggregates, but a significantly larger correlation of MSD with simulation time at high ibu conc. II (Figure A.15(a)). Similarly, the D reveals clear distinction between high ibu conc. II and other systems of aggregated ibuprofen on membrane, the former showing a significantly higher diffusivity of the membrane polar headgroups (Figure A.15(b)).

We further mapped the lipid hydrocarbon tail deuterium order parameters (S_{CD} , Figure A.15(c-g)) showing significant loss of lipid order at high ibu conc. II (Figure A.15(g)). Finally, we mapped the lipid heavy atoms number densities in the xy -plane and averaged over the z -axis to obtain a top view of lipid densities in the membrane

3. Label-free DHTM reveals ibuprofen-induced morphological changes to RBCs

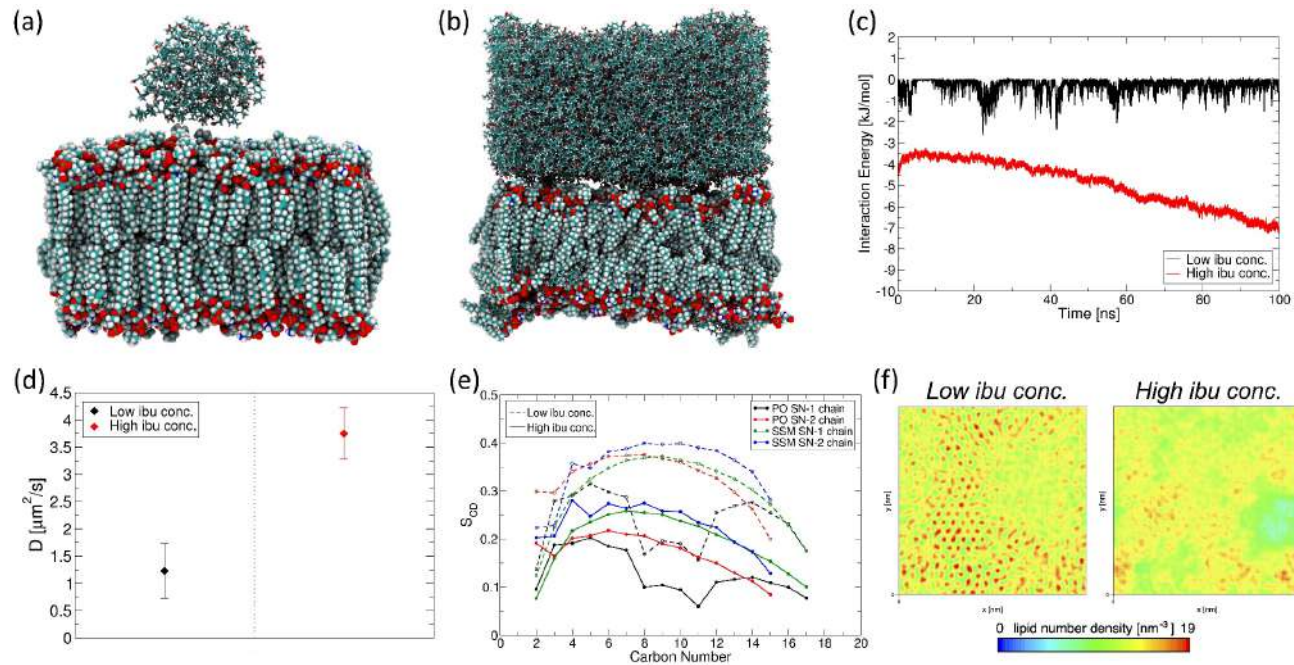


Figure 3.7. Representative structures of ibuprofen (ibu) aggregates on RBC outer membrane bilayer obtained from Molecular Dynamics (MD) simulations of (a) low concentration of ibuprofen adsorbed on membrane, and (b) densely packed high concentration of ibuprofen adsorbed on membrane. (c) Total interaction energies between ibuprofen and lipid membrane at low and high concentrations. (d) Comparison of the diffusion coefficient, D of RBC lipid headgroup atoms (P, N and O) at low (black) and high (red) concentrations of ibuprofen on membrane. (e) Deuterium order parameters (SCD) of the hydrocarbon tails, SN-1 and SN-2 of Palmitoyl Oleoyl (PO) and Stearoyl (SSM) lipids of the RBC membrane bilayer in presence of low and high concentrations of ibuprofen. (f) Maps of average (over the z -axis) lipid number density in the plane (xy) of the RBC membrane bilayer.

(Figure A.15(h-l)). An ibuprofen concentration-dependent loss of lipid structuring could be observed where a single ibuprofen does not affect the lipid density (Figure A.15(h)), while at low concentrations, an uneven distribution is revealed (Figure A.15(i-j)) with low-density pockets that are most prominent at high ibu conc. II (Figure A.15(l)). Overall, our modelling data predict that at low concentration, ibuprofen does not affect the RBC membrane structure (Figure 3.7(a)), but at high concentration, the lipid membrane is deformed (Figure 3.7(b)), due to large-area ibuprofen and lipid membrane interaction at high concentration (Figure 3.7(c)) driven by hydrophobic vdW forces (Figure 3.7(l,o)). The significantly higher lipid diffusion coefficient computed at high ibuprofen concentration reveals that the lipids are in constant motion, while at low concentration, the polar headgroups are more stable (Figure 3.7(d)). The disruption of lipid structural integrity at high concentration is supported also by the disordering of acyl carbon atoms (Figure 3.7(e)). Finally, lipid number density in the plane of the membrane clearly show the dense and ordered lipid packing at low ibuprofen concentration, as opposed to the non-uniform lipid distribution when highly concentrated densely packed ibuprofen is adsorbed on the RBC membrane (Figure 3.7(f)). The data suggests that the lipid molecules undergo a substantial RBC membrane morphological deformation when exposed to high doses of ibuprofen but experience little to no change at low ibuprofen doses.

3.4. Discussion

In this study, we investigated the ibuprofen-induced morphological alterations to RBCs in real-time and in a label-free manner using DHTM. From the 3D RI tomograms, we tracked the formation of spicules on the RBC membrane associated with a clear morphological transition from normocytes to echinocytes upon exposure to ibuprofen drug solutions. The morphological changes in the RBCs were observed to be concentration-dependent and were either transient, at 0.25-0.50 mM ibuprofen concentrations, or never recovered their original shape, at 1-3 mM ibuprofen concentrations, monitored over a period of 20 minutes. The RBC morphological parameters were extracted from 3D RI tomograms and quantified as first demonstrated for healthy, SCT and SCA blood samples. The extracted quantitative information on ibuprofen-treated RBCs supported the qualitative evidence. All RBCs exposed to ibuprofen exhibited a decrease in diameter and S/V ratio, which is driven by a lower cell surface area and volume. This change is associated with the transition from normocytes to echinocytes, with simultaneous increase in sphericity and Hb

3. Label-free DHTM reveals ibuprofen-induced morphological changes to RBCs

concentration in response to the decrease in RBC volume. Spicules were observed to form, merge, split and dissolve on the RBC membrane, correlating the cell shape alterations with the progression of both echinocytosis and spherocytosis processes. Both the cell parameters and shape of RBCs exposed to low ibuprofen concentrations (equivalent to a 200 mg and 400 mg tablet) gradually recovered after ~8 minutes from the introduction of ibuprofen particles, suggesting a reversible drug-induced effect on the RBC membrane. Previously, echinocytosis has also been observed using cell imaging techniques and attributed to presence of excessive EDTA, prolonged storage of RBCs prior to preparation of blood smears on solid surfaces and pathological causes such as in liver and kidney diseases [Hsi, 2017; Naeim et al., 2013]. However, in the present study we attribute the formation of spicules to the interaction of ibuprofen at high concentrations with RBCs. We deduce this result based on label-free imaging of healthy RBCs interacting with ibuprofen, urea (2M-8M), H₂O₂ (2M-8M) and ddH₂O, where spicule formation was only observed for RBCs interacting with ibuprofen molecules. In particular, higher ibuprofen concentrations (equivalent to 800 mg, 1200 mg and 2400 mg) caused RBC morphological changes that resulted in sphero-echinocytes that did not recover to normocytes, revealing a critical dose-dependent effect of ibuprofen and a potential implication for side effects concerning RBC health and function from overdose [Mullan et al., 2017].

Our results are consistent with previous findings based on SEM investigations, indicating progressive echinocytosis with increased ibuprofen concentrations [Manrique-Moreno et al., 2011]. In contrast to SEM-based investigations, we were able to track the dynamic behavior of RBCs upon introduction of ibuprofen and to determine the reversibility of the observed morphological changes over time. The morphological transition from a doughnut-like shape to an echinocyte morphology is suggested to originate from the interaction of the negatively charged ibuprofen particles with the RBC outer membrane bilayer, in accordance with the bilayer-couple hypothesis [Iglıc et al., 1998; Lim et al., 2002]. An increase in the area between the inner and the outer monolayers of the RBC membrane, initiated by the binding of ibuprofen molecules, triggers echinocytosis (Figure 3.8) [Iglıc et al., 1998]. Higher concentrations of echinocytogenic compounds may result in a sphero-echinocyte RBC morphology, with a more distinct spherical shape and less pronounced spicules [Hagerstrand & Isomaa, 1989], which is consistent with our results. Higher sphericity and qualitatively less sharp specular structures were observed with higher ibuprofen concentrations (1-3 mM). Our findings highlight the dynamic formation and movement of single spicules on the membrane of ibuprofen-treated RBCs in real-time

3. Label-free DHTM reveals ibuprofen-induced morphological changes to RBCs

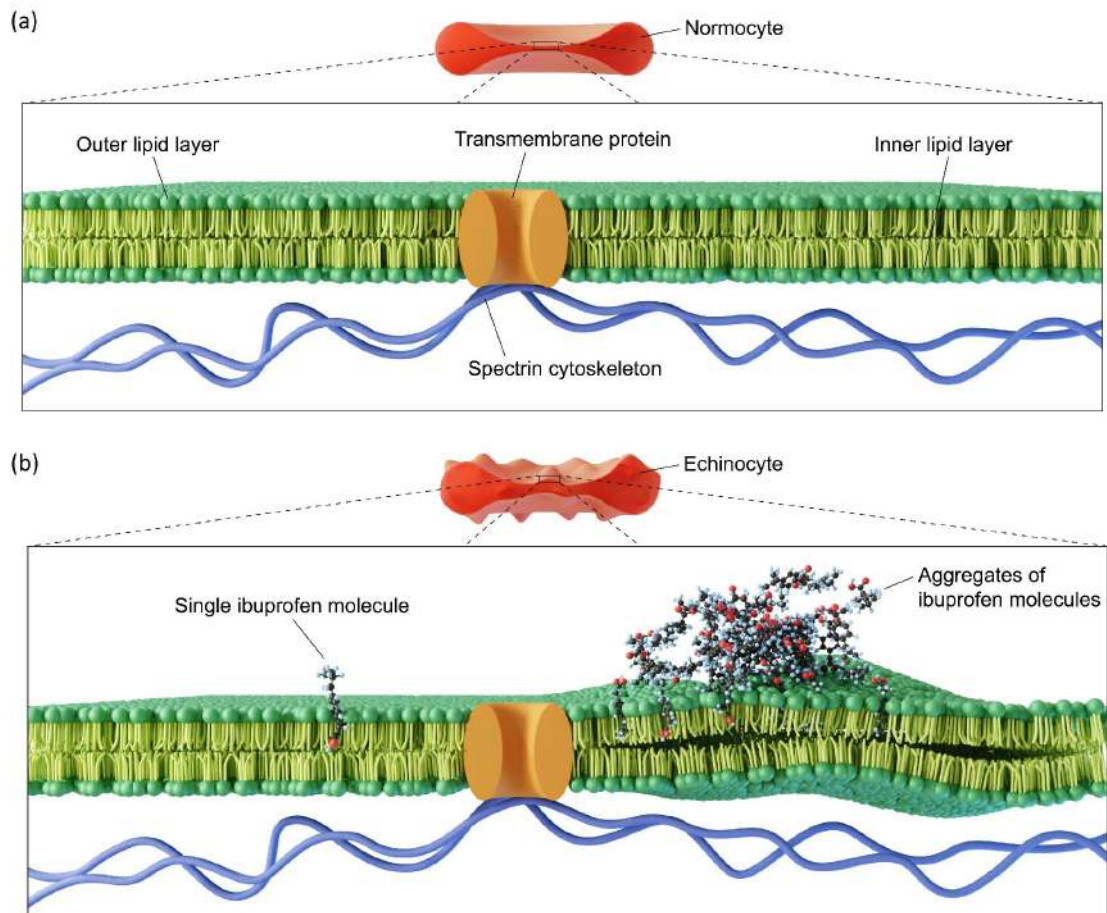


Figure 3.8. Summary schematic of the key findings in this study. (a) Schematic representation of a normocytic RBC membrane architecture showing the lipid bilayer, a transmembrane protein and the spectrin cytoskeleton. (b) Schematic representation of an echinocyte membrane architecture showing the interaction of one ibuprofen molecule (left) and multiple aggregates of ibuprofen molecules (right) with the lipid bilayer. A single ibuprofen molecule permeates and interacts with the RBC lipid outer layer while bigger ibuprofen molecule aggregates diffuse and deform the lipid bilayer, causing spicule formation.

3. Label-free DHTM reveals ibuprofen-induced morphological changes to RBCs

and provide evidence for a dose-dependent reversibility of RBC morphological alterations. The shape of the RBC is dependent on the interplay between the two main membrane components, which are the lipid bilayer and the spectrin cytoskeleton [Lazaro et al., 2013; Melzak et al., 2020]. Thus, when the membrane asymmetry between the inner and the outer layers increases in favor of the outer layers, spicule formation is triggered as a natural response to the expansion of the outer leaflet coupled with the resistance of the cytoskeleton to the morphological distortion [Lazaro et al., 2013]. The theoretical elastic membrane energy model and available experimental data support the preferential initial spicule formation on the RBC contour due to the highest curvature of the cytoskeleton [Lazaro et al., 2013]. Driven by the continuous expansion of the outer monolayer, specular structures tend to move from the rim of the cell towards regions with a lower curvature, including the central area where the distinctive dimple is lost following the progression of echinocytosis, and finally distribute uniformly around the cell membrane [Melzak et al., 2020]. RBCs treated with higher ibuprofen concentrations showed that specular structures are more likely to steadily stay in place towards the later stages of echinocytosis, when a sphero-echinocyte morphology prevails. Before this occurs, the dynamic movement of spicules associated with increased membrane tension can induce spontaneous spicule splitting [Melzak et al., 2020; Zhu et al., 2018]. Here, a singular specular structure separates into two smaller daughter spicules as observed between 7:13 min and 7:36 min time points in Figure 3.5(k-m). Spicules are also seen dissolving (Figure 3.5(n-p)) as the RBC shape returns to its discocyte morphology and the asymmetry between the two membrane leaflets is restored. Therefore, spicule motion tracking can provide real-time information on RBC nano-mechanics and it can act as a potential indicator for membrane bilayer defects [Melzak et al., 2020]. We suggest that in low ibuprofen concentration conditions, the rate of ibuprofen molecules interacting with the RBC membrane bilayer decreases over time, resulting in the transition back to a normocyte. With high ibuprofen concentrations, the constant interaction of ibuprofen molecules causes high RBC membrane asymmetry and the consequent inability of the sphero-echinocytes to recover their discocyte shape. Vesiculation and cell lysis are thought to occur at the final stages following sphero-echinocytosis [Lazaro et al., 2013]. Alterations of the normal discocyte morphology of RBCs have a direct effect on RBC deformability, which determines not only the rheological properties but also the health and life span of single RBCs [Huisjes et al., 2018; Reinhart & Chien, 1986]. Echinocytosis presents a rheological disadvantage characterized by higher viscosity as well as decreased deformability, mainly driven by the increase in sphericity, with a

direct impact on blood flow in large vessels and the ability of RBCs to squeeze through narrow capillaries, respectively [Geekiyana et al., 2019; Reinhart & Chien, 1986]. The increased rigidity of echinocytes may also drive RBC aggregation, potentially contributing to a higher risk of occlusions of blood vessels and an impairment in the transport of oxygen [Jacob, 1975; Lazaro et al., 2013]. The RBC shape changes reported in the present study and the associated alterations to the RBC morphological parameters, including a reduced surface area to volume ratio and an increased sphericity, are in agreement with a detrimental effect of ibuprofen on RBC rheological properties and overall health. Importantly, in our study, the inability of RBCs to recover their doughnut-like morphology was solely observed with high ibuprofen concentrations (1-3 mM), which correspond to 800 mg, 1200 mg and 2400 mg doses that should never be taken all at once, without a medical prescription. The most commonly used ibuprofen doses of 200 mg and 400 mg, corresponding to low ibuprofen concentration ranges used in the present study, showed a temporary echinocytosis progression. The widespread availability of ibuprofen as an OTC drug increases the risk for overdose and thus emphasizes the relevance of the observations reported in the present study in terms of drug safety. The potential risk from the continuous cumulative intake of standard ibuprofen doses over long periods of time, for instance for the treatment of rheumatoid arthritis, could not be assessed within the scope of this study.

3.5. Conclusions

In summary, the findings from our work highlight that the rheological properties of RBCs should be taken into account when formulating the safety levels for dose-dependent OTC and prescribed drugs intake, particularly NSAIDs. We anticipate that our ML-based label-free imaging approach operable with high spatial and temporal resolution even in resource-limited settings could be extended for detection of pathologies that can adversely affect RBC morphology, such as in neurocognitive disorders [Nardini et al., 2022; Nirmalraj et al., 2021; Synhaivska et al., 2022] and transmissible diseases such as malaria [Park et al., 2008].

3.6. Methods

3.6.1. Preparation of blood samples

Whole blood was freshly obtained with the consent of a healthy donor from a finger prick with safety lancets (VWR). Sickle cell trait (SCT) (ZenBio, SER-PRBC-AS) and sickle cell anemia (SCA) (BioIVT, HMRBC-SCKD) human red blood cell samples were commercially obtained from a single donor, respectively (Table A.1). For all blood samples, 10 μL of fresh blood was diluted in 10 mL PBS buffer (VWR) as a stock blood solution and 250 μL of the stock solution was transferred in a 35-mm Ibidi ibiTreat μ -Dish (Ibidi GmbH, Germany) for DHTM imaging. For AFM measurements, blood smears were prepared using 10 μL of fresh blood on SuperFrost glass slides (VWR) and were air-dried for 10 minutes.

3.6.2. Preparation of urea, H_2O_2 and ibuprofen solutions

Urea and H_2O_2 solutions were prepared by dissolving powder urea (~ 0.48 g/mL, Merk Millipore) and 30% H_2O_2 (Merk Millipore) in dd H_2O , respectively. 2M, 4M, 6M and 8M stock solutions were prepared for both urea (Figure A.7) and H_2O_2 (Figure A.8). For each experimental condition, 50 μL of stock solution were added to 250 μL of stock blood solution in the petri dish after ~ 40 s from the start of the live holo-tomographic video acquisition. The same volume of dd H_2O alone was also tested as control (Figure A.9). Ibuprofen powder was obtained by crashing a 400 mg ibuprofen tablet (Mylan Pharma GmbH; stored under standard laboratory conditions) and stock solutions were prepared by dissolving ibuprofen (2 mg/mL) in 2 mL of PBS (VWR) (Figure 3.1(c)). Five concentrations of ibuprofen solution were prepared (0.25 mM, 0.5 mM, 1 mM, 1.5 mM and 3 mM). Based on the healthy donor weight of 60 kg and estimated blood volume of 65 mL/kg, the ibuprofen stock solutions corresponded to ibuprofen dosages of 200 mg, 400 mg, 800 mg, 1200 mg and 2400 mg and ibuprofen plasma concentrations of 51 $\mu\text{g}/\text{mL}$, 103 $\mu\text{g}/\text{mL}$, 205 $\mu\text{g}/\text{mL}$, 308 $\mu\text{g}/\text{mL}$ and 615 $\mu\text{g}/\text{mL}$ [Martini et al., 2015] (Table A.5). 50 μL of each ibuprofen stock solution was added to the blood cells as described above. For AFM measurements, 250 μL of healthy blood was incubated with 50 μL of each ibuprofen solution for 1.5 hours at 37°C, after which 10 μL was deposited on a glass slide and air-dried for 10 minutes. Additionally, 10 μL of ibuprofen solution (9.7 mM) was deposited on a gold thin film and air-dried overnight before imaging.

3.6.3. Label-free digital holo-tomographic microscopy

Label-free holo-tomographic imaging was performed using a 3D Cell Explorer microscope (Nanolive SA, Switzerland). During imaging, a top-stage incubator (Okolab srl, Italy) was used in order to control temperature (25°C), humidity and CO₂. 4D RI tomograms were obtained at the highest temporal resolution of one frame every two seconds. Prior to each measurement, the petri dish containing the stock blood solution was placed inside the chamber of the top-stage incubator and the cells were allowed to sediment to the bottom of the petri dish for 10 minutes before imaging. For DHTM imaging of ibuprofen- treated blood smears, 25 µL of silicone oil (5 cSt, Merk Millipore) was added on the smear and a coverslip was placed on top and sealed with nail varnish (Figure A.11). Silicone oil was previously demonstrated to be a protective layer of cellular structures to conduct high resolution imaging under standard laboratory conditions by circumventing buildup of hydrocarbon and ambient contaminants [Nirmalraj et al., 2018].

3.6.4. Atomic force microscopy

AFM measurements were performed on air-dried blood smear samples using the NaniteAFM with scan head 110 µm (Nanosurf AG, Switzerland). The glass slide was mounted onto the sample stage using the Nanite sample holder and the integral topview camera was used to locate a region of interest and to position it under the cantilever. The sideview camera was then used to perform an initial approach of the cantilever to the sample before the AFM final automatic approach. A Dyn190AI-10 AFM cantilever (Nanosurf AG, Switzerland) with self-alignment grooves, aluminium reflection coating, force constant 48 n/m and resonance frequency 190 kHz was used in phase contrast mode. Large-area 80 µm x 80 µm AFM images were obtained in order to identify non-overlapping RBCs, subsequently followed by single cell ~13 µm x 13 µm high-resolution AFM images. All AFM measurements were conducted at a scan rate between 0.5 Hz and 1.3 Hz. For imaging ibuprofen particles AFM measurements were conducted using multimode AFM (Bruker) using Scout 70 HAR Si tips (70 KHz, 2N/m) on ibuprofen particles deposited on gold thin films on mica substrate (Phasis Inc).

3.6.5. Image processing and analysis

3D and 4D stacks obtained via DHTM were exported as TIFF files and imported into Imaris 9.8 (Bitplane AG, Switzerland). First, stacks were 3D cropped in the z-axis in order to include only slices that contained cells. Next, a 3x3x3 median filter was applied as a noise removal filter. Finally, a surface was fitted with background subtraction and automatic thresholding in order to achieve single cell segmentation. Additional filters were applied to the segmented image in order to filter out overlapping cells that could not be separated as well as partial cells touching the XY image borders. The morphologically-relevant features were quantitatively measured at the single cell level with Imaris, including the cell diameter, surface area, volume, thickness, sphericity and mean RI (Table A.3). The Hb concentration was calculated from the mean RI value of each single RBC, obtained from the 3D RI tomograms, using the following formula [Phillips et al., 2012]:

$$Hb_{Concentration} = \left(\frac{n_{RBC}}{n_{H2O}} - 1 \right) * \frac{1}{\alpha}$$

where n_{RBC} is the mean RI value of the RBC, n_{H2O} is the RI of water (1.333) and α is the wavelength-dependent RI increment for RBCs, which was set to 0.001983 for $\lambda = 520$ nm [Friebel & Meinke, 2006]. The Hb content was calculated for each single RBC by multiplying the V by the $Hb_{Concentration}$ [Kim et al., 2014]. For 4D tomograms, the fitted surface was tracked during the entire duration of the time-lapse and the morphological features extracted for each individual frame. For the quantification of 3D and 4D tomograms, the mean values for all measured RBCs were reported for each morphological and chemical feature. In order to benchmark the measurements for the morphological parameters with DHTM, we used micro-particles based on silicon dioxide (Merk Millipore) with diameters of 2 μ m and 5 μ m. The micro-particles were diluted in PBS, added to a glass slide and a coverslip was placed on top and sealed with nail polish in order to prevent drying. The morphological parameters were quantified with Imaris as described above and compared to the nominal values provided by the manufacturer (Figure A.2). For the ML-based classification, Imaris ML feature based on Random Forest classification was used. A train-test data split of 33%-67% was applied for each experimental condition. During the training phase, single RBCs were manually annotated based on their morphology as normocyte, stomatocyte, echinocyte, acanthocyte, spherocyte, ovalocyte, helmet cell, sickle cell and teardrop cell (Table A.2). Next, the classifier predicted the morphology of the remaining cells based on the training data. All predictions were manually checked for accuracy in view

of the low prevalence of some RBC types. For 4D tomograms, the ML-based classification was applied to each individual frame. For AFM image processing, the raw AFM data were analyzed using open source software Gwyddion 2.60. 2D levelling and scan line correction were applied before extraction of the height profile and surface roughness (RMS roughness, Sq) values. For the analysis of surface roughness distribution between healthy and ibuprofen-treated RBCs, a total of 250 single RBCs were analyzed for each sample. To calculate the size distribution of ibuprofen particles, a total of ~500 were analyzed.

3.6.6. Molecular dynamics simulations

Modelling

The details of modelling RBC membrane bilayer with CHARMM-GUI [Lee et al., 2019; Wu et al., 2014] based on the *in silico* lipid composition of the model erythrocyte membrane in ref. [Chan et al., 2020] is provided in Sub-section A.1.1. Details of preparation of the five ibuprofen-lipid systems and molecular dynamics simulations with Gromacs 2018.4 [Abraham et al., 2015] package using Charmm36m [Huang et al., 2017] force field to represent lipids and CHARMM General force field [Vanommeslaeghe & MacKerell, 2012; Vanommeslaeghe et al., 2012] (CGenFF) to represent ibuprofen is provided in Sub-section A.1.2. Analyses of ibu-lipid and ibu-ibuprofen interaction energies, lipid headgroup mean square displacements (MSD) and diffusion coefficients (D), lipid hydrocarbon tail deuterium order parameters (S_{CD}), and lipid heavy atom number density maps were performed by using *Gromacs tools*. The computed interaction energies plotted are normalized per ibuprofen molecule. The models were visualized using VMD [Humphrey et al., 1996].

4. 3D holo-tomographic mapping of COVID-19 microclots in blood to assess disease severity*



This chapter is licensed under a Creative Commons Attribution-NonCommercial-NoDerivatives 4.0 International License

4.1. Abstract

The coronavirus disease 2019 (COVID-19) has impacted health globally. Cumulative evidence points to long-term effects of COVID-19 such as cardiovascular and cognitive disorders diagnosed in patients even after the recovery period. In particular, micrometer-sized blood clots and hyperactivated platelets have been identified as potential indicators of long COVID. Here we resolve microclot structures in plasma of patients with different subphenotypes of COVID-19 in a label-free manner, using 3D digital holo-tomographic microscopy (DHTM). Based on 3D refractive index (RI) tomograms, the size, dry mass, and prevalence of microclot composites were quantified and then parametrically differentiated from fibrin-rich microclots and platelet aggregates in the plasma of COVID-19 patients. Importantly, fewer microclots and platelet aggregates were detected in the plasma of healthy controls when compared to COVID-19 patients. Our imaging and analysis workflow is built around a commercially available DHT microscope capable of operation in clinical settings with a two-hour time period from sample preparation, and data acquisition to results.

*[Bergaglio, T.](#), Synhaiska, O., Nirmalraj, P. N. *3D holo-tomographic mapping of COVID-19 microclots in blood to assess disease severity* (under review). *BioRxiv*, 2023.

DOI: doi.org/10.1101/2023.09.12.557318

*[Bergaglio, T.](#), Synhaiska, O., Nirmalraj, P. N. *3D holo-tomographic mapping of COVID-19 microclots in blood to assess disease severity*. *Chem. Biomed. Imaging*, 2 (3), 194–204, 2024.

DOI: doi.org/10.1021/cbmi.3c00126

Contribution: T.B. was involved in the planning of the study, conducted the holotomography measurements, image processing, data analysis, interpretation and visualization of results. T.B wrote the original draft of the manuscript and revised it based on the suggestions from the co-authors.

4.2. Introduction

Coronavirus disease 2019 (COVID-19) is a complex disorder caused by infection with severe acute respiratory syndrome coronavirus 2 (SARS-CoV-2) and affects many bodily functions, including excessive immunological response, autoimmunity, and endothelial dysfunction, that have been implicated in the risk of thrombotic events and coagulopathies [Bikdeli et al., 2020; Grobler et al., 2020; Gupta et al., 2020; Kell et al., 2022; Leng et al., 2023; Pretorius et al., 2021; Rahi et al., 2021]. While the acute phase of COVID-19 primarily manifests as a respiratory illness, with a wide range of symptoms including fever, headache, cough, fatigue, muscle pain, and shortness of breath, more severe clinical symptoms, such as systemic inflammatory response syndrome (SIRS), acute respiratory disease syndrome (ARDS), neurological and cardiovascular complications, have been associated with processes underlying coagulopathies and endotheliopathies [Bikdeli et al., 2020; Monje & Iwasaki, 2022; Pretorius et al., 2021]. Currently, it is estimated that approximately 30% of individuals with COVID-19 continue to suffer from a variety of different symptoms involving specific or multiple organ systems, with neurological, neuropsychiatric, and cardiorespiratory clinical presentations [Monje & Iwasaki, 2022; Pretorius et al., 2022], a condition known as post-acute sequelae of COVID (PASC) or long COVID [Monje & Iwasaki, 2022; Schiavone et al., 2023; Scholkmann & May, 2023]. Fatigue, cough, dyspnea, chest pain, headache, dizziness, cognitive impairment known as 'brain fog', and long-term smell and taste dysfunction are the most commonly reported symptoms in individuals suffering from long COVID [Nalbandian et al., 2021; Pretorius et al., 2022; Schiavone et al., 2023]. The World Health Organization defines long COVID as a condition in which individuals with a probable or confirmed infection with SARS-CoV-2 still experience COVID-19-related symptoms usually three months post-infection and lasting for at least two months, with no alternative diagnosis [World Health Organization, 2021]. Endotheliopathy, coagulopathy, and thrombosis are also now established complications of COVID-19 and can persist in individuals diagnosed with long COVID, contributing to the pathogenesis and clinical manifestations of these conditions [Leng et al., 2023; Ranucci et al., 2023; Thompson et al., 2023; Turner et al., 2023].

The pathogenic mechanisms underlying coagulopathy in COVID-19 and long COVID are complex and multifactorial, including a patient's pre-existing conditions [Rahi et al., 2023; Russell et al., 2023]. The presence of SARS-CoV-2 has been detected within endothelial cells, suggesting a direct viral effect on the vascular system [Ackermann et

al., 2020; Grobbelaar et al., 2021]. Additionally, the dysregulated immune response triggered by the viral infection can lead to excessive inflammation and cytokine release, further promoting a pro-thrombotic state [Perico et al., 2021]. More specifically, COVID-19-related coagulopathy was associated with elevated levels of von Willebrand Factor (VWF), D-dimer, fibrinogen, and markers of platelet activation, as well as damaged red blood cells (RBCs) and reduced fibrinolysis, reflecting ongoing coagulation activation [Grobler et al., 2020; Luzak et al., 2023; Venter et al., 2020]. In long COVID, persistent coagulation abnormalities may contribute to the chronic and debilitating symptoms experienced by affected individuals [Lee et al., 2021; Leng et al., 2023; Monje & Iwasaki, 2022]. The formation of microclots, or microthrombi, within the pulmonary vasculature has been observed, contributing to respiratory compromise [De Michele et al., 2022; Kell et al., 2022; Pretorius et al., 2020]. The mechanisms underlying these persistent coagulation disturbances are not yet fully understood, but they may involve a combination of residual inflammation, immune dysregulation, and vascular damage [Gupta et al., 2020; Kell et al., 2022; Rahi et al., 2021].

The incidence of microvascular injury in COVID-19 patients has been detected in the lungs, brain, heart, and other organs during autopsy, using magnetic resonance imaging (MRI) and upon histological examination [Gąsecka et al., 2021; Lee et al., 2021; Wallace Collett et al., 2021; Wool & Miller, 2021]. Previously, Pretorius and co-workers [Pretorius et al., 2020] reported on the presence of microclots in COVID-19 platelet-poor plasma (PPP), using thioflavin T (ThT) staining and fluorescent microscopy. These microclots, ranging in size between 1 and 200 μm , were determined to be amyloidogenic, indicated by the positive ThT signal, suggesting a more anomalous clot structure characterized by extensive β -sheet structures and presenting resistance to fibrinolysis [Grobbelaar et al., 2021; Kell et al., 2022; Pretorius & Lipinski, 2013; Pretorius et al., 2016; Pretorius et al., 2021]. Due to their size, microclots are known to block micro-capillaries and prevent efficient oxygen transport through the blood circulation, which seems to be responsible for part if, not most of, the symptomatology in both acute and long COVID [Han et al., 2023; Kell et al., 2022; Perico et al., 2021].

Scanning electron microscopy and microfluidic-based studies have also provided insights into the coagulation mechanisms in COVID-19 and long COVID compared to healthy plasma by inducing blood clot formation with/without thrombin and SARS-CoV-2 spike protein [Baker et al., 2023; Grobbelaar et al., 2021]. Denser structures with thicker fibrils in the range of ~ 50 - 150 nm in diameter were observed, in addition

to increased clot rigidity and platelet hyperactivation in the COVID-19 samples. Additionally, proteomic-based analysis of microclots revealed the presence of additional plasma proteins, including VWF, complement factors, C-reactive protein, α 2-antiplasmin and the SARS-CoV-2 virus, which may induce the production of different prothrombotic autoantibodies [Baker et al., 2023; Grobler et al., 2020; Kell et al., 2022; Kruger et al., 2022; Zuo et al., 2020].

To date, evidence for the presence of microclots in the plasma of COVID-19 and long COVID patients has been mainly obtained using *in vitro* ThT staining and fluorescent microscopy [Pretorius et al., 2022; Pretorius et al., 2020; Pretorius et al., 2021]. Currently available diagnostic methods for the assessment of coagulopathies include qualitative assessment using ThT labeling-based fluorescent microscopy, or using semi-quantitative Thromboelastography (TEG) and D-dimer analysis [Grobler et al., 2020; Kell et al., 2022; Laubscher et al., 2021; Pretorius et al., 2021]. Importantly, the presence of high levels of D-dimer can serve as an indicator for the production of blood clots and subsequent adequate fibrinolysis but does not sufficiently reflect the nature, composition, and number of the residual microclots in circulation [Kell et al., 2022]. Hence, it would be highly desirable to devise a methodology that would allow for direct determination of microclot morphology, composition, and prevalence in blood in a label-free manner compatible with operating even in resource-limited clinical settings. To address this pending need, we have developed an imaging methodology based on digital holo-tomographic microscopy (DHTM) to three-dimensionally map microclot structure and composition in plasma samples from patients diagnosed with COVID-19, with high spatial resolution and in a label-free manner. In this study, we have resolved chemically fixed micrometer-size blood clots and used them as samples for optimization of imaging protocols, and then extended the DHTM-based imaging methodology to directly characterize microclots in plasma under standard laboratory conditions. No fixation protocols were used to prepare the microclots in plasma samples.

First, the refractive index (RI) maps of synthetically prepared blood clot fragments in aqueous solution from a healthy individual and a convalescent COVID-19 patient were registered using DHTM (see Methods section for details on clot synthesis procedure). The structural information and blood clot composition were quantified by segmenting and digitally staining the 3D RI tomograms, to identify differences in size and composition between blood clot types. Raman spectroscopy measurements were also conducted to further characterize the blood clot structure and composition. Next, we extended the imaging and analysis protocols to directly examine the plasma of

individuals with different COVID-19 subphenotypes, including COVID-19 positive and recovered. Microclots with varying structure and composition were detected in plasma samples from all the COVID-19 patients, regardless of symptom severity. Microclots were classified based on their composition as either microclot composites, fibrin-rich microclots or platelet aggregates. To understand whether microclot structure and composition would differ between COVID-19 subphenotypes, we quantified the overall size distribution and prevalence of microclot subtypes in plasma from COVID-19 compared to healthy donors. Our findings highlight that label-free high-throughput microscopy can be used as a point-of-care technique to visualize and quantify the presence of microclots directly in plasma without the need for complicated sample preparation techniques. Knowledge gained from such microclot analytics could be useful for developing effective treatment strategies to prevent and manage thrombotic complications in COVID-19 and long COVID patients, thereby improving patient outcomes.

4.3. Results

4.3.1. Label-free digital holo-tomographic microscopy of synthetically prepared blood clots

Previously, we have shown that DHTM can be used to visualize and quantify the morphometry of red blood cells as they interact with ibuprofen drug in a non-invasive and label-free manner, with high spatial resolution [Bergaglio et al., 2023a]. In the current study, we first extended the use of DHTM (Figure B.1) to resolve the structure and composition of synthetically prepared blood clot fragments in aqueous solution (Figure 4.1). Blood from a healthy and a convalescent COVID-19 donor was collected and allowed to clot before imaging with DHTM (Methods). Details on the demographic information of the donors are provided in Table B.1. Figure 4.1(a) shows the 3D refractive index (RI) tomogram of synthetically prepared blood clot fragments from a healthy donor, revealing differences in the structural composition based on variations in RI values. From the corresponding segmented RI tomogram (Figure 4.1(b)), micrometer-sized blood clot fragments were digitally stained based on the RI values (Figure 4.1(c)) and a color-coded label was assigned to discriminate between different structural components, including fibrin strands and non-fibrin structures. The same RI classification was applied to spatially well-resolved blood clot fragments obtained

from a COVID-19 donor (Figure 4.1(d)), revealing similar structural components depicting a net-like fibrin network with smaller and circular non-fibrin structures.

To further understand the compositional differences within a micrometer-size blood clot structure, we performed Raman spectroscopy on the same samples (Methods) used previously for DHTM measurements based on which data are shown in Figure 4.1(a) and Figure 4.1(d) were obtained. Figure 4.1(e) shows the Raman spectra collected from synthetically prepared blood clot fragments of healthy (black spectrum) and COVID-19 (red spectrum) donors. Spectrochemical analysis revealed the presence of signal peaks in the spectral regions associated with the presence of fibrin (976, 1248, and 1342 cm^{-1}) [Virkler & Lednev, 2010], hemoglobin (567, 1000, 1368, 1542, and 1575 cm^{-1}) [Atkins et al., 2017; Virkler & Lednev, 2010], and lipids (1266, 1300, 1444 and 1655 cm^{-1}) [Blat et al., 2019]. The averaged spectral signature of blood clot fragments from a patient with COVID-19 presented spectral similarities to the healthy blood clots in the hemoglobin and lipid regions. In the hemoglobin region, an increase in the intensity of the peak at 561 cm^{-1} was detected in the COVID-19 blood clots, indicative of stretching of the Fe-O₂ bond [Atkins et al., 2017]. In contrast, a decrease in the intensity of the peak at 1360 cm^{-1} was observed in the COVID-19 compared to the healthy blood clots. In the lipid regions, a decrease in the intensity of the peaks at 1266 cm^{-1} and 1655 cm^{-1} as well as the peaks at 1305 cm^{-1} and 1450 cm^{-1} was detected in the COVID-19 blood clot samples. These peaks are associated with unsaturated and saturated lipids, respectively [Blat et al., 2019]. In the fibrin regions, a maximum peak at 976 cm^{-1} was detected in the COVID-19 but not in the healthy blood clot fragments. Here, the presence of a peak at 937 cm^{-1} may be indicative of a shift of the fibrin band in the healthy blood clots. In contrast, both blood clot samples presented a maximum peak in a secondary fibrin region at 1342 cm^{-1} , with a lower signal intensity in the COVID-19 blood clot fragments. The peak at 1100 cm^{-1} observed only in the blood clot fragments from a donor with COVID-19 has been previously reported to stem either from ghost RBCs or from heme present in biological samples [Atkins et al., 2017; Blat et al., 2019; Virkler & Lednev, 2010]. Such differences in the spectra between the healthy and COVID-19 blood clot samples may be indicative of changes occurring in the overall structure and composition of blood clots. The Raman spectroscopy data presented here is based on a combined average on several blood clot fragments distributed across the surface.

The structural parameters of healthy and COVID-19 blood clot fragments were extracted and quantified, including the overall size, the fibrin fibrils diameter, and the dry mass. A two-sample t-test revealed a significant increase in clot length (healthy:

50.1 ± 18.9 μm; COVID-19: 66.2 ± 21.5 μm) (Figure 4.1(f)) and width (healthy: 31.0 ± 14.5 μm; COVID-19: 49.1 ± 19.8 μm) (Figure 4.1(g)) in COVID-19 compared to healthy blood clots, suggesting an overall difference in the size of the clot fragments. In addition, the diameter of the fibrin fibrils was significantly larger in the COVID-19 compared to the healthy samples (healthy: 0.64 ± 0.13 μm; COVID-19: 0.77 ± 0.14 μm) (Figure 4.1(h)). Finally, the dry mass was obtained from the RI measurements (Methods). No significant difference was detected between the healthy (5.90 ± 1.57 g/dL) and COVID-19 (5.26 ± 1.5 g/dL) samples (Figure 4.1(i)), indicating a comparable structural composition of the analyzed blood clot fragments.

4.3.2. Structural analysis of microclots in COVID-19 plasma

The described DHTM imaging and analysis protocol was employed to assess the presence of microclots in plasma of five patients with COVID-19 (Table B.2). Different COVID-19 subphenotypes were identified, depending on the presence (positive or recovered) and severity of symptoms (mild, moderate, asymptomatic) at the time of blood collection. Microclots of varying sizes were observed during DHTM measurements in plasma from all five patients. The detected microclots were classified based on their composition: (i) microclot composites, defined as micrometer-size clot structures with mixed composition of plasma proteins [Kruger et al., 2022]; (ii) fibrin-rich microclots, defined as micrometer-size clot structures with prevalent fibrin fibrils and (iii) platelet aggregates, defined as aggregated platelets of different sizes depending on the number of platelets (<10 platelets, 10-50 platelets and >50 platelets). Microclots were found in all the analyzed COVID-19 plasma samples, regardless of age, symptomatology, and IgG and IgM antibody levels. Figure 4.2 shows the results of the DHTM-based analysis of plasma collected from a 27-year-old female patient (donor identified as sample PLS-CVDP2) with a COVID-19 positive and mild symptomatology subphenotype (Methods). The 3D RI tomograms show highly aggregated platelets and the presence of a fibrin-rich microclot of moderate size (~35 μm) (Figure 4.2(a,c)). The microclot structures were segmented and classified based on the microclot type and platelet aggregate size (Figure 4.2(b,d)). To morphologically characterize the microclots, the size, and the dry mass were extracted and quantified from the RI tomograms (Methods). Fibrin-rich microclots were bigger in size (mean = 23.2 ± 7.9 μm) compared to microclot composites (mean = 16.5 ± 5.6 μm), likely due to the length of the fibrin strands in a network format (Figure 4.2(e)). In contrast, the dry mass did not differ between the microclot structures (fibrin-rich microclots = 14.2 ± 0.7 g/dL, microclot composite = 14.9 ± 0.7 g/dL) (Figure 4.2(f)).

4. 3D holo-tomographic mapping of COVID-19 microclots in blood

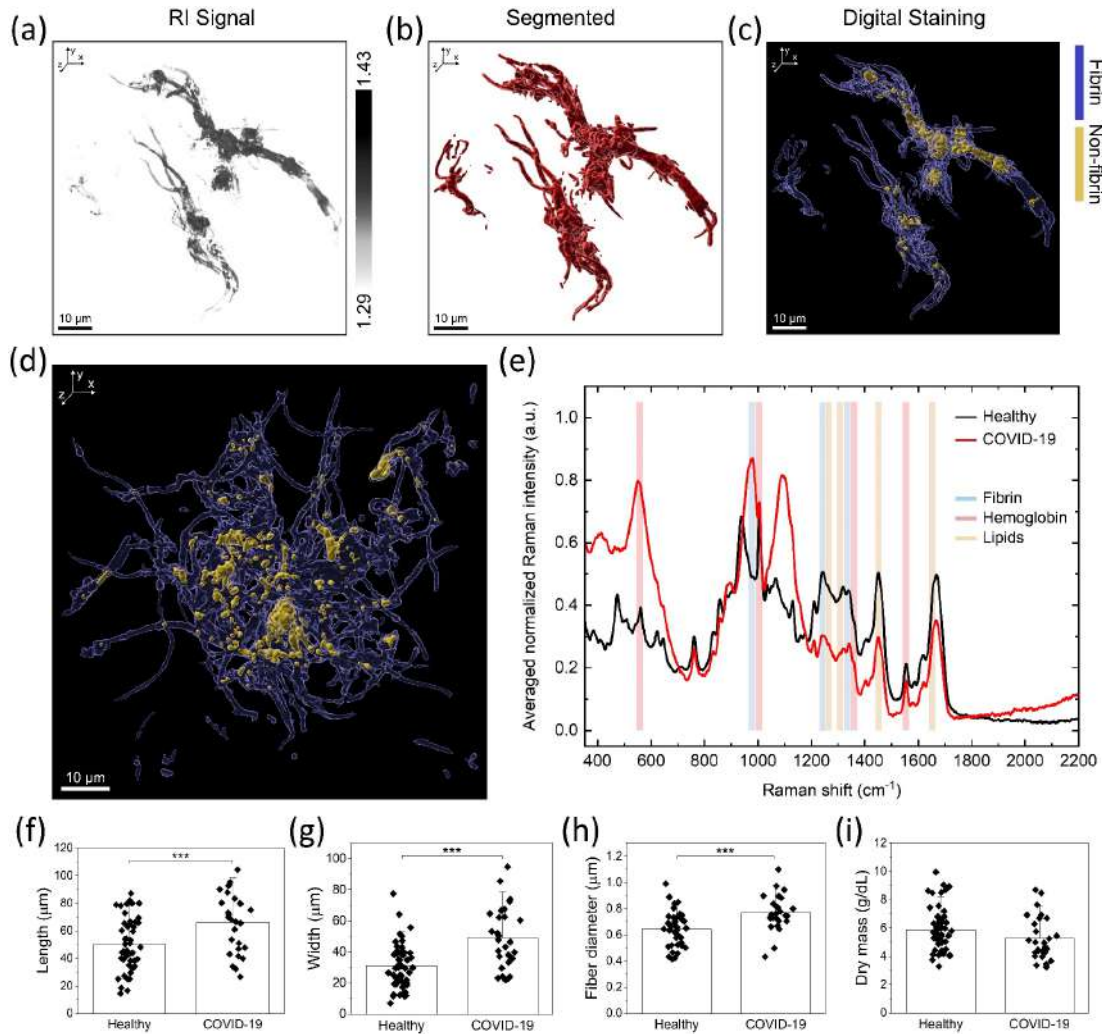


Figure 4.1. Structural and spectrochemical analysis of synthetically prepared fixed blood clots in aqueous solution. (a) Refractive index (RI) tomogram of a blood clot fragment obtained from a healthy donor. (b) Corresponding segmented RI tomogram and (c) digital RI staining for fibrin (blue) and non-fibrin structures (yellow). (d) Digital RI staining for fibrin (blue) and non-fibrin structures (yellow) of a blood clot obtained from a donor with COVID-19. (e) Averaged spectral signatures of blood clots obtained from a healthy donor (black line) and a donor with COVID-19 (red line). Quantification of (f) length, (g) width, (h) fibrin fibril diameter and (i) dry mass of blood clots from a healthy donor and a donor with COVID-19.

4. 3D holo-tomographic mapping of COVID-19 microclots in blood

The size of platelet aggregates differed markedly based on the number of platelets (<10 platelets = $2.6 \pm 1.3 \mu\text{m}$, 10-50 platelets = $13.8 \pm 8.2 \mu\text{m}$, >50 platelets = $26.8 \pm 9.1 \mu\text{m}$), with platelet aggregates of >50 platelets reaching sizes of up to $45 \mu\text{m}$ (Figure 4.2(g)). No major differences were observed in the dry mass of the platelet aggregates (<10 platelets = $15.3 \pm 1.3 \text{ g/dL}$, 10-50 platelets = $15.7 \pm 1.0 \text{ g/dL}$, >50 platelets = $15.7 \pm 0.7 \text{ g/dL}$) (Figure 4.2(h)), likely because these microclot structures are composed of mostly platelets. A total of ~ 4 microclot composite structures, ~ 5 fibrin-rich microclots, and ~ 1570 platelet aggregates were observed in $75 \mu\text{L}$ of plasma (Figure 4.2(i)), indicating extensive platelet pathology characterized by aggregated platelets in plasma from patient PLS-CVDP2.

Next, we analyzed the plasma of a 26-year-old female patient (donor identified as sample PLS-CVDP1) with a COVID-19 positive and moderate symptomatology subphenotype (Figure 4.3 and Methods). A total of ~ 20 microclots were detected in $75 \mu\text{L}$ of plasma, classified as either microclot composite (Figure 4.3(a)) or fibrin-rich microclots (Figure 4.3(c,e)). The segmented and classified 3D RI tomograms show the spatially magnified structure of a microclot composite (Figure 4.3(b)) and reveal the presence of single fibrin fibrils in the plasma of this individual (Figure 4.3(d,f)). A clear size difference was observed between the two types of microclot structures (Figure 4.3(g)). Similar to the PLS-CVDP2, the measured fibrin-rich microclots appeared larger in size (mean = $24.0 \pm 6.7 \mu\text{m}$) compared to the microclot composites (mean = $8.1 \pm 8.0 \mu\text{m}$). Interestingly, the dry mass did not differ between microclot structures (fibrin-rich microclots = $12.9 \pm 0.5 \text{ g/dL}$, microclot composite = $13.4 \pm 1.9 \text{ g/dL}$), except two microclot composites (Figure 4.3(h)). Overall, the described COVID-19 subphenotype was characterized by prevalent microclot composite structures and a few fibrin-rich microclots (Figure 4.3(i)). Platelet clumping was not observed in plasma from donor PLS-CVDP1.

Finally, we report the analysis of plasma collected from a 23-year-old female patient (donor identified as sample PLS-CVDR2) with a COVID-19 recovered and mild symptomatology subphenotype (Figure 4.4 and Methods). The presence of microclots was detected in $75 \mu\text{L}$ of plasma, despite this patient being classified as COVID-19 recovered and no longer experiencing symptoms at the time of blood collection. Microclot composites ($n = 16$) presented varying morphologies, including more dense structures with fibrin fibrils (Figure 4.4(a-b)) and net-like structures intertwined with platelets (Figure 4.4(c-f)). Platelet clumping was also observed ($n = 83$) (Figure 4.4(g-h)). The size of fibrin-rich microclots and microclot composites did not significantly differ (fibrin-rich microclots = $19.0 \pm 1.6 \mu\text{m}$, microclot composites = $20.1 \pm 19.1 \mu\text{m}$)

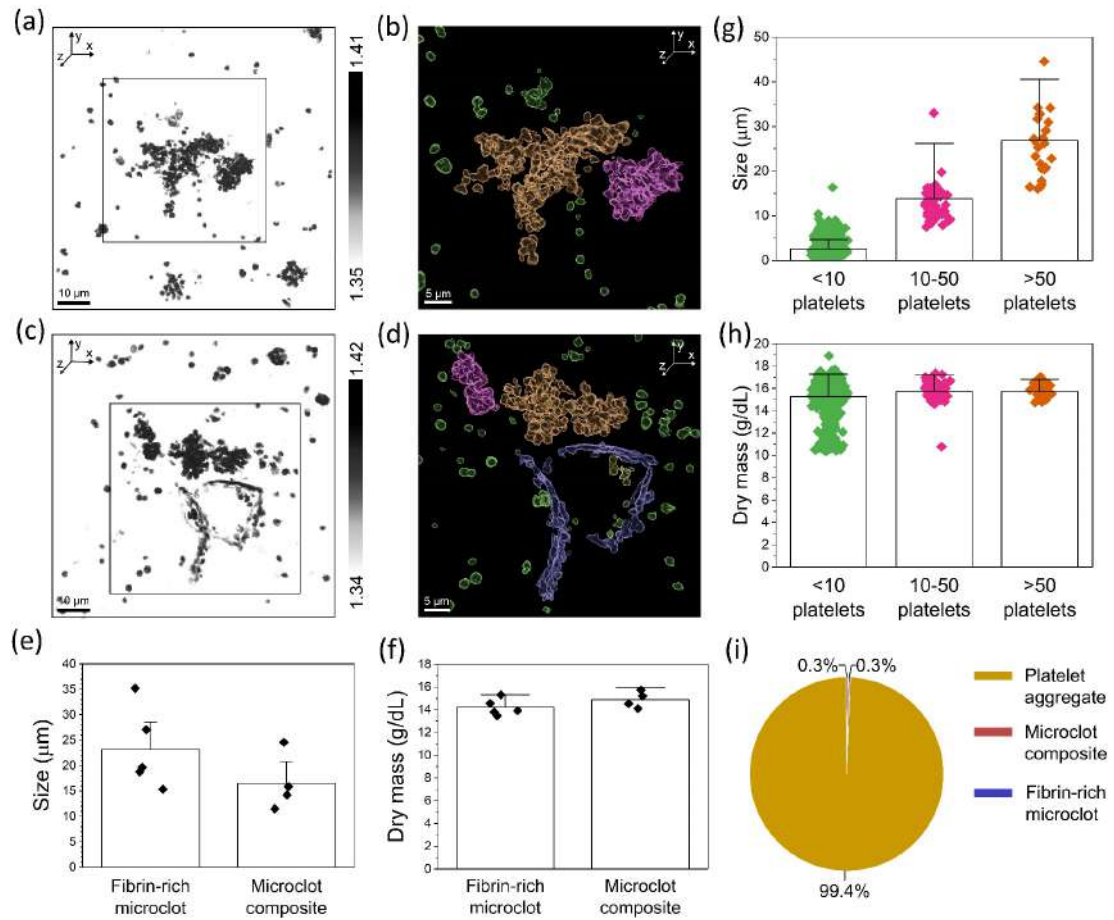


Figure 4.2. Structural analysis of microclots in plasma of a COVID-19 positive patient with mild symptomatology (PLS-CVDP2). (a) Refractive index (RI) tomogram of platelet aggregates in plasma. (b) Corresponding segmented RI tomogram of the platelet aggregates of different sizes from the inset in (a). (c) RI tomogram of a fibrin-rich microclot and platelet aggregates in plasma. (d) Corresponding segmented RI tomogram of the fibrin-rich microclot and the platelet aggregates of different sizes from the inset in (c). (e-f) Size and dry mass of fibrin-rich microclots and microclot composite structures in plasma. (g-h) Size and dry mass of platelet aggregates in plasma. Error bars represent the standard deviation from the mean. (i) Pie chart showing the microclot composition in plasma of donor PLS-CVDP2.

4. 3D holo-tomographic mapping of COVID-19 microclots in blood

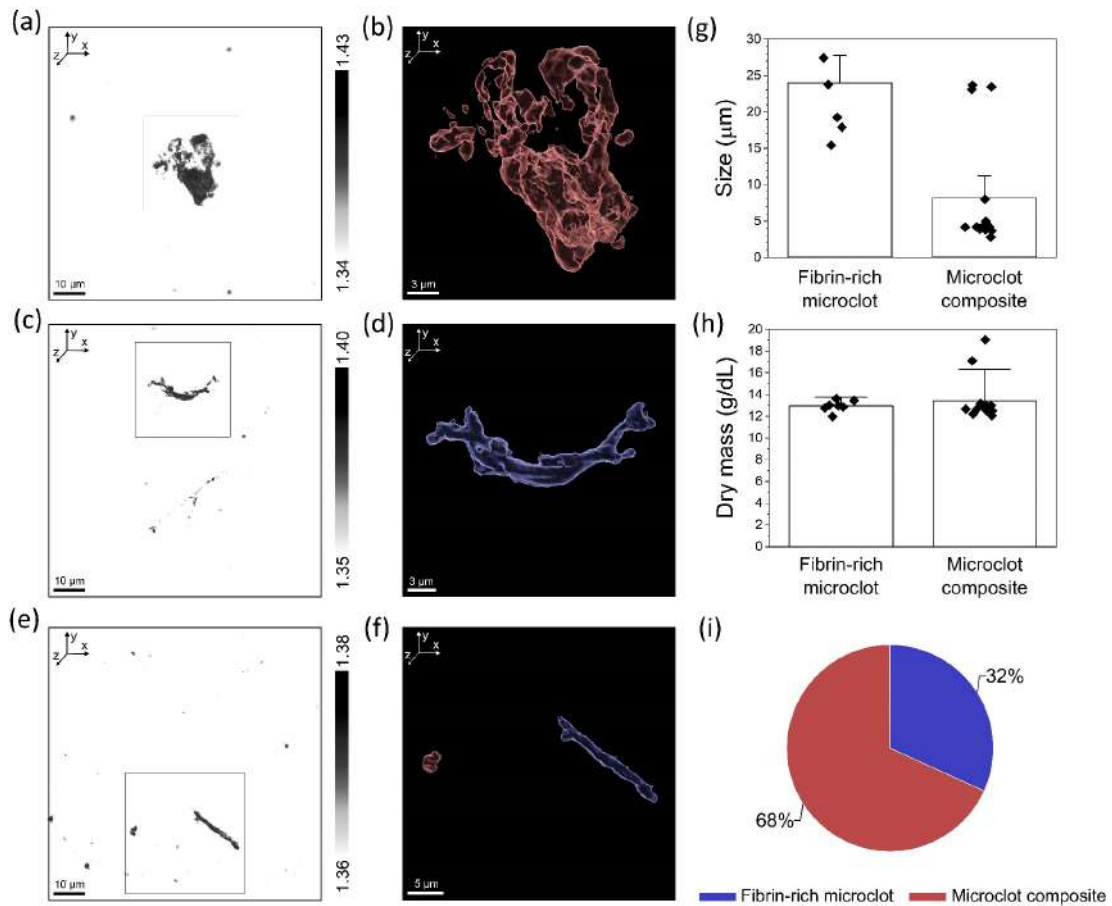


Figure 4.3. Structural analysis of microclots in plasma of a COVID-19 positive patient with moderate symptomatology (PLS-CVDP1). (a) Refractive index (RI) tomogram of a microclot composite in plasma. (b) Corresponding segmented RI tomogram of the microclot composite from the inset in (a). (c) RI tomogram of a fibrin-rich microclot in plasma. (d) Corresponding segmented RI tomogram of the fibrin-rich microclot from the inset in (c). (e) RI tomogram of a microclot composite and fibrin-rich microclots in plasma. (f) Corresponding segmented RI tomogram of a microclot composite and the fibrin-rich microclot from the inset in (e). (g-h) Size and dry mass of fibrin-rich microclots and microclot composite structures in plasma. Error bars represent the standard deviation from the mean. (i) Pie chart showing the microclot composition in plasma of donor PLS-CVDP1.

as shown in Figure 4.4(i). However, a few large microclot composite structures were detected, measuring up to ~ 80 μm in size. Similarly, the dry mass was consistent between the microclot structures (fibrin-rich microclots = 14.3 ± 0.6 g/dL, microclot composite = 14.1 ± 1.3 g/dL) (Figure 4.4(j)). Platelet aggregates varied in size depending on the number of platelets (<10 platelets = 3.5 ± 1.9 μm , 10-50 platelets = 15.5 ± 3.3 μm , >50 platelets = 37.9 ± 7.2 μm), reaching sizes of up to ~ 50 μm (Figure 4.4(k)). Instead, the dry mass did not differ between platelet aggregate structures (<10 platelets = 15.8 ± 0.6 g/dL, 10-50 platelets = 16.8 ± 0.4 g/dL, >50 platelets = 16.3 ± 0.6 g/dL) (Figure 4.4(l)). Overall, this diverse COVID-19 subphenotype presented a mixed composition of microclot structures, with platelet clumping representing the most prevalent feature (Figure 4.4(m)). The structural analysis of the remaining COVID-19 subphenotypes, including a COVID-19 positive female patient with no symptomatology (PLS-CVD3) and a COVID-19 recovered female patient with moderate symptomatology (PLS-CVDR1), and of the healthy controls are provided in the Figure B.2, Figure B.3 and Figure B.4, respectively. Interestingly, microclots were detected in plasma from PLS-CVD3 patient even in the absence of clinical features (Figure B.2).

4.3.3. Quantification of microclot structure and composition in COVID-19 subphenotypes

Following the in-depth description of the DHTM analysis of plasma from the single COVID-19 patients, we present the results on the quantification of microclot structure and composition of all COVID-19 subphenotypes as well as five healthy controls (Figure 4.5). Figure 4.5(a) shows the prevalence of fibrin-rich microclots and microclot composites in 75 μL of plasma from five healthy donors and five patients with different COVID-19 subphenotypes. Overall, these microclot structures were more prevalent in plasma from all COVID-19 samples compared to the healthy controls (fibrin-rich microclot: 1 ± 2 ; microclot composite: 2 ± 2). Within the COVID-19 samples, microclot composites were more prevalent compared to fibrin-rich microclots, except the COVID-19 positive patient with mild symptomatology, which presented an equal number of microclot structures (Figure 4.5(a)). Additionally, a trend for a higher prevalence of fibrin-rich microclots in COVID-19 positive compared to COVID-19 recovered patients can be observed (Figure 4.5(a)). Platelet clumping was also more prevalent in the COVID-19 positive compared to the recovered subphenotypes, although it was not observed in the COVID-19 positive patient with moderate symptomatology (Figure 4.5(b-e)). Aggregated platelets were not detected in any of

4. 3D holo-tomographic mapping of COVID-19 microclots in blood

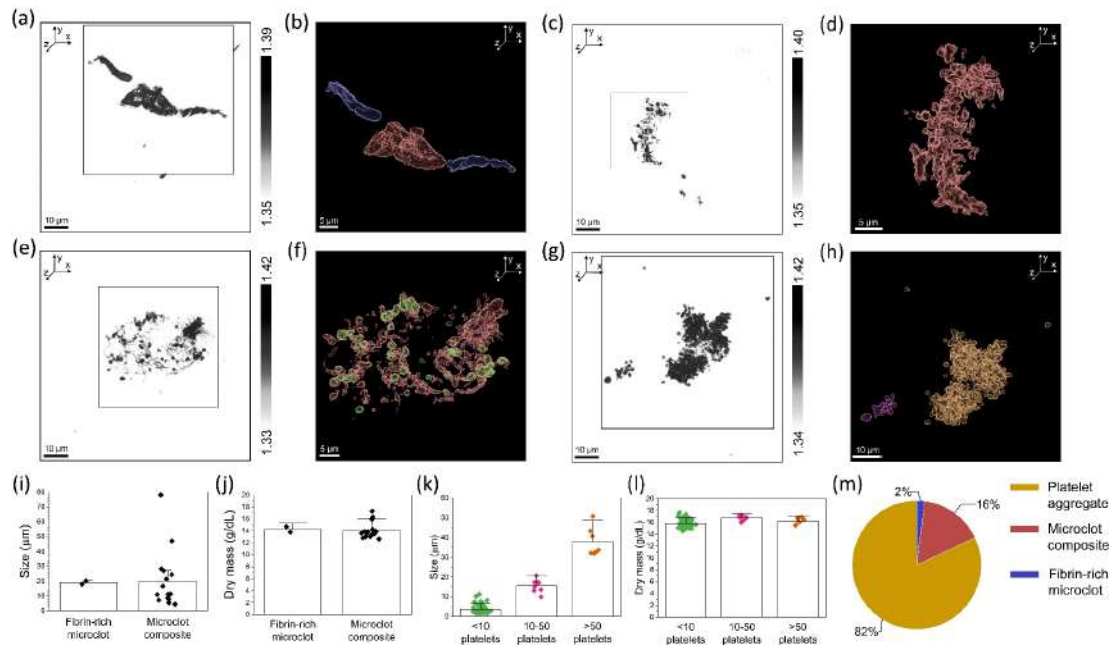


Figure 4.4. Structural analysis of microclots in plasma of a COVID-19 recovered patient with mild symptomatology (PLS-CVDR2). (a) Refractive index (RI) tomogram of a microclot composite and fibrin-rich microclots in plasma. (b) Corresponding segmented RI tomogram of the microclot composite and fibrin-rich microclots from the inset in (a). (c) RI tomogram of a microclot composite in plasma. (d) Corresponding segmented RI tomogram of the microclot composite from the inset in (c). (e) RI tomogram of a microclot composite with platelet aggregates in plasma. (f) Corresponding segmented RI tomogram of the microclot composite with platelet aggregates from the inset in (e). (g) RI tomogram of platelet aggregates in plasma. (h) Corresponding segmented RI tomogram of the platelet aggregates of different sizes from the inset in (g). (i-j) Size and dry mass of fibrin-rich microclots and microclot composite structures in plasma. (k-l) Size and dry mass of platelet aggregates in plasma. Error bars represent the standard deviation from the mean. (m) Pie chart showing the microclot composition in plasma of donor PLS-CVDR2.

the healthy samples. In all samples where platelet clumping was detected, platelet aggregates of <10 platelets were mostly prevalent (Figure 4.5(b-e)). Interestingly, larger platelet aggregates composed of >10 platelets were detected in the plasma of both COVID-19 patients (positive and recovered) with mild symptomatology (Figure 4.5(b-e)). However, a correlation between microclot type and prevalence with the analyzed COVID-19 subphenotypes could not be determined.

Due to the importance of microclot size in the risk of occlusion of micro-capillaries, the mean microclot size was plotted against the microclot type and grouped by healthy and COVID-19 subphenotypes (Figure 4.5(f)). The size of the detected microclots averaged between 1 and 60 μm . Size variation within fibrin-rich microclots and microclot composites between plasma samples was likely dependent on the length of the fibrin fibrils and on the mixed composition of the microclot composites, respectively (Figure 4.5(f)). The average size of platelet aggregates was comparable between COVID-19 subphenotypes and depended on the number of platelets in each aggregate (Figure 4.5(f)). The prevalence of microclots was also plotted against the microclot size and grouped by healthy and COVID-19 subphenotypes (Figure 4.5(g)). For all COVID-19 subphenotypes, microclots were mostly prevalent in the size range between 1 and 10 μm . Overall, the severity of COVID-19 symptomatology as well as the positive or recovered subphenotype did not seem to correlate with the size of the measured microclots. Moreover, a correlation between microclot prevalence and size and the patient age as well as the IgG and IgM antibodies levels was not observed (Figure B.5 and Figure B.6) within the limited number of patient samples analyzed in the present study.

4.4. Discussion

Microclots continue to receive clinical research interest as potential indicators of long COVID [Grobbelaar et al., 2021; Grobler et al., 2020; Kell et al., 2022; Laubscher et al., 2021; Leng et al., 2023; Monje & Iwasaki, 2022; Nalbandian et al., 2021; Pretorius et al., 2022; Pretorius et al., 2020; Pretorius et al., 2021; Turner et al., 2023]. In this study, we employed DHTM as an analytical tool to characterize the composition of plasma from patients with COVID-19 subphenotypes. To test our imaging and analysis protocol, we studied synthetically prepared fixed blood clot fragments in an aqueous solution using DHTM. The preliminary step was to identify and obtain the quantitative morphological parameters from 3D RI tomograms of synthetically prepared blood clot fragments. Blood clot structure can be described by parameters such as the fibrin fibril

4. 3D holo-tomographic mapping of COVID-19 microclots in blood

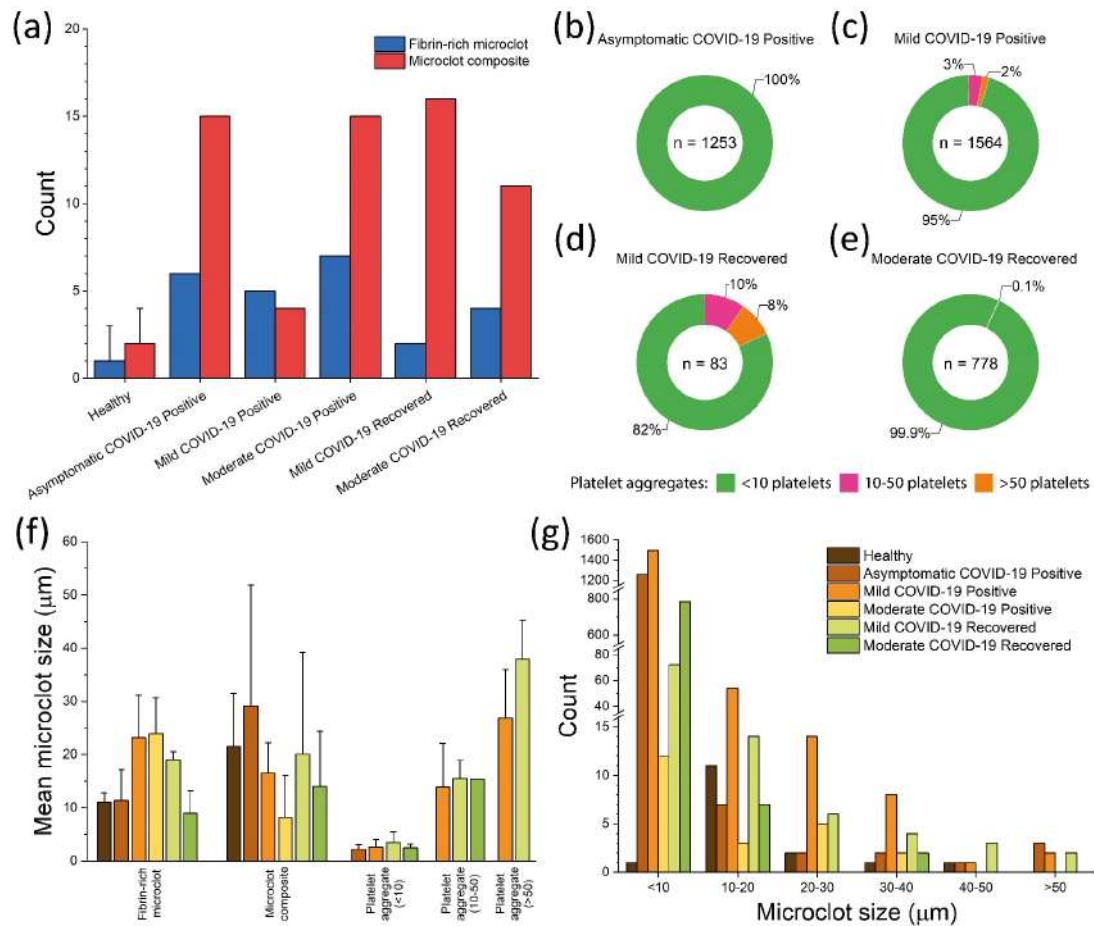


Figure 4.5. Morphological characterization of microclots in healthy and COVID-19 positive and recovered patients. (a) Prevalence of fibrin-rich microclots and microclot composites detected in 75 μL of plasma from healthy and COVID-19 positive and recovered patients. (b) Prevalence of platelet aggregates detected in 75 μL of plasma from a COVID-19 positive patient with no symptomatology, (c) a COVID-19 positive patient with mild symptomatology, (d) a COVID-19 recovered patient with mild symptomatology and (e) a COVID-19 recovered patient with moderate symptomatology. (f) Mean microclot size plotted against the microclot type and grouped by healthy and COVID-19 subphenotypes. Error bars correspond to the standard deviation. (g) Prevalence of microclots plotted against the microclot size and grouped by healthy and COVID-19 subphenotypes.

diameter, fibrin length, clot composition, clot density, and clot porosity [Mihalko & Brown, 2020]. These physical parameters also provide deeper insights into clot stiffness, stability, and degradation dynamics, which play a crucial role in hemolytic processes [Mihalko & Brown, 2020; Pretorius & Lipinski, 2013; Weisel, 2007]. Significant size differences were observed between healthy and COVID-19 blood clot fragments, with regard to the size and fibrin fibril thickness. Although these blood clots were passed through a 30 μm filter in order to fragment them, in general bigger fragments, evidenced by thicker fibrin fibrils, derived from COVID-19 patients, are suggestive of increased clot rigidity. Clot composition and density, estimated from the dry mass, were similar between the two samples, also supported by the spectrochemical signature from Raman measurements. Importantly, digital staining revealed details of an intricate network of fibrin fibrils with smaller and more circular structures trapped in between the fibrils. Similar to fluorescent markers in immunofluorescence, digital staining allows for specific labeling of multiple structures based on the refractive index values, but without altering the inherent features of the sample [Pollaro et al., 2016]. Although we were able to demonstrate the structural characterization of fixed blood clot fragments in an aqueous solution, we cannot explicitly identify the non-fibrin structures observed within these clot fragments. This is due to the inability to access the spatial RI distribution of protein and cellular structures smaller than the DHTM lateral resolution (~ 200 nm). Combining complementary techniques, such as fluorescent-based labeling or expansion microscopy with DHTM could be used to elucidate the nature of the non-fibrin structures. Taken together, DHTM analysis of micrometer-sized blood clot fragments reveals remarkable details of clot structure and composition in a label-free manner, which can be quantified and further classified into different blood clot types. The morphological parameters that we have identified in the first part of our study were then further extended to directly characterize microclots in plasma.

Next, we extended our DHTM-based imaging protocol to study the composition of plasma from patients with COVID-19 and from healthy donors. Similar to previous studies [Grobbeelaar et al., 2021; Laubscher et al., 2021; Pretorius et al., 2022; Pretorius et al., 2020; Pretorius et al., 2021; Venter et al., 2020], we observed microclots in all COVID-19 plasma samples. However, only fewer microclots were in plasma from healthy donors, suggesting microclotting as a salient feature of COVID-19. One of the most notable findings is the structural diversity of the observed microclots, which we have further classified based on their composition: microclot composites, fibrin-rich microclots and platelet aggregates. Microclot composites were found in all COVID-19

plasma samples, with the highest prevalence in the COVID-19 positive patient with moderate symptomatology. These composites structurally resemble the microclots previously reported by Pretorius and colleagues using fluorescence microscopy [Laubscher et al., 2021; Pretorius et al., 2022; Pretorius et al., 2020; Pretorius et al., 2021], with a likely mixed composition of fibrin and other proteins [Grobler et al., 2020; Kell et al., 2022; Kruger et al., 2022]. In some cases, platelets appear to be trapped in between the microclot composite structures. The structural variation in microclot composites observed throughout the COVID-19 plasma samples evidences the presence of a mixed population of fibrin structures and proteins. Microclots were also detected in the form of long fibrin networks. Single fibrin fibrils were also observed, which may stem from clot degradation and fibrinolysis [Grobelaar et al., 2021; Pretorius et al., 2021; Wallace Collett et al., 2021; Weisel, 2007]. Consistent with previous studies [Laubscher et al., 2021; Pretorius et al., 2022; Pretorius et al., 2021], platelet activation and persistent platelet clumping were prevalent features of platelet pathology in all COVID-19 plasma samples, with the exception of the COVID-19 positive patient with moderate symptomatology. Interestingly, the plasma of this patient was characterized by microclot composites and fibrin-rich microclots only, albeit presenting the most severe clinical presentation and high levels of IgG antibodies. Importantly, the size of the measured microclots in COVID-19 plasma samples using DHTM could be of potential clinical interest in regards to their ability to occlude microvasculature and thus impede oxygen transport [Kell et al., 2022]. Microclots formed in the vascular system are likely to explain the heterogeneous symptomatology and multi-organ dysfunction observed in COVID-19 and long COVID patients [Iba & Levy, 2023; Ranucci et al., 2023].

Based on our DHTM analysis, a correlation between microclot type, size and prevalence and COVID-19 subphenotypes could not be established in the small analyzed cohort. However, it is possible that many more pre-existing individual risk factors, aside from SARS-CoV-2 infection status (COVID-19 positive or recovered) and symptomatology, may contribute to the presence and to the extent of COVID-19-related microvascular injury, including a history of smoking, vitamin D deficiency, exposure to air pollutants and the presence of other pathologies such as cancer or diabetes mellitus, for which we could not account for in our study [Bikdeli et al., 2020; Kell et al., 2022; Leng et al., 2023; Pretorius et al., 2020]. The identification of comorbidities is particularly relevant in assessing an individual's risk of developing long COVID [Pretorius et al., 2022; Russell et al., 2023; Thompson et al., 2023]. It is important to note that the symptomatology reported for the analyzed cohort (e.g.

headache, fever) may not directly reflect the coagulopathy status of the patients upon SARS-CoV-2 infection, which in turn would explain why we did not observe a distinct correlation between microclot prevalence and size with COVID-19 subphenotypes. The role of potential risk factors associated with the presence of microclots and the wide spectrum of clinical manifestations of both acute and long COVID may only be unraveled with a larger cohort [Zhang et al., 2023]. Future studies aimed at validating our DHTM methodology will require a larger sample size to be analyzed, comprising patients suffering from both acute COVID-19 and long COVID conditions. Sample stratification also needs to be included in the study for the identification of different comorbidities and risk factors, as well as differentiation between SARS-CoV-2 variants.

In conclusion, the label-free DHTM-based approach demonstrated in our study could serve as a powerful tool for screening microclots in plasma. Information obtained in a label-free manner from such an approach, with high spatial resolution, could provide deeper insights into understanding the role of microclots in health and disease. Furthermore, the approach described in this paper is not only limited to microclot analysis in plasma, but can also be extended to resolve micrometer-size protein fibrils implicated in neurocognitive disorders in cerebrospinal fluid [Nirmalraj et al., 2023]. We anticipate that such an analytical technique, compatible with operation under standard laboratory conditions, could be easily integrated with the existing clinical pipeline for digitally monitoring protein aggregates in body fluids and assessing disease stages.

4.5. Methods

4.5.1. Patient characteristics

In this study, we present data from healthy individuals, COVID-19 positive patients and patients who recently recovered from coronavirus 2 (SARS-CoV-2) infection upon blood collection. The patient characteristics were determined by in-house clinicians at the commercial source from where the samples were purchased. Fixed blood clots fragments in aqueous solution were prepared from fresh human blood collected from one healthy donor and one COVID-19 convalescent donor in the United States (Zenbio). In contrast, plasma was collected from five healthy donors in the United Kingdom (BioIVT) and five adult COVID-19 convalescent donors in the United States (BioIVT). Three COVID-19 patients were classified as COVID positive as they tested positive for the SARS-coV-2 serology test (IgG/IgM positive, IgG positive/IgM negative)

and they were symptomatic at the time of blood collection. Blood samples were collected within one month from the diagnosis of SARS-CoV-2 infection. In contrast, two COVID-19 patients were classified as COVID recovered as they were no longer symptomatic at the time of blood collection and presented with either a positive or negative serology test (IgG positive/IgM negative and IgG/IgM negative). Blood samples were collected between two to three months after COVID-19 diagnosis. The type and severity of symptoms in COVID-19 patients were heterogeneous. Within the COVID positive donor group, one was asymptomatic, one presented mild symptoms (body or muscle aches, chills, and headache) and one had moderate symptoms (body or muscle aches, chest pain, chills, confusion, congestion, cough, diarrhea, fatigue, headache, loss of smell, runny nose, shortness of breath, sneezing, trouble breathing and weakness). Similarly, in the COVID recovered subgroup, one donor had experienced mild symptoms (fatigue, headache, loss of smell and taste) and one donor had experienced a more moderate symptomatology (body or muscle aches, cough, diarrhea, fatigue, fever, headache, loss of smell and taste and shortness of breath). Summaries of the demographics and SARS-CoV-2 serology test results are presented in Table B.2.

4.5.2. Preparation of fixed blood clot samples

Healthy and COVID-19 fixed blood clots samples were commercially obtained (ZenBio) from a single donor, respectively. Whole blood was collected via venipuncture, added to an empty tube, and allowed to clot. The clot was mechanically disrupted and passed through a 30 μm filter in order to generate smaller clot fragments. Finally, the clots were fixed in 4% paraformaldehyde (PFA) and they were provided as 1 mL aliquots and stored at 4°C. For DHTM imaging, 200 μL of blood clots in aqueous solution was transferred in a 35-mm Ibidi ibiTreat $\mu\text{-Dish}$ (Ibidi GmbH, Germany) for DHTM imaging.

4.5.3. Preparation of plasma

Plasma was commercially obtained (BioIVT) for healthy and convalescent COVID-19 donors. Whole blood was collected in K2EDTA vacutainers and centrifuged in order to separate plasma from the cell pallet. Plasma samples were transported and stored at -20°C. For all plasma samples, 50 μL of plasma was diluted in 200 μL of Alsever's solution (Sigma-Aldrich, A3551) and 250 μL was transferred in a 35-mm Ibidi ibiTreat $\mu\text{-Dish}$ (Ibidi GmbH, Germany) for DHTM imaging.

4.5.4. Label-free digital holo-tomographic microscopy

Label-free holo-tomographic imaging was performed using a 3D Cell Explorer microscope (Nanolive SA, Switzerland). Before each measurement, the petri dish containing either the fixed blood clots in aqueous solution or the plasma solution was placed in the microscope sample holder and blood clots were allowed to sediment to the bottom of the petri dish for 10 minutes before imaging. A total of 75 μL of plasma was analyzed for each patient, which would require approximately 1 hour per sample. Each image acquired with the digital holo-tomographic microscope corresponds to a field of view of 90 x 90 x 30 μm . DHTM was operated under standard laboratory conditions.

4.5.5. Image processing and analysis

3D RI stacks obtained by DHTM were exported as TIFF files and imported into the open-source software Tomviz for 3D RI visualization. For the visualization of clot-specific structures, 3D stacks obtained by DHTM were digitally stained based on the RI values using STEVE (Nanolive SA, Switzerland) and each channel was exported in the form of a 3D stack as a TIFF file. The single channel 3D stacks were imported into the open source software Fiji and a 2x2x2 mean filter was applied as a noise removal filter. The single channels were merged into one image, exported as a TIFF file and imported into Imaris 9.8 (Bitplane AG, Switzerland) in order to achieve a 3D surface segmentation. First, stacks were cropped along the x-axis and y-axis in order to exclude potential signal noise artefacts from the imaging process. Next, a surface was fitted for each channel with absolute intensity and automatic thresholding in order to achieve accurate signal segmentation. For the structural analysis and quantification of the blood clots, 3D RI stacks obtained by DHTM were imported into Imaris 9.8 and were cropped along the x-axis and y-axis in order to exclude potential signal noise artefacts. A 3x3x3 median filter was applied as a noise removal filter and a surface was fitted with absolute intensity and automatic thresholding. The morphologically-relevant features were quantitatively measured, including the clot length, width, surface area, volume and mean RI (Table B.3). The dry mass was calculated from the mean RI value of each blood clot, obtained from the 3D RI tomograms, using the following formula [Phillips et al., 2012]:

$$\text{Dry mass} = \left(\frac{n_{\text{clot}}}{n_{\text{H2O}}} - 1 \right) * \frac{1}{\alpha}$$

where n_{clot} is the mean RI value of the blood clot, n_{H_2O} is the RI of water (1.333) and α is the wavelength-dependent RI increment, which was set to 0.001983 for $\lambda = 520$ nm [Friebel & Meinke, 2006]. Approximately a one-hour time period per sample is required to perform the image analysis and quantification.

4.5.6. Raman spectroscopy setup and measurements

Raman spectra were obtained using NT-MDT NTEGRA Spectra system equipped with Olympus LMPLFLN 100× objective with numerical aperture NA = 0.8, and spectrometer grating of 600 g/mm. Samples were illuminated with the 561 nm wavelength laser (10 mW laser power at the sample). Spectra were acquired in the reflection mode, with the integration time of 20 s and 10 accumulations. To obtain a representative spectrum of the measured sample, multiple spectra were acquired in different locations of the sample and then averaged. Raman spectroscopy was conducted only on air-dried fixed blood clots in aqueous solution deposited on SuperFrost glass slides.

5. Urea as a fibrin solubilizer: revisited using nanoscale imaging*

5.1. Abstract

Blood clots play a major role in thrombotic diseases, such as heart attacks, strokes, and pulmonary embolism. Comprehensive understanding of the fibrin structure, a key component of blood clots, is crucial in advancing diagnostics, treatment, and prevention of thrombotic disorders. Here, we use 3D digital holo-tomographic microscopy (DHTM) and atomic force microscopy (AFM) to resolve and quantify the morphological changes of micrometer-sized blood clot fragments treated with urea and aspirin, in a label-free manner. Segmented three-dimensional (3D) refractive index (RI) tomograms revealed a change in clot structural composition upon treatment with urea and aspirin solutions. AFM-based nanoscale analysis of single fibrin fibrils unveiled a significant decrease in size and surface roughness for both aspirin and urea treated blood clot fragments. Evidence for partial denaturation of fibrin was observed upon treatment with 8M urea. Our work provides a deeper understanding on the concentration- and time-dependent effect of chemically- and drug-induced morphological changes to blood clots and corroborates the role of urea as a fibrin solubilizer. This combinatorial imaging approach could serve as a screening tool for blood clot characterization in thrombotic disease and for monitoring efficiency of prescribed therapeutic interventions.

*Hardmeier, S. C., [Bergaglio, T.](#), Nirmalraj, P. N. *Urea as a fibrin solubilizer: revisited using nanoscale imaging and simulations*. In preparation, 2023.

Contribution: T.B. was involved in the planning of the study, developing the methodology and data analysis and discussion. T.B wrote the original draft of the manuscript with S.C.H.

5.2. Introduction

Blood clot formation occurs physiologically as part of hemostasis in order to prevent excessive blood loss when vasculature is injured [Lippi et al., 2009]. The production of blood clots is a highly regulated process, however, under certain pathophysiological circumstances, blood clots can abnormally develop even in the absence of an extrinsic triggering event [Gailani & Renné, 2007]. The formation of anomalous blood clots may arise either due to congenital diseases, involving defects affecting various components of the coagulation cascade, such as antithrombin, protein C and protein S [Rosendaal & Reitsma, 2009], or due to external causes, such as immobilization, the use of oral contraceptives, hormonal replacement therapy and aging [Previtali et al., 2011; Rosendaal & Reitsma, 2009]. Moreover, conditions such as obesity, diabetes, hypertension, and smoking can increase the risk for blood clot formation in the arterial circulatory system [Previtali et al., 2011], contributing to an individual's risk of developing thrombotic complications [Favaloro & Gosselin, 2023]. Consequently, anomalous blood clot formation constitutes the major cause underlying thrombotic disorders such as a myocardial infarction (MI), acute ischemic stroke (AIS), deep vein thrombosis (DVT), and pulmonary embolism (PE) [Previtali et al., 2011; Roth et al., 2020]. In these conditions, blood clots can partially or completely obstruct blood flow in different parts of the body's vascular system, thus leading to a state of hypoxia in organs such as the heart and the brain [Alkarithi et al., 2021; Lippi et al., 2009; Mackman, 2008; Wolberg et al., 2015].

Among the different proteins participating in both extrinsic and intrinsic pathways of hemostasis, thrombin constitutes one of the most important players for the formation of blood clots [Gailani & Renné, 2007; Periyah et al., 2017]. Pathological blood clots are thus associated with either a loss of the regulatory mechanisms that control blood clot formation or with an increased activation of thrombin [Gailani & Renné, 2007; Macfarlane, 1977]. Different stages of hemostasis may be affected in thrombotic diseases [Favaloro & Gosselin, 2023]. Primary hemostasis, initiated by the contraction of blood vessels (vasoconstriction) as well as the formation of a platelet plug to stop the bleeding, [Favaloro & Gosselin, 2023; Periyah et al., 2017]; secondary hemostasis, characterized by the activation of the coagulation cascade, leading to the deposition of fibrin and the formation of a stable fibrin mesh [Favaloro & Gosselin, 2023]; and fibrinolysis, including the dissolution of the blood clot in order to facilitate the ongoing wound healing process [Favaloro & Gosselin, 2023; Periyah et al., 2017]. Importantly, fibrinolysis processes in pathological conditions likely result in unsuccessful clot

degradation and thus extend the presence of blood clots in the vasculature, ultimately increasing the risk for blood flow obstruction [Fatah et al., 1992; Pretorius & Lipinski, 2013].

Blood clots are physiologically heterogeneous structures mainly composed of platelets [Heemskerk et al., 2013], fibrin [Litvinov & Weisel, 2016] and red blood cells (RBCs) [Cines et al., 2014; Jolugbo & Ariëns, 2021], in addition to other plasma-borne proteins such as von Willebrand factor (VWF) [Ruggeri, 2007] and white blood cells [Hagberg et al., 1998; Vilalta et al., 2017], including monocytes, lymphocytes, neutrophils, as well as extracellular DNA namely neutrophil extracellular traps (NETS) [Jolugbo & Ariëns, 2021; Martinod & Wagner, 2014]. Interestingly, the distinct structure and composition of blood clots can provide crucial information concerning the risk for the development and re-occurrence a thrombotic disorder and can determine the efficiency of a targeted treatment strategy [Alkarithi et al., 2021; Jolugbo & Ariëns, 2021]. Characterization of blood clot composition, particularly fibrin structure and mechanical properties, is becoming a critical part for diagnostics, prevention and treatment of thrombotic diseases [Kattula et al., 2017]. Fibrin-rich clots found in thrombotic conditions such as MI, PE and DVT were found to have thicker fibers, smaller pores, less permeability and an extended lysis time [Mills et al., 2002; Undas et al., 2009; Zabczyk et al., 2017]. Altered fibrin composition was also observed in non-thrombotic diseases such as renal disease [Undas et al., 2008], chronic obstructive pulmonary disease [Undas et al., 2009], rheumatoid arthritis [Kwasny-Krochin et al., 2010], diabetes [Dunn et al., 2005; Dunn et al., 2006; Jörneskog et al., 1996] and COVID-19 [De Vries et al., 2021].

The structure and morphology of blood clots has been investigated with different imaging techniques, such as scanning electron microscopy (SEM) [Silvain et al., 2017; Silvain et al., 2011; Zalewski et al., 2015], laser scanning confocal microscopy [Collet et al., 2000; Pretorius & Lipinski, 2013], magnetic resonance imaging (MRI) [Oliveira & Caravan, 2017], Positron emission tomography (PET) [Blasi et al., 2015; Oliveira & Caravan, 2017], immunohistochemistry [Marder et al., 2006; Staessens et al., 2020], and proteomics [Alonso-Orgaz et al., 2014; Muñoz et al., 2018]. Currently available diagnostics methods often require a combination of different techniques in order to achieve a comprehensive blood clot assessment and characterization [Alkarithi et al., 2021]. For examples, AFM was used in combination with fluorescence microscopy to investigate the mechanisms of single fibrin fibres [Liu et al., 2010]. Extensive sample preparation processes, including specimen fixation and staining, coupled with low-resolution image acquisition and phototoxicity-induced artefacts, yield data that is

predominantly semi-quantitative in nature [Alkarithi et al., 2021; Kim et al., 2021]. To address these challenges, we used label-free digital holo-tomographic microscopy (DHTM) and atomic force microscopy (AFM) as a complementary imaging platform for the label-free quantitative characterization of blood clots.

Precise diagnostics and more accurate and personalized treatment strategies can be achieved by characterizing the structural components of blood clots. Efficient thrombus dissolution through thrombolysis primarily relies on the structural composition of the blood clots rather than the fibrinolytic agent itself [Lipinski, 2010]. Antithrombotic agents play an essential role in treating thrombosis and work through three distinct modes of action: antiplatelet, anticoagulant and fibrinolytic [Mackman et al., 2020]. Aspirin, a nonsteroidal anti-inflammatory drug (NSAID) classified as an antiplatelet agent, is often prescribed to patients at elevated risk of experiencing a thrombotic event such as MI or AIS [Antithrombotic Trialists, 2002; Mackman et al., 2020]. Altered fibrin clot structure, characterized by thicker fibers and bigger pores, and resulting in a higher lysis rate, was observed *in-vitro* in fibrin fibers treated with aspirin [Ajjan et al., 2009]. Additionally, urea has been investigated as a strong protein denaturant and fibrin solubilizer in blood clots, increasing clotting time and hindering clot formation in fresh mammalian blood [Canchi et al., 2010; Foulger & Mills, 1930; Wallqvist et al., 1998]. The rate of degradation in the presence of urea is contingent upon the specific bonding forces inherent to the fibrin proteins [Bickford & Sokolow, 1961; Laki & Lóránd, 1948; Lorand, 1950; Pérez-Escalante et al., 2020; Toyama et al., 2017].

In the present work, we demonstrate a combinatorial imaging platform, including DHTM and AFM analysis, in order to investigate the morphological changes of blood clot fragments upon treatment with urea and aspirin. First, 3D RI tomograms of untreated blood clot fragments and blood clot fragments treated with urea and aspirin were acquired with DHTM. The morphological information on blood clot structure and composition was quantified from the segmented 3D RI tomograms to identify differences in size and dry mass. Furthermore, AFM was employed to investigate the morphological changes of blood clot fragments at the nanoscale to measure the size, surface composition and persistence length of singular fibrin fibrils. Our data contributes to a comprehensive quantitative analysis of the structural composition of blood clots in a label-free manner, thereby highlighting the role of blood clot structure in thrombotic , with the ultimate goal of supporting the development of efficient and personalized treatment strategies.

5.3. Results

5.3.1. Characterization of untreated blood clot fragments

Previously, we have shown that DHTM can be used to visualize and quantify the morphometry of micrometer-size blood clots in aqueous solution in a non-invasive and label-free manner, with high spatial resolution [Bergaglio et al., 2023b]. The untreated blood clot fragments served as a control group in order to compare the morphological changes upon urea and aspirin treatment. Figure 5.1(a-c) shows the 3D RI tomograms of the blood clot fragments dissolved in PBS, unveiling differences in blood clot morphology. From the corresponding segmented 3D RI tomograms (Figure 5.1(d-f)), the size and the dry mass of single blood clots fragments were extracted. For the nanoscopic characterization of blood clot fragments, the AFM was employed to resolve and analyze the structure of the fibrin strands observed within the single fragments (Figure 5.1(g-i)). The AFM height image of three blood clot fragments and the corresponding height profile are shown in Figure 5.1(j-l).

5.3.2. Structural analysis of blood clot fragments treated with urea

The dose-dependent effect of urea on blood clot fragments dissolved in PBS was evaluated using DHTM (Figure 5.2). Figure 5.2(a-d) show the segmented RI tomograms of the blood clot fragments during incubation with different concentrations of urea (2M, 4M, 6M and 8M, respectively), over a period of 15 minutes. No structural effect, such as fibrin denaturation or fragmentation due to urea, was visible on the fibrin structures as observed in these RI tomograms. Figure 5.2(e) shows the size distribution between the untreated and the urea treated blood clot fragments. A one-way ANOVA revealed no significant differences in the mean size of the blood clot fragments between the untreated ($37.7 \pm 23.7 \mu\text{m}$) and urea-treated blood clot fragments ($42.7 \pm 25.6 \mu\text{m}$ for 2M concentration, $37.2 \pm 23.1 \mu\text{m}$ for 4M, $38.3 \pm 25.0 \mu\text{m}$ for 6M and $42.8 \pm 30.2 \mu\text{m}$ for 8M). In contrast, the dry mass was significantly lower in the blood clots incubated with urea at 2M ($5.9 \pm 0.9 \text{ g/dL}$), 4M ($6.1 \pm 1.1 \text{ g/dL}$) and 8M ($6.4 \pm 2.0 \text{ g/dL}$) compared to the untreated blood clot fragments ($7.3 \pm 2.4 \text{ g/dL}$) (Figure 5.2(f)). Treatment with 6M urea yielded a trend for a decrease in dry mass ($6.5 \pm 1.9 \text{ g/dL}$).

5. Urea as a fibrin solubilizer: revisited using nanoscale imaging

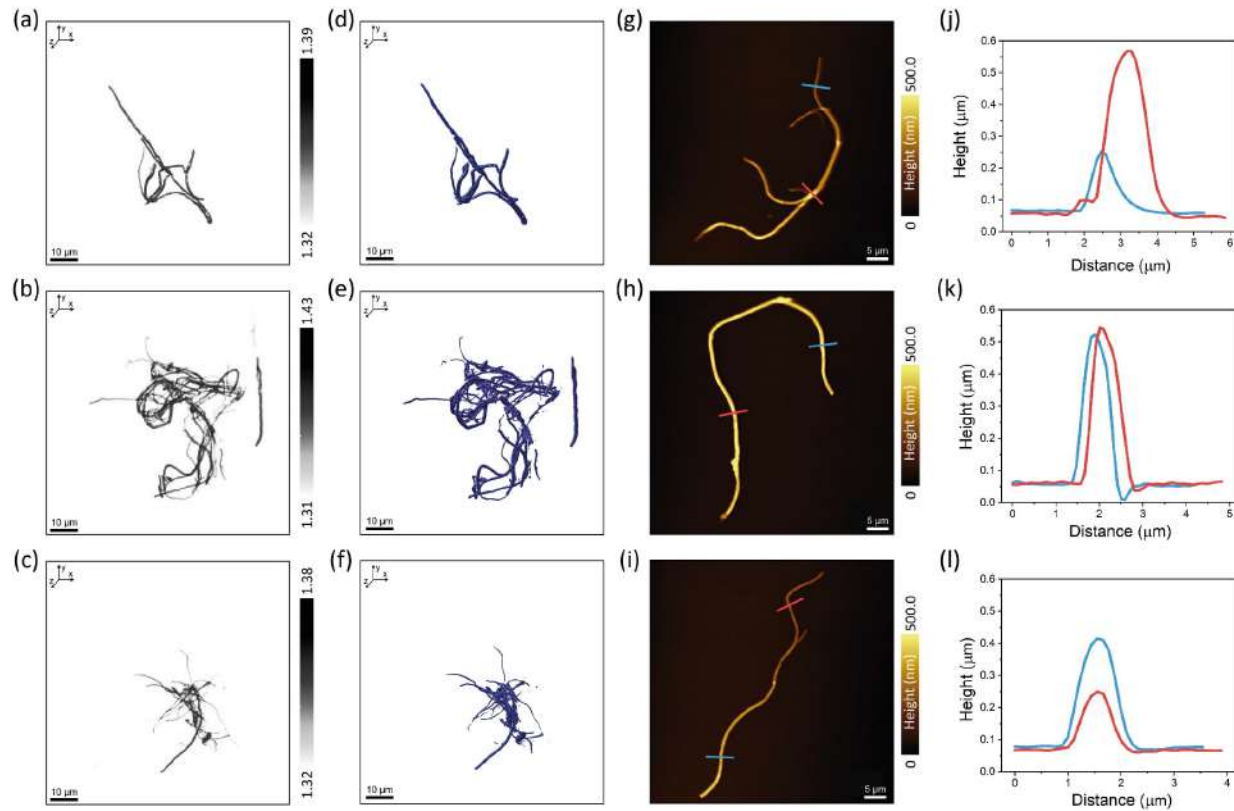


Figure 5.1. DHTM and AFM characterization of untreated blood clot fragments. (a-c) 3D Refractive Index (RI) tomograms of synthetically prepared blood clot fragments from a COVID-19 patient. (d-f) Segmented RI tomograms of synthetically prepared blood clot fragments from a COVID-19 patient. (g-i) AFM height image showing synthetically prepared blood clot fragments on glass slide from a COVID19 patient. (j-l) Height profile analysis of three cross-sectional areas of the blood clot fragments.

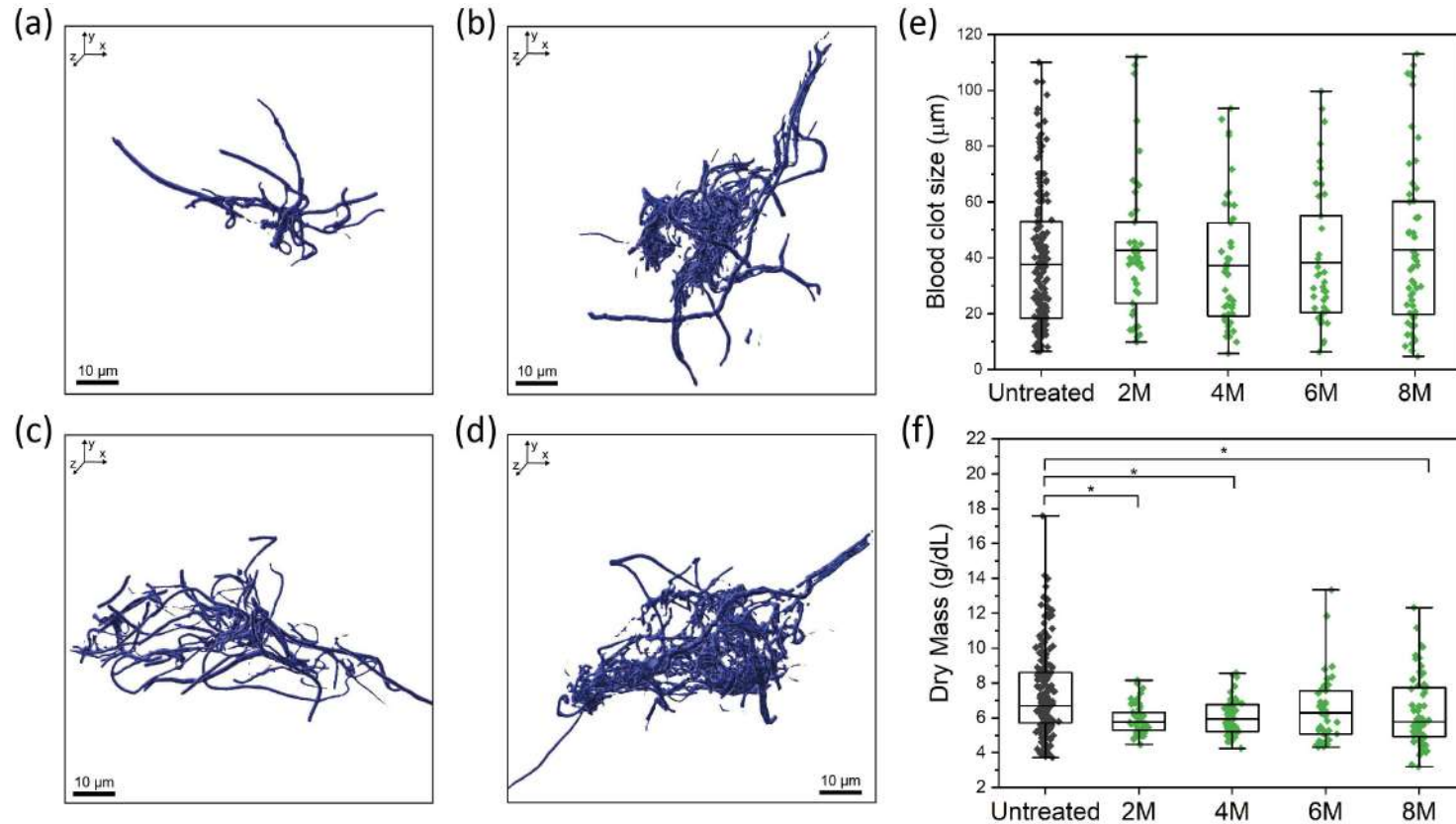


Figure 5.2. DHTM characterization of urea-treated blood clot fragments. (a-d) Segmented RI tomogram of synthetically prepared blood clot fragments from a COVID-19 patient with four different concentrations of urea (2M, 4M, 6M and 8M). (e) Fibrin size distribution across the untreated and urea treated blood clot fragments. (f) Dry mass distribution of the untreated versus the urea treated conditions.

Figure 5.3 shows the AFM-based analysis on the height profile distribution, surface roughness and persistence length quantification of blood clot fragments treated with urea, over two different incubation times (15 and 120 minutes). Figure 5.3(a) shows a blood clot fragment incubated with 8M urea over a period of 15 minutes. Similarly, blood clot fragments treated with 8M urea and incubated for 120 minutes are depicted in Figure 5.3(b-d). From each AFM height image, the corresponding topographic profile of single fibrin fibers was extracted (Figure 5.3(e-h)). The fibrin size distribution was quantified for the untreated and 8M urea-treated blood clot fragments with two incubation times (Figure 5.3(i)). A one-way ANOVA revealed an overall significant difference between conditions characterized by a treatment- and incubation time-dependent decrease in fibrin size (untreated = 483.0 ± 184.4 nm; 8M urea-15 min. = 312.9 ± 123.3 nm; 8M urea-120 min. = 251.4 ± 100.9 nm). Figure 5.3(j) shows the surface roughness distribution of the control and both 8M urea treatment conditions. A significant decrease in mean surface roughness between the untreated blood clot fragments (35.1 ± 18.6 nm), the urea treated clots with an incubation time of 15 minutes (28.8 ± 13.1 nm) and with an incubation of 120 minutes (17.1 ± 9.8 nm) was observed. Finally, the persistence length distribution of the measured fibrin fibers was quantified (Figure 5.3(k)) and yielded a significant decrease in the urea-treated blood clot fragments with 120 min. incubation time (1550.3 ± 335.5 nm) compared to the untreated clots (2041.9 ± 543.8 nm). Interestingly, no significant change in persistence length was observed between the untreated and the urea treated blood clot fragments with an incubation time of 15 minutes (2051.9 ± 556.2 nm).

5.3.3. Structural analysis of blood clot fragments treated with aspirin

Figure 5.4 shows the DHTM-based characterization of blood clot fragments dissolved in PBS and incubated with four different concentrations of aspirin (70 μ M, 140 μ M, 460 μ M, and 1.42 mM). Figure 5.4(a-d) shows the segmented 3D RI tomograms of the aspirin-treated blood clot fragments with different concentrations. Fibrin denaturation or fragmentation was not observed upon treatment with aspirin. Similarly to urea, the fibrin size distribution between the untreated and the aspirin-treated blood clot fragments was quantified (Figure 5.4(e)). A one-way ANOVA revealed no significant difference in mean blood clot size between the control and aspirin treatment groups (control = 37.7 ± 23.7 μ m; 70 μ M = 44.4 ± 27.4 μ m; 140 μ M = 45.1 ± 30.5 μ m; 460 μ M = 31.8 ± 19.4 μ m; 1.42 mM = 41.2 ± 28.8 μ m). In contrast, the dry mass was significantly decreased in the aspirin treated blood clot fragments (70 μ M = 6.3

5. Urea as a fibrin solubilizer: revisited using nanoscale imaging

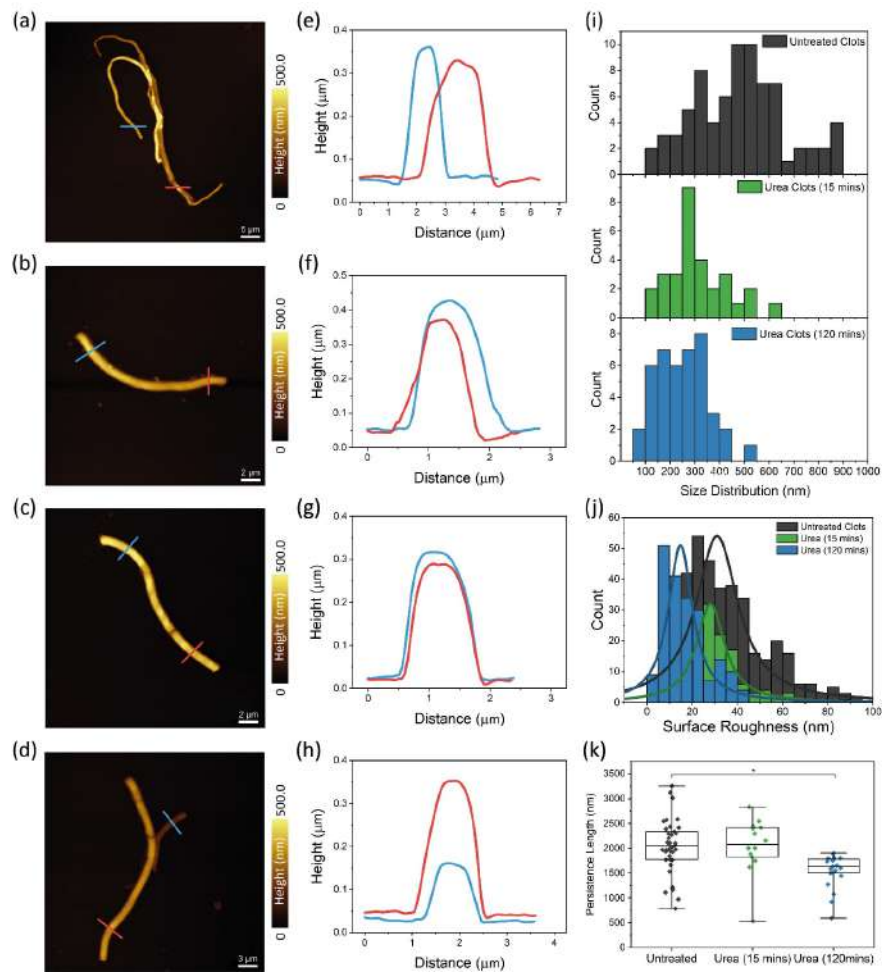


Figure 5.3. AFM characterization of urea treated blood clot fragments. (a) AFM height image showing synthetically prepared blood clot fragments on glass slide from a COVID-19 patient treated with 8M urea concentration with an incubation time of 15 minutes. (b-d) AFM height image showing synthetically prepared blood clot fragments on glass slide from a COVID-19 patient treated with 8M urea concentration with an incubation time of 120 minutes. (c) Height profile analysis of two cross-sectional areas of the blood clot fragments with an incubation time of 15 minutes. (f-h) Height profile analysis of two cross-sectional areas of the blood clot fragments with an incubation time of 120 minutes. (i) Fibrin size distribution of untreated blood clot fragments, urea treated blood clot fragments with 8M urea, 15 minutes incubation time and 120 minutes incubation time, respectively. (j) Surface roughness distribution of all untreated blood clot fragments and with 8M urea treated blood clot fragments with either 15 minutes or 120 minutes incubation time. (k) Persistence length distribution of the untreated fragments and both conditions of urea treated blood clot fragments (15 and 120 min.).

± 0.8 g/dL; $140 \mu\text{M} = 6.1 \pm 1.1$ g/dL; $460 \mu\text{M} = 6.2 \pm 1$ g/dL; $1.42 \text{ mM} = 6.3 \pm 1.2$ g/dL) compared to the untreated group (7.3 ± 2.4 g/dL) and (Figure 5.4(f)).

In order to characterize the nanoscopic changes of the blood clot fragments upon treatment with different aspirin concentrations, AFM was used to determine the effect of aspirin on the single fibrin strands (Figure 5.5). Figure 5.5(a-d) show the AFM height image of the resolved blood clot fragments incubated with 1.42 mM aspirin, with the corresponding height profiles (Figure 5.5(e-h)). A one-way ANOVA revealed a significant decrease in fibrin fiber size in the aspirin-treated ($335.4 \pm 119.8 \text{ nm}$) compared to the untreated blood clot fragments ($482.0 \pm 184.4 \text{ nm}$) (Figure 5.5(i)). Figure 5.5(j) shows the extracted surface roughness distribution in the untreated and aspirin-treated conditions. Fibrin fibers in the untreated blood clot fragments showed a significantly higher surface roughness ($35.1 \pm 18.6 \text{ nm}$) compared to the aspirin-treated clots ($27.2 \pm 11.9 \text{ nm}$). In contrast, no significant difference in persistence length was observed between the untreated blood clot fragments ($2041.9 \pm 543.8 \text{ nm}$) and the clots incubated with aspirin ($1815.7 \pm 471.8 \text{ nm}$) (Figure 5.5(k)).

5.4. Discussion

The primary aim of this study was to investigate and characterize the morphological changes occurring in blood clot fragments treated with urea and aspirin, in a label-free manner using DHTM and AFM. With the acquired 3D RI tomograms obtained from DHTM, we extracted the morphological features of the blood clot fragments, such as size and dry mass. Untreated blood clot fragments served as a control group in order to establish a baseline understanding of our samples. The DHTM measurements revealed variations in size and dry mass of the blood clot fragments. These variations can be attributed to the diverse composition of the blood clots, including fibrin and likely other proteins and cell fragments that we were not able to quantify in these samples. With the application of AFM, we achieved high-resolution, nanoscale insights into the variations of fibrin size, surface roughness and persistence length, which reflect the heterogeneous nature of the blood clot fragments.

From the DHTM measurements, we were able to resolve the intricate structure of micrometer-sized blood clots in 3D, with high-spatial, thus providing a greater level of detail of the morphology of single blood clot fragments. No significant size differences were observed after incubating the clot fragments with different concentrations urea (2M, 4M, 6M and 8M) and aspirin ($70 \mu\text{M}$, $140 \mu\text{M}$, $460 \mu\text{M}$, and 1.42 mM), indicating the absence of any structural alteration. Conversely, the measured decrease in dry

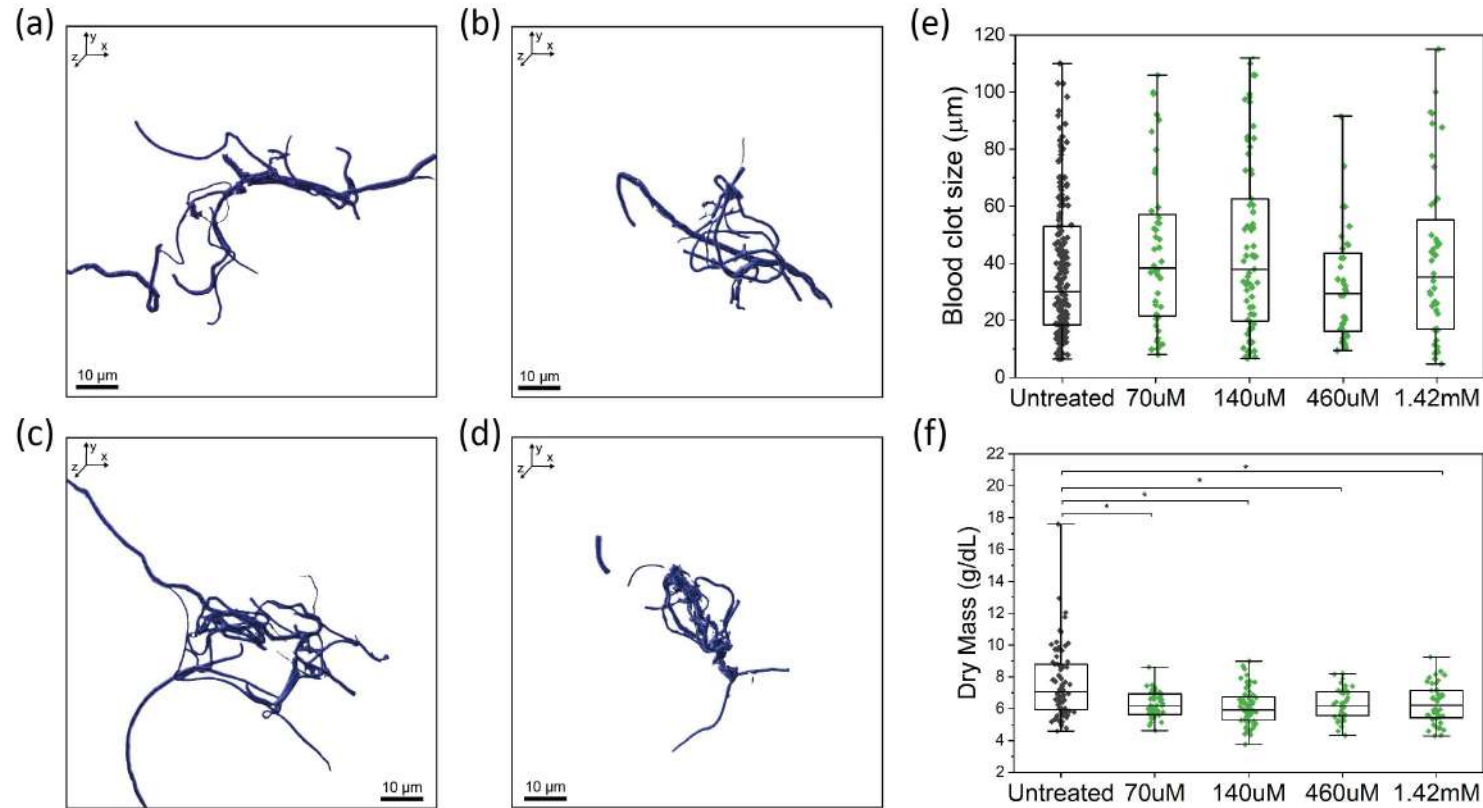


Figure 5.4. Digital Holo-tomographic Microscopy on aspirin treated blood clot fragments. (a-d) Segmented RI tomogram of synthetically prepared blood clot fragments from a COVID-19 patient with four different concentrations of aspirin (70 μM , 140 μM , 460 μM , and 1.42 mM). (e) Length distribution across the untreated and aspirin treated blood clot fragments. (f) Dry mass compared between the untreated blood clot fragments and the four aspirin concentrations (70 μM , 140 μM , 460 μM and 1.42 mM).

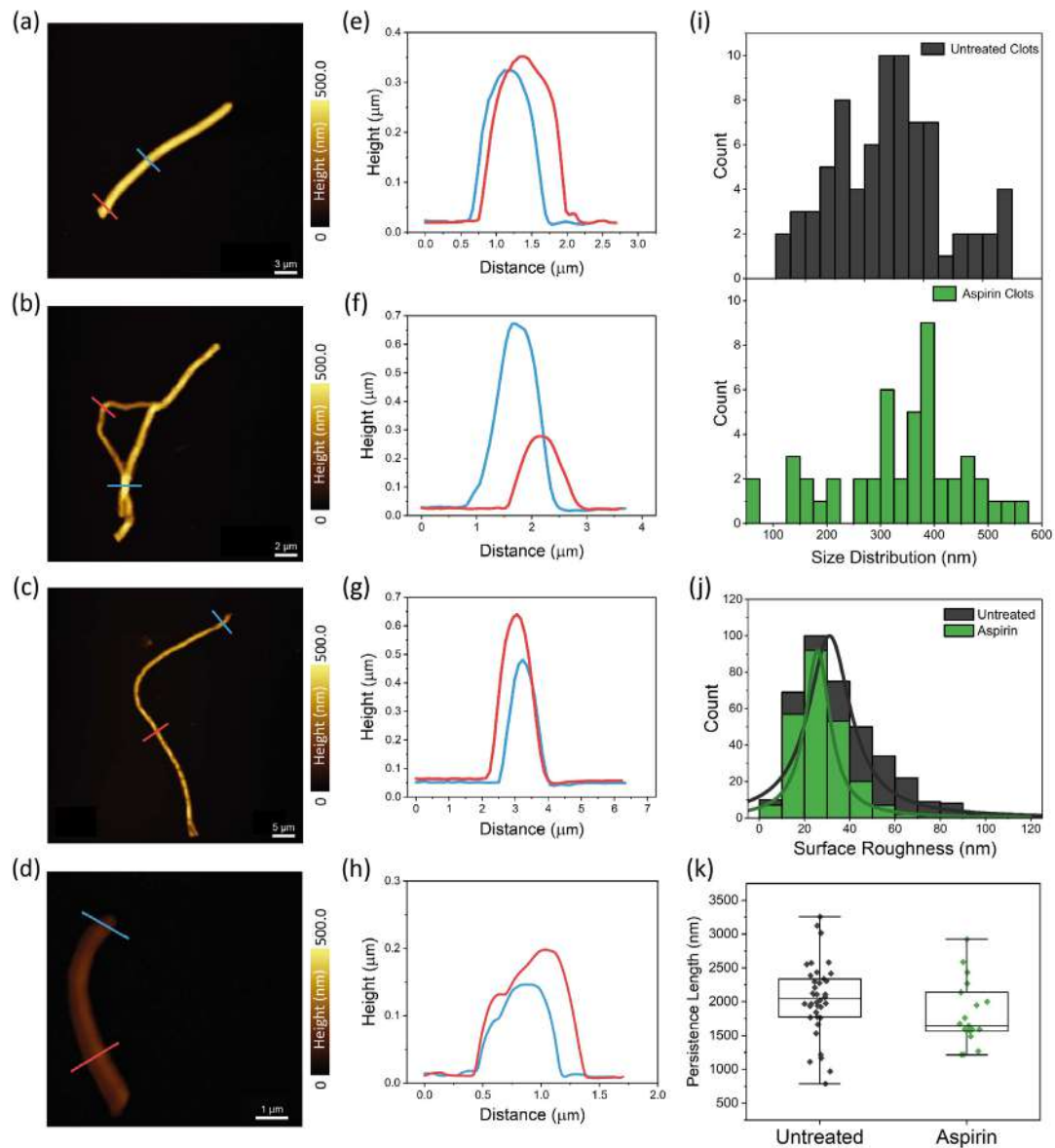


Figure 5.5. Atomic force microscopy of aspirin treated blood clot fragments. (a-d) AFM height image showing synthetically prepared blood clot fragments on glass slide from a COVID-19 patient treated with 1.42 mM of aspirin. (e-h) Height profile analysis of two cross-sectional areas of the blood clot fragments shown in a-c. (i) Fibrin size distribution of untreated and aspirin-treated blood clot fragments. (j) Surface roughness distribution of untreated and aspirin-treated blood clot fragments. (k) Persistence length distribution between the untreated and aspirin treated blood clot fragments.

mass of blood clot fragments treated with all concentrations of urea (except for the 6M concentration) and aspirin may be indicative of small, nanoscale changes to clot structural composition and density. Overall, we did not observe a concentration-dependent effect of urea and aspirin treatment upon clot characterization with DHTM. However, the measured difference in dry mass between the untreated and urea- and aspirin-treated samples could imply changes in the structural composition of the blood clot fragments.

In order to further study the effect of aspirin and urea on blood clots at the nanoscopic scale, we employed the AFM operating under standard laboratory conditions. From the AFM measurements, we were able to resolve single fibrin fibers within the blood clot fragments with nanometer-size spatial resolution. Based on the AFM height maps of the fibrin strands, we quantified the length, surface roughness and persistence length of individual fibrils. Overall, the fibrin size, surface roughness and persistence length were lower after treatment with urea when compared to the untreated clots. The decrease in fibrin size suggests that treatment with urea causes the fibrin strands to become smaller and more likely to fragment. Additionally, the lower persistence length values in the urea- and aspirin-treated clot fragments is indicative of a decrease in clot stiffness and rigidity. In this respect, the persistence length characterizes the flexibility or rigidity of a polymer by measuring the distance in nanometers over which the polymer maintains a straight conformation before undergoing any bending or flexing [Mackintosh et al., 1995]. The observed decrease in persistence length can be attributed to the interaction of urea and aspirin with the fibrin fibrils, characterized by the weakening of the protein's hydrogen bonds [Bennion & Daggett, 2003]. Finally, the decrease in surface roughness is an important observation, highlighting that urea, at a concentration of 8M and an incubation time of 120 minutes, has a partial denaturation effect on fibrin. In particular, the fibrin strands appeared to be more flat in morphology in the height profiles compared to untreated fibrin strands, which instead appeared cylindrical in morphology. This data suggests that urea molecules adsorb along the length of the fibrin strands and potentially loosen up the fibrin stack, leaving it rounder and flatter. Similar to the reduced persistence length, the decrease in surface roughness can be attributed to the interactions between urea and the protein's hydrogen bonding, leaving the fibrin fibers less compact and thus rounder [Bennion & Daggett, 2003]. Consistent with previous literature on the effect of urea on fibrin clots, urea seem to disrupt the weak intermolecular forces within a fibrin clot [Lorand, 1950]. The role of a globulin protein found in blood serum in rendering a fibrin clot more resistant to urea-induced dissolution may explain why the fibrin clots in the

experiments here did not completely dissolve or fragment into smaller pieces [Lorand, 1950]. In view of the structural analysis obtained with both DHTM and AFM measurements, the presence of protein residues such as the serum factor cannot be ruled out. The structural transition of fibrin strands upon treatment with urea needs to be studied further, for instance by incubating urea with the blood clot fragments at elevated temperatures (e.g. 37°C) to mimic the physiological temperature in the human body. Overall, the nanoscale characterization of the treated blood clot fragments highlight the role of urea as a partial fibrin solubilizer at room temperature conditions. These results have both biological and clinical relevance, as elevated concentrations of urea in the body could affect diverse biomolecular structures, including blood clots and blood cells. Elevated concentrations of urea due to renal failure can potentially contribute to conditions like gout [Scott & Higgins, 1992] and elevate the risk for diseases such as cardiovascular diseases including hypertension [Laville et al., 2023]. This highlights the need for imaging techniques that can effectively observe and analyze the impact of urea on biomolecules such as blood clots.

From the AFM measurements on the aspirin-treated blood clot fragments, only fibrin size and surface roughness were significantly reduced compared to the untreated clots. While aspirin notably reduced the size of blood clots, the individual fibrin strands did not appear flatter and more cylindrical as observed in the urea treated clots. This outcome differs from previous studies on the effect of aspirin on clot structure, where an increase in thickness of the fibrin fibers was observed [Ajjan et al., 2009]. Aspirin influences the fibrin clot through the action of acetylation during the process of fibrin cross-linking [Tehrani et al., 2012]. This modification enhances clot permeability, leading to more effective dissolution of the clot [Tehrani et al., 2012]. This mechanism operates in an antithrombotic manner and is beneficial for individuals with cardiovascular diseases in order to prevent any further thrombotic event [Neergaard-Petersen et al., 2013]. However, the efficacy of aspirin treatment may diminish in cases where individuals have additional comorbidities like diabetes or a history of thrombotic events, such as myocardial infarction [Neergaard-Petersen et al., 2013; Tehrani et al., 2012]. The diminished effect partially originate from variations in fibrin composition in diabetic patients and patients with thrombotic diseases compared to healthy individuals [Neergaard-Petersen et al., 2013; Tehrani et al., 2012]. This highlights the significance of studying the dose-dependent effect of aspirin on blood clot fragments, particularly for common treatment options like baby aspirin (= 81 mg of aspirin) [Dalen, 2010].

In summary, we have studied the concentration- and time-dependent effect of urea and aspirin on blood clot fragments at the nanoscopic scale. In the present experiments, we primarily focused on blood clot fragments that were chemically fixed with PFA. As a future step, it would be important to use non-fixed blood clots or fresh blood samples to enhance its applicability in clinical settings. Since our blood clot samples were obtained from a COVID-19 convalescent donor, it is possible that the disease itself may have influenced the structure and behavior of blood clots when subjected to urea and aspirin treatment. Thus, further experiments are required to validate our imaging and analysis framework in blood clot fragments obtained from healthy donors and donors who suffer from specific coagulopathies. Additionally, we could further expand our research to investigate other diseases where blood clots appear to play an increasingly significant role, such as diabetes [Ajjan et al., 2009]. Importantly, to comprehensively characterize blood clot fragments at the nanoscopic and microscopic scale, it is imperative to employ a combinatorial approach, utilizing both DHTM and AFM techniques. This enables the concurrent examination of the same clot regions and acquisition of morphologically complementary data.

In conclusion, the proposed imaging and analysis approach for blood clot characterization provides a deeper understanding of how blood clot morphology is influenced under different chemical environments. By combining nanoscale imaging with chemical analytics such as Raman or infrared spectroscopy on a common platform could provide additional details on the chemical composition of blood clots before and after treatment with chemicals, ranging from denaturants to over the counter and prescribed drugs.

5.5. Methods

5.5.1. Preparation of blood clot samples

Synthetically created blood clot fragments that were chemically fixed with paraformaldehyde (PFA) from a single donor with COVID-19 were obtained from ZenBio through commercial acquisition. To perform the DHTM measurements, 125 μL of blood clot fragments were diluted with 375 μL of PBS buffer (VWR) at a 1:4 ratio. 500 μL of blood clot fragments solution was then transferred into a 35-mm uncoated petri dish (Ibidi GmbH, Germany). For AFM measurements, 30 μL of untreated blood

clot fragments solution was deposited onto a SuperFrost glass slide (VWR) and air-dried overnight.

5.5.2. Preparation of urea and aspirin solutions

Urea solution was prepared by dissolving urea pellets (~0.48 g/mL, Merk Millipore) in ddH₂O (Merk Millipore) and stock solutions of 2M, 4M, 6M and 8M were obtained. Aspirin solution was prepared by crushing an aspirin tablet (Bayer) and dissolving it in PBS (3 mg/mL, VWR). From which four concentrations of aspirin stock solution were prepared (70 μ M, 160 μ M, 460 μ M and 1.46 mM). The aspirin stock solutions corresponded to aspirin dosages of ~50 mg/day, ~100mg/day, ~325 mg/day and ~1000 mg/day. For each DHTM experiment, 100 μ L of either urea or aspirin stock solution was added to 500 μ L of blood clot fragments solution and let incubate for ~15 minutes before continuing data acquisition. For AFM measurements, urea treated blood clots fragments were incubated first for 15 minutes and a second batch was incubated for 120 minutes. Aspirin treated clots were incubated for 120 minutes. The incubated blood clots were then deposited onto a glass slide and the excess liquid was removed using an air gun after 15 minutes.

5.5.3. Label-free digital holo-tomographic microscopy

A 3D Cell Explorer microscope (Nanolive SA, Switzerland) was used for the digital holo-tomographic measurements. Before each measurement, the petri dish containing the blood clot fragments solution was placed in the microscope sample holder and the blood clot fragments were allowed to sediment to the bottom of the petri dish for ~10 minutes before imaging. For the untreated control group, 100 well-adhered and isolated blood clot fragments were imaged. After incubation of urea and aspirin with the blood clot fragment solution for 15 minutes, 30 images of blood clot fragments were taken around the petri dish for each experimental condition, resulting in a total of 240 DHTM images for both the urea and aspirin experimental groups.

5.5.4. Atomic force microscopy

The NaniteAFM (Nanosurf AG, Switzerland) was used to image air-dried blood clot fragments on a glass slide. For imaging, a Dyn190AI-10 tip was used in tapping mode to scan the sample. The glass slide was mounted on the AFM sample stage, followed

by a manual approach of the cantilever towards the vicinity of the sample before the final automatic approach, resulting in contact between the cantilever and the sample. A scan area of 80 μm x 80 μm was used to establish the presence of blood clot fragments. Subsequently, high-resolution imaging was conducted with either 512 or 1024 points per line and a scan area ranging from 20 to 50 μm per single blood clot fragment.

5.5.5. Image processing and analysis

Imaris 9.9.0 (Bitplane AG, Switzerland) was used for the image and data analysis of the acquired 3D RI tomograms. DHTM images were imported into Imaris as TIFF files and converted into IMS files. The minimum and maximum intensity values were adjusted for each image manually in order to visually remove the background signal. A surface was fitted with the smooth parameter of 0.15 and enabled absolute intensity and automatic thresholding in order to segment each blood clot fragment. Additionally, any structure that was below 2 μm in size or touching the XY image border was manually deleted, in order to avoid potential artefacts. The morphologically relevant parameters were extracted from the segmented image, including the size (bounding box OO C) and mean intensity value of each blood clot fragment. Furthermore, the mean intensity value was used to calculate the dry mass of the blood clots, using the following formula [Phillips et al., 2012]:

$$[DryMass] = \left\{ \frac{RI}{RI_{H2O}} - 1 \right\} \times \frac{1}{k}$$

Where RI is the mean refractive index of the blood clots that was obtained from the 3D RI tomograms, RI_{H2O} is the mean refractive index for water (1.333) and the variable k is representative for materials that do not have any specific light absorbance characteristic and was set to 0.002 [Barer, 1952].

The open source software Gwyddion 2.63 [Nečas & Klapetek, 2012] was used to analyze the AFM images. 2D levelling with mean plane facets point upward and scan line correction were applied. The height profile and the surface roughness (Root mean square (RMS) roughness, S_q) were extracted for each blood clot fragment. For blood clot fragment analysis of surface roughness distribution, ten areas measuring $\sim 0.5 \mu\text{m}$ x $0.5 \mu\text{m}$ were averaged for each blood clot fragment. In total, 38 blood clot fragments

were analyzed for the untreated control group, 35 for the urea treated group and 24 for the aspirin treated group.

EasyWorm [Lamour et al., 2014] is an open-source software tool and was used to determine the persistence length of the blood clot fragments obtained through the AFM measurements. Lines were manually drawn along the longest axis of each blood clot fragment in EasyWorm 1, in order to establish the persistence length. The data was then processed by EasyWorm 2, where the persistence length was calculated using the contour / end-to-end method, yielding the persistence length measurement for each blood clot fragment in all three conditions.

6. Capturing the effect of Levodopa on α -Synuclein fibrils at the nanoscale*

6.1. Abstract

Neurodegenerative conditions, such as Parkinson's disease (PD) and Alzheimer's disease (AD), are characterized by the aggregation of otherwise soluble proteins, resulting in the formation of pathological fibrillar deposits. Abnormal aggregation of α -synuclein (α -Syn) is a defining pathological feature of PD, leading to the degeneration of dopaminergic neurons. To counter this process, dopamine replacement therapies, namely levodopa (L-dopa), are used to alleviate the motor symptoms and to restore dopamine levels in the affected brain regions. In this study, we investigated the effect of L-dopa on the aggregation pathway of α -Syn *in vitro*, using atomic force microscopy (AFM), by characterizing the morphology of α -Syn fibrils observed after incubation with and without L-dopa (100 μ M) over a period of 7 days. Our findings reveal the formation of shorter and thinner α -Syn fibrils, characterized by a lower persistence length, upon treatment with L-dopa, indicative of less-organized fibrils with reduced β -sheet content. The prospect of dissolving abnormally aggregated α -Syn fibrils holds promise for exploring the pathomechanisms

*[Bergaglio, T.](#), Kummer, N., Giovannini, G., Bhattacharya, S., Campioni, S., Thompson, D., Nirmalraj, P. N. *Capturing the effect of Levodopa on α -Synuclein and amyloid- β 42 fibrils at the nanoscale*. In preparation, 2023.

Contribution: T.B. was involved in the planning of the study, prepared the α -Synuclein (with S.C.) and Levodopa solutions, and conducted the AFM measurements on the α -Synuclein fibrils. T.B. performed the image processing, data analysis, interpretation and visualization of the AFM results. T.B wrote the original draft of the manuscript.

underlying PD and for the development of effective therapeutic strategies aimed at halting or reversing the course of the disease.

6.2. Introduction

Parkinson's disease (PD) is a complex neurodegenerative disorder characterized by the progressive loss of dopaminergic neurons in the substantia nigra region of the brain [Tolosa et al., 2021]. This degeneration is responsible for a spectrum of motor symptoms, including bradykinesia, resting tremors, and muscle rigidity, and non-motor symptoms like cognitive impairment, mood disorders, and autonomic dysfunction [Hayes, 2019]. Aberrant aggregation of the misfolded α -synuclein (α -Syn) protein, from its native soluble state to β -sheet-rich mature fibril structures, drives the formation of intracellular aggregates known as Lewy bodies and Lewy neurites, which constitute the central pathological hallmark of PD [Breydo et al., 2012; Magalhães & Lashuel, 2022; Mehra et al., 2019]. Disruption of cellular homeostasis, impairment of protein clearance pathways, mitochondrial dysfunction, and the initiation of neuroinflammatory responses, triggered by aggregated α -Syn species, are believed to induce neuronal toxicity [He et al., 2020; Picca et al., 2021]. Consequently, understanding the mechanisms underlying α -Syn aggregation and the impact of therapeutic interventions aimed at preventing or mitigating this process play a central role in unraveling the pathogenesis responsible for initiating and advancing PD.

Pathogenic processes underlying the onset of PD occur years prior to the emergence of detectable symptoms of neurodegeneration [Tolosa et al., 2021]. Simultaneously, existing therapeutic approaches designed to mitigate the motor symptoms of PD are only relevant once these symptoms manifest, suggesting that significant neuronal damage may have already taken place by that point [Ossig & Reichmann, 2015; Yedlapudi et al., 2016]. Levodopa (L-dopa) is a fundamental component in the pharmacological management of PD, where, as a precursor to dopamine, it replenishes dopamine levels in the brain's depleted regions, providing effective relief from motor symptoms in PD patients [Yuan et al., 2010]. While the distribution and degree of α -synuclein buildup throughout the brain of individuals with PD are well-documented, the effect of long-term dopamine replacement therapy on α -synuclein aggregation remains unknown [Deffains et al., 2021]. Importantly, prolonged L-dopa therapy can be associated with motor fluctuations, dyskinesia and a consequent reduction in the effectiveness of a given L-DOPA dose [Yedlapudi et al., 2016]. The generation of free radicals as well as L-dopa-induced toxicity to dopaminergic neurons

may in turn accelerate the neurodegenerative processes underlying PD [Ossig & Reichmann, 2015]. In addition, the simultaneous administration of decarboxylase inhibitors, such as carbidopa or benserazide, with L-dopa serves to minimize the occurrence of drug-induced adverse effects, like nausea and hypotension, while also enhancing the amount of medication capable of crossing the blood-brain-barrier [Ossig & Reichmann, 2015]. Although L-dopa cannot arrest or slow down the advancement of PD, nor reverse the course of the disease, *in vitro* studies have demonstrated that L-dopa can effectively hinder the formation of α -Syn fibrils and promote the disassembly of pre-existing fibrils [Conway et al., 2001; Li et al., 2004].

Understanding the complex mechanisms governing α -Syn aggregation and the mode of action of dopamine replacement therapies is essential for the advancement of effective therapeutic interventions designed to halt PD progression. In this study, we used atomic force microscopy (AFM) to assess the role of L-dopa in having α -Syn fibrillation. To achieve this, we characterized α -Syn aggregates incubated with and without L-dopa solution for a period of 7 days at 37°C and under constant mechanical agitation. The formation of α -Syn fibrils was observed even when α -Syn was incubated with 100 μ M L-dopa. However, treatment with L-dopa resulted in the formation of α -Syn fibrils that were shorter and more slender in structure, hinting at potential variations in their morphology and pathological impact. Furthermore, within the sample of α -Syn incubated with L-dopa, L-dopa particles of different sizes were detected, suggesting that L-dopa molecules could be mostly present in the form of aggregates when interacting with α -Syn. Overall, our study highlights the central importance of L-dopa therapy as in the management of PD, shedding light on the nanoscale interactions between L-dopa and α -Syn aggregation. Ongoing efforts to elucidate the dose-dependent effects of L-dopa, whether used as a sole treatment or in conjunction with other medications, will contribute further insights into the development of personalized treatment approaches.

6.3. Results

The aggregation pathway of α -Syn, including the morphological transition from monomers to fibrils, measured over a span of 10 days was previously demonstrated by Synhaivska and colleagues [Synhaivska et al., 2022]. Here, we performed AFM characterization of α -Syn fibrils that had incubated with and without 100 μ M L-dopa concentration for 6 days. Figure 6.1(a) shows an AFM image recorded after depositing the α -Syn solution, without L-dopa, after 6 days of incubation time under mechanical

agitation at 37°C. Aggregated α -Syn fibrils can be observed in the AFM height image. The corresponding AFM amplitude image provides a clearer depiction of the shape of the α -Syn fibrils (Figure 6.1(b)). Figure 6.1(c) illustrates the overlay between the height and amplitude AFM images of the untreated α -Syn fibrils. To determine the thickness of the single fibrils, we extracted the cross-sectional profiles from the height image (white and yellow lines, Figure 6.1(a)), as shown in Figure 6.1(c). Nanoscopic variations were observed between individual α -Syn fibrils, with the fibrils depicted in Figure 6.1(a) ranging from ~ 9 nm to ~ 12 nm in height. Next, we compared the α -Syn fibrils incubated with 100 μ M L-dopa for 6 days using AFM. The AFM height image (Figure 6.1(d)) shows the presence of α -Syn fibrils and L-dopa particles (black arrows), visible both on the fibrils as well as throughout the sample. Figure 6.1(e) illustrates the corresponding AFM amplitude image showing the distinct shape of the α -Syn fibrils and L-dopa particles. The cross-sectional profiles extracted from the height image (white and pink lines, Figure 6.1(d)) and shown in Figure 6.1(f) may suggest a decrease in fibril thickness upon incubation with L-dopa (height ranging from ~ 4 nm to ~ 8 nm).

In order to quantify the specific effect of L-dopa treatment on α -Syn aggregation, we extracted the height and length distribution, as well as the persistence length measurement, of α -Syn fibrils incubated without and with 100 μ M L-dopa concentration for 6 days, under the same experimental conditions of 37°C and mechanical agitation (Figure 6.2). The key finding when analyzing the α -Syn fibrils incubated with L-dopa was a significant decrease in fibril length (Figure 6.2(a)) and thickness (Figure 6.2(b)). Upon measuring the length distribution of the fibrils from the AFM height images, a two sample t-test revealed a significant reduction in fibril length (Figure 6.2(a)) when incubated with 100 μ M L-dopa (610 ± 330 nm) compared to the untreated fibrils (860 ± 590 nm). Similarly, the height (Figure 6.2(b)) of the individual fibrils was also reduced upon treatment with L-dopa (5.20 ± 1.83 nm) compared to the control condition (5.96 ± 1.95 nm). Additionally, we assessed the nanomechanical properties of the α -Syn fibrils with and without L-dopa treatment. Figure 6.2(c) shows the mean square end-to-end distance as a function of the contour length for untreated fibrils (blue) and fibrils incubated with 100 μ M L-dopa (red) for 6 days. The calculated persistence length revealed a trend for different mechanical properties between experimental conditions, where untreated α -Syn fibrils showed a slightly higher persistence length (14.94 ± 5.70) than L-dopa-treated α -Syn fibrils (14.85 ± 5.48). Furthermore, initial findings from a ThT kinetics assay indicated that the introduction of L-dopa led to a decelerated and reduced aggregation of α -Syn (Figure C.1). Results from three repetitions for each condition indicated that about 4 days of incubation at

37°C and under mechanical agitation, were necessary to detect α -Syn aggregation without the addition of L-dopa (Figure C.1). A dose-dependent effect of L-dopa (10 μ M, 50 μ M, and 100 μ M) on α -Syn aggregation appeared to be present throughout a 7-day incubation period (Figure C.1(a)). Specifically, L-dopa at a concentration of 100 μ M seemed to have the strongest effect at hindering α -Syn aggregation (Figure C.1(b)). Finally, we calculated the mean L-dopa particle size in order to characterize the L-dopa aggregates found in the samples with the α -Syn fibrils incubated with L-dopa and deposited as a thin film on mica substrates. A mean L-dopa particle size of 10.5 nm was calculated, with a confidence interval lower (CIL) bound of 10.3 nm and a confidence interval upper (CIU) bound of 10.7 nm. The quantitative analysis of the size distribution of L-dopa particles indicates that, when incubated with α -Syn solution *in vitro*, L-dopa molecules are likely to be predominantly found in the form of aggregates.

6.4. Discussion

With the aging global population, the prevalence of PD is on the rise, emphasizing the importance of understanding the disease pathogenesis for the development of effective treatment strategies. In this study, we used nanoscale imaging to elucidate the aggregation pathway of α -Syn when incubated both with and without L-dopa solution. We resolved and characterized α -Syn fibrils that formed during a 7-day incubation period at 37°C under constant mechanical agitation, using AFM. In line with prior research [Synhaivska et al., 2022], our findings revealed the onset of α -Syn fibrillar aggregation after 4 days of incubation, with evidence for the formation of protofibrils and fibrils at day 6. Exposure to micromolar concentrations of L-dopa solution was sufficient to delay and to some extent even hinder the aggregation of α -Syn during the incubation period. This is in agreement with previous studies showing the inhibition of fibril formation and even the disassembly of α -Syn *in vitro*, upon incubation with L-dopa [Conway et al., 2001; Li et al., 2004]. Additionally, our data indicate that the α -Syn fibrils that formed in the presence of L-dopa exhibited distinct characteristics, featuring shorter and thinner fibrils with a reduced persistence length.

The results from the present study highlight the significance of studying the size and conformation of α -Syn protein aggregates in response to treatment with dopamine replacement therapy, such as L-dopa. Extensive α -Syn fibril formation was observed in the absence of L-dopa treatment. . Conversely, incubation with 100 μ M of L-dopa solution resulted in α -Syn protein aggregates that were significantly shorter an

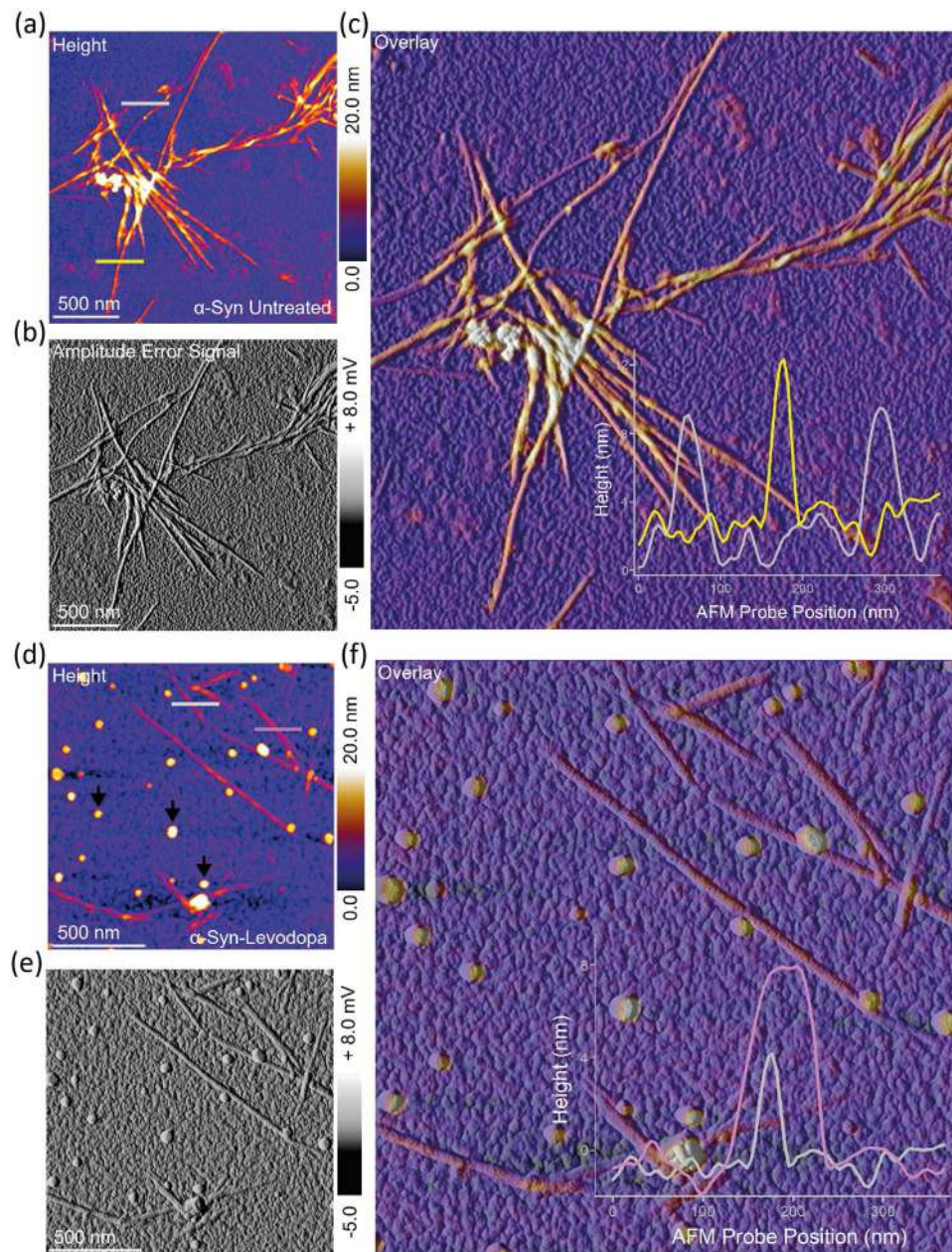


Figure 6.1. Characterization of α -Syn fibrils incubated with L-dopa. (a-b) Height and amplitude AFM images of untreated α -Syn fibrils. (c) Overlay of the height and amplitude AFM images and height profiles (shown in the bottom inset) extracted along the white and yellow lines indicated in (a) of untreated α -Syn fibrils. (d-e) Height and amplitude AFM images of α -Syn fibrils incubated with 100 μ M L-dopa solution for 6 days. Black arrows in (d) indicate L-dopa particles. (f) Overlay of the height and amplitude AFM images and height profiles (shown in the bottom inset) extracted along the white and pink lines indicated in (d) of α -Syn fibrils incubated with 100 μ M L-dopa.

6. The effect of Levodopa on α -synuclein fibrils at the nanoscale

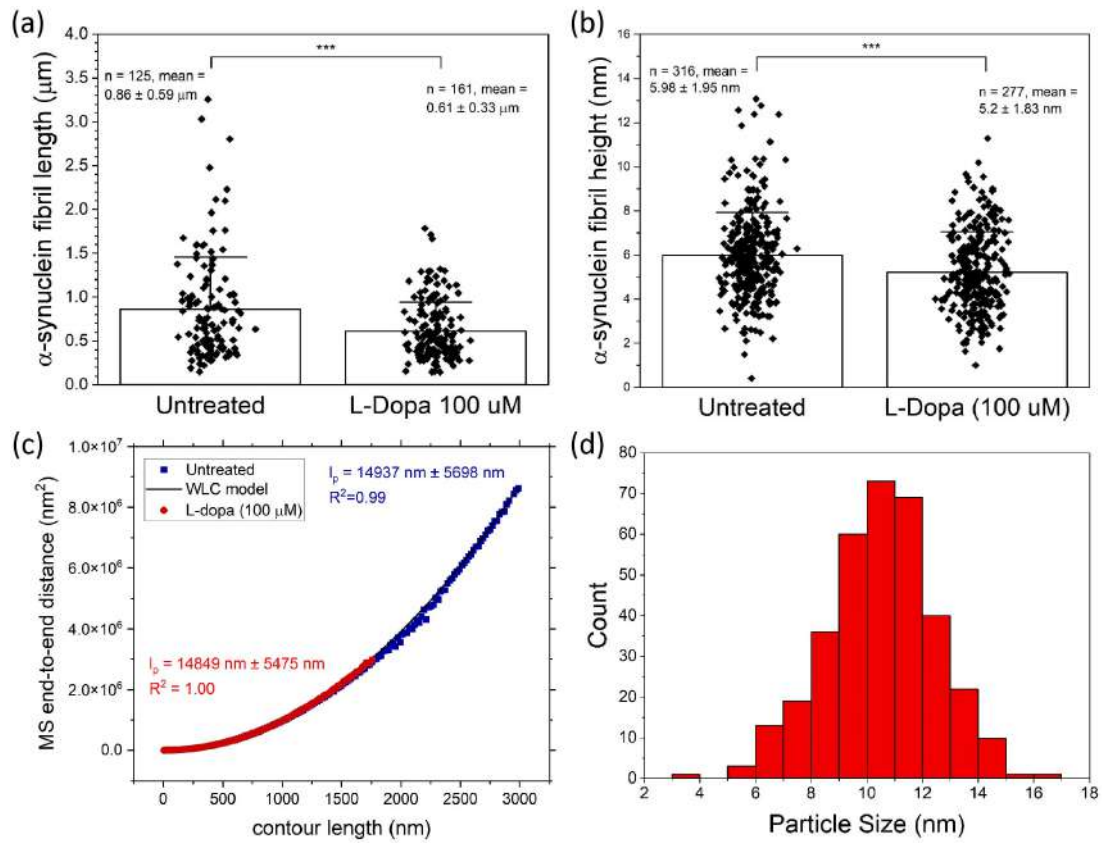


Figure 6.2. Morphological characterization of α -Syn fibrils incubated with L-dopa. (a-b) Bar plot of the mean α -Syn fibril length and height without and with incubation with 100 μM L-dopa. Error bars indicate the standard deviation from the mean. (c) Persistence length of α -Syn fibrils without (blue) and with incubation with 100 μM L-dopa (red). The WLC model is plotted in dark gray. (d) L-dopa particle size distribution; mean particle size: 10.5 nm, CIL: 10.3 nm and CIU: 10.7 nm.

presented significantly smaller diameters. This evidence is consistent with the presence and accumulation primarily of protofibrils [Synhaivska et al., 2022]. Assessment of the nanomechanical properties of α -Syn fibrils unveiled persistence length values between 12 and 15 μm , that are in agreement with previous studies [Makky et al., 2016]. Importantly, our data also revealed a lower mean persistence length when α -Syn was incubated with L-dopa, indicative of the presence of less-organized fibrils with reduced β -sheet content [Vandenakker et al., 2011]. This is further substantiated by the preliminary evidence from the ThT aggregation kinetics measurements. A trend indicating that L-dopa limits α -Syn aggregation was observed as a dose-dependent effect, with the most pronounced effect observed at the highest concentration of 100 μM . In view of the positive ThT signal originating from the β -sheet content in fibrillar structures, it is reasonable to assume that a decrease in ThT signal detected in the α -Syn samples incubated with L-dopa may be indicative of the partial inhibition of fibril formation and the presence of protofibrillar structures [Groenning, 2010]. The concentration of L-dopa used in our experiments aligns with the estimated concentration in the brain following administration, thereby reflecting a physiologically relevant impact [Spencer et al., 1996].

Dopamine replacement therapy has been shown to ameliorate α -Syn pathology both *in vitro* and *in vivo*, in a mouse model of PD [Deffains et al., 2021; Yedlapudi et al., 2016]. Nonetheless, extended L-dopa intake may result in the acceleration of neurodegenerative processes, driven by the generation of free radicals capable of inducing neurotoxicity [Ossig & Reichmann, 2015]. Additionally, the reduced efficacy of L-dopa over time is suggested to depend on the progressive loss in the ability of presynaptic neurons in the substantia nigra to store dopamine, thus highlighting the role of the chemical milieu in influencing the therapeutic effect of medications [Ossig & Reichmann, 2015]. In this context, evidence for L-dopa toxicity was investigated both *in vitro* and *in vivo* under conditions of oxidative stress that would normally be found in PD patients [Mytilineou et al., 2003]. L-dopa-induced toxicity was detected in cultured dopaminergic neurons but did not manifest when administered to neonatal rats [Mytilineou et al., 2003]. This prompts consideration of the challenges associated with the replication of such complex neurodegenerative diseases with *in vitro* and *in vivo* models and with the translation of these findings for the development of effective PD treatments. In addition, a recent study detected the formation of annular oligomers and accelerated α -Syn aggregation induced by exposure to copper, emphasizing their potential role as biomarkers for early detection and for the monitoring of neurodegenerative processes in PD [Synhaivska et al., 2022]. The role of

dopamine replacement therapies, specifically L-dopa, should be further explored within the context of different forms of α -Syn aggregates. Our findings that L-dopa particles are primarily present in the form of aggregates when incubated with α -Syn *in vitro* may play a crucial role in determining the pharmacokinetics, the effectiveness and the potential toxicity of the medication [Camargo et al., 2014].

Important considerations should also be directed towards the documented side effects resulting from L-dopa in-take. Reports of significant blood pressure decrease, especially in older PD patients, as well as anemia resulting from vitamin B6 deficiency, emphasize the need for tools to routinely monitor drug-induced adverse effects and for the development of personalized treatment strategies [Su et al., 2023; Yasuda et al., 2022]. The disease status of individual PD patients, including the extent of α -Syn deposition, should play a pivotal role in determining and adapting the dose-dependent administration of L-dopa, in order to mitigate the risk for drug-induced cytotoxicity. Our AFM-based approach can provide nanoscopic insights into the dynamics of α -Syn aggregation and into the therapeutic impact of dopamine replacement therapies.

6.5. Methods

6.5.1. Preparation of Wild-Type α -Synuclein and Levodopa solutions

Wild-type human α -Syn was obtained following the procedures outlined by Campioni et al. [Campioni et al., 2014]. To prepare the α -Syn solutions, the lyophilized protein (~ 30 mg/mL) was first dissolved in 700 μ L of PBS buffer (VWR). The pH was then adjusted to 7.4 using 1 M sodium hydroxide (NaOH). To filter the solution, the filter membrane of a 100 kDa NMWL centrifugal filter (Amicon Ultra-4 Centrifugal Filter Unit, Merk Millipore) was first hydrated with 4 mL of PBS buffer and centrifuged for 5 minutes at 3200g for three times. Next, the α -Syn solution (~ 700 μ L) was added to the centrifugal filter and centrifuged for 20 minutes at 3200g in order to filter out large α -Syn particles that had not fully dissolved. Lastly, to extract any remaining α -Syn from the bottom of the filter, 100 μ L of PBS buffer was added to the filter and mixed, followed by centrifugation for 5 min at 3200g. A spectrophotometer (Implen Nanophotometer NP80 UV-vis) was used to determine the final concentration of α -Syn ($\epsilon_{280} = 5960 \text{ M}^{-1} \text{ cm}^{-1}$). The obtained α -Syn stock solution was further diluted with PBS buffer in order to reach a final concentration of 300 μ M.

To investigate the effect of L-dopa on α -Syn aggregation dynamics, a stock solution was prepared by dissolving L-dopa (Merk Millipore) in 1 mL PBS buffer (1.9719 mg/mL). Three concentrations of L-dopa were prepared (20 μ M, 100 μ M, and 200 μ M). For each experimental condition, 250 μ L of L-dopa solution was added to 250 μ L of α -Syn (300 μ M), leading to a final concentration of L-dopa of 10 μ M, 50 μ M, 100 μ M, respectively. The α -Syn, with and without L-dopa, was incubated at 37°C for 7 days under mechanical agitation at 300 rpm. Only the α -Syn incubated with 100 μ M L-dopa concentration was used for AFM analysis.

6.5.2. Atomic Force Microscopy

Atomic force microscopy measurements were performed using a Dimension Icon AFM (Bruker). A SCOUT 70 HAR silicon AFM tip with a high aspect ratio, gold reflective backside coating, force constant 2 N/m, resonant frequency of 70 kHz, cone angle of $<15^\circ$ over the final 1 μ m of the tip apex (NuNano) was used in tapping mode. AFM measurements were conducted on air-dried α -Syn incubated without and with 100 μ L L-dopa concentration on day 6 and deposited as a thin film on mica discs. The raw AFM images were processed and analyzed using open source software Gwyddion 2.60. 2D leveling and scan line correction were applied, followed by measurements of the fibril height ($N_{\text{untreated}} = 316$; $N_{\text{L-dopa}} = 277$) and length ($N_{\text{untreated}} = 125$; $N_{\text{L-dopa}} = 161$). The size distribution of L-dopa particles observed in the treated α -Syn sample was calculated for a total of ~ 348 particles. The persistence length of the α -Syn fibrils ($N_{\text{untreated}} = 57$; $N_{\text{L-dopa}} = 92$) was calculated with the open source software EasyWorm, using the end-to-end distance approach derived from the WLC model for semi-flexible polymers.

7. Overall discussion and outlook

7.1. A bird's eye view of the thesis

In this thesis, we developed an innovative imaging platform for clinical level screening of pathological diseases and monitoring of drug-induced cytotoxic effects by detecting and characterizing the morphological and biochemical changes of blood components. Our primary emphasis was directed toward evaluating red blood cells (RBCs) and blood clots in view of the significance of their morphology and RBC rheological properties in the diagnostics of blood-related diseases and in designing appropriate treatments. Through the proposed imaging and analysis framework, it becomes possible to directly assess fresh blood in a label-free manner, thereby offering a quantitative insight into blood structures and, ultimately, enabling the assessment of an individual's health status. For instance, the RBC characterization framework developed in this thesis for the automatic assessment and classification of RBC morphology could prove highly beneficial in the diagnostics of sickle cell disease (SCD), where the presence of sickle RBCs serves as a pathological hallmark. This holds particularly true in regions with limited resources, which coincidentally overlap with the areas where a majority of SCD patients reside. In such regions, the scarcity of diagnostic facilities and hematologists stands as a primary factor contributing to mortality rates [Gregory J. Kato et al., 2018]. For this reason, current approaches in traditional pathology would benefit significantly from a greater degree of automation in their processes. The research presented in this thesis brings us a step closer to the digitization of diagnostic hematology, by providing a digital, high-throughput and automated approach for blood screening. Additionally, the prospect of real-time evaluation of drug-induced cytotoxic effects on blood can provide endless opportunities in the domains of drug discovery and surveillance.

The development of the imaging and analytical platform proposed in this thesis was based on the morphological assessment of RBCs. To benchmark our methodology, we developed all facets of our workflow, starting with the preparation of blood samples, extending to the optimization of DHTM-based imaging using Nanolive's *3D Cell*

Explorer microscope, and the creation of image and data analysis processes. By combining high-throughput DHTM and high-resolution AFM imaging, a comprehensive assessment and characterization of blood structures can be achieved. This is a step ahead of the state-of-the-art, as the nanoscale analysis of blood yields invaluable insights that are not always visually observable with conventional optical microscopy. A significant advantage of our blood screening platform is the possibility to analyze thousands of individual RBCs with only small blood volumes. This approach offers distinct benefits, including reduced patient discomfort and the potential for more frequent sampling, which is especially advantageous for drug monitoring and critical care or pediatric settings. Therefore, our approach strives for the realization of a point-of-care solution that ultimately leads to a more automated, non-invasive and quantitative blood screening platform.

As a non-invasive and clinically accessible approach, screening RBC morphology can significantly contribute to drug safety assessments and therapeutic optimization. For instance, changes in cell shape, size, or the presence of abnormal structures like microclots in blood can be indicative of adverse drug reactions or potential drug-induced hematological disorders. Moreover, the quantification of such morphological alterations provides valuable data for monitoring treatment response and adjusting drug regimens in personalized medicine. With our imaging and analysis framework, we could resolve RBC shape changes upon treatment with ibuprofen. A unique aspect of this approach is the label-free, real-time measurement of drug-cell interactions and the concomitant quantification of RBC morphological and chemical parameters. We are able to show the concurrent changes in cell diameter, surface area-to-volume ratio, thickness, sphericity, and hemoglobin concentration, which would then reflect the health and lifespan of RBCs and ultimately their ability to efficiently transport oxygen to all organs. Additionally, we demonstrated a dose-dependent effect of hydrogen peroxide-induced oxidative stress on RBC shape, characterized by a transient morphological transformation into stomatocytes. The chemical environment surrounding living cells holds profound significance, especially in pathological conditions, where alterations in the chemical milieu can lead to cellular dysfunction and contribute to the development of disease. Manipulation of the cellular microenvironment plays a pivotal role in comprehending the mechanisms underlying disease pathogenesis and serves as a focal point for therapeutic interventions. By exploiting RBC morphology to assess the effect of changes to the chemical environment, we demonstrated the detection and quantification of the dose-dependent effect of drugs and elevated levels of oxidative stress and urea. This is of

particular significance for individuals suffering from blood-related pathologies as well as other medical conditions, such as chronic kidney disease.

The method discussed in this thesis paves the way not only for studying alterations in RBC morphology, but also offers promising opportunities for elucidating disease pathogenesis and uncovering potential blood-based biomarkers. As an example, we found a higher prevalence of microclots in the plasma of individuals suffering from COVID-19 as opposed to healthy donors. On the one hand, we were able to demonstrate the possibility to detect and resolve microclots in plasma with high spatial resolution and in a label-free manner, thus contributing to the development of novel biomarkers for the diagnosis of COVID-19 and Long COVID pathologies. On the other hand, we resolved and quantified differences in microclot morphology and composition that may help elucidate the pathological mechanisms underlying symptom severity and coagulopathies in COVID-19. Hence, nanoscale analytics can act as a foundational step for the advancement and tailoring of therapeutic interventions. Another example is the study of the role of protein aggregates in neurodegenerative diseases. By investigating the effect of Levodopa treatment on α -Synuclein aggregation *in vitro*, at the nanoscopic scale, we were able to shed light on the structural changes and dynamics underlying fibril fragmentation. Future strategies for the dose-dependent administration of Levodopa to Parkinson's patients may consider the degree of pathology, thus the extent of α -Syn aggregation, and the risk of drug-induced adverse effects. Given that this is the sole symptomatic treatment available for Parkinson's disease, it becomes paramount to employ a personalized approach, tailored to an individual's specific condition and the severity of their symptoms.

Another important consideration is the involvement of clinicians and hematologists to validate and facilitate the integration of the proposed imaging and analysis platform into clinical practice. While there is a perception that AI-based tools may replace certain repetitive tasks performed by humans, it is important to emphasize that automated and machine learning-based analytical tools can never substitute the role of healthcare professionals. Therefore, engaging hospitals and clinicians in the development of these innovative tools would serve a dual purpose: firstly, to gain insights into their specific needs and challenges, and secondly, to facilitate a smoother transition from traditional healthcare practices to a more digitally-driven healthcare system.

The label-free aspect of the high-throughput and quantitative approach presented in this thesis enables the acquisition of artefact-free and biologically-relevant findings. In turn, this approach can be applied for the real-time analysis and characterization of

blood components, as well as for the development of personalized treatment strategies, enhancing the likelihood of therapeutic success but also optimizing the overall safety of medical interventions. Moreover, this approach can be extended for the characterization of morphological and chemical parameters of other blood components, such as WBCs and platelets. To achieve this, it may be necessary to optimize sample preparation and imaging procedures to adapt to the characteristics of the different cell types.

7.2. What's next?

Label-free DHTM-based imaging and analysis approaches offer a vast array of possibilities for expanding their utilization across various domains. The applications proposed throughout this thesis, in the field of diagnostic hematology, require further validation through the analysis of a larger sample size, in order to accelerate the integration into clinical settings. In this thesis, we demonstrated the label-free characterization and automatic classification of RBC morphology in health and sickle cell anemia. The analysis of samples from donors with other blood-related diseases characterized by RBC shape changes, such as other forms of sickle cells disease, thalassemia, and diabetes, would enrich the diversity of our dataset. This, in turn, would contribute to the establishment of a comprehensive digital repository containing both morphological and chemical parameters specific to each RBC shape variation, facilitating the exploration of associations with various diseases. The same process would be extended to the investigation of the morphological changes in RBCs induced by chemicals and drugs, such as chemotherapeutic agents, nanoparticle-based drug delivery systems and medications for neurodegenerative diseases, thereby enhancing our understanding of drug safety and efficacy, ultimately driving the advancement of personalized medicine. Access to biobanks would substantially enhance sample diversity, as it would grant access to donors with diverse comorbidities and ultimately facilitate sample stratification. This is of particular importance for the detection and characterization of microclots in COVID-19 and Long COVID, given the heterogeneous symptomatology and the uncertainty surrounding the role of COVID-19 variants and vaccine type on clinical outcomes.

As a next step, the proposed methodology for label-free detection and characterization of microclots in plasma could be extended to other medical conditions characterized by the presence of microvasculature injury, such as diabetes

7. Overall discussion and outlook

and neurodegenerative diseases [de Waal et al., 2018; Pretorius et al., 2020]. This approach has the potential to shed light on disease pathogenesis and to lead to the discovery of new blood-based biomarkers. Moreover, the integration of blood clot nanoscale analytics in the current diagnostic practices may facilitate the early diagnosis and continuous monitoring of thrombotic disorders, potentially predicting the likelihood of recurrent thrombotic events.

Another potential application of our label-free, high-throughput and quantitative framework for the automated assessment of RBC morphology lies in the characterization of WBCs. This approach could facilitate the monitoring of infections, inflammation, autoimmune responses, and the body's reaction to chemotherapeutic agents, thereby adding an additional layer of blood-based biomarker analysis to our system. The use of ML-based techniques would allow for the efficient processing of large quantities of data obtained from our DHTM-based platform. Customizing ML algorithms for each specific application of the proposed system would subsequently accelerate the digitization of diagnostic hematology across healthcare environments. This, in turn, could enable the development of versatile point-of-care solutions for disease diagnostics and for the monitoring of drug-induced adverse effects, applicable also in resource-limited settings.

Furthermore, our DHTM-based platform could be enhanced by integrating supplementary imaging and analysis systems. For instance, expansion microscopy (ExM) is an emerging transformative technique that allows to physically expand biological specimens, such as cells or tissues, while preserving their molecular and structural details [Chen et al., 2015; Wassie et al., 2019]. This expansion process is achieved through the incorporation of a swellable polymer mesh into the specimen, which, when triggered, expands uniformly, leading to a significant increase in the size of the sample [Wen et al., 2023]. As a result, structures that were once beyond the diffraction limit of conventional optical microscopy become resolvable [Gallagher & Zhao, 2023]. The integration of this groundbreaking approach with our DHTM-based system has the potential to unlock new opportunities for high-resolution imaging of subcellular structures in a label-free manner, with implications for protein analytics directly in blood.

7.2.1. Merits and challenges of integrating DHTM with microfluidics

Additional systems capable of closely mimicking the physiological conditions inside the body could be combined with label-free imaging modalities. One such example is the integration of microfluidics to better replicate the physiological blood flow *in vitro*. Microfluidic devices offer a versatile platform for precise and efficient analysis of blood structures via the intricate network of channels and chambers that allow for the manipulation of small volumes of blood samples with exceptional control and precision [Matthews et al., 2017; Sebastian & Dittrich, 2018]. The use of microfluidic systems in diagnostic hematology could enhance the sensitivity and specificity of blood analysis and would enable rapid and cost-effective blood cell counting, blood typing, and the assessment of cellular morphology while aligning more closely with physiological conditions [McNamee et al., 2021]. Additionally, emerging technologies in microfluidics and tissue-on-a-chip platforms are enabling researchers to precisely control and manipulate the chemical microenvironment, opening new avenues for investigating cellular behavior and developing innovative therapeutic strategies in the field of precision medicine [Rizzuto et al., 2021]. However, important challenges arise when combining microfluidic devices with DHTM. Most importantly, a high frame rate (e.g. ~100 frames/second) during the image acquisition process is imperative in order to detect and resolve cells passing through the microfluidic channel with high resolution. In the context of the DHT microscope employed for this thesis, a frame rate of one frame every two seconds poses a limitation on the integration of microfluidics. Furthermore, the dimensions of the microfluidic channels may also hinder the integration of microfluidics in a DHT setup. Important considerations pertaining to the DHT microscope used in this thesis include the channel thickness (max. 170 μm), sample thickness (max. 30 μm) and volume of medium (max 1.5 mL) inside the channel.

Overall, our proposed DHTM-based analytical platform for blood screening plays a crucial role in the digitalization of diagnostic hematology, offering valuable insights into both normal physiology and disease pathology. The versatility of the proposed approach paves the way for its integration across multiple domains, including biomarker discovery, early disease diagnostics, and drug monitoring.

Bibliography

- Abraham, M. J., Murtola, T., Schulz, R., Páll, S., Smith, J. C., Hess, B., & Lindahl, E. (2015). GROMACS: High performance molecular simulations through multi-level parallelism from laptops to supercomputers. *SoftwareX*, *1*, 19-25.
- Ackermann, M., Verleden, S. E., Kuehnel, M., Haverich, A., Welte, T., Laenger, F., Vanstapel, A., Werlein, C., Stark, H., Tzankov, A., Li, W. W., Li, V. W., Mentzer, S. J., & Jonigk, D. (2020). Pulmonary Vascular Endothelialitis, Thrombosis, and Angiogenesis in Covid-19. *N Engl J Med*, *383*(2), 120-128.
- Ajjan, R. A., Standeven, K. F., Khanbhai, M., Phoenix, F., Gersh, K. C., Weisel, J. W., Kearney, M. T., Ariens, R. A. S., & Grant, P. J. (2009). Effects of Aspirin on Clot Structure and Fibrinolysis Using a Novel In Vitro Cellular System. *Arteriosclerosis Thrombosis and Vascular Biology*, *29*(5), 712-U196.
- Alkarithi, G., Duval, C., Shi, Y., Macrae, F. L., & Ariëns, R. A. S. (2021). Thrombus Structural Composition in Cardiovascular Disease. *Arteriosclerosis, Thrombosis, and Vascular Biology*, *41*(9), 2370-2383.
- Alonso-Orgaz, S., Moreno-Luna, R., López, J. A., Gil-Dones, F., Padial, L. R., Moreu, J., de la Cuesta, F., & Barderas, M. G. (2014). Proteomic characterization of human coronary thrombus in patients with ST-segment elevation acute myocardial infarction. *Journal of Proteomics*, *109*, 368-381.
- Antithrombotic Trialists, C. (2002). Collaborative meta-analysis of randomised trials of antiplatelet therapy for prevention of death, myocardial infarction, and stroke in high risk patients. *BMJ (Clinical research ed.)*, *324*(7329), 71-86.
- Arishi, W. A., Alhadrami, H. A., & Zourob, M. (2021). Techniques for the Detection of Sickle Cell Disease: A Review. *Micromachines (Basel)*, *12*(5).
- Atkins, C. G., Buckley, K., Blades, M. W., & Turner, R. F. B. (2017). Raman Spectroscopy of Blood and Blood Components. *Appl Spectrosc*, *71*(5), 767-793.
- Bain, B. J. (2015). *Blood Cells: A Practical Guide* (5th ed.). John Wiley & Sons.
- Baker, S. R., Halliday, G., Ząbczyk, M., Alkarithi, G., Macrae, F. L., Undas, A., Hunt, B. J., & Ariëns, R. A. S. (2023). Plasma from patients with pulmonary embolism show aggregates that reduce after anticoagulation. *Communications Medicine*, *3*(1).

Bibliography

- Barbaryan, A., Iyinagoro, C., Nwankwo, N., Ali, A. M., Saba, R., Kwatra, S. G., Hussain, N., Uzoka, C. C., Prueksaritanond, S., & Mirrakhimov, A. E. (2013). Ibuprofen-induced hemolytic anemia. *Case Rep Hematol*, 2013, 142865.
- Barbour, R., Kling, K., Anderson, J. P., Banducci, K., Cole, T., Diep, L., Fox, M., Goldstein, J. M., Soriano, F., Seubert, P., & Chilcote, T. J. (2008). Red blood cells are the major source of alpha-synuclein in blood. *Neurodegener Dis*, 5(2), 55-59.
- Barer, R. (1952). Interference Microscopy and Mass Determination. *Nature*, 169(4296), 366-367.
- Baxi, V., Edwards, R., Montalto, M., & Saha, S. (2022). Digital pathology and artificial intelligence in translational medicine and clinical practice. *Modern Pathology*, 35(1), 23-32.
- Beck, N. (2009). *Diagnostic Hematology* (1 ed.). Springer London.
- Bennion, B. J., & Daggett, V. (2003). The molecular basis for the chemical denaturation of proteins by urea. *Proceedings of the National Academy of Sciences of the United States of America*, 100(9), 5142-5147.
- Bergaglio, T., Bhattacharya, S., Thompson, D., & Nirmalraj, P. N. (2023a). Label-Free Digital Holotomography Reveals Ibuprofen-Induced Morphological Changes to Red Blood Cells. *ACS Nanoscience Au*, 3(3), 241-255.
- Bergaglio, T., Synhaivska, O., & Nirmalraj, P. N. (2023b). Digital holo-tomographic 3D maps of COVID-19 microclots in blood to assess disease severity. *BioRxiv*.
- Bickford, A. F., & Sokolow, M. (1961). Fibrinolysis as Related to the Urea Solubility of Fibrin. *Thrombosis and Haemostasis*, 05(03), 480-488.
- Bikdeli, B., Madhavan, M. V., Jimenez, D., Chuich, T., Dreyfus, I., Driggin, E., Nigoghossian, C., Ageno, W., Madjid, M., Guo, Y., Tang, L. V., Hu, Y., Giri, J., Cushman, M., Quere, I., Dimakakos, E. P., Gibson, C. M., Lippi, G., Favaloro, E. J., . . . Lip, G. Y. H. (2020). COVID-19 and Thrombotic or Thromboembolic Disease: Implications for Prevention, Antithrombotic Therapy, and Follow-Up: JACC State-of-the-Art Review. *J Am Coll Cardiol*, 75(23), 2950-2973.
- Blasi, F., Oliveira, B. L., Rietz, T. A., Rotile, N. J., Naha, P. C., Cormode, D. P., Izquierdo-Garcia, D., Catana, C., & Caravan, P. (2015). Multisite Thrombus Imaging and Fibrin Content Estimation With a Single Whole-Body PET Scan in Rats. *Arteriosclerosis, Thrombosis, and Vascular Biology*, 35(10), 2114-2121.
- Blat, A., Dybas, J., Chrabaszcz, K., Bulat, K., Jaształ, A., Kaczmarska, M., Pulyk, R., Popiela, T., Slowik, A., Malek, K., Adamski, M. G., & Marzec, K. M. (2019). FTIR, Raman and AFM characterization of the clinically valid biochemical parameters of the thrombi in acute ischemic stroke. *Sci Rep*, 9(1), 15475.

Bibliography

- Boonstra, S., Onck, P. R., & Giessen, E. (2016). CHARMM TIP3P Water Model Suppresses Peptide Folding by Solvating the Unfolded State. *J Phys Chem B*, *120*(15), 3692-3698.
- Breydo, L., Wu, J. W., & Uversky, V. N. (2012). Alpha-synuclein misfolding and Parkinson's disease. *Biochim Biophys Acta*, *1822*(2), 261-285.
- Cable, R. G., Steele, W. R., Melmed, R. S., Johnson, B., Mast, A. E., Carey, P. M., Kiss, J. E., Kleinman, S. H., Wright, D. J., & NHLBI Retrovirus Epidemiology Donor Study, I. (2012). The difference between fingerstick and venous hemoglobin and hematocrit varies by sex and iron stores. *Transfusion*, *52*(5), 1031-1040.
- Camargo, S. M. R., Vuille-Dit-Bille, R. N., Mariotta, L., Ramadan, T., Huggel, K., Singer, D., Götze, O., & Verrey, F. (2014). The Molecular Mechanism of Intestinal Levodopa Absorption and Its Possible Implications for the Treatment of Parkinson's Disease. *Journal of Pharmacology and Experimental Therapeutics*, *351*(1), 114-123.
- Campioni, S., Carret, G., Jordens, S., Nicoud, L., Mezzenga, R., & Riek, R. (2014). The presence of an air-water interface affects formation and elongation of alpha-Synuclein fibrils. *J Am Chem Soc*, *136*(7), 2866-2875.
- Canchi, D. R., Paschek, D., & García, A. E. (2010). Equilibrium Study of Protein Denaturation by Urea. *Journal of the American Chemical Society*, *132*(7), 2338-2344.
- Canham, P. B., & Burton, A. C. (1968). Distribution of size and shape in populations of normal human red cells. *Circ Res*, *22*(3), 405-422.
- Carelli-Alinovi, C., Dinarelli, S., Sampaolese, B., Misiti, F., & Girasole, M. (2019). Morphological changes induced in erythrocyte by amyloid beta peptide and glucose depletion: A combined atomic force microscopy and biochemical study. *Biochimica Et Biophysica Acta-Biomembranes*, *1861*(1), 236-244.
- Chahine, L. M., Stern, M. B., & Chen-Plotkin, A. (2014). Blood-based biomarkers for Parkinson's disease. *Parkinsonism Relat Disord*, *20* Suppl 1, S99-103.
- Chaichompoo, P., Qillah, A., Sirankapracha, P., Kaewchuchuen, J., Rimthong, P., Paiboonsukwong, K., Fucharoen, S., Svasti, S., & Worawichawong, S. (2019). Abnormal red blood cell morphological changes in thalassaemia associated with iron overload and oxidative stress. *J Clin Pathol*, *72*(8), 520-524.
- Chan, R., Falato, M., Liang, H., & Chen, L. Y. (2020). In silico simulations of erythrocyte aquaporins with quantitative in vitro validation. *RSC Adv*, *10*(36), 21283-21291.
- Charbuty, B., & Abdulazeez, A. (2021). Classification Based on Decision Tree Algorithm for Machine Learning. *Journal of Applied Science and Technology Trends*, *2*(01), 20-28.

Bibliography

- Chen, F., Tillberg, P. W., & Boyden, E. S. (2015). Expansion microscopy. *Science*, 347(6221), 543-548.
- Chen, F., & Zhan, Z. Y. (2014). Severe drug-induced immune haemolytic anaemia due to ceftazidime. *Blood Transfusion*, 12(3), 435-437.
- Chen, J. Y., & Huestis, W. H. (1997). Role of membrane lipid distribution in chlorpromazine-induced shape change of human erythrocytes. *Biochim Biophys Acta*, 1323(2), 299-309.
- Chen, M. J., Sorette, M. P., Chiu, D. T., & Clark, M. R. (1991). Prehemolytic effects of hydrogen peroxide and t-butylhydroperoxide on selected red cell properties. *Biochim Biophys Acta*, 1066(2), 193-200.
- Cines, D. B., Lebedeva, T., Nagaswami, C., Hayes, V., Masefski, W., Litvinov, R. I., Rauova, L., Lowery, T. J., & Weisel, J. W. (2014). Clot contraction: compression of erythrocytes into tightly packed polyhedra and redistribution of platelets and fibrin. *Blood*, 123(10), 1596-1603.
- Collet, J. P., Park, D., Lesty, C., Soria, J., Soria, C., Montalescot, G., & Weisel, J. W. (2000). Influence of Fibrin Network Conformation and Fibrin Fiber Diameter on Fibrinolysis Speed. *Arteriosclerosis, Thrombosis, and Vascular Biology*, 20(5), 1354-1361.
- Conway, K. A., Rochet, J. C., Bieganski, R. M., & Lansbury, P. T. (2001). Kinetic stabilization of the alpha-synuclein protofibril by a dopamine-alpha-synuclein adduct. *Science*, 294(5545), 1346-1349.
- Cotte, Y., Toy, F., Jourdain, P., Pavillon, N., Boss, D., Magistretti, P., Marquet, P., & Depeursinge, C. (2013). Marker-free phase nanoscopy. *Nature Photonics*, 7(2), 113-117.
- Dalen, J. E. (2010). Aspirin for the Primary Prevention of Stroke and Myocardial Infarction: Ineffective or Wrong Dose? *The American Journal of Medicine*, 123(2), 101-102.
- Dawson, H. (2022). Digital pathology - Rising to the challenge. *Front Med (Lausanne)*, 9, 888896.
- de Haan, K., Ceylan Koydemir, H., Rivenson, Y., Tseng, D., Van Dyne, E., Bakic, L., Karınca, D., Liang, K., Ilango, M., Gumustekin, E., & Ozcan, A. (2020). Automated screening of sickle cells using a smartphone-based microscope and deep learning. *NPJ Digit Med*, 3, 76.
- De Michele, M., d'Amati, G., Leopizzi, M., Iacobucci, M., Berto, I., Lorenzano, S., Mazzuti, L., Turriziani, O., Schiavo, O. G., & Toni, D. (2022). Evidence of SARS-CoV-2 spike protein on retrieved thrombi from COVID-19 patients. *Journal of Hematology & Oncology*, 15(1).

Bibliography

- De Vries, J. J., Visser, C., Geers, L., Slotman, J. A., Endeman, H., Kruip, M. J. H. A., de Maat, M. P. M., Dutch, C., & Thrombosis Coalition, T. (2021). Does Fibrin Structure Contribute to the Increased Risk of Thrombosis in COVID-19 ICU Patients? *Blood*, *138*(Supplement 1), 3208-3208.
- de Waal, G. M., Engelbrecht, L., Davis, T., de Villiers, W. J. S., Kell, D. B., & Pretorius, E. (2018). Correlative Light-Electron Microscopy detects lipopolysaccharide and its association with fibrin fibres in Parkinson's Disease, Alzheimer's Disease and Type 2 Diabetes Mellitus. *Scientific Reports*, *8*(1).
- Deffains, M., Canron, M. H., Teil, M., Li, Q., Dehay, B., Bezard, E., & Fernagut, P. O. (2021). L-DOPA regulates α -synuclein accumulation in experimental parkinsonism. *Neuropathology and Applied Neurobiology*, *47*(4), 532-543.
- Di Foggia, M., Bonora, S., Tinti, A., & Tugnoli, V. (2017). DSC and Raman study of DMPC liposomes in presence of Ibuprofen at different pH. *Journal of Thermal Analysis and Calorimetry*, *127*(2), 1407-1417.
- Doan, M., Sebastian, J. A., Caicedo, J. C., Siegert, S., Roch, A., Turner, T. R., Mykhailova, O., Pinto, R. N., McQuin, C., Goodman, A., Parsons, M. J., Wolkenhauer, O., Hennig, H., Singh, S., Wilson, A., Acker, J. P., Rees, P., Kolios, M. C., & Carpenter, A. E. (2020). Objective assessment of stored blood quality by deep learning. *Proc. Natl. Acad. Sci. U.S.A.*, *117*(35), 21381-21390.
- Du, L. W., Liu, X. H., Huang, W. M., & Wang, E. K. (2006). A study on the interaction between ibuprofen and bilayer lipid membrane. *Electrochimica Acta*, *51*(26), 5754-5760.
- Dufaux, F. (2021). Grand Challenges in Image Processing. *Frontiers in Signal Processing*, *1*.
- Dunn, E. J., Ariëns, R. A. S., & Grant, P. J. (2005). The influence of type 2 diabetes on fibrin structure and function. *Diabetologia*, *48*(6), 1198-1206.
- Dunn, E. J., Philippou, H., Ariëns, R. A. S., & Grant, P. J. (2006). Molecular mechanisms involved in the resistance of fibrin to clot lysis by plasmin in subjects with type 2 diabetes mellitus. *Diabetologia*, *49*(5), 1071-1080.
- El Alaoui, Y., Elomri, A., Qaraqe, M., Padmanabhan, R., Yasin Taha, R., El Omri, H., El Omri, A., & Aboumarzouk, O. (2022). A Review of Artificial Intelligence Applications in Hematology Management: Current Practices and Future Prospects. *Journal of Medical Internet Research*, *24*(7), e36490.
- Fan, L., Zhang, F., Fan, H., & Zhang, C. (2019). Brief review of image denoising techniques. *Visual Computing for Industry, Biomedicine, and Art*, *2*(1).
- Fatah, K., Hamsten, A., Blombäck, B., & Blombäck, M. (1992). Fibrin Gel Network Characteristics and Coronary Heart Disease: Relations to Plasma Fibrinogen

Bibliography

- Concentration, Acute Phase Protein, Serum Lipoproteins and Coronary Atherosclerosis. *Thrombosis and Haemostasis*, 68(02), 130-135.
- Favaloro, E. J., & Gosselin, R. C. (2023). *Hemostasis and Thrombosis: Methods and Protocols* (2nd ed.). Humana New York.
- Fliervoet, L. A. L., Tiel Groenestege, W. M., & Huisman, A. (2022). Comparison of capillary and venous blood sampling for routine coagulation assays. *Clin Biochem*, 104, 30-35.
- Foulds, P. G., Diggle, P., Mitchell, J. D., Parker, A., Hasegawa, M., Masuda-Suzukake, M., Mann, D. M., & Allsop, D. (2013). A longitudinal study on alpha-synuclein in blood plasma as a biomarker for Parkinson's disease. *Sci Rep*, 3, 2540.
- Foulger, J. H., & Mills, C. A. (1930). The influence of urea upon blood clotting *American Journal of Physiology*, 94(1), 51-59.
- Friebel, M., & Meinke, M. (2006). Model function to calculate the refractive index of native hemoglobin in the wavelength range of 250-1100 nm dependent on concentration. *Applied Optics*, 45(12), 2838-2842.
- Gailani, D., & Renné, T. (2007). Intrinsic Pathway of Coagulation and Arterial Thrombosis. *Arteriosclerosis, Thrombosis, and Vascular Biology*, 27(12), 2507-2513.
- Gallagher, B. R., & Zhao, Y. (2023). Imaging pathology goes nanoscale with a low-cost strategy. *Nature Nanotechnology*, 18(4), 324-325.
- Garratty, G. (2010). Immune hemolytic anemia associated with drug therapy. *Blood Rev*, 24(4-5), 143-150.
- Garratty, G. (2012). Immune hemolytic anemia caused by drugs. *Expert Opin Drug Saf*, 11(4), 635-642.
- Gąsecka, A., Borovac, J. A., Guerreiro, R. A., Giustozzi, M., Parker, W., Caldeira, D., & Chiva-Blanch, G. (2021). Thrombotic Complications in Patients with COVID-19: Pathophysiological Mechanisms, Diagnosis, and Treatment. *Cardiovascular Drugs and Therapy*, 35(2), 215-229.
- Geekiyanage, N. M., Balanant, M. A., Sauret, E., Saha, S., Flower, R., Lim, C. T., & Gu, Y. (2019). A coarse-grained red blood cell membrane model to study stomatocyte-discocyte-echinocyte morphologies. *PLoS One*, 14(4), e0215447.
- Goldstein, J. L., Chan, F. K., Lanas, A., Wilcox, C. M., Peura, D., Sands, G. H., Berger, M. F., Nguyen, H., & Scheiman, J. M. (2011). Haemoglobin decreases in NSAID users over time: an analysis of two large outcome trials. *Aliment Pharmacol Ther*, 34(7), 808-816.

Bibliography

- Gram, A. S., Skov, J., Thorkil, P., Sidelmann, J. J., Stallknecht, B. M., & Bladbjerg, E. M. (2014). Biomarkers of coagulation, fibrinolysis, endothelial function, and inflammation in arterialized venous blood. *Blood Coagul Fibrinolysis*, *25*(4), 349-352.
- Grobbelaar, L. M., Venter, C., Vlok, M., Ngoepe, M., Laubscher, G. J., Lourens, P. J., Steenkamp, J., Kell, D. B., & Pretorius, E. (2021). SARS-CoV-2 spike protein S1 induces fibrin(ogen) resistant to fibrinolysis: implications for microclot formation in COVID-19. *Biosci Rep*, *41*(8).
- Grobler, C., Maphumulo, S. C., Grobbelaar, L. M., Bredenkamp, J. C., Laubscher, G. J., Lourens, P. J., Steenkamp, J., Kell, D. B., & Pretorius, E. (2020). Covid-19: The Rollercoaster of Fibrin(Ogen), D-Dimer, Von Willebrand Factor, P-Selectin and Their Interactions with Endothelial Cells, Platelets and Erythrocytes. *International Journal of Molecular Sciences*, *21*(14), 5168.
- Groenning, M. (2010). Binding mode of Thioflavin T and other molecular probes in the context of amyloid fibrils—current status. *Journal of Chemical Biology*, *3*(1), 1-18.
- Gupta, A., Madhavan, M. V., Sehgal, K., Nair, N., Mahajan, S., Sehrawat, T. S., Bikdeli, B., Ahluwalia, N., Ausiello, J. C., Wan, E. Y., Freedberg, D. E., Kirtane, A. J., Parikh, S. A., Maurer, M. S., Nordvig, A. S., Accili, D., Bathon, J. M., Mohan, S., Bauer, K. A., . . . Landry, D. W. (2020). Extrapulmonary manifestations of COVID-19. *Nature Medicine*, *26*(7), 1017-1032.
- Hagberg, I. A., Roald, H. E., & Lyberg, T. (1998). Adhesion of leukocytes to growing arterial thrombi. *Thrombosis and Haemostasis*, *80*(5), 852-858.
- Hagerstrand, H., & Isomaa, B. (1989). Vesiculation induced by amphiphiles in erythrocytes. *Biochim Biophys Acta*, *982*(2), 179-186.
- Han, K., Zhou, W., Ma, S., Wang, S., Qi, X., Guo, L., & Li, X. (2023). A computational study of fibrinogen-induced alteration in microvascular blood flow in COVID-19. *The European Physical Journal Special Topics*.
- Hayes, M. T. (2019). Parkinson's Disease and Parkinsonism. *Am J Med*, *132*(7), 802-807.
- He, S., Zhong, S., Liu, G., & Yang, J. (2020). Alpha-Synuclein: The Interplay of Pathology, Neuroinflammation, and Environmental Factors in Parkinson's Disease. *Neurodegener Dis*, *20*(2-3), 55-64.
- Heemskerk, J. W. M., Mattheij, N. J. A., & Cosemans, J. M. E. M. (2013). Platelet-based coagulation: different populations, different functions. *Journal of Thrombosis and Haemostasis*, *11*(1), 2-16.
- Holstege, C. P. (2005). Ibuprofen. In P. Wexler (Ed.), *Encyclopedia of Toxicology* (Second ed., pp. 566-567). Academic Press.

- Hsi, E. D. (2017). *Hematopathology* (Third ed.). Elsevier.
- Huang, J., Rauscher, S., Nawrocki, G., Ran, T., Feig, M., de Groot, B. L., Grubmuller, H., & MacKerell, A. D., Jr. (2017). CHARMM36m: an improved force field for folded and intrinsically disordered proteins. *Nat Methods*, *14*(1), 71-73.
- Huisjes, R., Bogdanova, A., van Solinge, W. W., Schiffelers, R. M., Kaestner, L., & van Wijk, R. (2018). Squeezing for Life - Properties of Red Blood Cell Deformability. *Front Physiol*, *9*, 656.
- Humphrey, W., Dalke, A., & Schulten, K. (1996). VMD: visual molecular dynamics. *J Mol Graph*, *14*(1), 33-38.
- Hur, J., Kim, K., Lee, S., Park, H., & Park, Y. (2017). Melittin-induced alterations in morphology and deformability of human red blood cells using quantitative phase imaging techniques. *Sci Rep*, *7*(1), 9306.
- Iba, T., & Levy, J. H. (2023). A commentary on "Thromboinflammation in long COVID – the elusive key to post-infection sequelae?". *Journal of Thrombosis and Haemostasis*, *21*(8), 2061-2063.
- Iglic, A., Kralj-Iglic, V., & Hagerstrand, H. (1998). Amphiphile induced echinocyte-spherocyte transformation of red blood cell shape. *European Biophysics Journal with Biophysics Letters*, *27*(4), 335-339.
- Irmady, K., Hale, C. R., Qadri, R., Fak, J., Simelane, S., Carroll, T., Przedborski, S., & Darnell, R. B. (2023). Blood transcriptomic signatures associated with molecular changes in the brain and clinical outcomes in Parkinson's disease. *Nature Communications*, *14*(1).
- Iturria-Medina, Y., Khan, A. F., Adewale, Q., Shirazi, A. H., & Alzheimer's Disease Neuroimaging, I. (2020). Blood and brain gene expression trajectories mirror neuropathology and clinical deterioration in neurodegeneration. *Brain*, *143*(2), 661-673.
- Jacob, H. S. (1975). Effect of drugs on red cell membranes: insights into normal red cell shape. *J Clin Pathol Suppl (R Coll Pathol)*, *9*, 40-45.
- Jaferzadeh, K., Moon, I., Bardyn, M., Prudent, M., Tissot, J. D., Rappaz, B., Javidi, B., Turcatti, G., & Marquet, P. (2018). Quantification of stored red blood cell fluctuations by time-lapse holographic cell imaging. *Biomed Opt Express*, *9*(10), 4714-4729.
- Javidi, B., Markman, A., Rawat, S., O'Connor, T., Anand, A., & Andemariam, B. (2018). Sick cell disease diagnosis based on spatio-temporal cell dynamics analysis using 3D printed shearing digital holographic microscopy. *Opt Express*, *26*(10), 13614-13627.

- Jolugbo, P., & Ariëns, R. A. S. (2021). Thrombus Composition and Efficacy of Thrombolysis and Thrombectomy in Acute Ischemic Stroke. *Stroke*, *52*(3), 1131-1142.
- Jörneskog, G., Egberg, N., Fagrell, B., Fatah, K., Hessel, B., Johnsson, H., Brismar, K., & Blombäck, M. (1996). Altered properties of the fibrin gel structure in patients with IDDM. *Diabetologia*, *39*(12), 1519-1523.
- Kato, G. J., Piel, F. B., Reid, C. D., Gaston, M. H., Ohene-Frempong, K., Krishnamurti, L., Smith, W. R., Panepinto, J. A., Weatherall, D. J., Costa, F. F., & Vichinsky, E. P. (2018). Sickle cell disease. *Nature Reviews Disease Primers*, *4*(1), 18010.
- Kato, G. J., Piel, F. B., Reid, C. D., Gaston, M. H., Ohene-Frempong, K., Krishnamurti, L., Smith, W. R., Panepinto, J. A., Weatherall, D. J., Costa, F. F., & Vichinsky, E. P. (2018). Sickle cell disease. *Nat Rev Dis Primers*, *4*, 18010.
- Kattula, S., Byrnes, J. R., & Wolberg, A. S. (2017). Fibrinogen and Fibrin in Hemostasis and Thrombosis. *Arteriosclerosis, Thrombosis, and Vascular Biology*, *37*(3), e13-e21.
- Kell, D. B., Laubscher, G. J., & Pretorius, E. (2022). A central role for amyloid fibrin microclots in long COVID/PASC: origins and therapeutic implications. *Biochemical Journal*, *479*(4), 537-559.
- Khairy, K., Foo, J., & Howard, J. (2010). Shapes of Red Blood Cells: Comparison of 3D Confocal Images with the Bilayer-Couple Model. *Cell Mol Bioeng*, *1*(2-3), 173-181.
- Kim, D., Lee, S., Lee, M., Oh, J., Yang, S. A., & Park, Y. (2021). Holotomography: Refractive Index as an Intrinsic Imaging Contrast for 3-D Label-Free Live Cell Imaging. *Adv Exp Med Biol*, *1310*, 211-238.
- Kim, E., Park, S., Hwang, S., Moon, I., & Javidi, B. (2022). Deep Learning-Based Phenotypic Assessment of Red Cell Storage Lesions for Safe Transfusions. *IEEE J Biomed Health Inform*, *26*(3), 1318-1328.
- Kim, Y., Shim, H., Kim, K., Park, H., Jang, S., & Park, Y. (2014). Profiling individual human red blood cells using common-path diffraction optical tomography. *Sci Rep*, *4*, 6659.
- Koníčková, D., Menšíková, K., Tučková, L., Hényková, E., Strnad, M., Friedecký, D., Stejskal, D., Matěj, R., & Kaňovský, P. (2022). Biomarkers of Neurodegenerative Diseases: Biology, Taxonomy, Clinical Relevance, and Current Research Status. *Biomedicines*, *10*(7), 1760.
- Kruger, A., Vlok, M., Turner, S., Venter, C., Laubscher, G. J., Kell, D. B., & Pretorius, E. (2022). Proteomics of fibrin amyloid microclots in long COVID/post-acute sequelae of COVID-19 (PASC) shows many entrapped pro-inflammatory molecules

that may also contribute to a failed fibrinolytic system. *Cardiovascular Diabetology*, 21(1).

- Kwasny-Krochin, B., Gluszko, P., & Undas, A. (2010). Unfavorably altered fibrin clot properties in patients with active rheumatoid arthritis. *Thrombosis Research*, 126(1), e11-e16.
- Laki, K., & Lóránd, L. (1948). On the Solubility of Fibrin Clots. *Science*, 108(2802), 280-280.
- Lamour, G., Kirkegaard, J. B., Li, H., Knowles, T. P., & Gsponer, J. (2014). Easyworm: an open-source software tool to determine the mechanical properties of worm-like chains. *Source code for biology and medicine*, 9, 16-16.
- Laubscher, G. J., Lourens, P. J., Venter, C., Kell, D. B., & Pretorius, E. (2021). TEG((R)), Microclot and Platelet Mapping for Guiding Early Management of Severe COVID-19 Coagulopathy. *J Clin Med*, 10(22).
- Laville, S. M., Couturier, A., Lambert, O., Metzger, M., Mansencal, N., Jacquelinet, C., Laville, M., Frimat, L., Fouque, D., Combe, C., Robinson, B. M., Stengel, B., Liabeuf, S., Massy, Z. A., & collaborators, C.-R. s. (2023). Urea levels and cardiovascular disease in patients with chronic kidney disease. *Nephrol Dial Transplant*, 38(1), 184-192.
- Lazaro, G. R., Melzak, K. A., Toca-Herrera, J. L., Pagonabarraga, I., & Hernandez-Machado, A. (2013). Elastic energies and morphologies of the first stages of the discoechinocyte transition. *Soft Matter*, 9(28), 6430-6441.
- Lee, J., Patel, D. S., Stahle, J., Park, S. J., Kern, N. R., Kim, S., Lee, J., Cheng, X., Valvano, M. A., Holst, O., Knirel, Y. A., Qi, Y., Jo, S., Klauda, J. B., Widmalm, G., & Im, W. (2019). CHARMM-GUI Membrane Builder for Complex Biological Membrane Simulations with Glycolipids and Lipoglycans. *J Chem Theory Comput*, 15(1), 775-786.
- Lee, M.-H., Perl, D. P., Nair, G., Li, W., Maric, D., Murray, H., Dodd, S. J., Koretsky, A. P., Watts, J. A., Cheung, V., Masliah, E., Horkayne-Szakaly, I., Jones, R., Stram, M. N., Moncur, J., Hefti, M., Folkerth, R. D., & Nath, A. (2021). Microvascular Injury in the Brains of Patients with Covid-19. *New England Journal of Medicine*, 384(5), 481-483.
- Lee, S., Park, H., Kim, K., Sohn, Y., Jang, S., & Park, Y. (2017). Refractive index tomograms and dynamic membrane fluctuations of red blood cells from patients with diabetes mellitus. *Sci Rep*, 7(1), 1039.
- Leng, A., Shah, M., Ahmad, S. A., Premraj, L., Wildi, K., Li Bassi, G., Pardo, C. A., Choi, A., & Cho, S.-M. (2023). Pathogenesis Underlying Neurological Manifestations of Long COVID Syndrome and Potential Therapeutics. *Cells*, 12(5), 816.

Bibliography

- Li, J., Zhu, M., Manning-Bog, A. B., Di Monte, D. A., & Fink, A. L. (2004). Dopamine and L-dopa disaggregate amyloid fibrils: implications for Parkinson's and Alzheimer's disease. *The FASEB Journal*, *18*(9), 962-964.
- Lim, H. W. G., Wortis, M., & Mukhopadhyay, R. (2002). Stomatocyte-discocyte-echinocyte sequence of the human red blood cell: evidence for the bilayer- couple hypothesis from membrane mechanics. *Proc Natl Acad Sci U S A*, *99*(26), 16766-16769.
- Lin, E., Fuda, F., Luu, H. S., Cox, A. M., Fang, F. Q., Feng, J. L., & Chen, M. Y. (2023). Digital pathology and artificial intelligence as the next chapter in diagnostic hematopathology. *Seminars in Diagnostic Pathology*, *40*(2), 88-94.
- Lipinski, B. (2010). Modification of fibrin structure as a possible cause of thrombolytic resistance. *Journal of Thrombosis and Thrombolysis*, *29*(3), 296-298.
- Lippi, G., Favaloro, E., Franchini, M., & Guidi, G. (2009). Milestones and Perspectives in Coagulation and Hemostasis. *Seminars in Thrombosis and Hemostasis*, *35*(01), 009-022.
- Litvinov, R. I., & Weisel, J. W. (2016). What Is the Biological and Clinical Relevance of Fibrin? *Seminars in Thrombosis and Hemostasis*, *42*(4), 333-343.
- Liu, P. Y., Chin, L. K., Ser, W., Chen, H. F., Hsieh, C. M., Lee, C. H., Sung, K. B., Ayi, T. C., Yap, P. H., Liedberg, B., Wang, K., Bourouina, T., & Leprince-Wang, Y. (2016). Cell refractive index for cell biology and disease diagnosis: past, present and future. *Lab on a Chip*, *16*(4), 634-644.
- Liu, W., Carlisle, C. R., Sparks, E. A., & Guthold, M. (2010). The mechanical properties of single fibrin fibers. *Journal of thrombosis and haemostasis : JTH*, *8*(5), 1030-1036.
- Lorand, L. (1950). Fibrin Clots. *Nature*, *166*, 694-695.
- Luzak, B., Rozalski, M., Przygodzki, T., Boncler, M., Wojkowska, D., Kosmalski, M., & Watala, C. (2023). SARS-CoV-2 Spike Protein and Neutralizing Anti-Spike Protein Antibodies Modulate Blood Platelet Function. *International Journal of Molecular Sciences*, *24*(6), 5312.
- Macfarlane, R. G. (1977). Haemostasis: Introduction. *British Medical Bulletin*, *33*(3), 183-186.
- MacKintosh, F. C., Käs, J., & Janmey, P. A. (1995). Elasticity of Semiflexible Biopolymer Networks. *Physical Review Letters*, *75*(24), 4425-4428.
- Mackman, N. (2008). Triggers, targets and treatments for thrombosis. *Nature*, *451*(7181), 914-918.

- Mackman, N., Bergmeier, W., Stouffer, G. A., & Weitz, J. I. (2020). Therapeutic strategies for thrombosis: new targets and approaches. *Nature Reviews Drug Discovery*, *19*(5), 333-352.
- Magalhães, P., & Lashuel, H. A. (2022). Opportunities and challenges of alpha-synuclein as a potential biomarker for Parkinson's disease and other synucleinopathies. *npj Parkinson's Disease*, *8*(1).
- Makky, A., Bousset, L., Polesel-Maris, J., & Melki, R. (2016). Nanomechanical properties of distinct fibrillar polymorphs of the protein α -synuclein. *Scientific Reports*, *6*(1), 37970.
- Manrique-Moreno, M., Villena, F., Sotomayor, C. P., Edwards, A. M., Munoz, M. A., Garidel, P., & Suwalsky, M. (2011). Human cells and cell membrane molecular models are affected in vitro by the nonsteroidal anti-inflammatory drug ibuprofen. *Biochim Biophys Acta*, *1808*(11), 2656-2664.
- Marder, V. J., Chute, D. J., Starkman, S., Abolian, A. M., Kidwell, C., Liebeskind, D., Ovbiagele, B., Vinuela, F., Duckwiler, G., Jahan, R., Vespa, P. M., Selco, S., Rajajee, V., Kim, D., Sanossian, N., & Saver, J. L. (2006). Analysis of Thrombi Retrieved From Cerebral Arteries of Patients With Acute Ischemic Stroke. *Stroke*, *37*(8), 2086-2093.
- Martini, W. Z., Deguzman, R., Rodriguez, C. M., Guerra, J., Martini, A. K., Pusateri, A. E., & Dubick, M. A. (2015). Effect of Ibuprofen dose on platelet aggregation and coagulation in blood samples from pigs. *Mil Med*, *180*(3 Suppl), 80-85.
- Martinod, K., & Wagner, D. D. (2014). Thrombosis: tangled up in NETs. *Blood*, *123*(18), 2768-2776.
- Matthews, K., Duffy, S. P., Myrand-Lapierre, M. E., Ang, R. R., Li, L., Scott, M. D., & Ma, H. (2017). Microfluidic analysis of red blood cell deformability as a means to assess hemin-induced oxidative stress resulting from Plasmodium falciparum intraerythrocytic parasitism. *Integr Biol (Camb)*, *9*(6), 519-528.
- McNamee, A. P., Simmonds, M. J., Inoue, M., Horobin, J. T., Hakozaki, M., Fraser, J. F., & Watanabe, N. (2021). Erythrocyte morphological symmetry analysis to detect sublethal trauma in shear flow. *Sci Rep*, *11*(1), 23566.
- Mehra, S., Sahay, S., & Maji, S. K. (2019). alpha-Synuclein misfolding and aggregation: Implications in Parkinson's disease pathogenesis. *Biochim Biophys Acta Proteins Proteom*, *1867*(10), 890-908.
- Melzak, K. A., Moreno-Flores, S., & Bieback, K. (2020). Spicule movement on RBCs during echinocyte formation and possible segregation in the RBC membrane. *Biochim Biophys Acta Biomembr*, *1862*(10), 183338.

Bibliography

- Memmolò, P., Miccio, L., Merola, F., Gennari, O., Netti, P. A., & Ferraro, P. (2014). 3D morphometry of red blood cells by digital holography. *Cytometry A*, *85*(12), 1030-1036.
- Mihalko, E., & Brown, A. C. (2020). Clot Structure and Implications for Bleeding and Thrombosis. *Semin Thromb Hemost*, *46*(1), 96-104.
- Mills, J. D., Ariëns, R. A. S., Mansfield, M. W., & Grant, P. J. (2002). Altered Fibrin Clot Structure in the Healthy Relatives of Patients With Premature Coronary Artery Disease. *Circulation*, *106*(15), 1938-1942.
- Mohanty, J. G., Shukla, H. D., Williamson, J. D., Launer, L. J., Saxena, S., & Rifkind, J. M. (2010). Alterations in the red blood cell membrane proteome in alzheimer's subjects reflect disease-related changes and provide insight into altered cell morphology. *Proteome Sci*, *8*, 11.
- Monje, M., & Iwasaki, A. (2022). The neurobiology of long COVID. *Neuron*, *110*(21), 3484-3496.
- Moon, I., Javidi, B., Yi, F., Boss, D., & Marquet, P. (2012). Automated statistical quantification of three-dimensional morphology and mean corpuscular hemoglobin of multiple red blood cells. *Opt Express*, *20*(9), 10295-10309.
- Moon, I., Yi, F., Lee, Y. H., Javidi, B., Boss, D., & Marquet, P. (2013). Automated quantitative analysis of 3D morphology and mean corpuscular hemoglobin in human red blood cells stored in different periods. *Opt Express*, *21*(25), 30947-30957.
- Mullan, J., Weston, K. M., Bonney, A., Burns, P., Mullan, J., & Rudd, R. (2017). Consumer knowledge about over-the-counter NSAIDs: they don't know what they don't know. *Australian and New Zealand Journal of Public Health*, *41*(2), 210-214.
- Muñoz, R., Santamaría, E., Rubio, I., Ausín, K., Ostolaza, A., Labarga, A., Roldán, M., Zandio, B., Mayor, S., Bermejo, R., Mendigaña, M., Herrera, M., Aymerich, N., Olier, J., Gállego, J., Mendioroz, M., & Fernández-Irigoyen, J. (2018). Mass Spectrometry-Based Proteomic Profiling of Thrombotic Material Obtained by Endovascular Thrombectomy in Patients with Ischemic Stroke. *International Journal of Molecular Sciences*, *19*(2), 498.
- Muravyov, A., & Tikhomirova, I. (2015). Red blood cell microrheological changes and drug transport efficiency. *Journal of Cellular Biotechnology*, *1*(1), 45-51.
- Mytilineou, C., Walker, R. H., Jnobaptiste, R., & Olanow, C. W. (2003). Levodopa is toxic to dopamine neurons in an in vitro but not an in vivo model of oxidative stress. *Journal of Pharmacology and Experimental Therapeutics*, *304*(2), 792-800.
- Naeim, F., Song, S. X., Rao, P. N., & Grody, W. W. (2013). *Atlas of Hematopathology* (First ed.). Academic Press.

- Nalbandian, A., Sehgal, K., Gupta, A., Madhavan, M. V., McGroder, C., Stevens, J. S., Cook, J. R., Nordvig, A. S., Shalev, D., Sehrawat, T. S., Ahluwalia, N., Bikdeli, B., Dietz, D., Der-Nigoghossian, C., Liyanage-Don, N., Rosner, G. F., Bernstein, E. J., Mohan, S., Beckley, A. A., . . . Wan, E. Y. (2021). Post-acute COVID-19 syndrome. *Nature Medicine*, *27*(4), 601-615.
- Nardini, M., Ciasca, G., Lauria, A., Rossi, C., Di Giacinto, F., Romano, S., Di Santo, R., Papi, M., Palmieri, V., Perini, G., Basile, U., Alcaro, F. D., Di Stasio, E., Bizzarro, A., Masullo, C., & De Spirito, M. (2022). Sensing red blood cell nano-mechanics: Toward a novel blood biomarker for Alzheimer's disease. *Frontiers in Aging Neuroscience*, *14*, 932354.
- Nečas, D., & Klapeček, P. (2012). Gwyddion: an open-source software for SPM data analysis. *Open Physics*, *10*(1).
- Neergaard-Petersen, S., Ajjan, R., Hvas, A.-M., Hess, K., Larsen, S. B., Kristensen, S. D., & Grove, E. L. (2013). Fibrin clot structure and platelet aggregation in patients with aspirin treatment failure. *PLoS One*, *8*(8), e71150-e71150.
- Nirmalraj, P., Lehner, R., Thompson, D., Rothen-Rutishauser, B., & Mayer, M. (2018). Subcellular Imaging of Liquid Silicone Coated-Intestinal Epithelial Cells. *Sci Rep*, *8*(1), 10763.
- Nirmalraj, P. N., Schneider, T., & Felbecker, A. (2021). Spatial organization of protein aggregates on red blood cells as physical biomarkers of Alzheimer's disease pathology. *Sci Adv*, *7*(39), eabj2137.
- O'Connor, T., Shen, J. B., Liang, B. T., & Javidi, B. (2021). Digital holographic deep learning of red blood cells for field-portable, rapid COVID-19 screening. *Opt Lett*, *46*(10), 2344-2347.
- Obstfeld, A. E. (2023). Hematology and Machine Learning. *J Appl Lab Med*, *8*(1), 129-144.
- Oliveira, B. L., & Caravan, P. (2017). Peptide-based fibrin-targeting probes for thrombus imaging. *Dalton transactions (Cambridge, England : 2003)*, *46*(42), 14488-14508.
- Ossig, C., & Reichmann, H. (2015). Treatment strategies in early and advanced Parkinson disease. *Neurol Clin*, *33*(1), 19-37.
- Park, Y., Depeursinge, C., & Popescu, G. (2018). Quantitative phase imaging in biomedicine. *Nature Photonics*, *12*(10), 578-589.
- Park, Y., Diez-Silva, M., Popescu, G., Lykotraftitis, G., Choi, W., Feld, M. S., & Suresh, S. (2008). Refractive index maps and membrane dynamics of human red blood cells parasitized by Plasmodium falciparum. *Proc Natl Acad Sci U S A*, *105*(37), 13730-13735.

- Pérez-Escalante, E., Cruz-Guerrero, A. E., Álvarez-Romero, G. A., Mendoza-Huizar, L. H., Flores-Aguilar, J. F., & González-Olivares, L. G. (2020). Urea as the best fibrin solubilizer in the thrombin inhibition analysis: Theoretical and experimental modeling of fibrinogen denaturation. *Chemical Physics Letters*, 748.
- Periyah, M. C., Halim, A. S., & Mat Saad, A. Z. (2017). Mechanism Action of Platelets and Crucial Blood Coagulation Pathways in Hemostasis. *Int J Hematol Oncol Stem Cell Res*, 11(4), 319-327.
- Perico, L., Benigni, A., Casiraghi, F., Ng, L. F. P., Renia, L., & Remuzzi, G. (2021). Immunity, endothelial injury and complement-induced coagulopathy in COVID-19. *Nature Reviews Nephrology*, 17(1), 46-64.
- Phillips, K. G., Jacques, S. L., & McCarty, O. J. T. (2012). Measurement of Single Cell Refractive Index, Dry Mass, Volume, and Density Using a Transillumination Microscope. *Physical Review Letters*, 109(11), 118105.
- Picca, A., Guerra, F., Calvani, R., Romano, R., Coelho-Junior, H. J., Bucci, C., & Marzetti, E. (2021). Mitochondrial Dysfunction, Protein Misfolding and Neuroinflammation in Parkinson's Disease: Roads to Biomarker Discovery. *Biomolecules*, 11(10).
- Pollaro, L., Equis, S., Dalla Piazza, B., & Cotte, Y. (2016). Stain-free 3D Nanoscopy of Living Cells. *Optik & Photonik*, 11, 38-42.
- Pretini, V., Koenen, M. H., Kaestner, L., Fens, M., Schiffelers, R. M., Bartels, M., & Van Wijk, R. (2019). Red Blood Cells: Chasing Interactions. *Front Physiol*, 10, 945.
- Pretorius, E., & Lipinski, B. (2013). Differences in Morphology of Fibrin Clots Induced with Thrombin and Ferric Ions and Its Pathophysiological Consequences. *Heart Lung and Circulation*, 22(6), 447-449.
- Pretorius, E., Mbotwe, S., Bester, J., Robinson, C. J., & Kell, D. B. (2016). Acute induction of anomalous and amyloidogenic blood clotting by molecular amplification of highly substoichiometric levels of bacterial lipopolysaccharide. *Journal of The Royal Society Interface*, 13(122), 20160539.
- Pretorius, E., Venter, C., Laubscher, G. J., Kotze, M. J., Oladejo, S. O., Watson, L. R., Rajaratnam, K., Watson, B. W., & Kell, D. B. (2022). Prevalence of symptoms, comorbidities, fibrin amyloid microclots and platelet pathology in individuals with Long COVID/Post-Acute Sequelae of COVID-19 (PASC). *Cardiovasc Diabetol*, 21(1), 148.
- Pretorius, E., Venter, C., Laubscher, G. J., Lourens, P. J., Steenkamp, J., & Kell, D. B. (2020). Prevalence of readily detected amyloid blood clots in 'unclotted' Type 2 Diabetes Mellitus and COVID-19 plasma: a preliminary report. *Cardiovasc Diabetol*, 19(1), 193.

Bibliography

- Pretorius, E., Vlok, M., Venter, C., Bezuidenhout, J. A., Laubscher, G. J., Steenkamp, J., & Kell, D. B. (2021). Persistent clotting protein pathology in Long COVID/Post-Acute Sequelae of COVID-19 (PASC) is accompanied by increased levels of antiplasmin. *Cardiovascular Diabetology*, *20*(1).
- Previtali, E., Bucciarelli, P., Passamonti, S. M., & Martinelli, I. (2011). Risk factors for venous and arterial thrombosis. *Blood Transfus*, *9*(2), 120-138.
- Rahi, M. S., Jindal, V., Reyes, S.-P., Gunasekaran, K., Gupta, R., & Jaiyesimi, I. (2021). Hematologic disorders associated with COVID-19: a review. *Annals of Hematology*, *100*(2), 309-320.
- Rahi, M. S., Parekh, J., Pednekar, P., Mudgal, M., Jindal, V., & Gunasekaran, K. (2023). Role of Therapeutic Anticoagulation in COVID-19: The Current Situation. *Hematology Reports*, *15*(2), 358-369.
- Ranucci, M., Baryshnikova, E., Anguissola, M., Pugliese, S., Falco, M., & Menicanti, L. (2023). The Long Term Residual Effects of COVID-Associated Coagulopathy. *International Journal of Molecular Sciences*, *24*(6), 5514.
- Rawat, S., Komatsu, S., Markman, A., Anand, A., & Javidi, B. (2017). Compact and field-portable 3D printed shearing digital holographic microscope for automated cell identification. *Appl Opt*, *56*(9), D127-D133.
- Reinhart, W. H., & Chien, S. (1986). Red cell rheology in stomatocyte-echinocyte transformation: roles of cell geometry and cell shape. *Blood*, *67*(4), 1110-1118.
- Rizzuto, V., Mencattini, A., Alvarez-Gonzalez, B., Di Giuseppe, D., Martinelli, E., Beneitez-Pastor, D., Manu-Pereira, M. D. M., Lopez-Martinez, M. J., & Samitier, J. (2021). Combining microfluidics with machine learning algorithms for RBC classification in rare hereditary hemolytic anemia. *Sci Rep*, *11*(1), 13553.
- Roberts, I., & De Montalembert, M. (2007). Sickle cell disease as a paradigm of immigration hematology: new challenges for hematologists in Europe. *Haematologica*, *92*(7), 865-871.
- Rosendaal, F. R., & Reitsma, P. H. (2009). Genetics of venous thrombosis. *Journal of Thrombosis and Haemostasis*, *7*, 301-304.
- Roth, G. A., Mensah, G. A., Johnson, C. O., Addolorato, G., Ammirati, E., Baddour, L. M., Barengo, N. C., Beaton, A. Z., Benjamin, E. J., Benziger, C. P., Bonny, A., Brauer, M., Brodmann, M., Cahill, T. J., Carapetis, J., Catapano, A. L., Chugh, S. S., Cooper, L. T., Coresh, J., . . . Group, G.-N.-J. G. B. o. C. D. W. (2020). Global Burden of Cardiovascular Diseases and Risk Factors, 1990-2019: Update From the GBD 2019 Study. *J Am Coll Cardiol*, *76*(25), 2982-3021.
- Ruggeri, Z. M. (2007). The role of von Willebrand factor in thrombus formation. *Thrombosis research*, *120 Suppl 1*(Suppl 1), S5-S9.

Bibliography

- Russell, C. D., Lone, N. I., & Baillie, J. K. (2023). Comorbidities, multimorbidity and COVID-19. *Nature Medicine*, *29*(2), 334-343.
- Sandoz, P. A., Tremblay, C., Van Der Goot, F. G., & Frechin, M. (2019). Image-based analysis of living mammalian cells using label-free 3D refractive index maps reveals new organelle dynamics and dry mass flux. *PLOS Biology*, *17*(12), e3000553.
- Schiavone, B., Dore, G. J., Stone, E., Matthews, G. V., & Darley, D. R. (2023). An update on long COVID and its management. *Medicine Today*, *24*(5), 37-43.
- Scholkmann, F., & May, C. A. (2023). COVID-19, post-acute COVID-19 syndrome (PACS, "long COVID") and post-COVID-19 vaccination syndrome (PCVS, "post-COVIDvac-syndrome"): Similarities and differences. *Pathol Res Pract*, *246*, 154497.
- Schwarzenbach, H., Hoon, D. S. B., & Pantel, K. (2011). Cell-free nucleic acids as biomarkers in cancer patients. *Nature Reviews Cancer*, *11*(6), 426-437.
- Scott, J. T., & Higgs, C. S. (1992). Diuretic induced gout: a multifactorial condition. *Annals of the rheumatic diseases*, *51*(2), 259-261.
- Sebastian, B., & Dittrich, P. S. (2018). Microfluidics to Mimic Blood Flow in Health and Disease. *Annual Review of Fluid Mechanics*, *50*(1), 483-504.
- Silvain, J., Collet, J.-P., Guedeney, P., Varenne, O., Nagaswami, C., Maupain, C., Empana, J.-P., Boulanger, C., Tafflet, M., Manzo-Silberman, S., Kerneis, M., Brugier, D., Vignolles, N., Weisel, J. W., Jouven, X., Montalescot, G., & Spaulding, C. (2017). Thrombus composition in sudden cardiac death from acute myocardial infarction. *Resuscitation*, *113*, 108-114.
- Silvain, J., Collet, J.-P., Nagaswami, C., Beygui, F., Edmondson, K. E., Bellemain-Appaix, A., Cayla, G., Pena, A., Brugier, D., Barthelemy, O., Montalescot, G., & Weisel, J. W. (2011). Composition of coronary thrombus in acute myocardial infarction. *Journal of the American College of Cardiology*, *57*(12), 1359-1367.
- Sinha, A., Chu, T. T. T., Dao, M., & Chandramohanadas, R. (2015). Single-cell evaluation of red blood cell bio-mechanical and nano-structural alterations upon chemically induced oxidative stress. *Scientific Reports*, *5*.
- Spencer, J. P., Jenner, A., Butler, J., Aruoma, O. I., Dexter, D. T., Jenner, P., & Halliwell, B. (1996). Evaluation of the pro-oxidant and antioxidant actions of L-DOPA and dopamine in vitro: implications for Parkinson's disease. *Free Radic Res*, *24*(2), 95-105.
- Staessens, S., Denorme, F., Francois, O., Desender, L., Dewaele, T., Vanacker, P., Deckmyn, H., Vanhoorelbeke, K., Andersson, T., & De Meyer, S. F. (2020). Structural analysis of ischemic stroke thrombi: histological indications for therapy resistance. *Haematologica*, *105*(2), 498-507.

Bibliography

- Stoltz, J. F. (1981). Drugs Affecting Blood Rheology - a Review. *Scandinavian Journal of Clinical & Laboratory Investigation*, *41*, 287-290.
- Su, D., Zhang, X., Su, Y., Chan, P., & Xu, E. (2023). Effects of different levodopa doses on blood pressure in older patients with early and middle stages of Parkinson's disease. *Heliyon*, *9*(7), e17876.
- Sung, Y., Lue, N., Hamza, B., Martel, J., Irimia, D., Dasari, R. R., Choi, W., Yaqoob, Z., & So, P. (2014). Three-Dimensional Holographic Refractive-Index Measurement of Continuously Flowing Cells in a Microfluidic Channel. *Phys Rev Appl*, *1*.
- Synhaivska, O., Bhattacharya, S., Campioni, S., Thompson, D., & Nirmalraj, P. N. (2022). Single-Particle Resolution of Copper-Associated Annular alpha-Synuclein Oligomers Reveals Potential Therapeutic Targets of Neurodegeneration. *ACS Chem Neurosci*, *13*(9), 1410-1421.
- Tehrani, S., Antovic, A., Mobarrez, F., Mageed, K., Lins, P.-E., Adamson, U., Wallén, H. N., & Jörneskog, G. (2012). High-dose aspirin is required to influence plasma fibrin network structure in patients with type 1 diabetes. *Diabetes care*, *35*(2), 404-408.
- Thompson, R. C., Simons, N. W., Wilkins, L., Cheng, E., Del Valle, D. M., Hoffman, G. E., Cervia, C., Fennessy, B., Mouskas, K., Francoeur, N. J., Johnson, J. S., Lepow, L., Le Berichel, J., Chang, C., Beckmann, A. G., Wang, Y.-C., Nie, K., Zaki, N., Tuballes, K., . . . Beckmann, N. D. (2023). Molecular states during acute COVID-19 reveal distinct etiologies of long-term sequelae. *Nature Medicine*, *29*(1), 236-246.
- Tolosa, E., Garrido, A., Scholz, S. W., & Poewe, W. (2021). Challenges in the diagnosis of Parkinson's disease. *Lancet Neurology*, *20*(5), 385-397.
- Toyama, Y., Shimizu, M., Ochiai, M., & Dobashi, T. (2017). Effects of urea and NaCl on the fibrinogen cryogelation. *Journal of Biorheology*, *31*(1), 12-15.
- Turner, S., Khan, M. A., Putrino, D., Woodcock, A., Kell, D. B., & Pretorius, E. (2023). Long COVID: pathophysiological factors and abnormalities of coagulation. *Trends in Endocrinology & Metabolism*, *34*(6), 321-344.
- Undas, A., Kolarz, M., Kopec, G., & Tracz, W. (2008). Altered fibrin clot properties in patients on long-term haemodialysis: relation to cardiovascular mortality. *Nephrology Dialysis Transplantation*, *23*(6), 2010-2015.
- Undas, A., Zawilska, K., Ciesla-Dul, M., Lehmann-Kopydłowska, A., Skubiszak, A., Ciepluch, K., & Tracz, W. (2009). Altered fibrin clot structure/function in patients with idiopathic venous thromboembolism and in their relatives. *Blood*, *114*(19), 4272-4278.
- Van Der Spoel, D., Lindahl, E., Hess, B., Groenhof, G., Mark, A. E., & Berendsen, H. J. (2005). GROMACS: fast, flexible, and free. *J Comput Chem*, *26*(16), 1701-1718.

Bibliography

- Vandenakker, C. C., Engel, M. F. M., Velikov, K. P., Bonn, M., & Koenderink, G. H. (2011). Morphology and Persistence Length of Amyloid Fibrils Are Correlated to Peptide Molecular Structure. *Journal of the American Chemical Society*, *133*(45), 18030-18033.
- Vanommeslaeghe, K., & MacKerell, A. D., Jr. (2012). Automation of the CHARMM General Force Field (CGenFF) I: bond perception and atom typing. *J Chem Inf Model*, *52*(12), 3144-3154.
- Vanommeslaeghe, K., Raman, E. P., & MacKerell, A. D., Jr. (2012). Automation of the CHARMM General Force Field (CGenFF) II: assignment of bonded parameters and partial atomic charges. *J Chem Inf Model*, *52*(12), 3155-3168.
- Veenstra, T. D., Conrads, T. P., Hood, B. L., Avellino, A. M., Ellenbogen, R. G., & Morrison, R. S. (2005). Biomarkers: Mining the Biofluid Proteome. *Molecular & Cellular Proteomics*, *4*(4), 409-418.
- Venter, C., Bezuidenhout, J. A., Laubscher, G. J., Lourens, P. J., Steenkamp, J., Kell, D. B., & Pretorius, E. (2020). Erythrocyte, Platelet, Serum Ferritin, and P-Selectin Pathophysiology Implicated in Severe Hypercoagulation and Vascular Complications in COVID-19. *Int J Mol Sci*, *21*(21).
- Viallat, A., & Abkarian, M. (2014). Red blood cell: from its mechanics to its motion in shear flow. *Int J Lab Hematol*, *36*(3), 237-243.
- Vilalta, N., Santiago, M. V., Cuevas, B., Macho, R., Remacha, A., Carrasco, M., Mateo, J., Millon, J., Soria, J. M., & Souto, J. C. (2017). The Relationship between Leukocyte Counts and Venous Thromboembolism: Results from RETROVE Study. *Biology and Medicine*, *09*(04).
- Virkler, K., & Lednev, I. K. (2010). Raman spectroscopic signature of blood and its potential application to forensic body fluid identification. *Anal Bioanal Chem*, *396*(1), 525-534.
- Wallace Collett, L., Gluck, S., Strickland, R. M., & Reddi, B. J. n. (2021). Evaluation of coagulation status using viscoelastic testing in intensive care patients with coronavirus disease 2019 (COVID-19): An observational point prevalence cohort study. *Australian Critical Care*, *34*(2), 155-159.
- Wallqvist, A., Covell, D. G., & Thirumalai, D. (1998). Hydrophobic Interactions in Aqueous Urea Solutions with Implications for the Mechanism of Protein Denaturation. *Journal of the American Chemical Society*, *120*(2), 427-428.
- Walter, W., Haferlach, C., Nadarajah, N., Schmidts, I., Kühn, C., Kern, W., & Haferlach, T. (2021). How artificial intelligence might disrupt diagnostics in hematology in the near future. *Oncogene*, *40*(25), 4271-4280.

Bibliography

- Wassie, A. T., Zhao, Y., & Boyden, E. S. (2019). Expansion microscopy: principles and uses in biological research. *Nature Methods*, *16*(1), 33-41.
- Weisel, J. W. (2007). Structure of fibrin: impact on clot stability. *Journal of Thrombosis and Haemostasis*, *5*, 116-124.
- Weiss, C., & Jelkmann, W. (1989). *Functions of the blood*. Springer. https://doi.org/https://doi.org/10.1007/978-3-642-73831-9_18
- Wen, G., Leen, V., Rohand, T., Sauer, M., & Hofkens, J. (2023). Current Progress in Expansion Microscopy: Chemical Strategies and Applications. *Chemical Reviews*, *123*(6), 3299-3323.
- Wolberg, A. S., Rosendaal, F. R., Weitz, J. I., Jaffer, I. H., Agnelli, G., Baglin, T., & Mackman, N. (2015). Venous thrombosis. *Nature Reviews Disease Primers*, *1*(1).
- Wool, G. D., & Miller, J. L. (2021). The Impact of COVID-19 Disease on Platelets and Coagulation. *Pathobiology*, *88*(1), 15-27.
- World Health Organization. (2010). *WHO guidelines on drawing blood: best practices in phlebotomy*. WHO.
- World Health Organization. (2021, 6 October 2021). *A clinical case definition of post COVID-19 condition by a Delphi consensus*. WHO. Retrieved June 2023 from https://www.who.int/publications/i/item/WHO-2019-nCoV-Post_COVID-19_condition-Clinical_case_definition-2021.1
- Wu, E. L., Cheng, X., Jo, S., Rui, H., Song, K. C., Davila-Contreras, E. M., Qi, Y., Lee, J., Monje-Galvan, V., Venable, R. M., Kluda, J. B., & Im, W. (2014). CHARMM-GUI Membrane Builder toward realistic biological membrane simulations. *J Comput Chem*, *35*(27), 1997-2004.
- Xu, X., & Veenstra, T. D. (2008). Analysis of biofluids for biomarker research. *PROTEOMICS – Clinical Applications*, *2*(10-11), 1403-1412.
- Yasuda, H., Hatano, T., Honda, T., Tsutsui, M., Hattori, N., Ando, M., & Komatsu, N. (2022). Vitamin B6 Deficiency Anemia Attributed to Levodopa/Carbidopa Intestinal Gel Therapy for Parkinson's Disease: A Diagnostic Pitfall for Myelodysplastic Syndrome with Ring Sideroblasts. *Internal Medicine*, *61*(24), 3719-3722.
- Yedlapudi, D., Joshi, G. S., Luo, D., Todi, S. V., & Dutta, A. K. (2016). Inhibition of alpha-synuclein aggregation by multifunctional dopamine agonists assessed by a novel in vitro assay and an in vivo Drosophila synucleinopathy model. *Scientific Reports*, *6*.
- Yi, F., Moon, I., & Javidi, B. (2017). Automated red blood cells extraction from holographic images using fully convolutional neural networks. *Biomed Opt Express*, *8*(10), 4466-4479.

Bibliography

- Yi, F., Moon, I., Javidi, B., Boss, D., & Marquet, P. (2013). Automated segmentation of multiple red blood cells with digital holographic microscopy. *Journal of Biomedical Optics*, *18*(2), 26006.
- Yoon, J., Kim, K., Park, H., Choi, C., Jang, S., & Park, Y. (2015). Label-free characterization of white blood cells by measuring 3D refractive index maps. *Biomed Opt Express*, *6*(10), 3865-3875.
- Yuan, H., Zhang, Z. W., Liang, L. W., Shen, Q., Wang, X. D., Ren, S. M., Ma, H. J., Jiao, S. J., & Liu, P. (2010). Treatment strategies for Parkinson's disease. *Neurosci Bull*, *26*(1), 66-76.
- Zabczyk, M., Plens, K., Wojtowicz, W., & Undas, A. (2017). Prothrombotic Fibrin Clot Phenotype Is Associated With Recurrent Pulmonary Embolism After Discontinuation of Anticoagulant Therapy. *Arteriosclerosis, Thrombosis, and Vascular Biology*, *37*(2), 365-373.
- Zalewski, J., Bogaert, J., Sadowski, M., Woznicka, O., Doulaptsis, K., Ntoumpanaki, M., Zabczyk, M., Nessler, J., & Undas, A. (2015). Plasma fibrin clot phenotype independently affects intracoronary thrombus ultrastructure in patients with acute myocardial infarction. *Thromb Haemost*, *113*(6), 1258-1269.
- Zhang, H., Zang, C., Xu, Z., Zhang, Y., Xu, J., Bian, J., Morozjuk, D., Khullar, D., Zhang, Y., Nordvig, A. S., Schenck, E. J., Shenkman, E. A., Rothman, R. L., Block, J. P., Lyman, K., Weiner, M. G., Carton, T. W., Wang, F., & Kaushal, R. (2023). Data-driven identification of post-acute SARS-CoV-2 infection subphenotypes. *Nature Medicine*, *29*(1), 226-235.
- Zhu, C., Shi, W., Daleke, D. L., & Baker, L. A. (2018). Monitoring dynamic spiculation in red blood cells with scanning ion conductance microscopy. *Analyst*, *143*(5), 1087-1093.
- Zuo, Y., Estes, S. K., Ali, R. A., Gandhi, A. A., Yalavarthi, S., Shi, H., Sule, G., Gockman, K., Madison, J. A., Zuo, M., Yadav, V., Wang, J., Woodard, W., Lezak, S. P., Lugogo, N. L., Smith, S. A., Morrissey, J. H., Kanthi, Y., & Knight, J. S. (2020). Prothrombotic autoantibodies in serum from patients hospitalized with COVID-19. *Sci Transl Med*, *12*(570).

List of figures

Figure 1.1. Overview of biofluids and the role of biomarkers for clinical applications, such as disease detection and monitoring.....	1
Figure 1.2. Overview of blood-based biomarkers used for diagnostics and prognostics in the clinical practice.....	2
Figure 1.3. Overview of the transition from traditional to digital pathology.....	4
Figure 1.4. Overview of the DHT microscope.....	9
Figure 2.1. Blood composition.....	12
Figure 2.2. Blood collection methods.....	13
Figure 2.3. Sample preparation procedures for blood imaging with DHTM.....	15
Figure 2.4. Optimization of the best combination of blood dilution (in PBS buffer) and volume to add to the petri dish.....	16
Figure 2.5. Preparation of blood smears for DHTM imaging.....	17
Figure 2.6. Image processing and analysis workflow for blood imaging using label-free DHTM.....	19
Figure 2.7. Quantitative morphological and chemical parameters that can be extracted from 3D and 4D refractive index tomograms acquired with DHTM.....	20
Figure 3.1. Principle of DHTM and sample preparation procedure for blood and ibuprofen solutions.....	26
Figure 3.2. 3D holotomographic imaging of RBCs and classification using machine learning (ML).....	27
Figure 3.3. Quantification of size and shape variations in healthy, SCT and SCA RBC populations based on 3D tomograms.....	30
Figure 3.4. 3D rendering and classification of RBCs treated with ibuprofen at varying concentrations during a 20-minute time-lapse using 3D digital holotomographic microscopy.....	32
Figure 3.5. RBC morphological changes upon exposure to low and high concentrations of ibuprofen during a 20-minute time-lapse.....	34
Figure 3.6. Characterization of spicules on ibuprofen-treated RBCs.....	36

List of figure

Figure 3.7. Representative structures of ibuprofen (ibu) aggregates on RBC outer membrane bilayer obtained from Molecular Dynamics (MD) simulations	39
Figure 3.8. Summary schematic of the key findings in this study.	42
Figure 3.1. Principle of DHTM and sample preparation procedure for blood and ibuprofen solutions. (a) The holo-tomographic setup includes a low power laser beam ($\lambda = 520$ nm) that splits into the reference and the object beam before rejoining below the objective, where the interference is recorded. A 3D RI map is obtained by recording holograms with a rotational arm at 360° around the sample, at a 45° angle. Morphological and chemical parameters can be quantified for individual RBCs from the 3D RI tomogram. (b) 10 μ L of whole blood is obtained from a finger prick and diluted in PBS buffer at a final concentration of 1:1000. 250 μ L of blood solution is added to a petri dish for imaging. (c) Ibuprofen powder is obtained by crushing an ibuprofen tablet and is dissolved in PBS buffer to obtain five final concentrations (0.25 mM, 0.5 mM, 1 mM, 1.5 mM, 3 mM). 50 μ L of each ibuprofen solution is added to the blood solution in the petri dish during the live cell imaging experiments.....	26
Figure 3.2. 3D holotomographic imaging of RBCs and classification using machine learning (ML). (a) 3D refractive index (RI) tomogram of RBCs obtained from a healthy donor. The corresponding segmented RI tomogram and ML-classified RBC types are shown in (b) and (c). (d) 3D RI tomogram of RBCs from a donor with sickle cell trait (SCT). The corresponding segmented RI tomogram and ML-classified RBC types are shown in (e) and (f). (g) 3D RI tomogram of RBCs from a donor diagnosed with sickle cell anemia (SCA). The corresponding segmented RI tomogram and ML-classified RBC types are shown in (h) and (i). Field of view 90x90x30 μ m.	27
Figure 3.3. Quantification of size and shape variations in healthy, SCT and SCA RBC populations based on 3D tomograms. Single cell level comparison of (a) diameter, (b) surface area, (c) volume, (d) thickness, (e) sphericity and (f) Hb concentration between ML-based classified RBC types in healthy, SCT and SCA samples. Bars indicate mean values plus minimum and maximum values of all counted cells in each group.	30
Figure 3.4. 3D rendering and classification of RBCs treated with ibuprofen at varying concentrations during a 20-minute time-lapse using 3D digital holo-tomographic microscopy. (A) 0.25 mM, (B) 0.5 mM, (C) 1 mM, (D) 1.5 mM and (E) 3 mM. Red and yellow color coding indicates normocytes and echinocytes, respectively. Field of view 90x90x30 μ m. ibu = ibuprofen.	32
Figure 3.5. RBC morphological changes upon exposure to low and high concentrations of ibuprofen during a 20-minute time-lapse. (a) 3D renderings of a single RBC treated with 0.25 mM ibuprofen showing the transient morphological alteration from a	

List of figure

normocyte to an echinocyte (scale bar: $x = 7.57 \mu\text{m}$, $y = 7.36 \mu\text{m}$, $z = 3.28 \mu\text{m}$). Insets in (a) show the corresponding 2D RI maps at each time point. (b-e) Quantification of time-dependent morphological parameters: diameter, S/V ratio, sphericity and Hb concentration. (f) 3D renderings of a single RBC treated with 1.5 mM ibuprofen showing sphero-echinocytosis (scale bar: $x = 7.74 \mu\text{m}$, $y = 6.92 \mu\text{m}$, $z = 2.82 \mu\text{m}$). Insets in (f) show the corresponding 2D RI maps at each time point. (g-j) Quantification of time-dependent morphological parameters: diameter, S/V ratio, sphericity and Hb concentration. (k-m) 3D rendering of a single RBC treated with 0.25 mM ibuprofen showing spicule splitting. (n-p) 3D rendering of a single RBC treated with 0.25 mM ibuprofen showing spicule dissolution. 34

Figure 3.6. Characterization of spicules on ibuprofen-treated RBCs. (a) 3D AFM image of an echinocyte. White arrows indicate spicules on RBC membrane. (b) and (c) Height and phase-contrast AFM images of an echinocyte. (d) Height profile extracted along the blue line indicated in (b) across an echinocyte. The green line indicates the corresponding height profile of a normocyte taken from the inset in (d). (e) Statistical distribution of surface roughness values obtained from AFM based analysis of healthy and ibuprofen-treated RBCs. (f) AFM height image of ibuprofen particles on gold surface. (g) Height profiles of ibuprofen particles extracted along the corresponding lines indicated in (f). (h) Ibuprofen particle size distribution; mean particle size: 13.5 nm, CIL: 11.5 nm and CIU: 14.9 nm. 36

Figure 3.7. Representative structures of ibuprofen (ibu) aggregates on RBC outer membrane bilayer obtained from Molecular Dynamics (MD) simulations of (a) low concentration of ibuprofen adsorbed on membrane, and (b) densely packed high concentration of ibuprofen adsorbed on membrane. (c) Total interaction energies between ibuprofen and lipid membrane at low and high concentrations. (d) Comparison of the diffusion coefficient, D of RBC lipid headgroup atoms (P, N and O) at low (black) and high (red) concentrations of ibuprofen on membrane. (e) Deuterium order parameters (SCD) of the hydrocarbon tails, SN-1 and SN-2 of Palmitoyl Oleoyl (PO) and Stearoyl (SSM) lipids of the RBC membrane bilayer in presence of low and high concentrations of ibuprofen. (f) Maps of average (over the z -axis) lipid number density in the plane (xy) of the RBC membrane bilayer. 39

Figure 3.8. Summary schematic of the key findings in this study. (a) Schematic representation of a normocytic RBC membrane architecture showing the lipid bilayer, a transmembrane protein and the spectrin cytoskeleton. (b) Schematic representation of an echinocyte membrane architecture showing the interaction of one ibuprofen molecule (left) and multiple aggregates of ibuprofen molecules (right) with the lipid bilayer. A single ibuprofen molecule permeates and interacts with the RBC lipid outer

List of figure

layer while bigger ibuprofen molecule aggregates diffuse and deform the lipid bilayer, causing spicule formation.....	42
Figure 4.1. Structural and spectrochemical analysis of synthetically prepared fixed blood clots in aqueous solution.....	56
Figure 4.2. Structural analysis of microclots in plasma of a COVID-19 positive patient with mild symptomatology (PLS-CVDP2)	58
Figure 4.3. Structural analysis of microclots in plasma of a COVID-19 positive patient with moderate symptomatology (PLS-CVDP1).	59
Figure 4.4. Structural analysis of microclots in plasma of a COVID-19 recovered patient with mild symptomatology (PLS-CVDR2).	61
Figure 4.5. Morphological characterization of microclots in healthy and COVID-19 positive and recovered patients.....	63
Figure 5.1. DHTM and AFM characterization of untreated blood clot fragments.....	75
Figure 5.2. DHTM characterization of urea-treated blood clot fragments.....	76
Figure 5.3. AFM characterization of urea treated blood clot fragments.....	78
Figure 5.4. Digital Holo-tomographic Microscopy on aspirin treated blood clot fragments.....	80
Figure 5.5. Atomic force microscopy of aspirin treated blood clot fragments.....	81
Figure 6.1. Characterization of α -Syn fibrils incubated with L-dopa.....	93
Figure 6.2. Morphological characterization of α -Syn fibrils incubated with L-dopa ...	94
Figure A.1. Evolution of RBC quality over 11-days of storage time. 3D rendering of healthy RBCs diluted in PBS and stored at 4°C on (a) day 0, (b) day1, (c) day 2, (d) day 3, (e) day 4, (f) day 7, (g) day 8, (h) day 9, (i) day 10, (j) day 11. (k) Percentage of normocytes and echinocytes in the same blood solution over 11 days. (l-q) Quantification of RBC morphological parameters over storage time: diameter, surface area, volume, thickness, sphericity and Hb concentration. Error bars depict the standard deviation. Field of view 90x90x30 μ m.....	136
Figure A.2. Benchmark for the quantification of the morphological parameters using micro-particles based on silicon dioxide (Merk Millipore). (a) 3D rendering of 2 μ m beads with corresponding RI tomogram in the inset, obtained with DHTM. Comparison of the quantification of (b) the diameter, (c) the surface area and (d) the volume, between the Imaris-based image analysis and the nominal values provided by the manufacturer. (e) 3D rendering of 5 μ m beads with corresponding RI tomogram in the inset, obtained with DHTM. (f) Comparison of the quantification of the diameter, (g)	

List of figure

the surface area and (h) the volume, between the Imaris-based image analysis and the nominal values provided by the manufacturer. Error bars depict the minimum and maximum values. Field of view 90x90x30 μm	137
Figure A.3. Quantification of Hb content in healthy, SCT and SCA RBC populations based on 3D tomograms. Single cell level comparison between ML-based classified RBC types in healthy, SCT and SCA samples. Bars indicate mean values plus minimum and maximum values of all counted cells in each group.	138
Figure A.4. Quantification of RBC morphological changes in diameter, thickness surface area to volume ratio (S/V Ratio), sphericity, Hb concentration and Hb content upon exposure to different concentrations of ibuprofen (0.25 mM, 0.5 mM, 1 mM, 1.5 mM and 3mM) during a 20-minute time-lapse. (a) 0.25 mM, (b) 0.5 mM, (c) 1 mM, (d) 1.5 mM and (e) 3 mM ibuprofen concentration. Blue line = field of view 1; red line = field of view 2.	139
Figure A.5. Quantification of RBC morphological changes in surface area, volume and Hb content upon exposure to low and high concentrations of ibuprofen during a 20-minute time-lapse. (a-c) Time-dependent changes to surface area, volume and Hb content of a single RBC treated with 0.25 mM ibuprofen. (d-f) Time-dependent changes to surface area, volume and Hb content of a single RBC treated with 1.5 mM ibuprofen.	140
Figure A.6. Ratio of normocytes and echinocytes in blood incubated with 0.25 mM, 0.5 mM, 1.5 mM and 3 mM ibuprofen concentrations for 1.5 hours at 37°C.....	141
Figure A.7. 3D holo-tomographic imaging of RBCs treated with urea at varying concentrations, during a 10-minute time-lapse. (a) 3D RI tomograms of RBCs treated with 2M urea, resulting in mild spherocytosis (t1: 0 s; t2: 1:24 min, urea added; t3: 1:48 min; t4: 5:20 min; t5: 10 min). (b) 3D RI tomograms of RBCs treated with 4M urea, resulting in mild spherocytosis (t1: 0 s; t2: 1:02 min, urea added; t3: 1:26 min; t4: 4:58 min; t5: 10 min). (c) 3D RI tomograms of RBCs treated with 6M urea, resulting in mild spherocytosis (t1: 0 s; t2: 1:22 min, urea added; t3: 1:46 min; t4: 5:18 min; t5: 10 min). (d) 3D RI tomograms of RBCs treated with 8M urea, resulting in spherocytosis and cell lysis, with formation of ghost cells (t1: 0 s; t2: 48 s, urea added; t3: 1:08 min; t4: 2:20 min; t5: 10 min). (e-j) Quantification of time-dependent morphological parameters in urea-treated RBCs, (e) diameter, (f) surface area, (g) volume, (h) thickness, (i) sphericity and (j) Hb concentration (red = 2M; green = 4M; blue = 6M; black = 8M). Field of view 90x90x30 μm	143
Figure A.8. 3D holo-tomographic imaging of RBCs treated with H ₂ O ₂ at varying concentrations, during a 10-minute time-lapse. (a) 3D RI tomograms of RBCs treated with 2M H ₂ O ₂ , resulting in mild stomatocytosis (t1: 0 s; t2: 1:02 min, H ₂ O ₂ added; t3: 1:48 min; t4: 7:44 min; t5: 15 min). (b) 3D RI tomograms of RBCs treated with 4M	

List of figure

H₂O₂, resulting in mild stomatocytosis (t1: 0 s; t2: 54 s, H₂O₂ added; t3: 1:34 min; t4: 6:34 min; t5: 15 min). (c) 3D RI tomograms of RBCs treated with 6M H₂O₂, resulting in mild stomatocytosis (t1: 0 s; t2: 44 s, H₂O₂ added; t3: 1:28 min; t4: 6:24 min; t5: 15 min). (d) 3D RI tomograms of RBCs treated with 8M H₂O₂, resulting in more pronounced stomatocytosis (t1: 0 s; t2: 1:40 min, H₂O₂ added; t3: 2:20 min; t4: 7:20 min; t5: 15 min). (e-j) Quantification of time-dependent morphological parameters in urea-treated RBCs, (e) diameter, (f) surface area, (g) volume, (h) thickness, (i) sphericity and (j) Hb concentration (red = 2M; green = 4M; blue = 6M; black = 8M). Field of view 90x90x30 μm145

Figure A.9. 3D holo-tomographic imaging of RBCs treated with ddH₂O, during a 10-minute time-lapse. (a) 3D RI tomograms of RBCs treated with ddH₂O, resulting in no morphological alteration (t1: 0 s; t2: 44 s, ddH₂O added; t3: 1:04 min; t4: 4:00 min; t5: 10 min). (b-g) Quantification of time-dependent morphological parameters in urea-treated RBCs, (b) diameter, (c) surface area, (d) volume, (e) thickness, (f) sphericity and (g) Hb concentration. Field of view 90x90x30 μm146

Figure A.10. Effect of petri dish surface used to image blood solutions with DHTM. (a) Echinocytosis resulting from RBCs contact with a glass surface. (b) Polymer-coated surface resulting in unaltered RBC morphology.....147

Figure A.11. Comparison between PBS and silicone oil (5 cSt) coating for optimal blood smear imaging with DHTM. (a) RI tomogram of healthy RBCs from a blood smear coated with PBS. (b) RI tomogram of healthy RBCs from a blood smear coated with silicone oil (5 cSt). (c) Example of storage artifacts in a blood smear coated with PBS and sealed with a coverslip and nail varnish after 4 days storage at room temperature. (d) Example of absence of storage artifacts in a blood smear coated with silicone oil (5 cSt) and sealed with a coverslip and nail varnish after 4 days storage at room temperature.148

Figure A.12. (a) Model RBC lipid bilayer composition at the outer/top and inner/bottom leaflets used in this study also showing the (b) membrane dimensions in the xy-plane. (c) Stick representation of a single molecule of ibuprofen (ibu). (d) Preformed aggregates of ibuprofen molecules (at low concentration) obtained in this study from 1 ns dynamics in explicit water.149

Figure A.13. (a-e) Initial and (f-j) final snapshots of (a, f) single ibuprofen molecule, aggregates of (b, g) 80 ibuprofen molecules, (c, h) 100 ibuprofen molecules, densely packed (d, i) 1903 ibuprofen molecules under NPT conditions, and (e, j) 1903 ibuprofen molecules under NVT conditions. (k-o) Ibuprofen–membrane interaction energies and their Coulombic electrostatic and van der Waals (vdW) components for all systems modelled in this study.....150

List of figure

Figure A.14. Ibuprofen–ibuprofen interaction energies and their electrostatic and vdW components for (a) low conc. I, (b) low conc. II, (c) high conc. I, and (d) high conc. II (see Appendix to Chapter 3 A.1.2 for these definitions). (e-i) Average density profiles of all species in the simulation box for all systems used in this study.	151
Figure A.15. Comparison of (a) Mean Square Displacement (MSD) and (b) diffusion coefficient, D for all systems modelled in this study. (c-g) Lipid hydrocarbon tail deuterium order parameter (SCD) for RBC membrane lipids (Palmitoyl Oleoyl and Stearoyl) with two acyl chains, SN-1 and SN-2, and (h-l) lipid heavy atoms number densities in the xy-plane averaged over the z-axis to obtain a top view of lipid densities in the membrane for all systems.....	152
Figure B.1. Sample preparation procedure and principle of DHTM for plasma imaging. (a) Plasma was obtained after blood collection in K2EDTA vacutainers and centrifugation in order to separate each blood component. 50 μL of plasma is diluted in Alsever's solution at a final concentration of 1:5. 250 μL of plasma solution is transferred to a petri dish for imaging. (b) Digital holotomographic microscopy uses a low-power laser beam ($\lambda = 520 \text{ nm}$) that splits into the reference and the sample laser beams before rejoining below the objective (60x, NA = 0.8), where the interference (hologram) is recorded. A rotational arm, located above the sample holder, rotates 360° around the sample at a 45° angle in order to obtain a 3D refractive index (RI) map. The presence of microclots and platelet pathology can be detected in a label-free manner from the 3D RI tomograms.	164
Figure B.2. Structural analysis of microclots in plasma of a COVID-19 positive patient without clinical symptomatology (PLS-CVDP3). (a) Refractive index (RI) tomogram of a fibrin-rich microclot in plasma. (b) Corresponding segmented RI tomogram of the fibrin-rich microclot from the inset in (a). (c) RI tomogram of a microclot composite and platelet aggregates in plasma. (d) Corresponding segmented RI tomogram of the microclot composite and platelet aggregates from the inset in (c). (e) RI tomogram of a microclot composite in plasma. (f) Corresponding segmented RI tomogram of the microclot composite from the inset in (e). (g-h) Size and dry mass of fibrin-rich microclots, microclot composite structures and platelet aggregates (<10 platelets) in plasma. Error bars represent the standard deviation from the mean. (i) Pie chart showing the microclot composition in plasma of donor PLS-CVDP3.	165
Figure B.3. Structural analysis of microclots in plasma of a COVID-19 recovered patient with moderate symptomatology (PLS-CVDR1). (a) Refractive index (RI) tomogram of a microclot composite and platelet aggregates in plasma. (b) Corresponding segmented RI tomogram of the microclot composite and platelet aggregates from the inset in (a). (c) RI tomogram of a fibrin-rich microclot and platelet aggregates in plasma. (d)	

List of figure

Corresponding segmented RI tomogram of the fibrin-rich microclot and platelet aggregates from the inset in (c). (e-f) Size and dry mass of fibrin-rich microclots and microclot composite structures in plasma. (g-h) Size and dry mass of platelet aggregates in plasma. Error bars represent the standard deviation from the mean. (i) Pie chart showing the microclot composition in plasma of donor PLS-CVDR1. 166

Figure B.4. DHTM tomograms of plasma of healthy controls (PLS-HC). (a) Refractive index (RI) tomogram of a small fibrin-rich microclot in PLS-HC1. (b) RI tomogram of a microclot composite in PLS-HC2. (c) RI tomogram showing individual platelets in PLS-HC3. (d) RI tomogram showing individual platelets in PLS-HC4. (e) RI tomogram showing individual platelets in PLS-HC5. 167

Figure B.5. Age dependence of microclot prevalence and morphology in healthy and COVID-19 positive and recovered patients. (a) Prevalence of microclots detected in 75 μ L of plasma from healthy and COVID-19 positive and recovered patients plotted against the patient age and grouped by healthy and COVID-19 subphenotypes. (b) Mean microclot size of fibrin-rich microclots and microclot composites plotted against the patient age and grouped by healthy and COVID-19 subphenotypes. 168

Figure B.6. IgM and IgG antibodies dependence of microclot prevalence and morphology in COVID-19 positive and recovered patients. (a) Prevalence of microclots detected in 75 μ L of plasma from COVID-19 positive and recovered patients plotted against the IgM antibodies level and grouped by COVID-19 subphenotypes. (b) Prevalence of microclots detected in 75 μ L of plasma from COVID-19 positive and recovered patients plotted against the IgG antibodies level and grouped by COVID-19 subphenotypes. (c) Mean microclot size of fibrin-rich microclots and microclot composites plotted against the IgM antibodies level and grouped by COVID-19 subphenotypes. (d) Mean microclot size of fibrin-rich microclots and microclot composites plotted against the IgG antibodies level and grouped by COVID-19 subphenotypes. 169

Figure C.1. Effect of L-dopa on α -Syn aggregation at 300 μ M concentration. (a) Relative ThT emission data points of α -Syn incubated without (blue) and with different concentrations (green: 10 μ M; purple: 50 μ M; red: 100 μ M) of L-dopa, over a period of 7 days. The symbol indicates each repetition. (b) Relative ThT emission data points of α -Syn incubated without and with L-dopa (100 μ M) for each repetition, over a period of 7 days. 174

Movie A.1. Effect of 0.25 mM ibuprofen on RBCs. RI tomograms were acquired at 2 sec intervals over a period of 20 min. 3D renderings of extracted frames from the video are provided in Figure 3.4(a). Timecode is min:sec. 158

List of figure

Movie A.2. Effect of 0.5 mM ibuprofen on RBCs. RI tomograms were acquired at 2 sec intervals over a period of 20 min. 3D renderings of extracted frames from the video are provided in Figure 3.4(b). Timecode is min:sec.159

Movie A.3. Effect of 1 mM ibuprofen on RBCs. RI tomograms were acquired at 2 sec intervals over a period of 20 min. 3D renderings of extracted frames from the video are provided in Figure 3.4(c). Timecode is min:sec.....160

Movie A.4. Effect of 1.5 mM ibuprofen on RBCs. RI tomograms were acquired at 2 sec intervals over a period of 20 min. 3D renderings of extracted frames from the video are provided in Figure 3.4(d). Timecode is min:sec.161

Movie A.5. Effect of 3 mM ibuprofen on RBCs. RI tomograms were acquired at 2 sec intervals over a period of 20 min. 3D renderings of extracted frames from the video are provided in Figure 3.4(e). Timecode is min:sec.162

Movie A.6. 3D segmented rendering of a single RBC exposed to low (0.25 mM) ibuprofen concentration and measured with DHTM, showing transient spicule formation, movement and dissolution across the RBC membrane. Timecode is min:sec.....163

Movie A.7. 3D segmented rendering of a single RBC exposed to high (1.5 mM) ibuprofen concentration and measured with DHTM, showing irreversible spicule formation and movement across the RBC membrane. Timecode is min:sec.....164

List of tables

Table A.1. Summary of the demographics of the healthy blood and SCT and SCA RBC samples.....	155
Table A.2. Overview of the total number of analyzed RBCs for the healthy, SCT and SCA samples and the percentages of each RBC type that was present in each sample. .	155
Table A.3. Description of the extracted morphological parameters from Imaris 9.7.	156
Table A.4. Composition of RBC membrane lipid bilayer molecular model. CHL = Cholesterol, POPC = Palmitoyl Oleoyl PhosphoCholine, POPE = Palmitoyl Oleoyl PhosphoEthanolamine, POPS = Palmitoyl Oleoyl PhosphoSerine, and SSM = Stearoyl SphingoMyelin.....	156
Table A.5. Overview of the ibuprofen concentrations and the corresponding ibuprofen dosage and ibuprofen plasma concentration.....	156
Table A.6. Overview of the total number of analyzed RBCs for each ibuprofen concentration (0.25 mM, 0.5 mM, 1 mM, 1.5 mM and 3 mM), during a 20-minute time-lapse.....	157
Table B.1. Summary of the demographics for the samples of the fixed blood clots in aqueous solution.	171
Table B.2. Summary of the demographics, SARS-coV-2 serology test results (IgM and IgG antibodies), symptomatology and sample collection details for healthy and COVID-19 plasma samples.	172
Table B.3. Description of the quantified morphological parameters extracted from Imaris 9.8.	173

Appendix

A. Appendix to Chapter 3

A.1. Molecular dynamics model details

A.1.1. RBC membrane lipid bilayer model

We modelled the RBC membrane lipid bilayer based on the *in silico* lipid composition of the model erythrocyte membrane in ref. [Chan et al., 2020], which have been previously experimentally validated. The membrane model was built using CHARMM-GUI [Lee et al., 2019; Wu et al., 2014] web-interface and is composed of 20% and 20% cholesterol (CHL), 11% and 25% Palmitoyl Oleoyl PhosphoCholine (POPC), 38% and 10% Palmitoyl Oleoyl PhosphoEthanolamine (POPE), 22% and 0% Palmitoyl Oleoyl PhosphoSerine (POPS), and 9% and 35% Stearoyl SphingoMyelin (SSM) in the inner and outer leaflets, respectively (Table A.4 and Figure A.12(a)), with 200 lipid molecules in each leaflet. The surface area of the lipid bilayer was 10.5 X 10.5 nm² (Figure A.12(b)), large enough to study adsorption of ibuprofen aggregates on membrane surface.

A.1.2. Preparation of the ibuprofen-lipid systems and molecular dynamics simulations

Molecular Dynamics (MD) simulations were performed using Gromacs 2018.4 [Van Der Spoel et al., 2005] software. The ibuprofen molecules and RBC lipid bilayer were represented by CHARMM General force field [Vanommeslaeghe & MacKerell, 2012; Vanommeslaeghe et al., 2012] (CGenFF) and CHARMM36m [Huang et al., 2017] force field parameters, respectively. Five different ibuprofen aggregates were studied on top of RBC membrane bilayer – (1) single molecule of ibuprofen (Figure A.12(c)), preformed aggregates of (2) 80 ibuprofen molecules, representing very low concentration, and (3) 100 ibuprofen molecules representing low concentration, but higher than 80-molecule aggregate, densely packed box of ibuprofen containing 1903 molecules under (4) isothermal-isobaric ensemble (NPT) conditions at constant

pressure, where the volume of the system is adjusted during simulation representing high concentration, and (5) canonical ensemble (NVT) at constant volume to model very high concentration of ibuprofen aggregates. System (1) will henceforth be regarded as “single ibu”, system (2) as “low ibu conc. I”, system (3) as “low ibu conc. II”, system (4) as “high ibu conc. I”, and system (5) as “high ibu conc. II”. The preformed aggregates of ibuprofen (80 and 100 molecules) were modelled by running a MD simulation of randomly dispersed molecules of ibuprofen in water with counter ions (Na^+ and Cl^-) (Figure A.12(d)). The ibuprofen aggregates formed instantly within 1 ns dynamics (Figure A.12(d)) due to strong hydrophobic intermolecular forces. The starting configuration of all five systems are shown in Figure A.12(a-e). All ibuprofen–membrane complexes were solvated by filling the area above and below the membrane with water molecules represented by the modified TIP3P water model [Boonstra et al., 2016], creating a $>20\text{-\AA}$ thick water layer above the ibuprofen and below the membrane to mimic bulk solvation in the z-plane. Each simulation cell was neutralized by adding the appropriate number of counterions. After 5000 steps of energy minimization, each system was equilibrated over six consecutive steps (100 ps each), with the values of the force constants of position and dihedral restraints of lipids gradually decreased from 1000 to 0 (the unit for position and dihedral restraints are $\text{kJ}/(\text{mol}\cdot\text{nm}^2)$ and $\text{kJ}/(\text{mol}\cdot\text{rad}^2)$, respectively). During equilibration, the Berendsen thermostat and barostat were applied to maintain the temperature at 310 K and pressure at 1 atm. Semi-isotropic pressure coupling was applied to allow the lipid bilayer to fluctuate in the xy plane independent of the z-axis. For the production run, the Velocity rescaling thermostat and Parrinello-Rahman barostat were applied. Long-range electrostatic interactions were treated using the particle-mesh Ewald (PME) method. The time step used in our MD simulations is 2 fs, and the structures were saved every 100 ps during 0.1 μs of production dynamics.

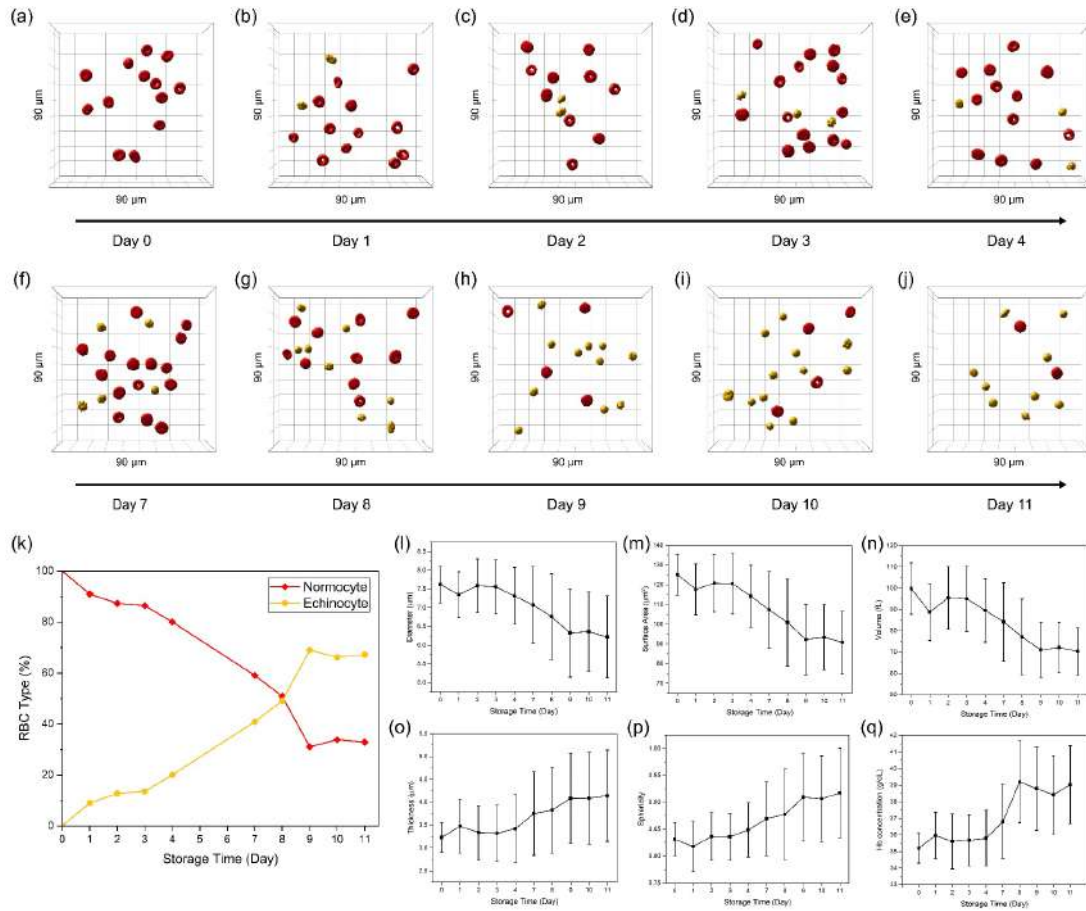


Figure A.1. Evolution of RBC quality over 11-days of storage time. 3D rendering of healthy RBCs diluted in PBS and stored at 4°C on (a) day 0, (b) day1, (c) day 2, (d) day 3, (e) day 4, (f) day 7, (g) day 8, (h) day 9, (i) day 10, (j) day 11. (k) Percentage of normocytes and echinocytes in the same blood solution over 11 days. (l-q) Quantification of RBC morphological parameters over storage time: diameter, surface area, volume, thickness, sphericity and Hb concentration. Error bars depict the standard deviation. Field of view 90x90x30 µm.

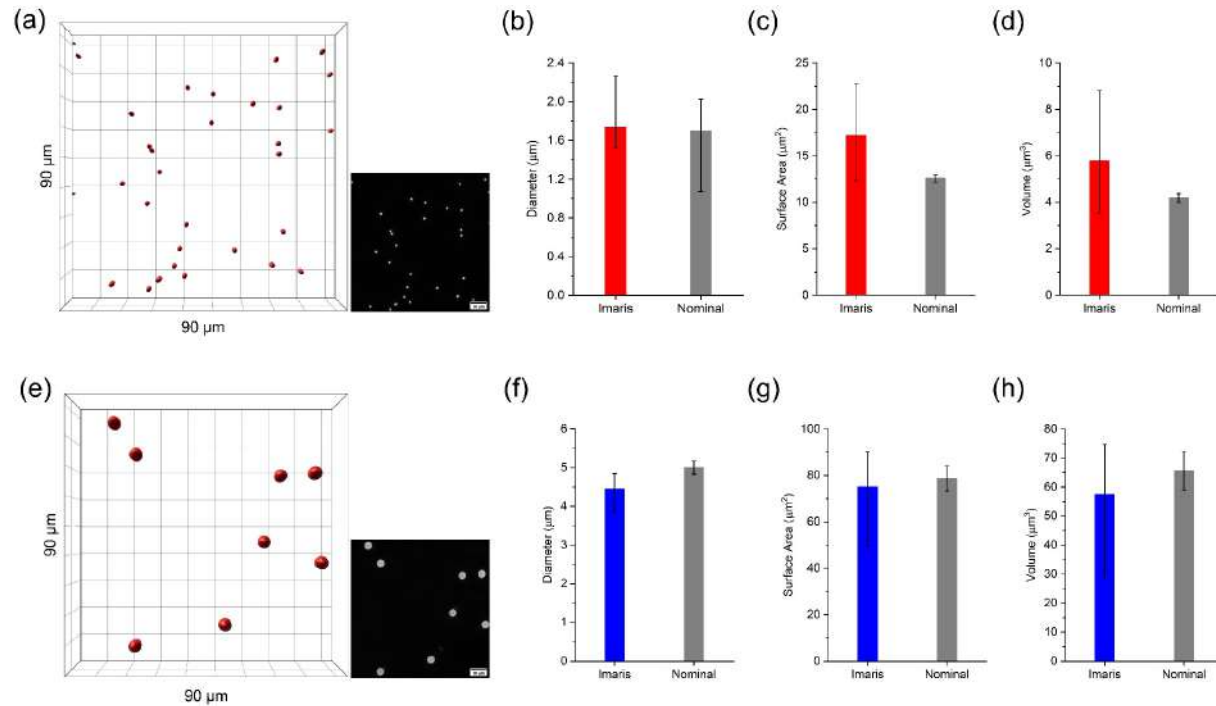


Figure A.2. Benchmark for the quantification of the morphological parameters using micro-particles based on silicon dioxide (Merk Millipore). (a) 3D rendering of 2 μm beads with corresponding RI tomogram in the inset, obtained with DHTM. Comparison of the quantification of (b) the diameter, (c) the surface area and (d) the volume, between the Imaris-based image analysis and the nominal values provided by the manufacturer. (e) 3D rendering of 5 μm beads with corresponding RI tomogram in the inset, obtained with DHTM. (f) Comparison of the quantification of the diameter, (g) the surface area and (h) the volume, between the Imaris-based image analysis and the nominal values provided by the manufacturer. Error bars depict the minimum and maximum values. Field of view 90x90x30 μm.

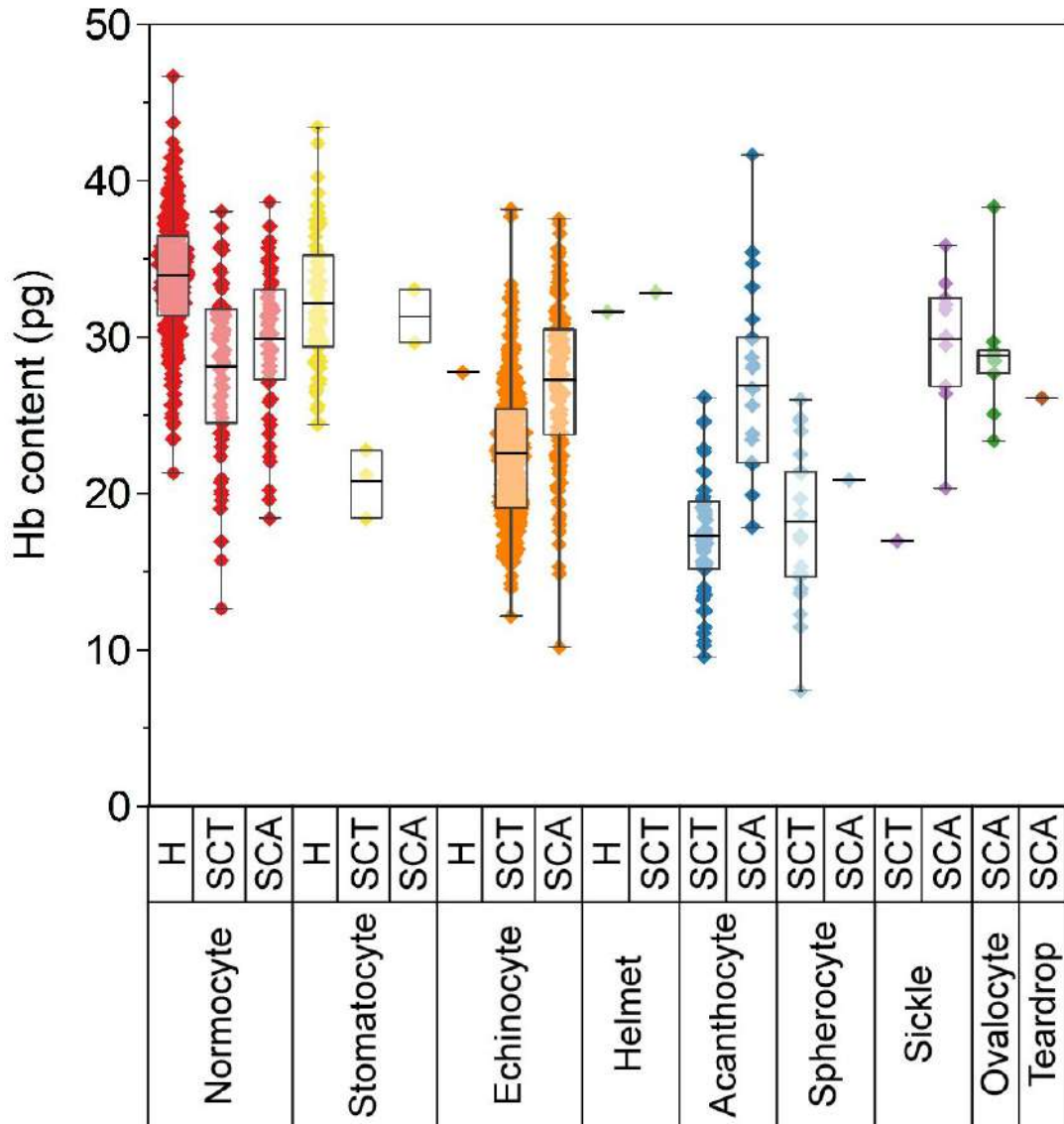


Figure A.3. Quantification of Hb content in healthy, SCT and SCA RBC populations based on 3D tomograms. Single cell level comparison between ML-based classified RBC types in healthy, SCT and SCA samples. Bars indicate mean values plus minimum and maximum values of all counted cells in each group.

A. Appendix to Chapter 3

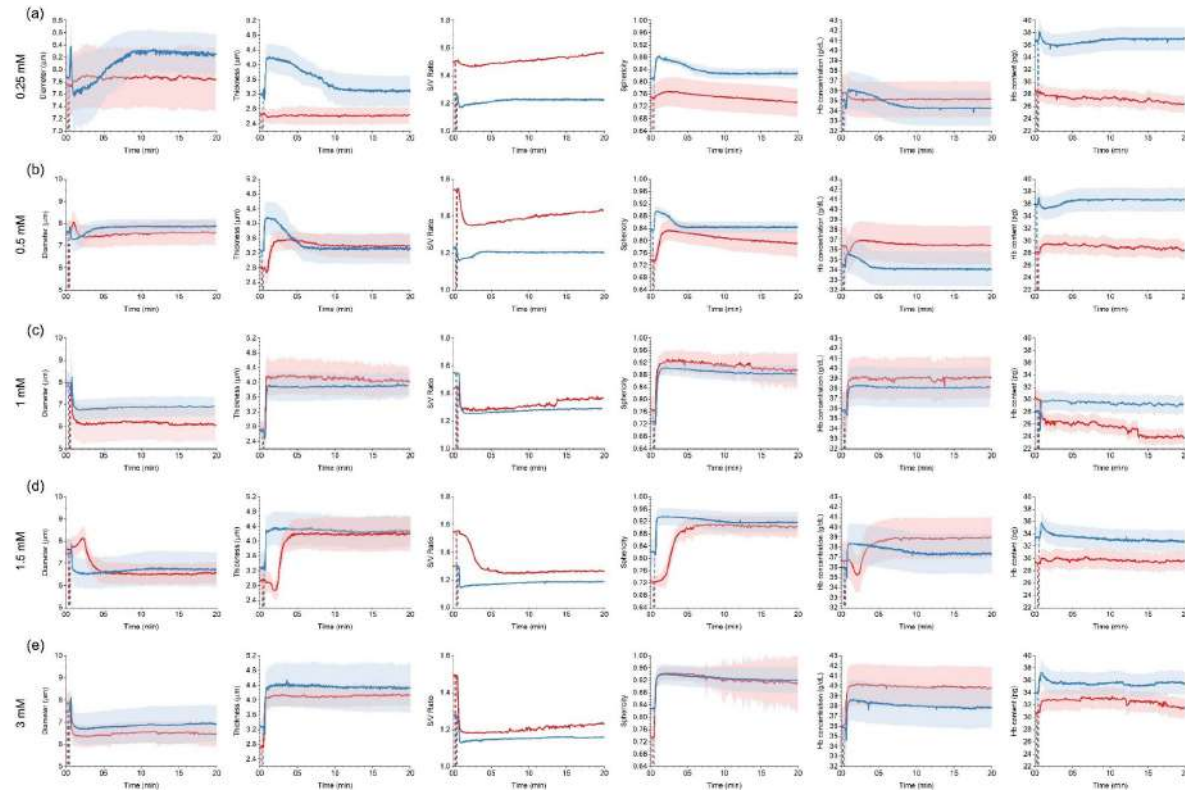


Figure A.4. Quantification of RBC morphological changes in diameter, thickness surface area to volume ratio (S/V Ratio), sphericity, Hb concentration and Hb content upon exposure to different concentrations of ibuprofen (0.25 mM, 0.5 mM, 1 mM, 1.5 mM and 3mM) during a 20-minute time-lapse. (a) 0.25 mM, (b) 0.5 mM, (c) 1 mM, (d) 1.5 mM and (e) 3 mM ibuprofen concentration. Blue line = field of view 1; red line = field of view 2.

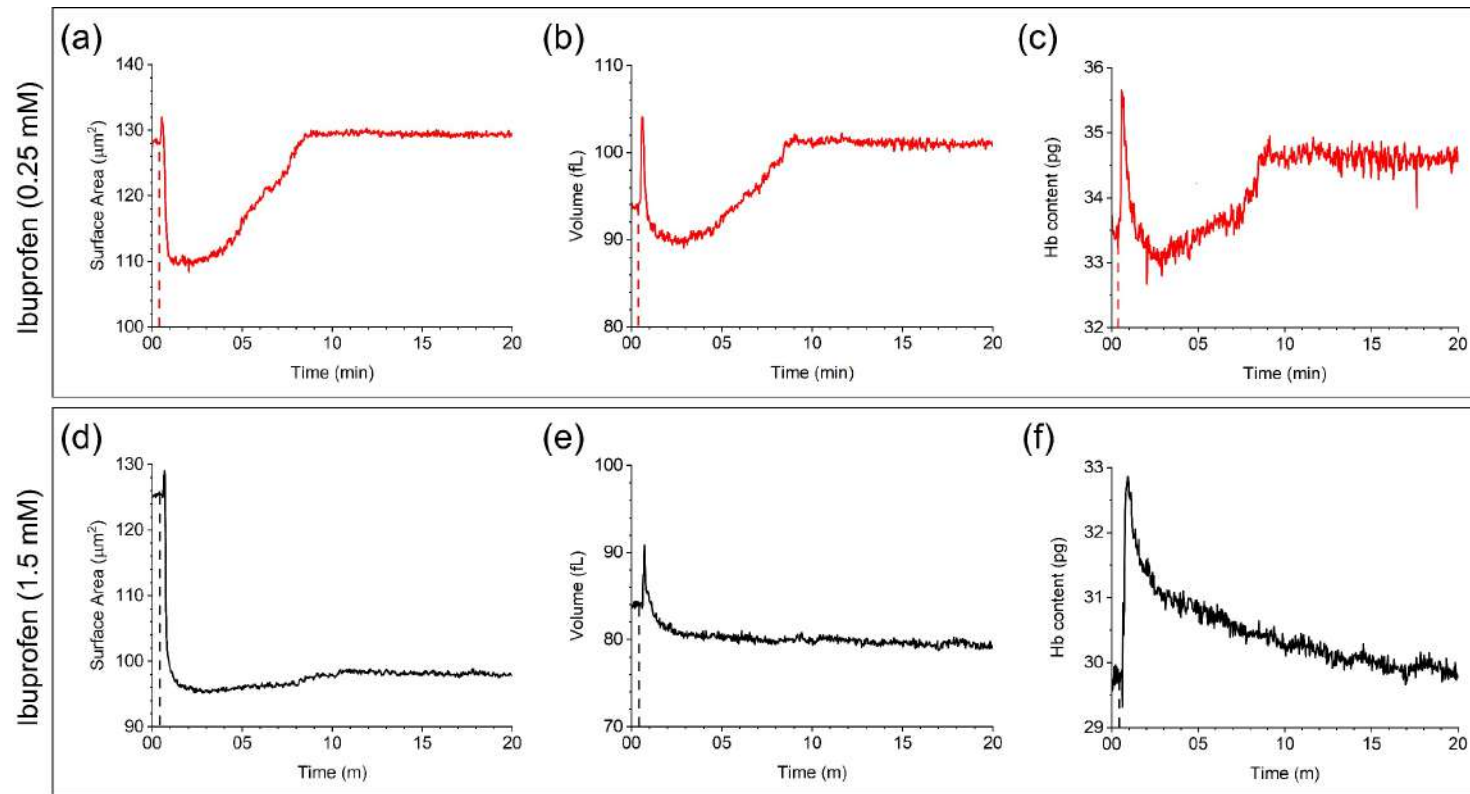


Figure A.5. Quantification of RBC morphological changes in surface area, volume and Hb content upon exposure to low and high concentrations of ibuprofen during a 20-minute time-lapse. (a-c) Time-dependent changes to surface area, volume and Hb content of a single RBC treated with 0.25 mM ibuprofen. (d-f) Time-dependent changes to surface area, volume and Hb content of a single RBC treated with 1.5 mM ibuprofen.

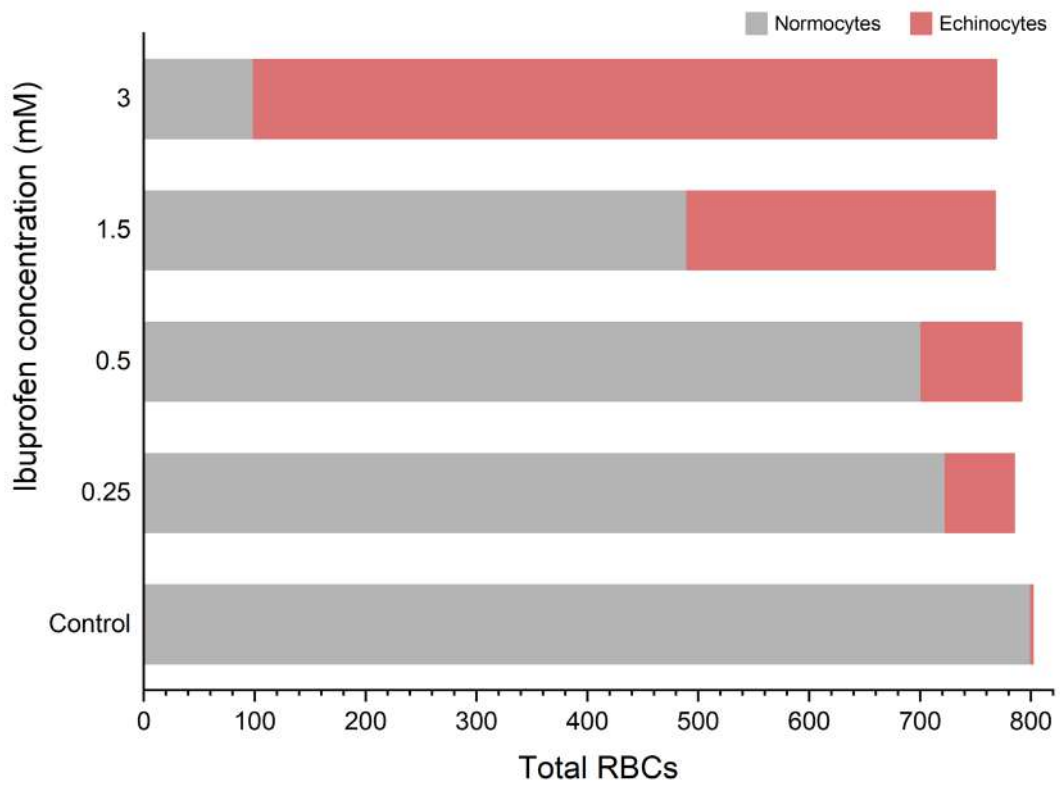


Figure A.6. Ratio of normocytes and echinocytes in blood incubated with 0.25 mM, 0.5 mM, 1.5 mM and 3 mM ibuprofen concentrations for 1.5 hours at 37°C.

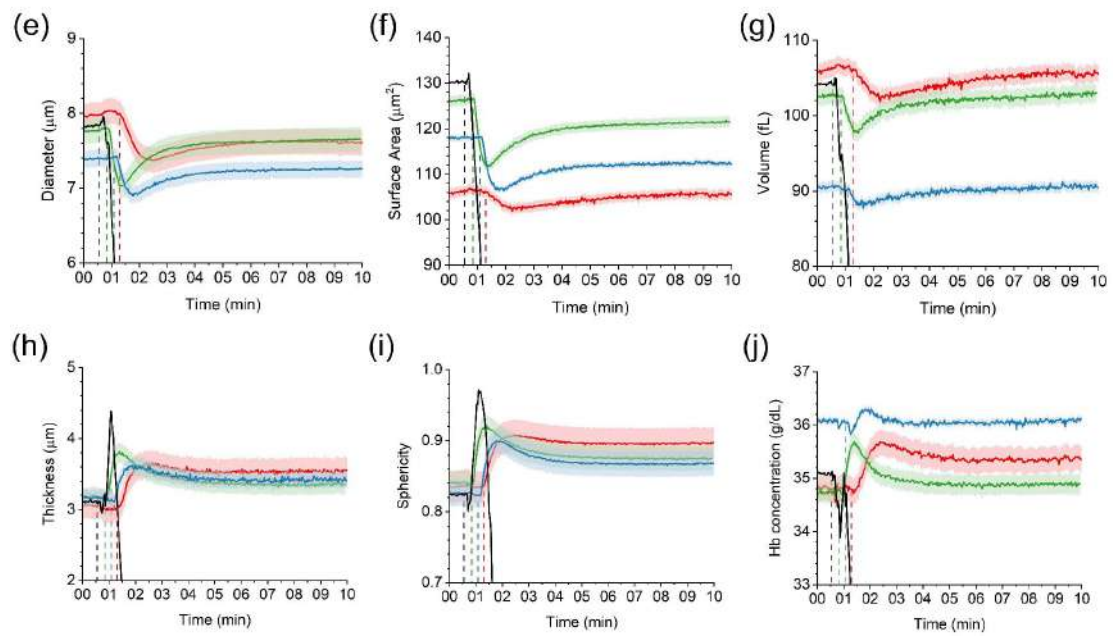
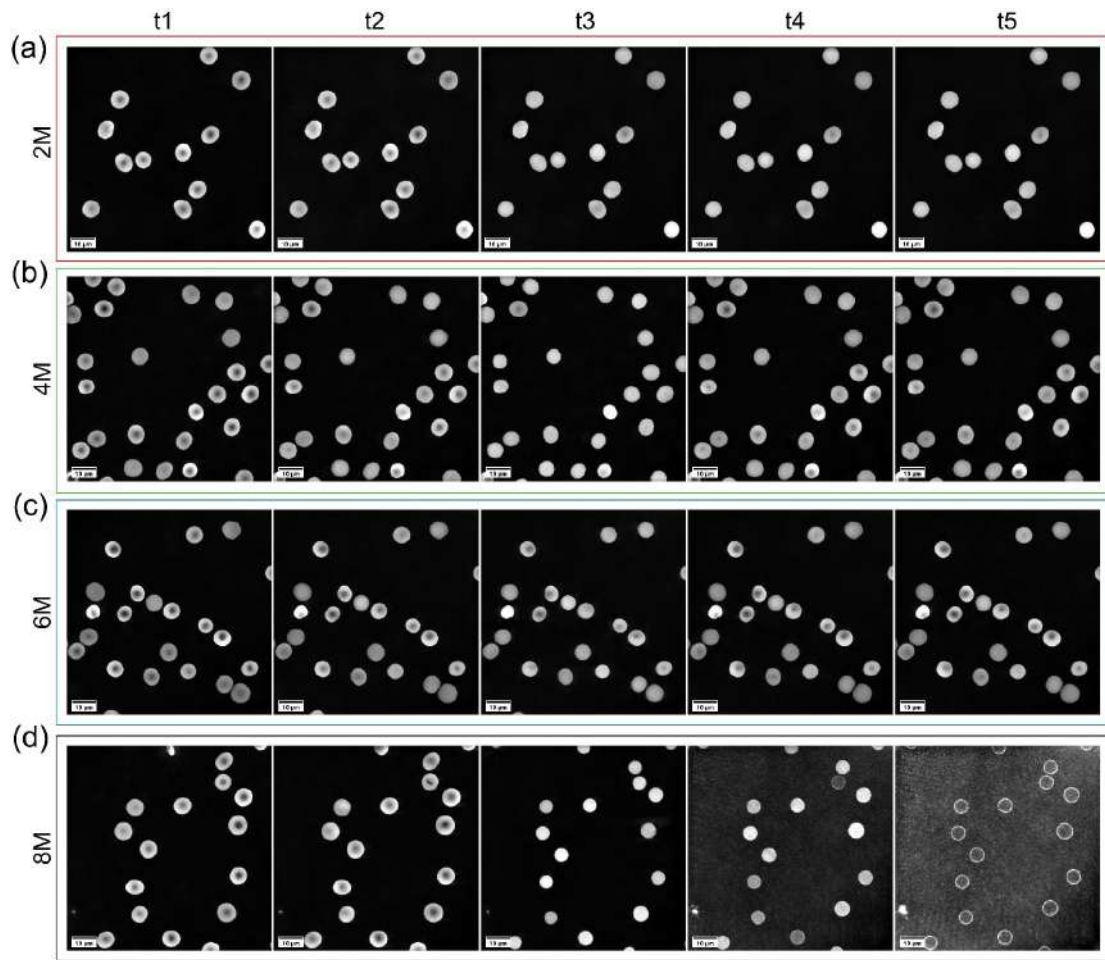


Figure A.7. 3D holo-tomographic imaging of RBCs treated with urea at varying concentrations, during a 10-minute time-lapse. (a) 3D RI tomograms of RBCs treated with 2M urea, resulting in mild spherocytosis (t1: 0 s; t2: 1:24 min, urea added; t3: 1:48 min; t4: 5:20 min; t5: 10 min). (b) 3D RI tomograms of RBCs treated with 4M urea, resulting in mild spherocytosis (t1: 0 s; t2: 1:02 min, urea added; t3: 1:26 min; t4: 4:58 min; t5: 10 min). (c) 3D RI tomograms of RBCs treated with 6M urea, resulting in mild spherocytosis (t1: 0 s; t2: 1:22 min, urea added; t3: 1:46 min; t4: 5:18 min; t5: 10 min). (d) 3D RI tomograms of RBCs treated with 8M urea, resulting in spherocytosis and cell lysis, with formation of ghost cells (t1: 0 s; t2: 48 s, urea added; t3: 1:08 min; t4: 2:20 min; t5: 10 min). (e-j) Quantification of time-dependent morphological parameters in urea-treated RBCs, (e) diameter, (f) surface area, (g) volume, (h) thickness, (i) sphericity and (j) Hb concentration (red = 2M; green = 4M; blue = 6M; black = 8M). Field of view 90x90x30 μm .

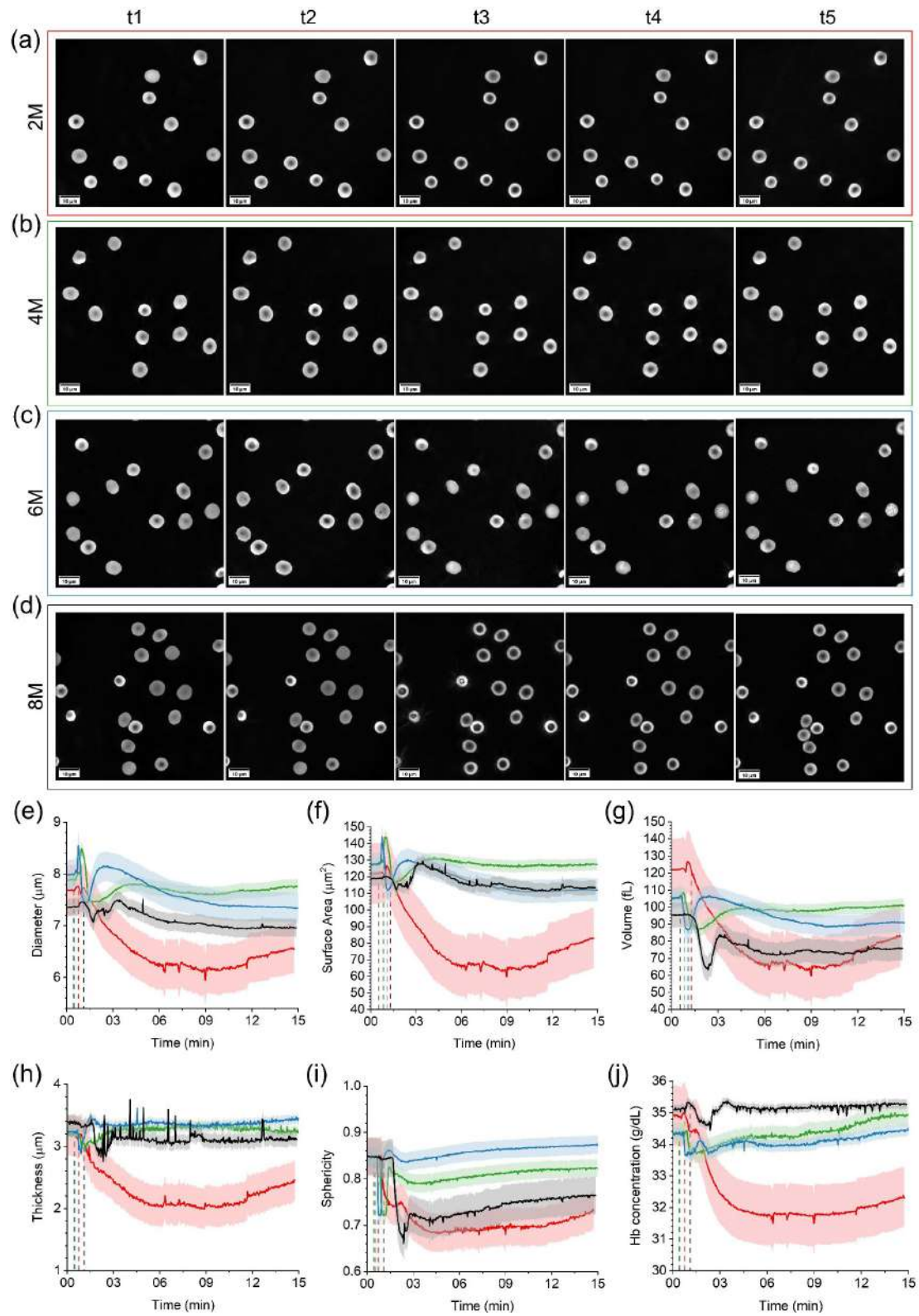


Figure A.8. 3D holo-tomographic imaging of RBCs treated with H₂O₂ at varying concentrations, during a 10-minute time-lapse. (a) 3D RI tomograms of RBCs treated with 2M H₂O₂, resulting in mild stomatocytosis (t1: 0 s; t2: 1:02 min, H₂O₂ added; t3: 1:48 min; t4: 7:44 min; t5: 15 min). (b) 3D RI tomograms of RBCs treated with 4M H₂O₂, resulting in mild stomatocytosis (t1: 0 s; t2: 54 s, H₂O₂ added; t3: 1:34 min; t4: 6:34 min; t5: 15 min). (c) 3D RI tomograms of RBCs treated with 6M H₂O₂, resulting in mild stomatocytosis (t1: 0 s; t2: 44 s, H₂O₂ added; t3: 1:28 min; t4: 6:24 min; t5: 15 min). (d) 3D RI tomograms of RBCs treated with 8M H₂O₂, resulting in more pronounced stomatocytosis (t1: 0 s; t2: 1:40 min, H₂O₂ added; t3: 2:20 min; t4: 7:20 min; t5: 15 min). (e-j) Quantification of time-dependent morphological parameters in urea-treated RBCs, (e) diameter, (f) surface area, (g) volume, (h) thickness, (i) sphericity and (j) Hb concentration (red = 2M; green = 4M; blue = 6M; black = 8M). Field of view 90x90x30 μ m.

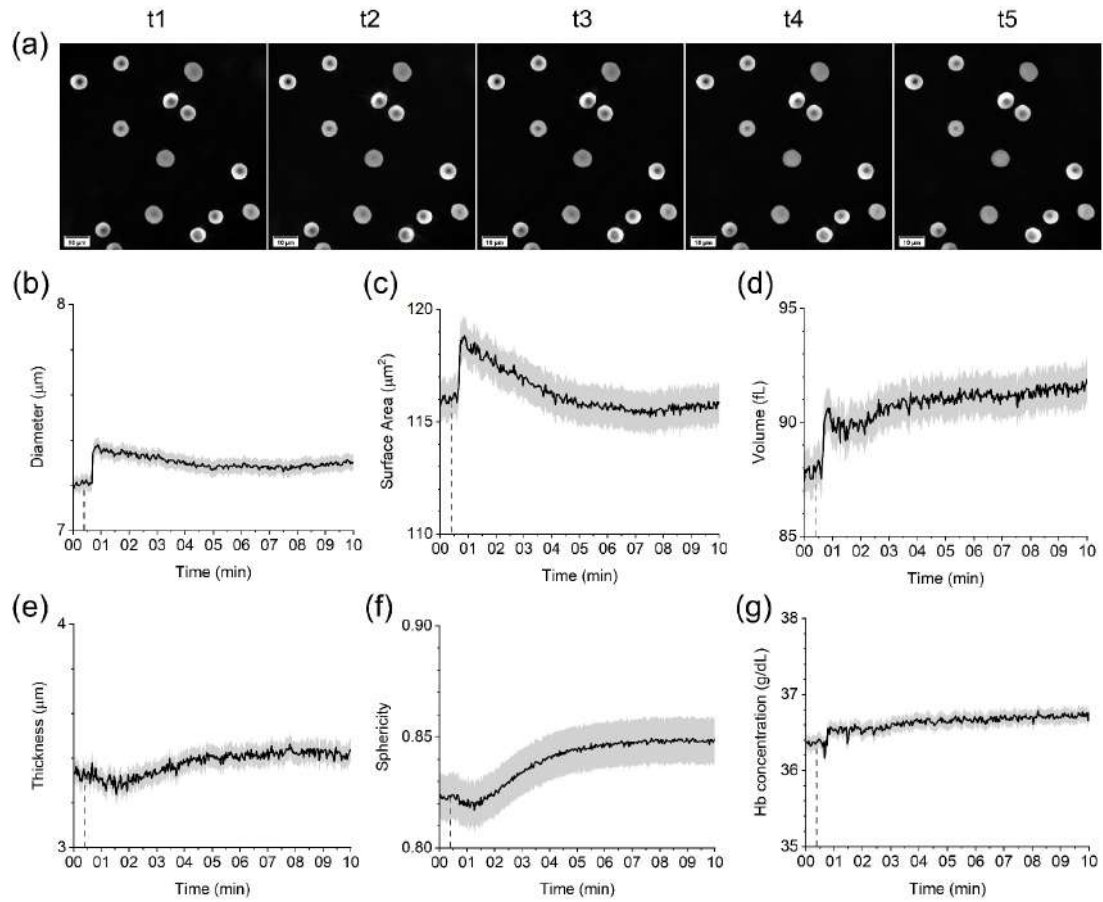


Figure A.9. 3D holo-tomographic imaging of RBCs treated with ddH₂O, during a 10-minute time-lapse. (a) 3D RI tomograms of RBCs treated with ddH₂O, resulting in no morphological alteration (t1: 0 s; t2: 44 s, ddH₂O added; t3: 1:04 min; t4: 4:00 min; t5: 10 min). (b-g) Quantification of time-dependent morphological parameters in urea-treated RBCs, (b) diameter, (c) surface area, (d) volume, (e) thickness, (f) sphericity and (g) Hb concentration. Field of view 90x90x30 μm .

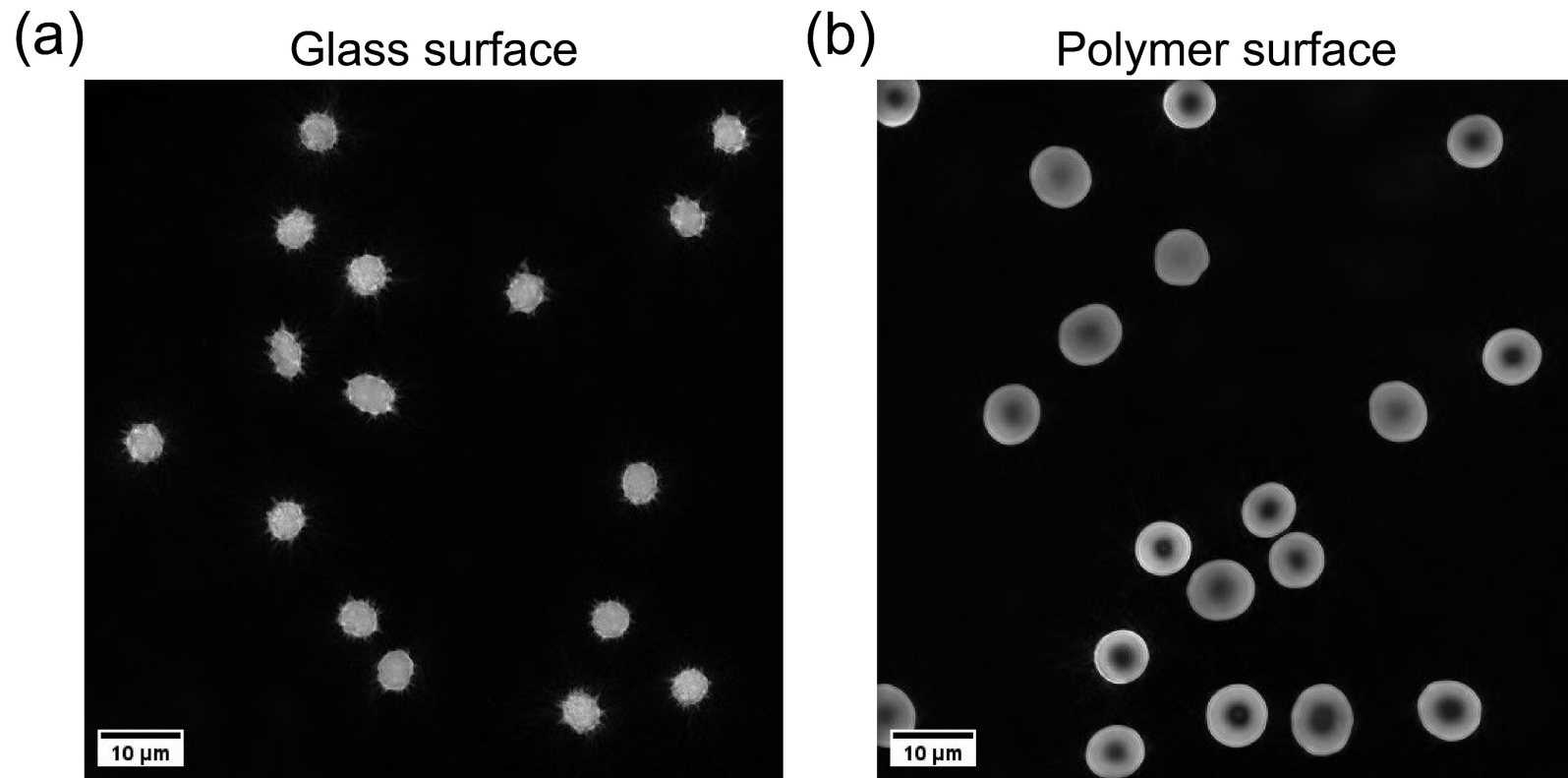


Figure A.10. Effect of petri dish surface used to image blood solutions with DHTM. (a) Echinocytosis resulting from RBCs contact with a glass surface. (b) Polymer-coated surface resulting in unaltered RBC morphology.

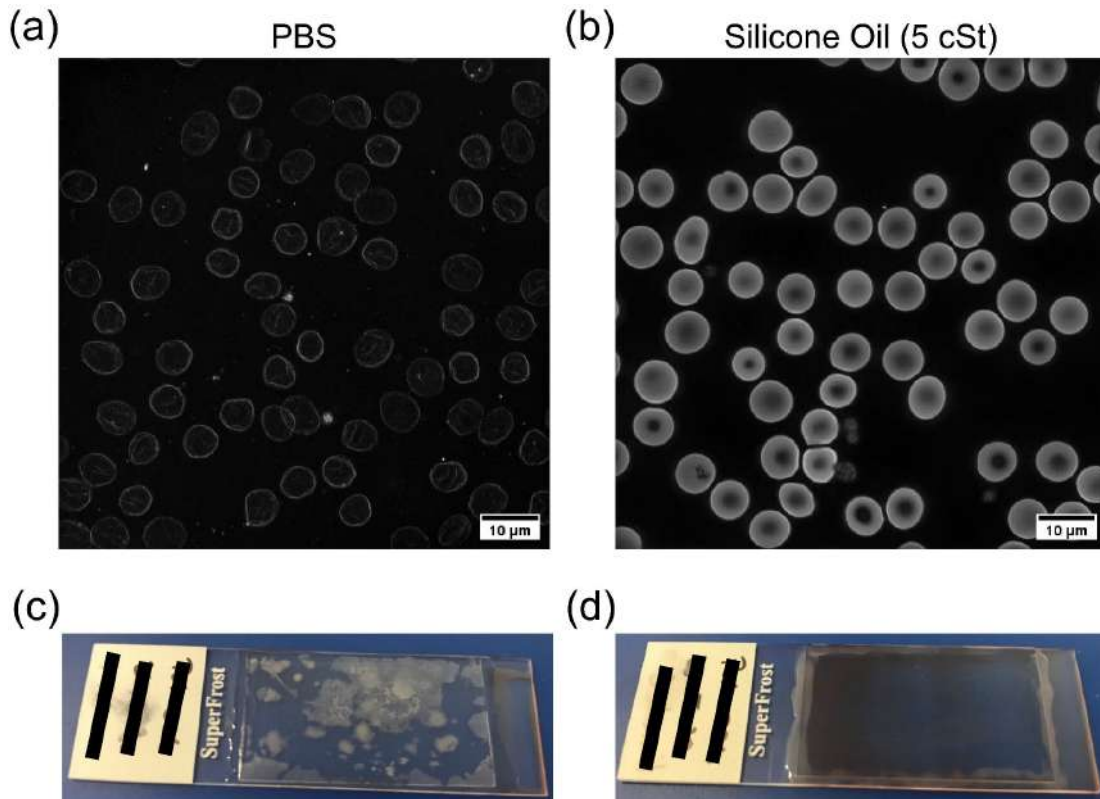


Figure A.11. Comparison between PBS and silicone oil (5 cSt) coating for optimal blood smear imaging with DHTM. (a) RI tomogram of healthy RBCs from a blood smear coated with PBS. (b) RI tomogram of healthy RBCs from a blood smear coated with silicone oil (5 cSt). (c) Example of storage artifacts in a blood smear coated with PBS and sealed with a coverslip and nail varnish after 4 days storage at room temperature. (d) Example of absence of storage artifacts in a blood smear coated with silicone oil (5 cSt) and sealed with a coverslip and nail varnish after 4 days storage at room temperature.

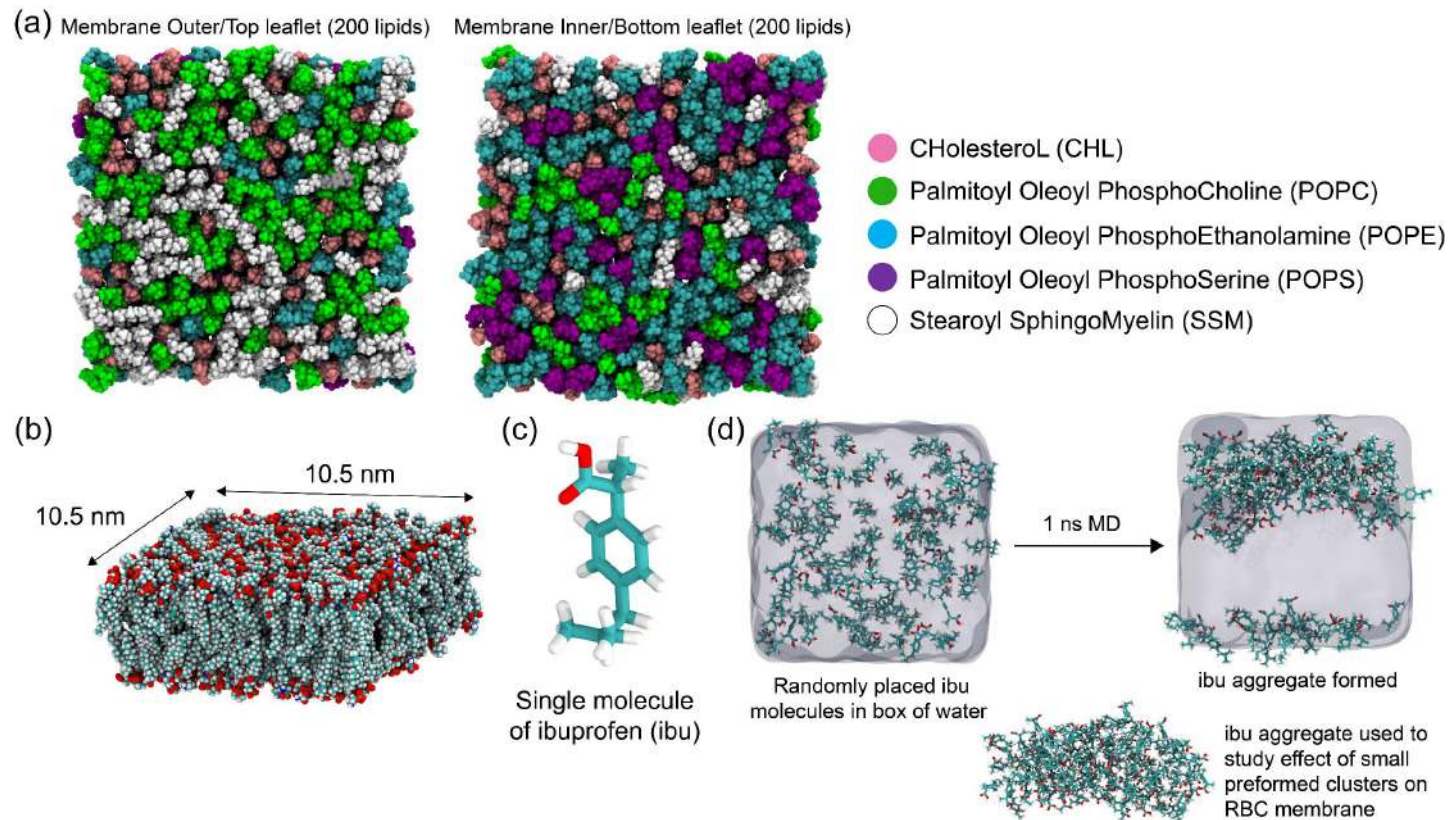


Figure A.12. (a) Model RBC lipid bilayer composition at the outer/top and inner/bottom leaflets used in this study also showing the (b) membrane dimensions in the xy-plane. (c) Stick representation of a single molecule of ibuprofen (ibu). (d) Preformed aggregates of ibuprofen molecules (at low concentration) obtained in this study from 1 ns dynamics in explicit water.

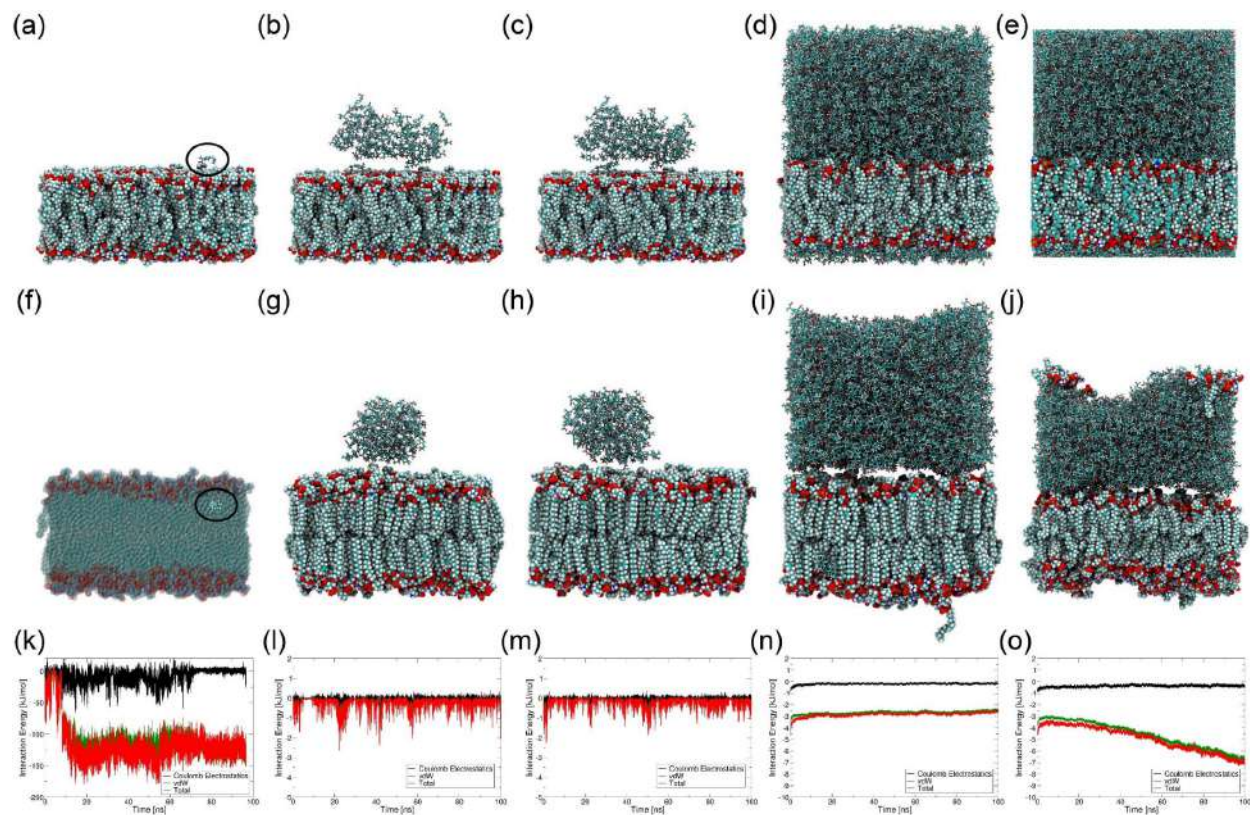


Figure A.13. (a-e) Initial and (f-j) final snapshots of (a, f) single ibuprofen molecule, aggregates of (b, g) 80 ibuprofen molecules, (c, h) 100 ibuprofen molecules, densely packed (d, i) 1903 ibuprofen molecules under NPT conditions, and (e, j) 1903 ibuprofen molecules under NVT conditions. (k-o) Ibuprofen–membrane interaction energies and their Coulombic electrostatic and van der Waals (vdW) components for all systems modelled in this study.

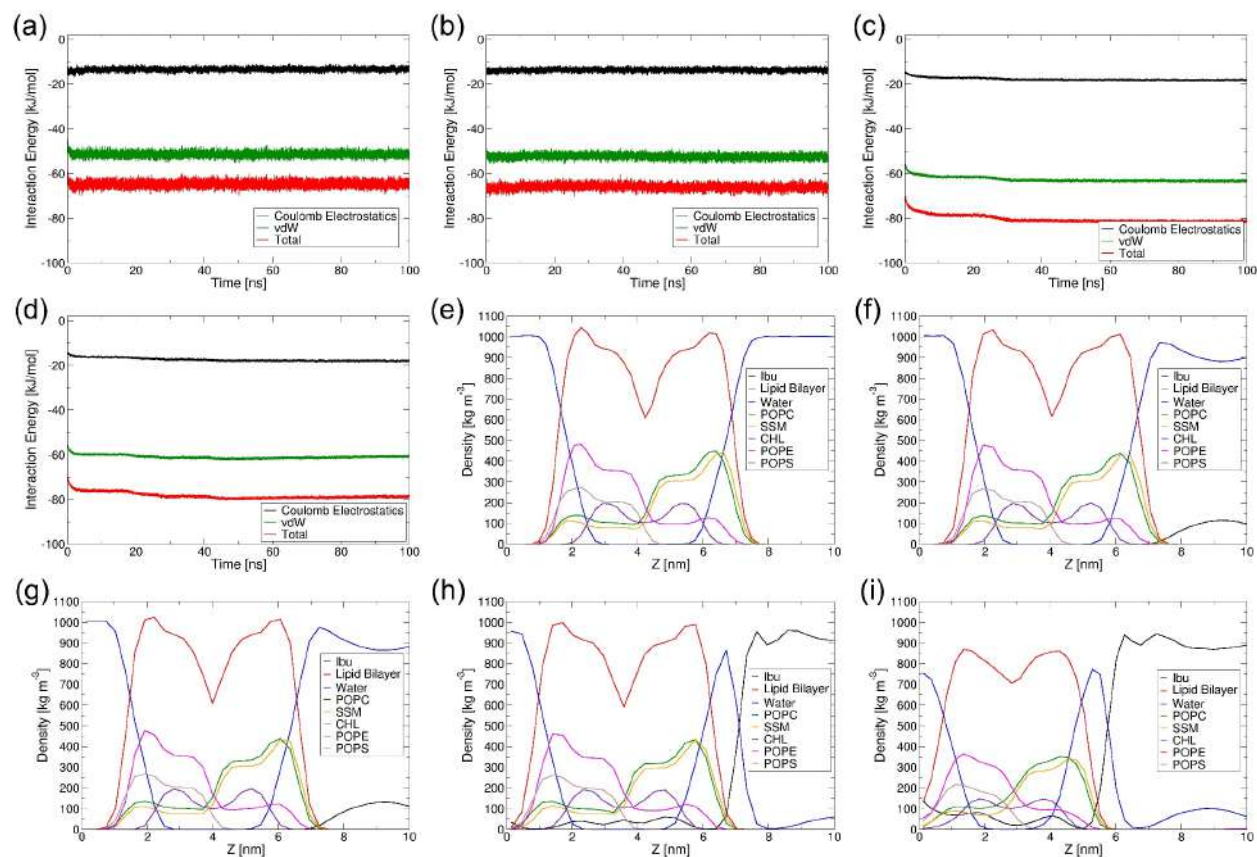


Figure A.14. Ibuprofen–ibuprofen interaction energies and their electrostatic and vdW components for (a) low conc. I, (b) low conc. II, (c) high conc. I, and (d) high conc. II (see Appendix to Chapter 3 A.1.2 for these definitions). (e-i) Average density profiles of all species in the simulation box for all systems used in this study.

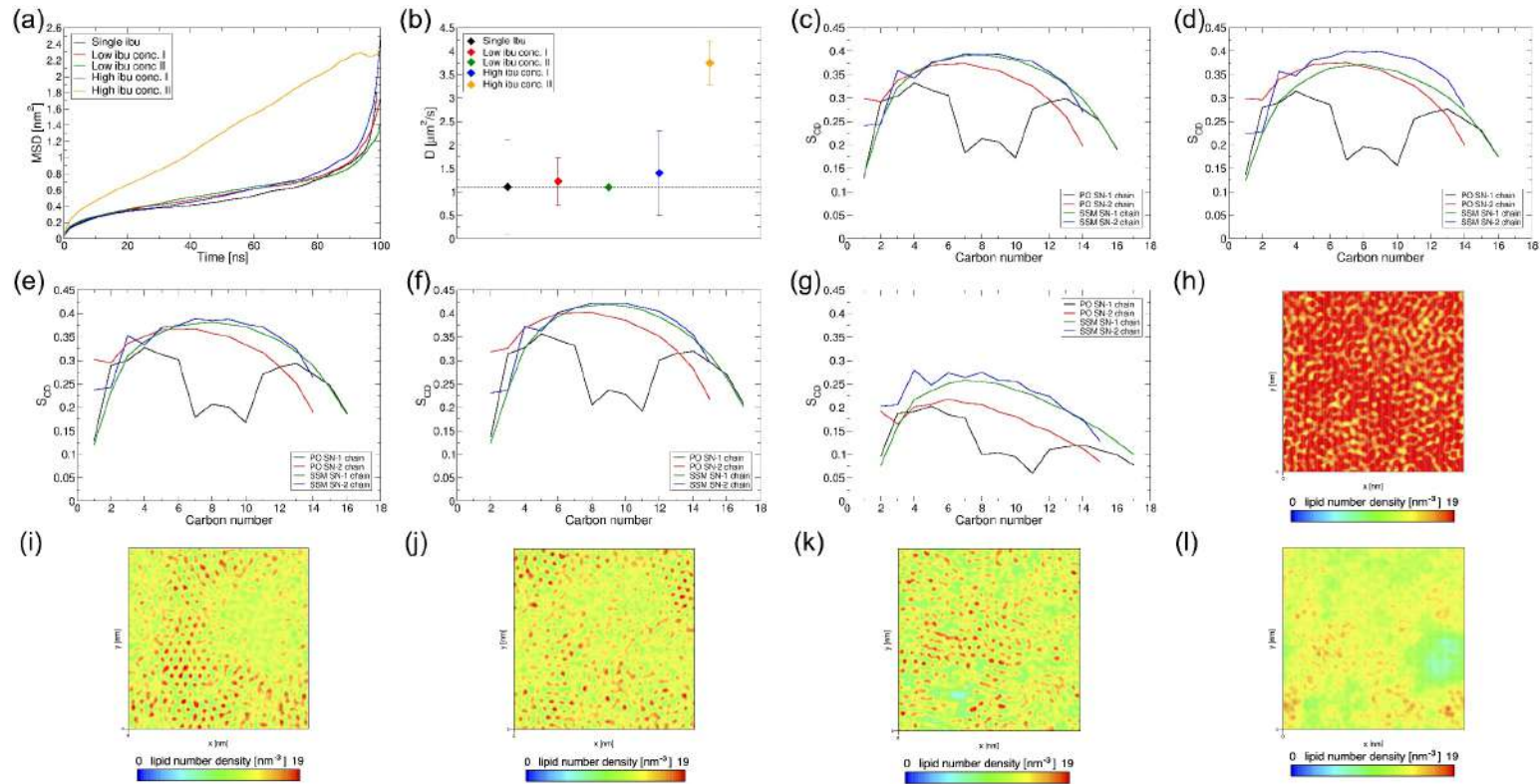


Figure A.15. Comparison of (a) Mean Square Displacement (MSD) and (b) diffusion coefficient, D for all systems modelled in this study. (c-g) Lipid hydrocarbon tail deuterium order parameter (SCD) for RBC membrane lipids (Palmitoyl Oleoyl and Stearoyl) with two acyl chains, SN-1 and SN-2, and (h-l) lipid heavy atoms number densities in the xy -plane averaged over the z -axis to obtain a top view of lipid densities in the membrane for all systems.

Table A.1. Summary of the demographics of the healthy blood and SCT and SCA RBC samples.

	Gender	Age	Ethnicity
Healthy	F	27	Caucasian
SCT	M	34	Caucasian
SCA	F	28	African American

Table A.2. Overview of the total number of analyzed RBCs for the healthy, SCT and SCA samples and the percentages of each RBC type that was present in each sample.

	Total number of cells	RBC type								
		Normocyte	Stomatocyte	Echinocyte	Helmet	Acanthocyte	Spherocyte	Sickle	Ovalocyte	Teardrop
Healthy	351	272 (77.5%)	77 (21.9%)	1 (0.3%)	1 (0.3%)	0 (0%)	0 (0%)	0 (0%)	0 (0%)	0 (0%)
SCT	459	71 (15.5%)	0 (0%)	306 (66.7%)	1 (0.2%)	55 (12%)	25 (5.4%)	1 (0.2%)	0 (0%)	0 (0%)
SCA	230	62 (27%)	2 (0.9%)	122 (53%)	0 (0%)	23 (10%)	1 (0.4%)	10 (4.3%)	9 (4%)	1 (0.4%)

Table A.3. Description of the extracted morphological parameters from Imaris 9.7.

Morphological Parameter	Description
Diameter	The length of the longest principal axis inside the object (<i>BoundingBoxOO Length C</i>)
Surface Area	The sum of the triangle surfaces
Volume	Quantification of how much a surface object occupies
S/V Ratio	Surface area divided by the volume
Thickness	The length of the shortest principal axis (<i>BoundingBoxOO Length A</i>)
Sphericity	The ratio of the surface area of a sphere to the surface area of the particle
Mean RI	Mean intensity of voxels enclosed within the surface

Table A.4. Composition of RBC membrane lipid bilayer molecular model. CHL = Cholesterol, POPC = Palmitoyl Oleoyl PhosphoCholine, POPE = Palmitoyl Oleoyl PhosphoEthanolamine, POPS = Palmitoyl Oleoyl PhosphoSerine, and SSM = Stearoyl SphingoMyelin.

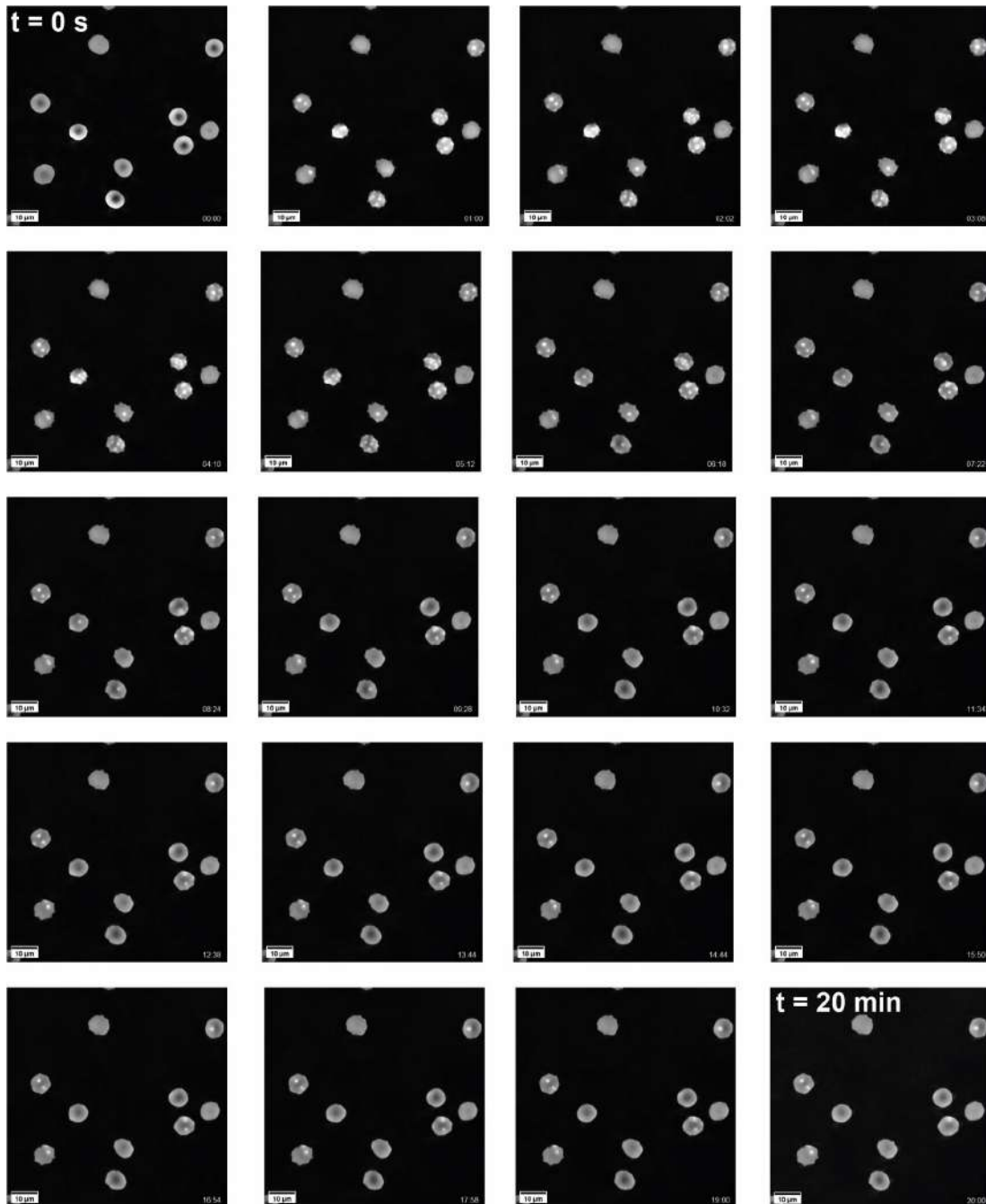
	CHL	POPC	POPE	POPS	SSM
Inner leaflet	40 (20%)	22 (11%)	76 (38%)	44 (22%)	18 (9%)
Outer leaflet	40 (20%)	70 (35%)	20 (10%)	0 (0%)	70 (35%)

Table A.5. Overview of the ibuprofen concentrations and the corresponding ibuprofen dosage and ibuprofen plasma concentration.

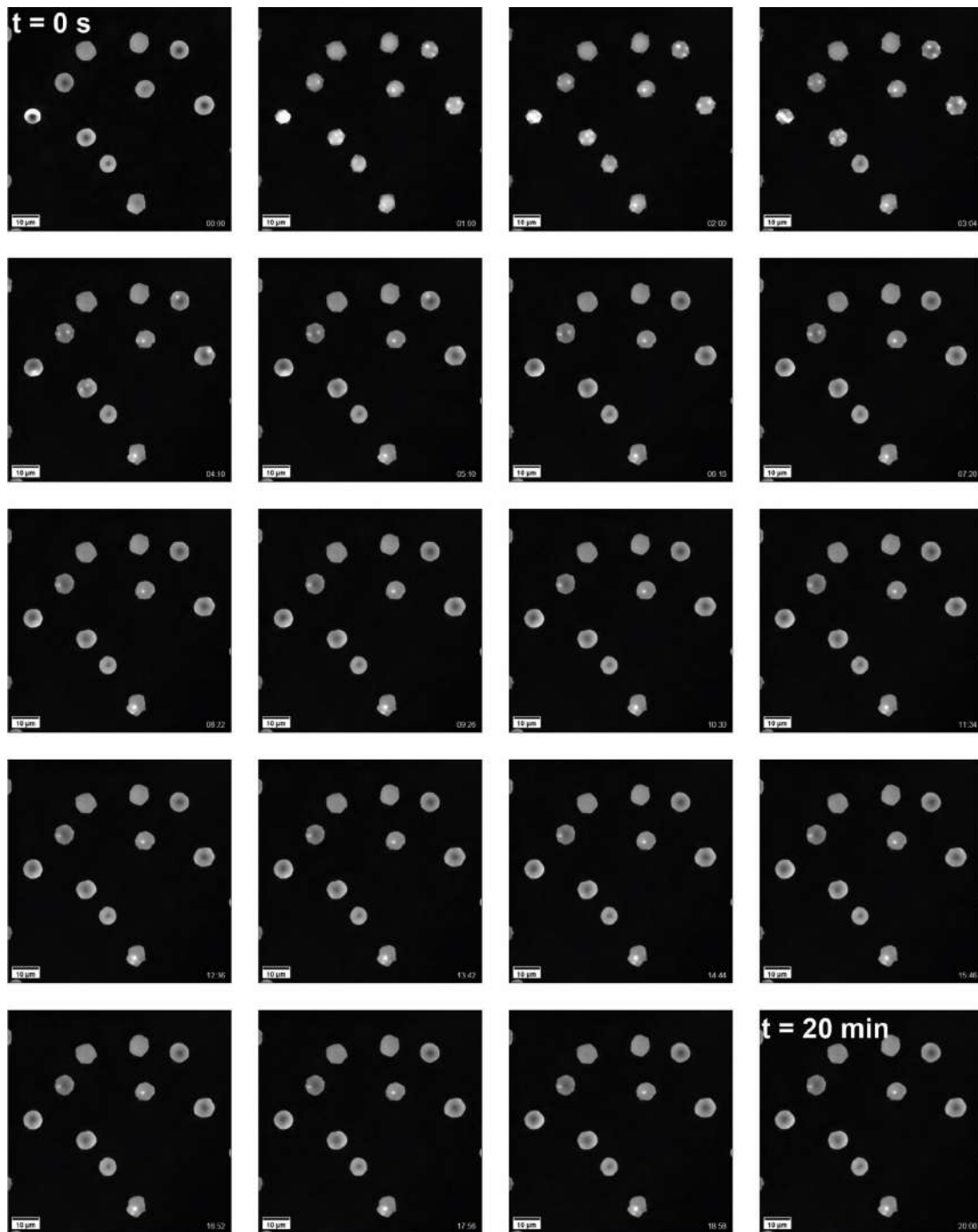
	Ibuprofen concentration				
	0.25 mM	0.5 mM	1 mM	1.5 mM	3 mM
Ibuprofen dosage	200 mg	400 mg	800 mg	1200 mg	2400 mg
Ibuprofen plasma concentration	51 µg/mL	103 µg/mL	205 µg/mL	308 µg/mL	615 µg/mL

Table A.6. Overview of the total number of analyzed RBCs for each ibuprofen concentration (0.25 mM, 0.5 mM, 1 mM, 1.5 mM and 3 mM), during a 20-minute time-lapse.

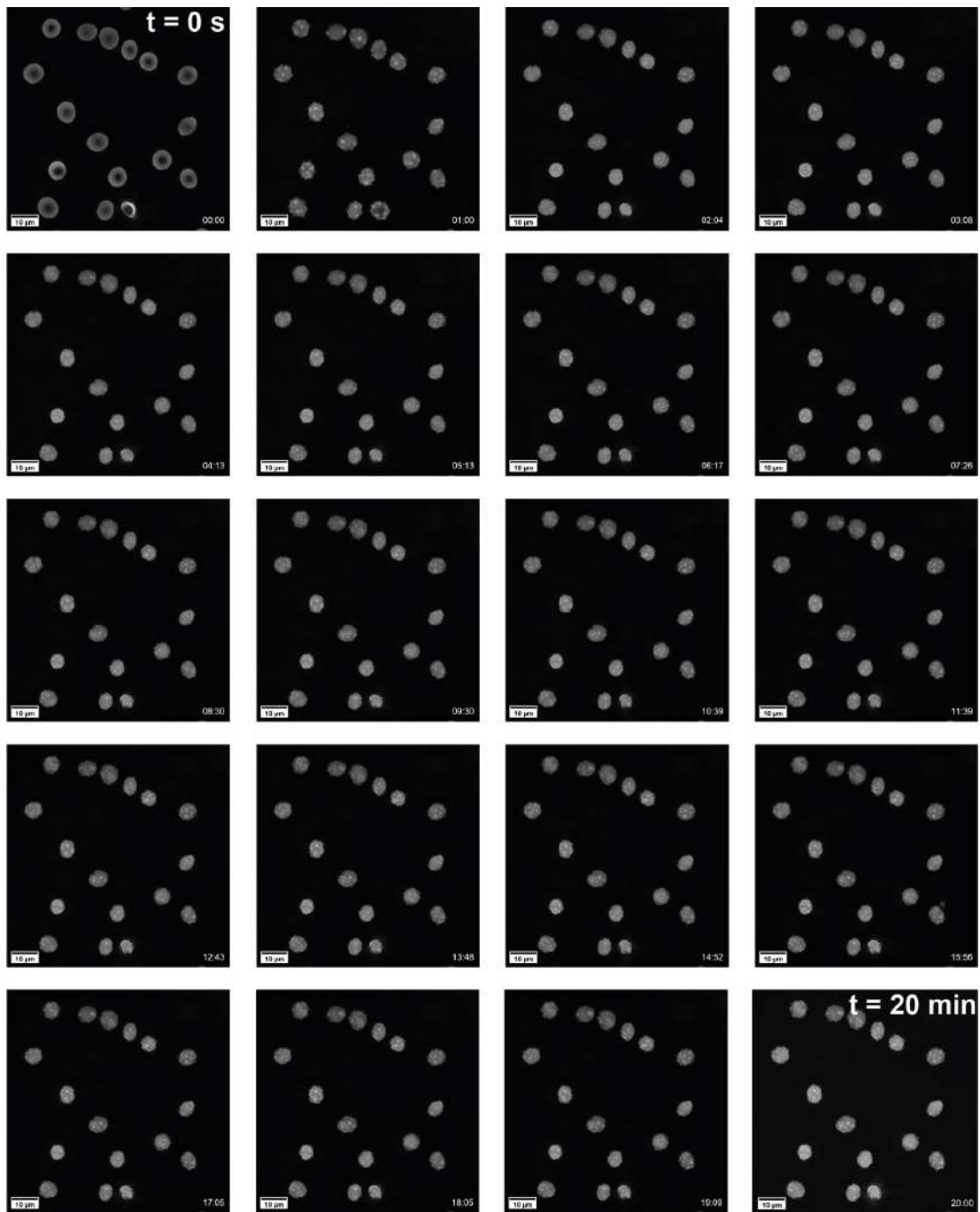
		Field of view 1	Field of view 2	Total
Ibuprofen concentration	0.25 mM	10	16	26
	0.5 mM	10	13	23
	1 mM	17	14	31
	1.5 mM	12	14	26
	3 mM	11	18	29



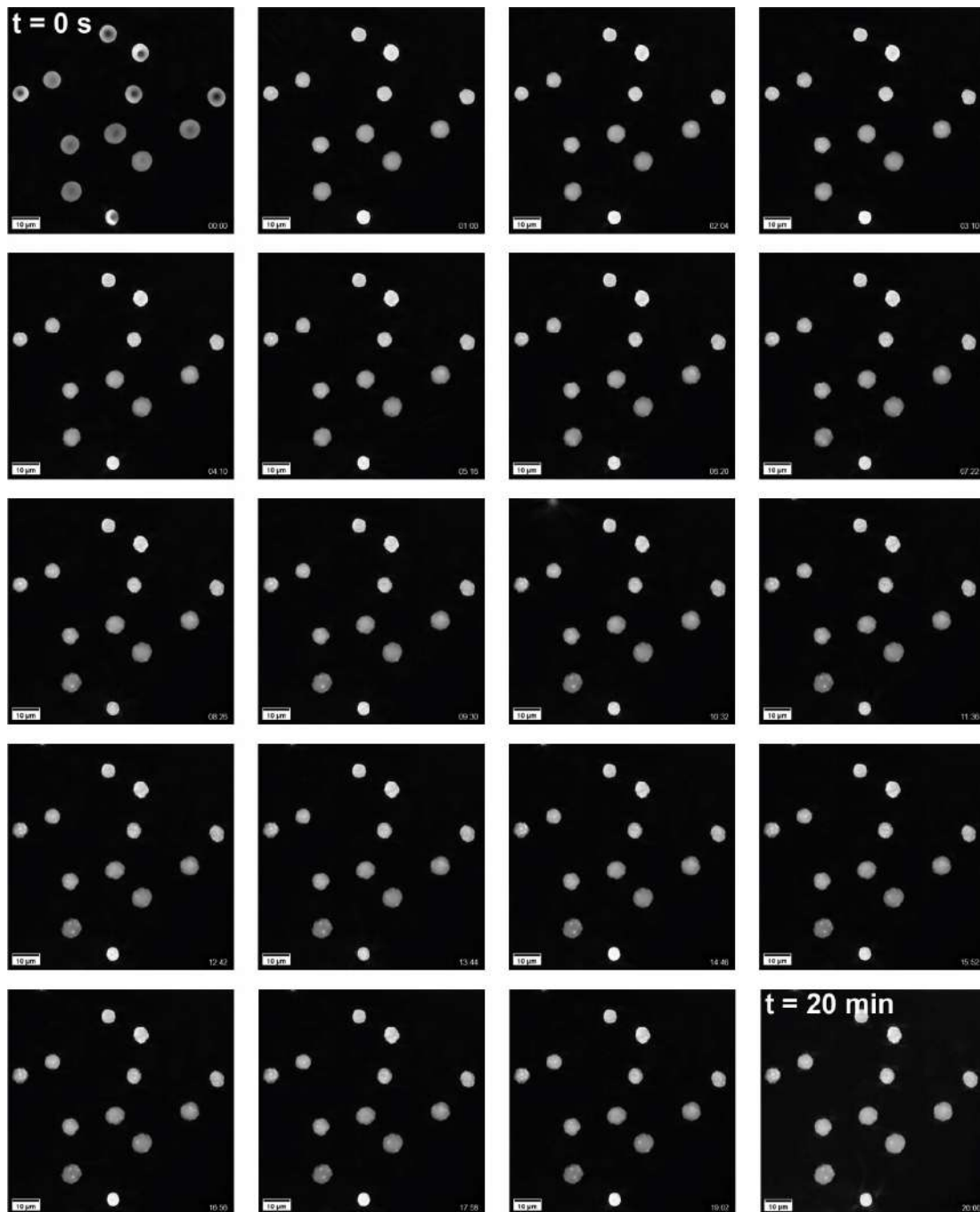
Movie A.1. Effect of 0.25 mM ibuprofen on RBCs. RI tomograms were acquired at 2 sec intervals over a period of 20 min. 3D renderings of extracted frames from the video are provided in Figure 3.4(a). Timecode is min:sec.



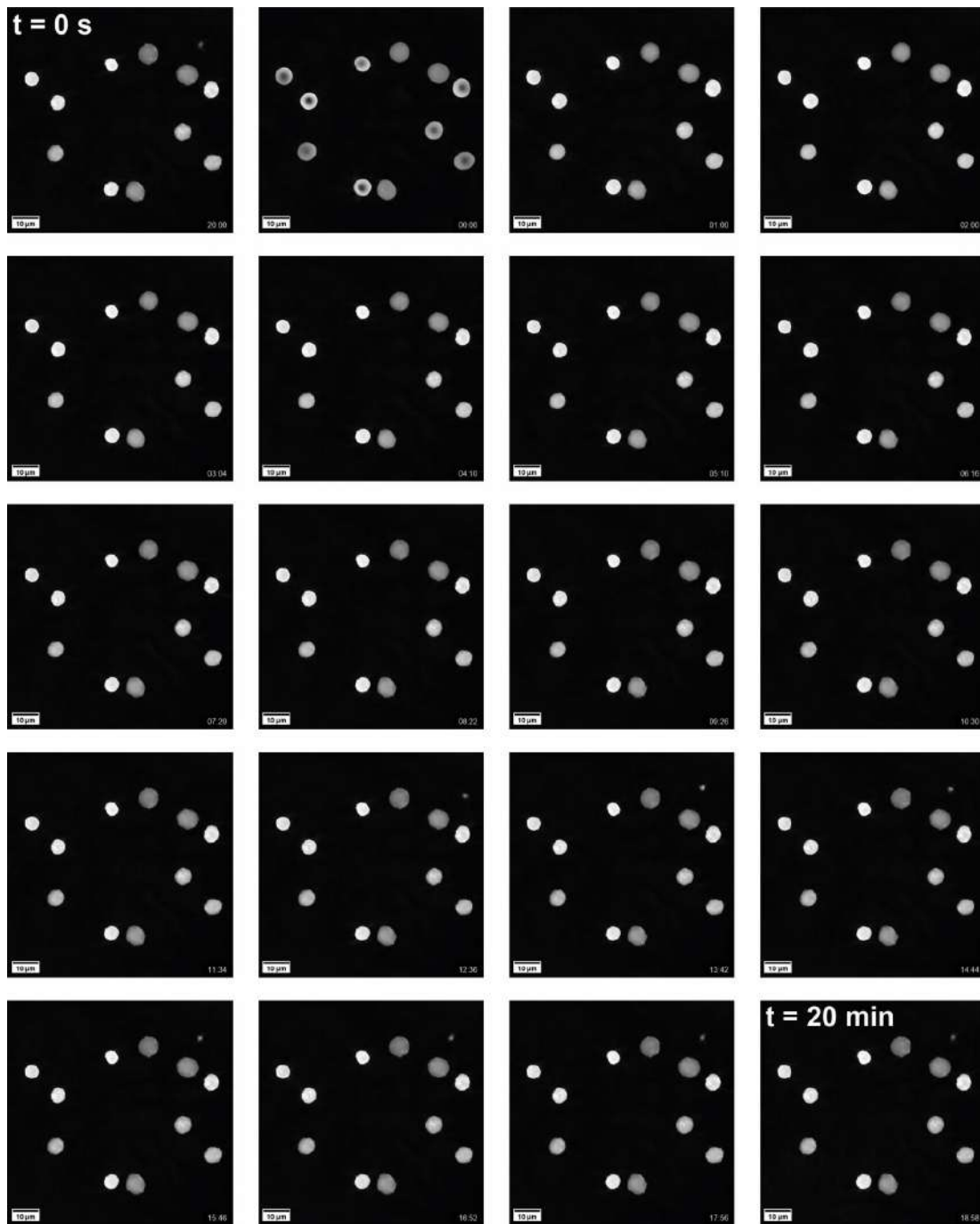
Movie A.2. Effect of 0.5 mM ibuprofen on RBCs. RI tomograms were acquired at 2 sec intervals over a period of 20 min. 3D renderings of extracted frames from the video are provided in Figure 3.4(b). Timecode is min:sec.



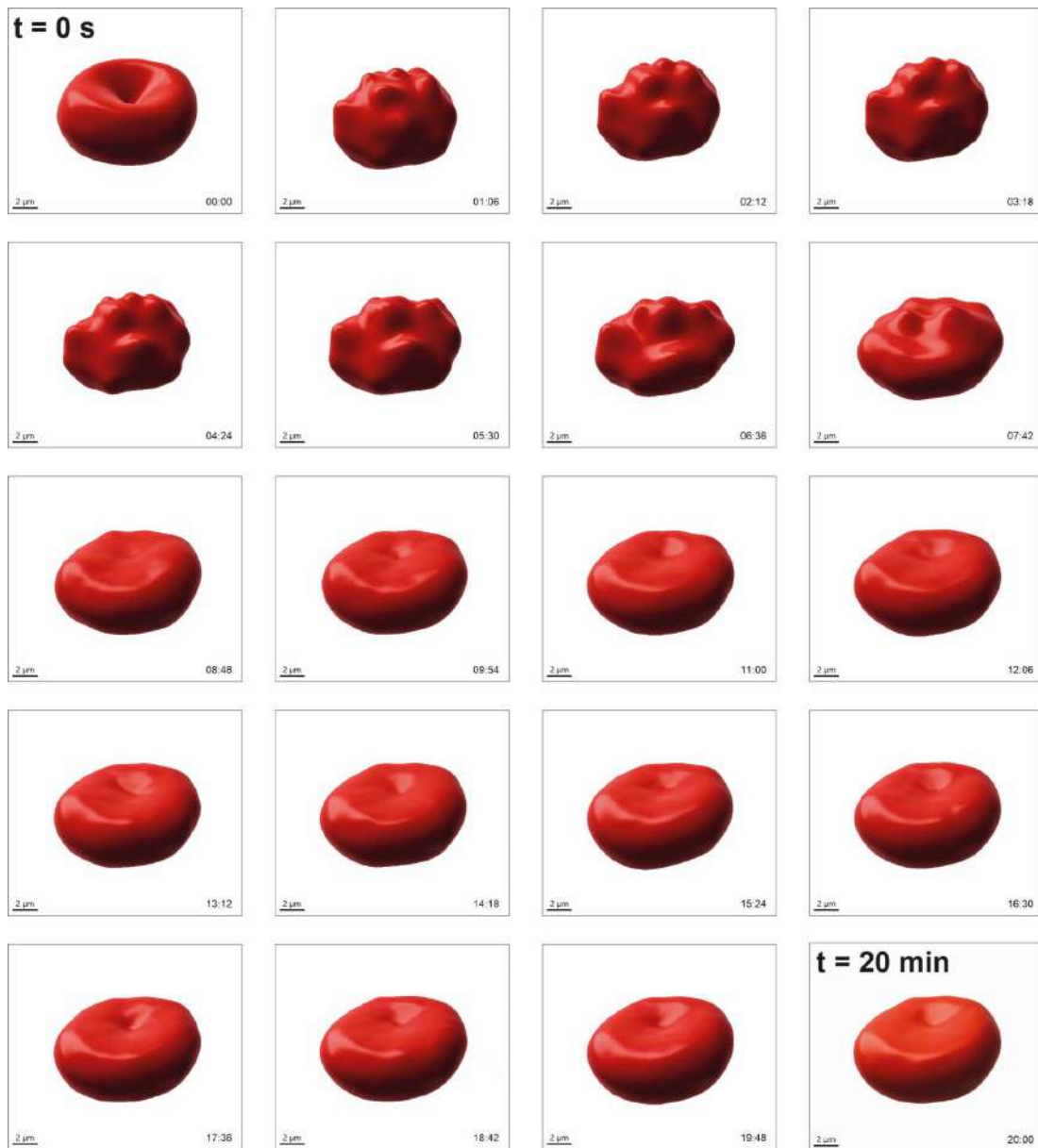
Movie A.3. Effect of 1 mM ibuprofen on RBCs. RI tomograms were acquired at 2 sec intervals over a period of 20 min. 3D renderings of extracted frames from the video are provided in Figure 3.4(c). Timecode is min:sec.



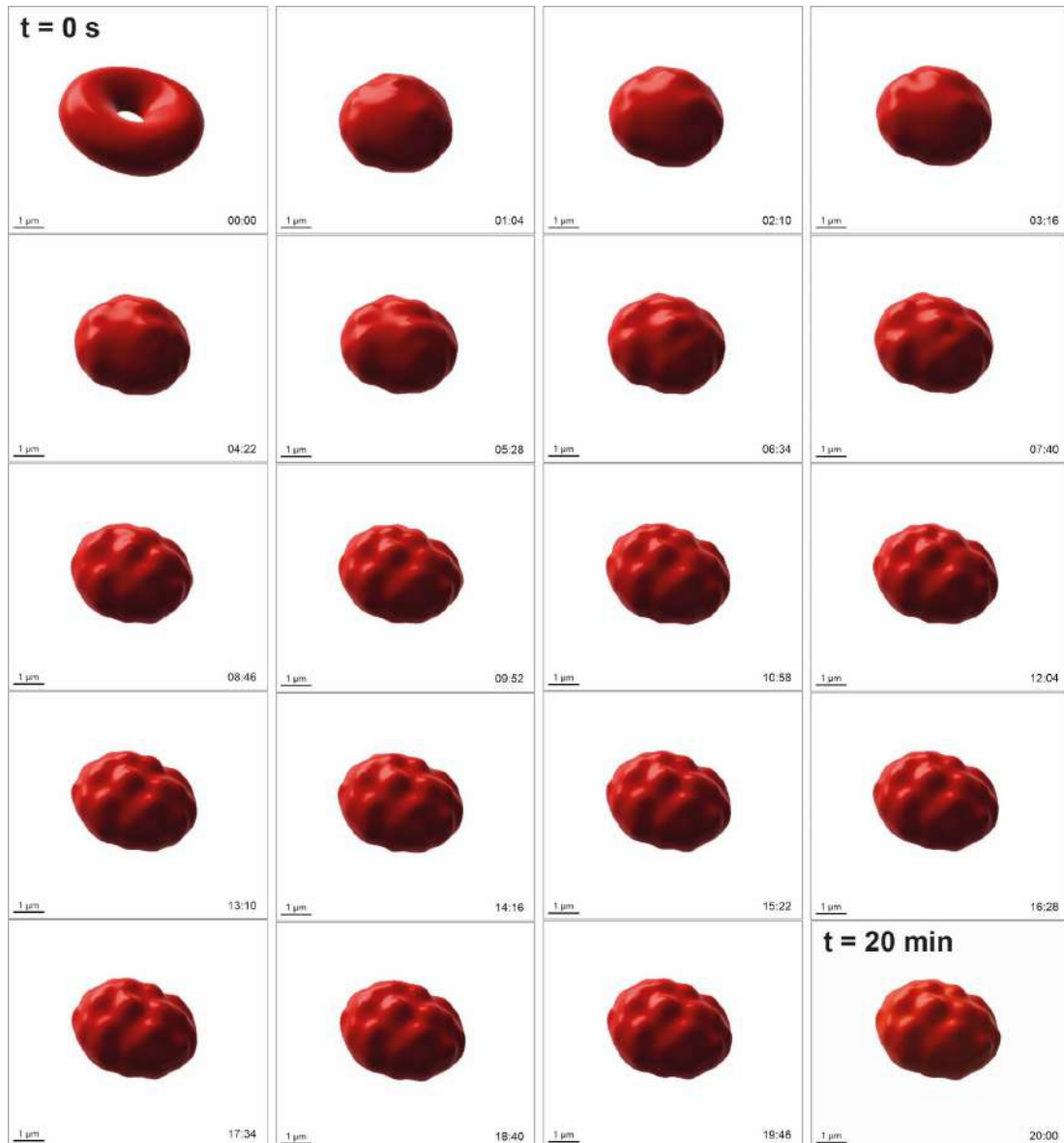
Movie A.4. Effect of 1.5 mM ibuprofen on RBCs. RI tomograms were acquired at 2 sec intervals over a period of 20 min. 3D renderings of extracted frames from the video are provided in Figure 3.4(d). Timecode is min:sec.



Movie A.5. Effect of 3 mM ibuprofen on RBCs. RI tomograms were acquired at 2 sec intervals over a period of 20 min. 3D renderings of extracted frames from the video are provided in Figure 3.4(e). Timecode is min:sec.



Movie A.6. 3D segmented rendering of a single RBC exposed to low (0.25 mM) ibuprofen concentration and measured with DHTM, showing transient spicule formation, movement and dissolution across the RBC membrane. Timecode is min:sec.



Movie A.7. 3D segmented rendering of a single RBC exposed to high (1.5 mM) ibuprofen concentration and measured with DHTM, showing irreversible spicule formation and movement across the RBC membrane. Timecode is min:sec.

B. Appendix to Chapter 4

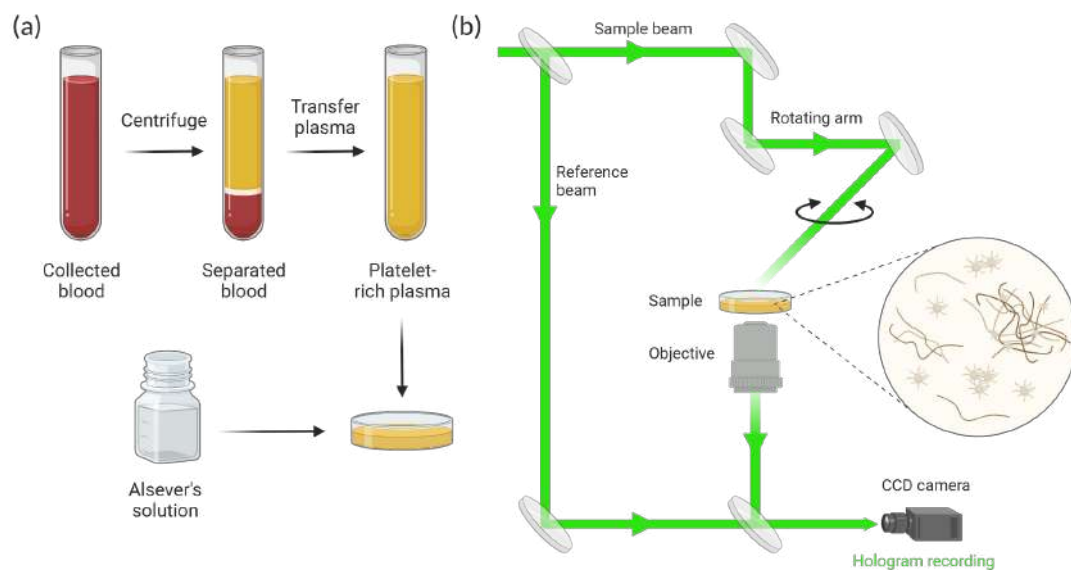


Figure B.1. Sample preparation procedure and principle of DHTM for plasma imaging. (a) Plasma was obtained after blood collection in K2EDTA vacutainers and centrifugation in order to separate each blood component. 50 μL of plasma is diluted in Alsever's solution at a final concentration of 1:5. 250 μL of plasma solution is transferred to a petri dish for imaging. (b) Digital holotomographic microscopy uses a low-power laser beam ($\lambda = 520 \text{ nm}$) that splits into the reference and the sample laser beams before rejoining below the objective (60x, NA = 0.8), where the interference (hologram) is recorded. A rotational arm, located above the sample holder, rotates 360° around the sample at a 45° angle in order to obtain a 3D refractive index (RI) map. The presence of microclots and platelet pathology can be detected in a label-free manner from the 3D RI tomograms.

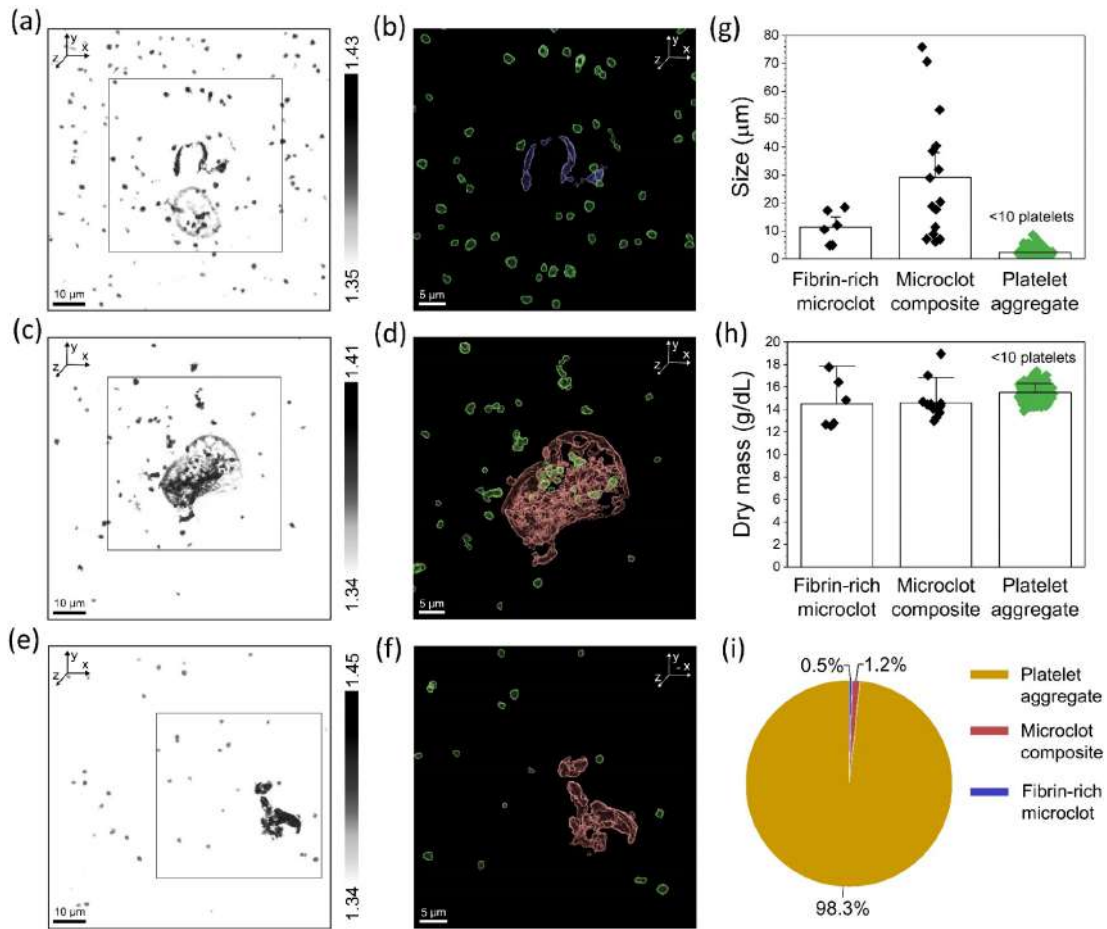


Figure B.2. Structural analysis of microclots in plasma of a COVID-19 positive patient without clinical symptomatology (PLS-CVDP3). (a) Refractive index (RI) tomogram of a fibrin-rich microclot in plasma. (b) Corresponding segmented RI tomogram of the fibrin-rich microclot from the inset in (a). (c) RI tomogram of a microclot composite and platelet aggregates in plasma. (d) Corresponding segmented RI tomogram of the microclot composite and platelet aggregates from the inset in (c). (e) RI tomogram of a microclot composite in plasma. (f) Corresponding segmented RI tomogram of the microclot composite from the inset in (e). (g-h) Size and dry mass of fibrin-rich microclots, microclot composite structures and platelet aggregates (<10 platelets) in plasma. Error bars represent the standard deviation from the mean. (i) Pie chart showing the microclot composition in plasma of donor PLS-CVDP3.

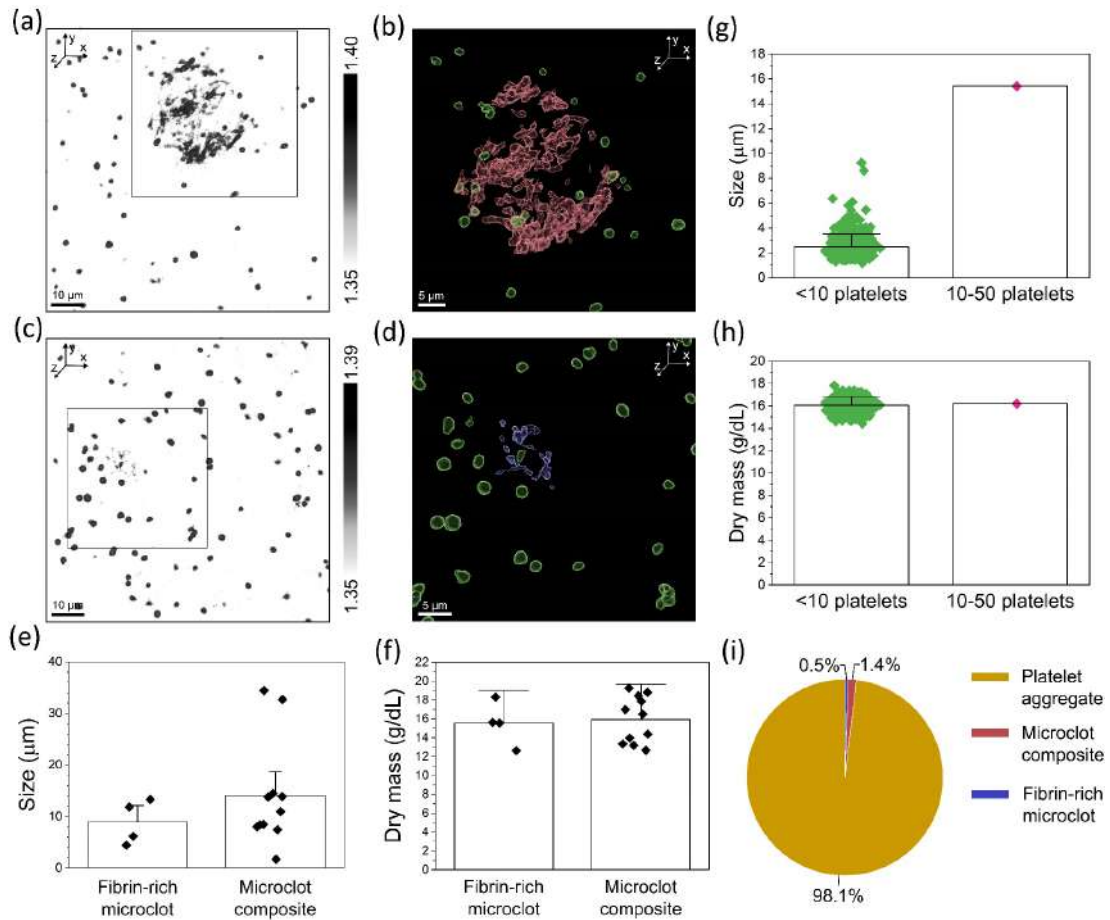


Figure B.3. Structural analysis of microclots in plasma of a COVID-19 recovered patient with moderate symptomatology (PLS-CVDR1). (a) Refractive index (RI) tomogram of a microclot composite and platelet aggregates in plasma. (b) Corresponding segmented RI tomogram of the microclot composite and platelet aggregates from the inset in (a). (c) RI tomogram of a fibrin-rich microclot and platelet aggregates in plasma. (d) Corresponding segmented RI tomogram of the fibrin-rich microclot and platelet aggregates from the inset in (c). (e-f) Size and dry mass of fibrin-rich microclots and microclot composite structures in plasma. (g-h) Size and dry mass of platelet aggregates in plasma. Error bars represent the standard deviation from the mean. (i) Pie chart showing the microclot composition in plasma of donor PLS-CVDR1.

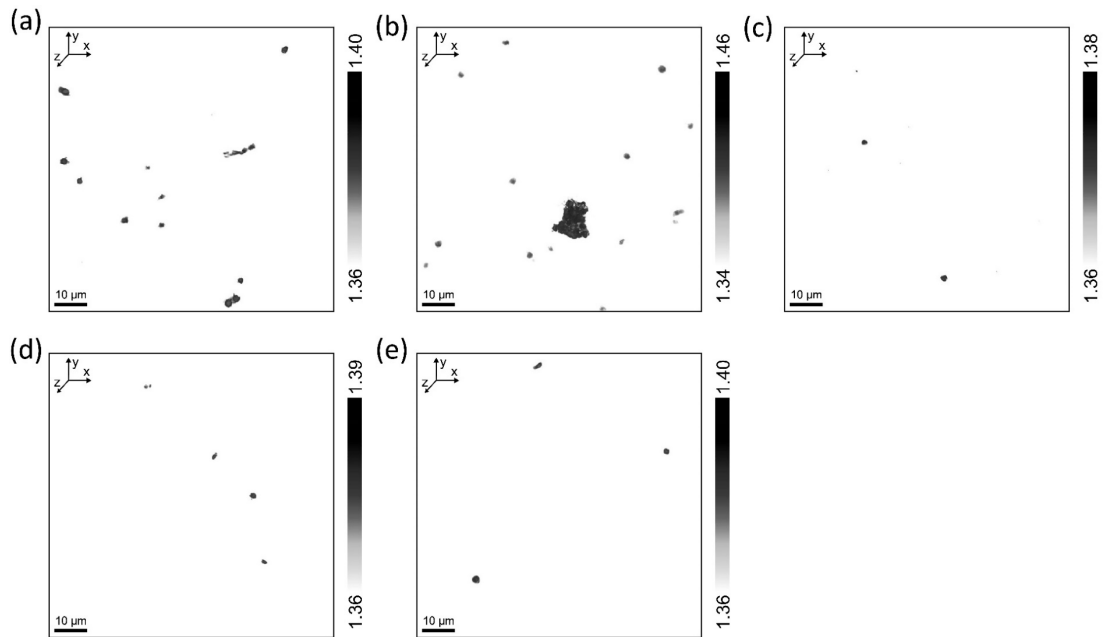


Figure B.4. DHTM tomograms of plasma of healthy controls (PLS-HC). (a) Refractive index (RI) tomogram of a small fibrin-rich microclot in PLS-HC1. (b) RI tomogram of a microclot composite in PLS-HC2. (c) RI tomogram showing individual platelets in PLS-HC3. (d) RI tomogram showing individual platelets in PLS-HC4. (e) RI tomogram showing individual platelets in PLS-HC5.

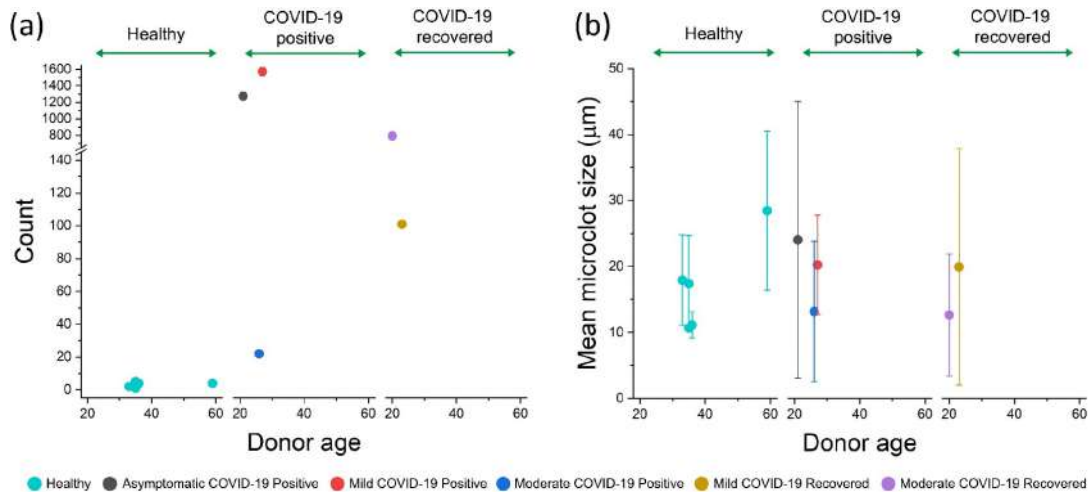


Figure B.5. Age dependence of microclot prevalence and morphology in healthy and COVID-19 positive and recovered patients. (a) Prevalence of microclots detected in 75 μL of plasma from healthy and COVID-19 positive and recovered patients plotted against the patient age and grouped by healthy and COVID-19 subphenotypes. (b) Mean microclot size of fibrin-rich microclots and microclot composites plotted against the patient age and grouped by healthy and COVID-19 subphenotypes.

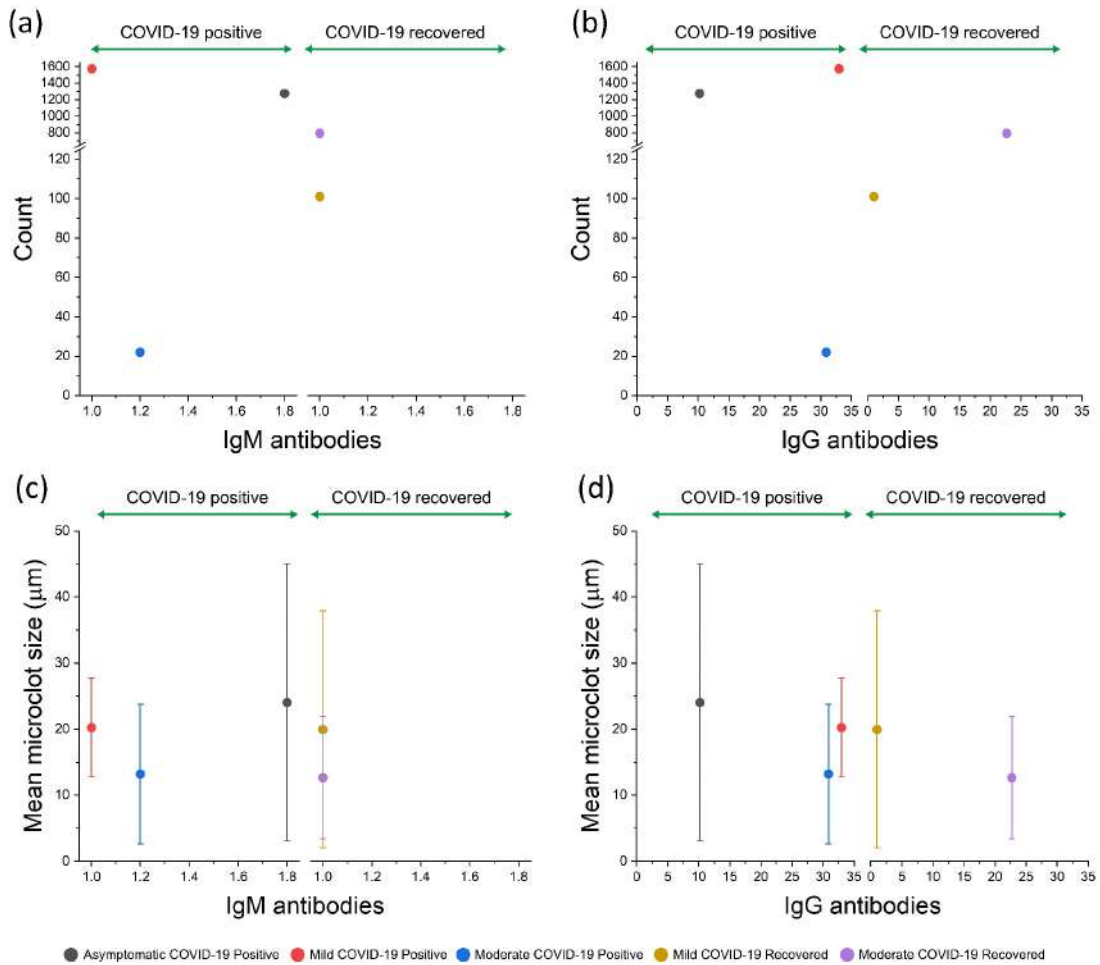


Figure B.6. IgM and IgG antibodies dependence of microclot prevalence and morphology in COVID-19 positive and recovered patients. (a) Prevalence of microclots detected in 75 μL of plasma from COVID-19 positive and recovered patients plotted against the IgM antibodies level and grouped by COVID-19 subphenotypes. (b) Prevalence of microclots detected in 75 μL of plasma from COVID-19 positive and recovered patients plotted against the IgG antibodies level and grouped by COVID-19 subphenotypes. (c) Mean microclot size of fibrin-rich microclots and microclot composites plotted against the IgM antibodies level and grouped by COVID-19 subphenotypes. (d) Mean microclot size of fibrin-rich microclots and microclot composites plotted against the IgG antibodies level and grouped by COVID-19 subphenotypes.

Table B.1. Summary of the demographics for the samples of the fixed blood clots in aqueous solution.

	Fixed blood clots	
	FC-HC	FC-CVD
Donor classification	Healthy	COVID-19 convalescent
Gender	F	F
Age	49	42
Ethnicity	African American	African American
Collection date	-	15/09/2021

B. Appendix to Chapter 4

Table B.2. Summary of the demographics, SARS-coV-2 serology test results (IgM and IgG antibodies), symptomatology and sample collection details for healthy and COVID-19 plasma samples.

	Plasma									
	PLS-HC1	PLS-HC2	PLS-HC3	PLS-HC4	PLS-HC5	PLS-CVDP1	PLS-CVDP2	PLS-CVDP3	PLS-CVDR1	PLS-CVDR2
Donor classification	Healthy	Healthy	Healthy	Healthy	Healthy	COVID-19 positive	COVID-19 positive	COVID-19 positive	COVID-19 recovered	COVID-19 recovered
Gender	F	F	F	M	M	F	F	F	F	F
Age	35	33	59	36	35	26	27	21	20	23
Ethnicity	White	White	Other	White	Asian	Hispanic/Latino	White	White	White	White
SARS-coV-2 serological test										
IgM antibodies	-	-	-	-	-	Positive (1.2)	Negative (1)	Positive (1.8)	Negative (1)	Negative (1)
IgG antibodies	-	-	-	-	-	Positive (30.9)	Positive (33)	Positive (10.2)	Positive (22.7)	Negative (1)
Symptomatology	-	-	-	-	-	Moderate	Mild	Asymptomatic	Moderate	Mild
Diagnosis date	-	-	-	-	-	17/12/2020	07/11/2020	01/10/2020	12/10/2020	16/11/2020
Collection date	19/12/2022	04/07/2023	04/07/2023	04/07/2023	04/07/2023	13/01/2021	04/12/2020	20/10/2020	13/01/2021	06/01/2021
Days from diagnosis	-	-	-	-	-	27	27	19	93	51

Table B.3. Description of the quantified morphological parameters extracted from Imaris 9.8.

Morphological parameter	Description
Length/Size	The length of the longest principal axis inside the object (<i>BoundingBoxOO Length C</i>)
Width	The length of the second longest principal axis inside the object (<i>BoundingBoxOO Length B</i>)
Surface area	The sum of the triangle surfaces
Volume	Quantification of how much a surface object occupies
SA:V	Surface area divided by the volume
Mean RI	Mean intensity of voxels enclosed within the surface

C. Appendix to Chapter

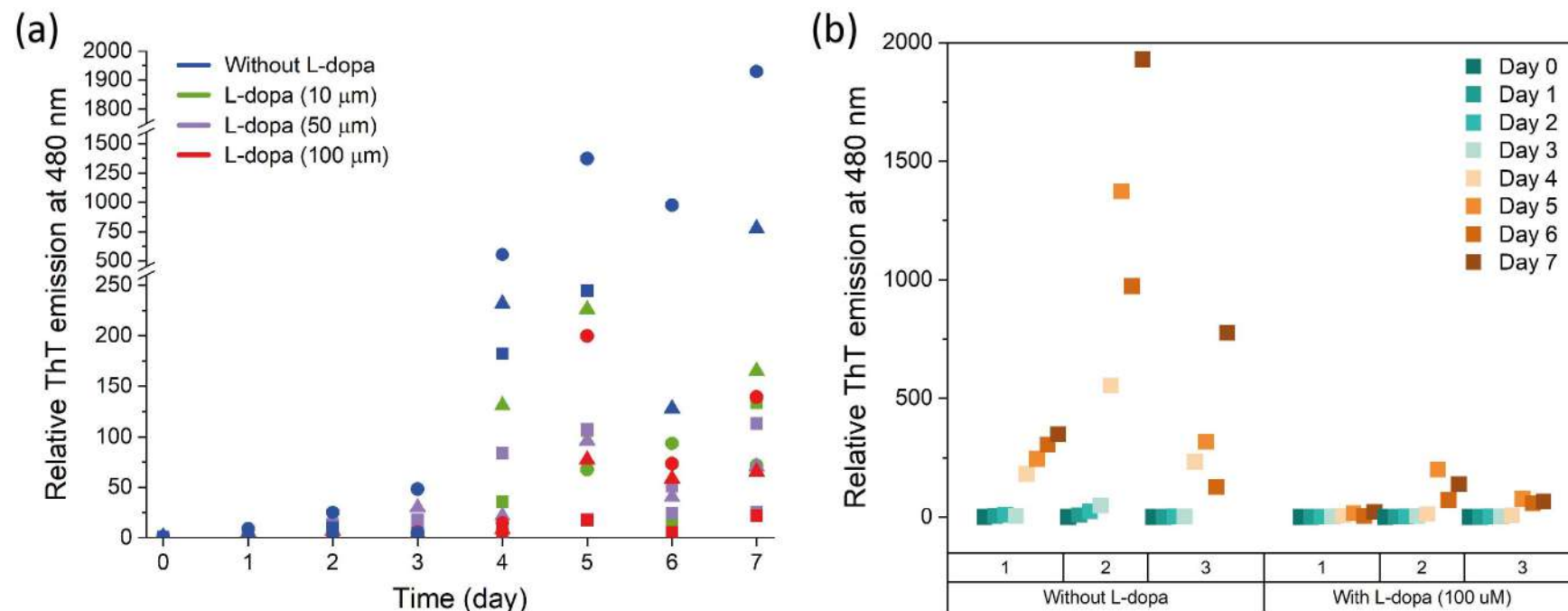


Figure C.1. Effect of L-dopa on α -Syn aggregation at 300 μM concentration. (a) Relative ThT emission data points of α -Syn incubated without (blue) and with different concentrations (green: 10 μM ; purple: 50 μM ; red: 100 μM) of L-dopa, over a period of 7 days. The symbol indicates each repetition. (b) Relative ThT emission data points of α -Syn incubated without and with L-dopa (100 μM) for each repetition, over a period of 7 days.

List of scientific publications and presentations

Publications in international peer-reviewed journals

Bergaglio, T., Bhattacharya, S., Thompson, D., Nirmalraj, P. N. *Label-free Digital Holotomography Reveals Ibuprofen-Induced Morphological Changes to Red Blood Cells*. ACS Nanoscience Au, 3 (3), 241-255, 2023.

DOI: doi.org/10.1021/acsnanoscienceau.3c00004

Bergaglio, T., Synhaivska, O., Nirmalraj, P. N. *Digital holo-tomographic 3D maps of COVID-19 microclots in blood to assess disease severity* (submitted). BioRxiv, 2023.

DOI: doi.org/10.1101/2023.09.12.557318

Hillen, A. E. J., Leferink, P. S., Breeuwsma, N. B., Dooves, S., Bergaglio, T., Van Der Knaap, M. S., Heine, V. M. *Therapeutic potential of human stem cell transplantations for Vanishing White Matter: A quest for the Goldilocks graft*. CNS Neuroscience & Therapeutics, 28 (9), 1315-1325, 2022. DOI: [10.1111/cns.13872](https://doi.org/10.1111/cns.13872)

Bergaglio, T., Luchicchi, A., Schenk, G. J. *Engine Failure in Axo-Myelinic Signaling: A Potential Key Player in the Pathogenesis of Multiple Sclerosis*. Frontiers in Cellular Neuroscience, 15, 610295, 2021. DOI: [10.3389/fncel.2021.610295](https://doi.org/10.3389/fncel.2021.610295)

Bergaglio, T., Kummer, N., Bhattacharya, S., Campioni, S., Thompson, D., Nirmalraj, P. N. *Capturing the effect of Levodopa on α -Synuclein and amyloid β 42 fibrils at the nanoscale*. In preparation, 2023.

Hardmeier, S. C., Bergaglio, T., Nirmalraj, P. N. *Urea as a fibrin solubilizer: revisited using nanoscale imaging and simulations*. In preparation, 2023.

Poster Contributions and Presentations

GCB PhD Symposium, Bern, Switzerland (June 2023). *Effect of ibuprofen on red blood cells studied using label-free digital holotomography*. (Poster and Flash Talk)

Bioimaging 2023, Lisbon, Portugal (February 2023). *Effect of ibuprofen on red blood cells studied using label-free digital holotomography.* (Poster)

EMPA PhD Symposium, Dübendorf, Switzerland (November 2022). Label-free digital holotomography reveals ibuprofen-induced morphological changes to red blood cells (Poster)

EMPA PhD Seminar, St. Gallen, Switzerland (August 2022). *Machine learning augmented red blood cell imaging and analytics.* (Talk)

Day of Biomedical Research (DBMR), Bern, Switzerland (July 2022). *Machine learning augmented red blood cell imaging and analytics.* (Poster)

LS² Annual Meeting, Zürich, Switzerland (April 2022). *Machine learning augmented red blood cell imaging and analytics.* (Poster and Short Talk) - **Best Short Talk Award**

GCB PhD Symposium, Bern, Switzerland (January 2022). *Machine learning augmented red blood cell imaging and analytics.* (Poster and Flash Talk)

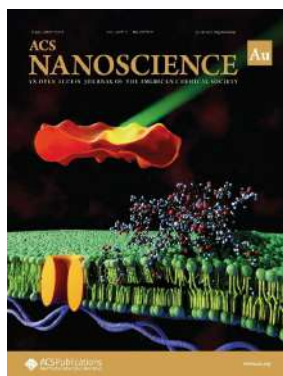
EMPA PhD Symposium, online (November 2021). *Machine learning augmented red blood cell imaging and analytics.* (Poster)

EMPA PhD Symposium, online (November 2020). *Machine learning augmented red blood cell imaging and analytics.* (Science Slam Video)

EXCITE Summer School in Biomedical Research, Zürich, Switzerland (September 2020). *Machine learning augmented red blood cell imaging and analytics.* (Poster) – **Best Poster Award**

Journal Cover Images

Front cover: *ACS Nanoscience Au*, volume 3, issue 3, June 2023



Declaration of Originality

Last name, first name: Bergaglio, Talia

Matriculation number: 19-130-335

I hereby declare that this thesis represents my original work and that I have used no other sources except as noted by citations.

All data, tables, figures and text citations which have been reproduced from any other source, including the internet, have been explicitly acknowledged as such.

I am aware that in case of non-compliance, the Senate is entitled to withdraw the doctorate degree awarded to me on the basis of the present thesis, in accordance with the “Statut der Universität Bern (Universitätsstatut; UniSt)”, Art. 69, of 7 June 2011.

Place, date

Dübendorf, 10.10.2023

Signature

Talia Bergaglio Digitally signed by Talia Bergaglio
Date: 2023.10.10 10:25:57 +02'00'